

**Evaluation of the Mechanical Strength of  
Bund Walls under the Catastrophic  
Failure of Storage Tanks via Fluid  
Structure Interaction**

**Islem Megdiche**

**A thesis submitted in partial fulfilment of  
the requirements of Liverpool John  
Moores University for the degree of  
Doctor of Philosophy**

**December 2018**

# Declaration

I declare that I am the sole author of this thesis and that no part of the thesis has been submitted for any other degree or qualification at another university.

# Abstract

The catastrophic failure of storage tanks is a serious problem that can have disastrous effects on the environment, local community and the economy. Bund walls are structures used around storage tanks where hazardous substances are stored and handled for the purpose of retaining the losses in materials. This study investigates the performance of bund wall structures under the impact loading caused by the collapse of storage tanks.

Research on this subject has taken place at Liverpool John Moores University over two decades. Studies have included investigating the dynamic pressures exerted on the bund wall, the overtopping fractions of the material representing the ratio of the quantity of fluid that escapes the banded area to the quantity of fluid that was initially in the tank, and mitigation measures to reduce the incurred losses. These previous studies along with other publications indicate clearly that bund walls are not designed to withstand dynamic loading that arises in the wake of sudden collapse of storage tanks. The novelty of this research lies in studying the performance of bund walls under the impact loading exerted by the sudden release of the stored material and proposing a new design of bund walls using Ultra-High Performance Fibre Reinforced Concrete (UHP-FRC). The investigation was carried out using the Fluid Structure Interaction (FSI) approach.

InterFOAM solver in OpenFOAM software was used to model the multiphase flow of the sudden release of the fluid. The available experimental data sets were used to validate the performance of the solver in terms of the prediction of dynamic pressures and overtopping fractions. The solver gives good results for many of the simulations investigated. An optimisation study on the optimum configuration of mitigation technique was conducted. FSI modelling was used to study the behaviour of the bund wall by coupling the explicit solver of Abaqus 2017 to InterFOAM via the MpCCI coupling environment. Bund walls with different shapes and under different loading conditions were simulated. Results show that bund walls made of plain concrete fail with the exception of circular bund walls. The use of UHP-FRC with the

incorporation of Catastrophic Overtopping Alleviation of Storage Tanks (COAST) mitigation technique allows the reduction of the overtopping fractions and minimises the damage to the bund wall. Results of the research allow the operators and site managers to gain an insight into the behaviour of bund walls under impact loading and perform more meaningful risk assessments.

# Dedication

To my beloved father Abdellaziz Megdiche and dear mother Fatma Smaoui for their encouragement to pursue my PhD abroad, their love and continuous support;  
to Mr. Mohammed Nouri and the spirit of Prof. Mustapha Zghal for their invaluable help;

to my brothers, sister, friends and everyone who encouraged me to undertake this challenge in life;

to the amazing friends who made my stay special in Liverpool, especially Ruba, Rana and Ikoko,

This work is dedicated to you.

# Acknowledgements

I would like to express my sincere gratitude to my director of studies, Dr. William Atherton for his continuous support, encouragement and guidance during this study. I am also indebted to my supervision team, Dr. Clare Harris and Dr. Glynn Rothwell for their help. I would like to thank Dr. David Allanson and Dr. Mehdi Seddighi for their invaluable support and advice on CFD.

I would like to thank the technicians of the Department of Civil Engineering and my colleagues for the good working environment.

In addition, I want to extend my appreciation and thanks to the examiners, Prof. Nawal Prinja and Prof. Rafid Al Khaddar for dedicating their valuable time to review my thesis.

Finally, I am grateful to Liverpool John Moores University for the financial support to undertake this research.

# List of publications

## Conference papers

Megdiche, I., Atherton, W., Harris, C. and Rothwell, G. (2017), Evaluating the mechanical strength of bund wall using smoothed particle hydrodynamics (sph) in abaqus, in ‘Proceeding of the 3rd BUiD Doctoral Research Conference’, Dubai, pp. 239-256.

Megdiche, I., Atherton, W., Harris, C. and Rothwell, G. (2017), A review of ultra-high performance fibre reinforced concrete, in ‘Proceeding of the Faculty Research Week’, Liverpool, UK, pp. 80-83.

Megdiche, I., Atherton, W., Harris, C., Rothwell, G. and Allanson, D. (2017), Computational fluid dynamics modelling of catastrophic failure of storage tanks, in ‘Proceeding of NAFEMS World Congress’, Stockholm, Sweden.

Megdiche, I., Atherton, W., Harris, C., Rothwell, G. and Allanson, D. (2018), Assessment of the performance of bund wall systems under impact loading, in ‘Proceeding of 6th European Conference on Computational Mechanics and 7th European Conference on Computational Fluid Dynamics’, Glasgow, UK.

Megdiche, I., Atherton, W., Allanson, D., Harris, C. and Rothwell, G. (2018), Effect of mitigation on partial failure of storage tank using computational fluid dynamics, in ‘Proceeding of NAFEMS 18 UK Conference’, Milton Keynes, UK, pp. 89-92.

Megdiche, I., Atherton, W., Harris, C., Rothwell, G. and Allanson, D. (2018), Evaluation of the performance of bund wall systems under the effect of catastrophic failure of storage tanks via numerical modelling, in ‘Proceeding of 13th World Congress on Computational Mechanics and 2nd Pan American Congress on Computational Me-

chanics', New York City, USA, pp. 180-192.

Megdiche, I., Atherton, W., Harris, C. and Rothwell, G. (2018), Predicting the dynamic properties of plain concrete under the impact load, in 'Proceeding of 2nd International Conference Trends and Recent Advances in Civil Engineering', Noida, India.

### **Oral Presentations**

Megdiche, I., The evaluation of the mechanical strength of bund walls under the action of catastrophic wave impact, The 8th Manchester Metropolitan University Postgraduate Research Conference, 5th November 2015.

Megdiche, I., Computational fluid dynamics modelling of catastrophic failure of storage tanks, OpenFOAM 12th workshop, 24th-27th July 2017, Exeter, UK.

### **Journal papers in preparation**

Megdiche, I., Atherton, W., Allanson, D., Harris, C. and and, G. R. (n.d.), 'Experimental investigation of the collapse of storage tanks', Journal of Loss Prevention in the Process Industries.

Megdiche, I., Atherton, W., Allanson, D., Harris, C. and and, G. R. (n.d.), 'Effect of mitigation measures on the catastrophic failure of storage tanks using computational fluid dynamic', International Journal of Multiphase Flow.

Megdiche, I., Atherton, W., Allanson, D., Harris, C. and and, G. R. (n.d.), 'New design of impact resistant bund wall system', Journal of Fluids and Structures.

# Contents

<b>Declaration</b>	<b>ii</b>
<b>Abstract</b>	<b>iv</b>
<b>Dedication</b>	<b>v</b>
<b>Acknowledgements</b>	<b>vi</b>
<b>List of publications</b>	<b>viii</b>
<b>List of Figures</b>	<b>xxii</b>
<b>List of Tables</b>	<b>xxiv</b>
<b>Nomenclature</b>	<b>xxix</b>
<b>List of Acronyms</b>	<b>xxxii</b>
<b>1 Introduction</b>	<b>1</b>
1.1 Project background . . . . .	1
1.2 Research aim and objectives . . . . .	5
1.3 Thesis outline . . . . .	6
<b>2 Literature review</b>	<b>7</b>
2.1 Introduction . . . . .	7
2.2 History of major incidents . . . . .	8
2.2.1 Modes of collapse, causes and consequences . . . . .	8
2.2.2 Incidents caused by natural disasters . . . . .	12
2.2.3 Incidents caused by accidental releases . . . . .	14
2.3 Current requirements . . . . .	20
2.3.1 Code of practice . . . . .	21
2.3.2 Legislation . . . . .	21

2.3.2.1	SEVESO III Directive . . . . .	21
2.3.2.2	COMAH Regulations . . . . .	22
2.4	Previous work . . . . .	22
2.4.1	Clark et al (2001) . . . . .	22
2.4.2	Atherton (2008) . . . . .	23
2.4.3	Ash (2010) . . . . .	24
2.5	Need for a new design . . . . .	25
2.6	Summary . . . . .	26
<b>3</b>	<b>Different approaches</b>	<b>28</b>
3.1	Introduction . . . . .	28
3.2	Physical and numerical modelling . . . . .	28
3.3	Computational Fluid Dynamics (CFD) . . . . .	29
3.3.1	Mathematical Modelling . . . . .	29
3.3.1.1	Governing equations of fluid dynamics . . . . .	30
3.3.1.2	Governing equations of two-phase flow . . . . .	31
3.3.1.3	Turbulence Modelling . . . . .	32
3.3.2	Numerical Modelling . . . . .	37
3.3.2.1	Discretisation of the solution domain . . . . .	38
3.3.2.2	Discretisation of the transport equation . . . . .	38
3.3.2.3	Implementation of boundary conditions . . . . .	42
3.3.2.4	Solution procedure . . . . .	43
3.3.2.5	Solution Procedure for two-phase flow . . . . .	43
3.3.2.6	Source of errors . . . . .	45
3.4	Finite Element Analysis (FEA) . . . . .	45
3.4.1	Load application analysis procedure . . . . .	50
3.4.1.1	Impact loading types . . . . .	50
3.4.1.2	Different techniques for impact load modelling . . . . .	51
3.4.2	Geometric modelling . . . . .	51
3.4.3	Material modelling . . . . .	53
3.4.3.1	Concrete Damage Plasticity model . . . . .	53

3.4.3.2	Steel reinforcement constitutive model . . . . .	56
3.5	Ultra High Performance Fibre Reinforced Concrete UHP-FRC . . . . .	57
3.5.1	Principle of UHP-FRC . . . . .	58
3.5.2	Mechanical properties of UHP-FRC under low strain rate . . . . .	58
3.5.2.1	Compressive behaviour . . . . .	58
3.5.2.2	Tensile behaviour . . . . .	59
3.5.2.3	Fracture behaviour . . . . .	60
3.6	Material behaviour at high strain . . . . .	60
3.7	Fluid Structure Interaction (FSI) . . . . .	61
3.7.1	Types of approach . . . . .	62
3.7.2	MpCCI workflow . . . . .	62
3.8	Dimensional analysis . . . . .	64
3.9	Summary . . . . .	65
<b>4</b>	<b>Methodology</b>	<b>66</b>
4.1	Introduction . . . . .	66
4.2	Modelling methodology for the CFD . . . . .	66
4.2.1	Validation test . . . . .	66
4.2.2	Software used . . . . .	68
4.2.3	Test matrix for the standard configurations . . . . .	68
4.2.4	Test matrix for configurations incorporating mitigation techniques . . . . .	72
4.2.5	Test matrix for the asymmetric configurations . . . . .	75
4.2.6	Mathematical model . . . . .	76
4.2.6.1	Two-phase flow solver . . . . .	76
4.2.6.2	Turbulence model . . . . .	76
4.2.6.3	Material physical properties . . . . .	76
4.2.7	Numerical model . . . . .	77
4.2.7.1	Discretisation of the solution domain . . . . .	77
4.2.7.2	Discretisation of transport equations . . . . .	80
4.2.7.3	Boundary conditions . . . . .	81

4.2.7.4	Solution procedure . . . . .	82
4.3	Modelling methodology for the FEA . . . . .	82
4.3.1	Validation test . . . . .	82
4.3.2	Software used . . . . .	84
4.3.3	Test matrix . . . . .	85
4.3.4	Development of 3D-FE model . . . . .	87
4.3.4.1	Geometric modelling, boundary conditions and mesh	87
4.3.4.2	Geometric modelling of reinforced concrete wall . . .	88
4.3.4.3	Material constitutive models . . . . .	89
4.4	Modelling methodology for the Co-simulation . . . . .	93
4.4.1	Software used . . . . .	93
4.4.2	Coupling process . . . . .	94
4.5	Summary . . . . .	99
<b>5</b>	<b>CFD results</b>	<b>100</b>
5.1	Introduction . . . . .	100
5.2	Experimental results for the standard cases . . . . .	101
5.2.1	Presentation and analysis of the results . . . . .	101
5.2.1.1	The effect of the separation distance and capacity of the bund wall . . . . .	101
5.2.1.2	The effect of high collar bund wall . . . . .	103
5.2.1.3	The effect of the fluid height and the shape of bund wall . . . . .	104
5.2.1.4	The effect of the fluid temperature . . . . .	106
5.3	CFD results for the standard cases . . . . .	106
5.3.1	Presentation and analysis of the results . . . . .	106
5.3.1.1	The effect of the separation distance and capacity of bund wall . . . . .	106
5.3.1.2	The effect of high collar bund wall . . . . .	114
5.3.1.3	The effect of the fluid height and shape of bund wall	117
5.3.1.4	The effect of the fluid temperature . . . . .	129

5.3.2	Critical appraisal of InterFOAM . . . . .	130
5.4	CFD results for standard cases incorporating mitigation techniques .	130
5.4.1	Presentation and analysis of the results . . . . .	130
5.4.1.1	The effect of COAST on the capacity and shapes of the bund wall . . . . .	136
5.5	CFD results for the partial failure cases . . . . .	137
5.5.1	Presentation and analysis of the results . . . . .	137
5.6	Similitude of fluid model . . . . .	139
5.7	Summary . . . . .	140
<b>6</b>	<b>FEA results</b>	<b>142</b>
6.1	Introduction . . . . .	142
6.2	Validation of the FSI simulation . . . . .	142
6.3	Presentation and analysis of the results . . . . .	145
6.3.1	Simulation results of the plain concrete wall . . . . .	146
6.3.1.1	Simulation results of the circular wall . . . . .	146
6.3.1.2	Comparison of the behaviour of a circular wall sub- jected to a centred and an off-centred loads . . . . .	159
6.3.1.3	Simulations results of the square wall . . . . .	159
6.3.1.4	Comparison of the behaviour of a square wall sub- jected to a centred and an off-centred loads . . . . .	168
6.3.1.5	Simulation results of the rectangular wall . . . . .	169
6.3.1.6	Comparison of the behaviour of a rectangular wall subjected to a centred and an off-centred loads . . . . .	185
6.3.1.7	Comparison of the behaviour of different shapes of the wall . . . . .	185
6.3.2	Simulation results of the reinforced concrete wall . . . . .	187
6.3.3	Simulation results of UHP-FRC wall . . . . .	191
6.3.3.1	Comparison between plain UHP-FRC wall and UHP- FRC wall incorporating starter rebars . . . . .	205
6.3.4	Comparison between plain and UHP-FRC walls . . . . .	206

6.4	Critical appraisal of the FSI simulation . . . . .	207
6.5	Similitude of structural model . . . . .	210
6.6	Summary . . . . .	215
<b>7</b>	<b>Conclusions and future works</b>	<b>218</b>
7.1	Introduction . . . . .	218
7.2	Conclusions . . . . .	219
7.2.1	The performance of InterFOAM . . . . .	219
7.2.2	The optimisation of mitigation measure . . . . .	220
7.2.3	The structural integrity of the bund wall . . . . .	220
7.2.4	The benefit to stakeholders and beneficiaries . . . . .	221
7.3	Recommendations for future work . . . . .	221
7.3.1	Recommendations related to CFD . . . . .	221
7.3.2	Recommendations related to FEA . . . . .	222
7.3.3	Recommendations related to dimensional analysis . . . . .	223
7.4	Summary . . . . .	223
	<b>References</b>	<b>231</b>
	<b>Appendix A CFD appendix</b>	<b>233</b>
	<b>Appendix B FEA appendix</b>	<b>243</b>

# List of Figures

2.1	Collapse of the tanks of Vest Tank Company <sup>1</sup> (Skjold et al., 2008) . . .	16
2.2	Rupture of the bund wall of the Buncefield oil storage depot . . . . .	18
3.1	C3D8R element . . . . .	52
3.2	Uniaxial stress-strain curves in CDP model (Simulia, 2016) . . . . .	56
3.3	Typical compressive behaviour of UHP-FRC (Fehling et al., 2004) . . .	59
3.4	Typical tensile behaviour of UHP-FRC (Fehling et al., 2004) . . . . .	60
3.5	Fracture energy of UHP-FRC (Othman, 2016) . . . . .	60
3.6	Serial coupling . . . . .	63
3.7	Parallel coupling . . . . .	63
4.1	Experiment of the collapse of the storage tank - front view . . . . .	67
4.2	Experiment of the collapse of the storage tank - side view . . . . .	67
4.3	Tank and bund wall nomenclature of the different shapes . . . . .	68
4.4	Tank and bund wall nomenclature - front view . . . . .	69
4.5	Tank and bund arrangements incorporating MOTIF and COAST . . .	73
4.6	Bund wall incorporating COAST . . . . .	73
4.7	Angle of COAST . . . . .	73
4.8	Tank and bund nomenclature for partial failure . . . . .	75
4.9	Mesh and boundary conditions of the fluid domain . . . . .	78
4.10	Mesh of the fluid domain - inside view . . . . .	79
4.11	Mesh of the fluid domain - front view . . . . .	79
4.12	Mesh of the fluid domain - bottom view . . . . .	80
4.13	Experimental set-up . . . . .	83
4.14	Geometry of the wall and strain gauge position . . . . .	83
4.15	Experiment: prior to the release of the gate . . . . .	84
4.16	Experiment: at the time of impact . . . . .	84

4.17	Geometry and boundary conditions of a square wall incorporating COAST . . . . .	88
4.18	Mesh of a square wall incorporating COAST . . . . .	88
4.19	Geometric modelling of reinforced concrete wall . . . . .	89
4.20	Reinforcements arrangement . . . . .	89
4.21	Model step . . . . .	95
4.22	Coupling step: Global quantity . . . . .	95
4.23	Coupling step: Build regions . . . . .	96
4.24	Coupling step: Define quantity sets . . . . .	96
4.25	Coupling step: Assign quantity sets . . . . .	97
4.26	Go step . . . . .	97
4.27	MpCCI grid morpher . . . . .	98
4.28	Go step: MpCCI workflow . . . . .	98
5.1	Position of the transducers along the bund wall . . . . .	100
5.2	Effect of the separation distance and the capacity of the wall . . . . .	102
5.3	Effect of the high collar bund wall . . . . .	104
5.4	Effect of the height of fluid and shape of the wall . . . . .	104
5.5	Effect of the shape of bund wall . . . . .	105
5.6	Effect of the temperature . . . . .	106
5.7	Flow structure corresponding to a standard configuration - test $B_1$ (circular wall) . . . . .	108
5.8	Experimental flow structure corresponding to a standard configura- tion - test $B_1$ (circular wall) . . . . .	109
5.9	Effect of the separation distance (circular wall, tall tank, capacity 110%) . . . . .	110
5.10	Effect of the separation distance (circular wall, tall tank, capacity 120%) . . . . .	111
5.11	Effect of the separation distance (circular wall, tall tank, capacity 150%) . . . . .	112

5.12	Effect of the separation distance (circular wall, tall tank, capacity 200%) . . . . .	113
5.13	High collar bund wall, $h/H = 1$ . . . . .	115
5.14	High collar bund wall, $h/H = 1.2$ . . . . .	116
5.15	Flow structure corresponding to a standard configuration - test <i>Wall</i> <sub>1</sub> (triangular wall) . . . . .	118
5.16	Experimental flow structure corresponding to a standard configuration - test <i>Wall</i> <sub>1</sub> (triangular wall) . . . . .	119
5.17	Effect of the height of the fluid (triangular wall, capacity 110%) . . . . .	120
5.18	Flow structure corresponding to a standard configuration - test <i>Wall</i> <sub>2</sub> (square wall) . . . . .	122
5.19	Experimental flow structure corresponding to a standard configuration - test <i>Wall</i> <sub>2</sub> (square wall) . . . . .	123
5.20	Effect of the height of the fluid (square wall, capacity 110%) . . . . .	124
5.21	Flow structure corresponding to a standard configuration - test <i>Wall</i> <sub>3</sub> (rectangular wall) . . . . .	126
5.22	Experimental flow structure corresponding to a standard configuration - test <i>Wall</i> <sub>3</sub> (rectangular wall) . . . . .	127
5.23	Effect of the height of the fluid (rectangular wall, capacity 110%) . . . . .	128
5.24	Effect of the temperature of the fluid (circular wall, tall tank, capacity 110%) . . . . .	129
5.25	Effect of the temperature of the fluid (square wall, tall tank, capacity 110%) . . . . .	129
5.26	Optimisation of the angle of COAST . . . . .	131
5.27	Zone of the highest dynamic pressure . . . . .	132
5.28	Flow structure corresponding to a configuration incorporating MOTIF	133
5.29	Flow structure corresponding to a configuration incorporating MOTIF and COAST . . . . .	134
5.30	Flow structure corresponding to a configuration incorporating COAST	135
5.31	Selection of the mitigation technique . . . . .	136

5.32	Effect of COAST with different capacities of the bund wall . . . . .	137
5.33	Effect of COAST on the overtopping fraction for different shapes of the bund wall . . . . .	137
5.34	Flow structure corresponding to a partial failure of a tank . . . . .	138
6.1	Flow structure of the water release . . . . .	142
6.2	Pressure field of the water flow . . . . .	143
6.3	Numerical results of the strain in the wall . . . . .	143
6.4	Non symmetry in the flow structure . . . . .	144
6.5	Experimental results of the strain . . . . .	145
6.6	Non symmetric distribution of tensile damage . . . . .	146
6.7	Flow behaviour and tensile damage of a plain concrete circular wall subjected to a centred load at $t = 0.1s$ . . . . .	147
6.8	Flow behaviour and tensile damage of a plain concrete circular wall subjected to a centred load at $t = 0.9s$ . . . . .	148
6.9	Flow behaviour and tensile damage of a plain concrete circular wall subjected to a centred load at $t = 1s$ . . . . .	149
6.10	Flow behaviour and tensile damage of a plain concrete circular wall subjected to a centred load at $t = 1.2s$ . . . . .	150
6.11	Flow behaviour and tensile damage of a plain concrete circular wall subjected to a centred load at $t = 1.7s$ . . . . .	151
6.12	Flow behaviour and tensile damage of a plain concrete circular wall subjected to a centred load at $t = 2s$ . . . . .	152
6.13	Flow behaviour and tensile damage of a plain concrete circular wall subjected to an off-centred load at $t = 0.1s$ . . . . .	153
6.14	Flow behaviour and tensile damage of a plain concrete circular wall subjected to an off-centred load at $t = 0.9s$ . . . . .	154
6.15	Flow behaviour and tensile damage of a plain concrete circular wall subjected to an off-centred load at $t = 1s$ . . . . .	155
6.16	Flow behaviour and tensile damage of a plain concrete circular wall subjected to an off-centred load at $t = 1.2s$ . . . . .	156

6.17	Flow behaviour and tensile damage of a plain concrete circular wall subjected to an off-centred load at $t = 1.7s$ . . . . .	157
6.18	Flow behaviour and tensile damage of a plain concrete circular wall subjected to an off-centred load at $t = 2s$ . . . . .	158
6.19	Comparison of the structural response of a plain concrete circular wall under a centred and an off-centred loads . . . . .	159
6.20	Flow behaviour and tensile damage of a plain concrete square wall subjected to a centred load at $t = 0.1s$ . . . . .	160
6.21	Flow behaviour and tensile damage of a plain concrete square wall subjected to a centred load at $t = 0.4s$ . . . . .	161
6.22	Flow behaviour and tensile damage of a plain concrete square wall subjected to a centred load at $t = 0.5s$ . . . . .	162
6.23	Flow behaviour and tensile damage of a plain concrete square wall subjected to a centred load at $t = 0.6s$ . . . . .	163
6.24	Flow behaviour and tensile damage of a plain concrete square wall subjected to an off-centred load at $t = 0.1s$ . . . . .	164
6.25	Flow behaviour and tensile damage of a plain concrete square wall subjected to an off-centred load at $t = 0.4s$ . . . . .	165
6.26	Flow behaviour and tensile damage of a plain concrete square wall subjected to an off-centred load at $t = 0.5s$ . . . . .	166
6.27	Flow behaviour and tensile damage of a plain concrete square wall subjected to an off-centred load at $t = 0.6s$ . . . . .	167
6.28	Comparison of the structural response of a plain concrete square wall under a centred and an off-centred loads . . . . .	168
6.29	Flow behaviour and tensile damage of a plain concrete rectangular wall subjected to a centred load at $t = 0.1s$ . . . . .	170
6.30	Flow behaviour and tensile damage of a plain concrete rectangular wall subjected to a centred load at $t = 0.3s$ . . . . .	171
6.31	Flow behaviour and tensile damage of a plain concrete rectangular wall subjected to a centred load at $t = 0.4s$ . . . . .	172

6.32	Flow behaviour and tensile damage of a plain concrete rectangular wall subjected to a centred load at $t = 0.5s$ . . . . .	173
6.33	Flow behaviour and tensile damage of a plain concrete rectangular wall subjected to a centred load at $t = 0.6s$ . . . . .	174
6.34	Flow behaviour and tensile damage of a plain concrete rectangular wall subjected to an off-centred load along the $x$ axis at $t = 0.1s$ . . .	175
6.35	Flow behaviour and tensile damage of a plain concrete rectangular wall subjected to an off-centred load along the $x$ axis at $t = 0.3s$ . . .	176
6.36	Flow behaviour and tensile damage of a plain concrete rectangular wall subjected to an off-centred load along the $x$ axis at $t = 0.4s$ . . .	177
6.37	Flow behaviour and tensile damage of a plain concrete rectangular wall subjected to an off-centred load along the $x$ axis at $t = 0.5s$ . . .	178
6.38	Flow behaviour and tensile damage of a plain concrete rectangular wall subjected to an off-centred load along the $x$ axis at $t = 0.6s$ . . .	179
6.39	Flow behaviour and tensile damage of a plain concrete rectangular wall subjected to an off-centred load along the $y$ axis at $t = 0.1s$ . . .	180
6.40	Flow behaviour and tensile damage of a plain concrete rectangular wall subjected to an off-centred load along the $y$ axis at $t = 0.3s$ . . .	181
6.41	Flow behaviour and tensile damage of a plain concrete rectangular wall subjected to an off-centred load along the $y$ axis at $t = 0.4s$ . . .	182
6.42	Flow behaviour and tensile damage of a plain concrete rectangular wall subjected to an off-centred load along the $y$ axis at $t = 0.5s$ . . .	183
6.43	Flow behaviour and tensile damage of a plain concrete rectangular wall subjected to an off-centred load along the $y$ axis at $t = 0.6s$ . . .	184
6.44	Comparison of the structural response of a plain concrete rectangular wall under a centred and an off-centred loads . . . . .	185
6.45	Comparison between different shapes of bund wall in terms of tensile damage . . . . .	186
6.46	Flow behaviour and tensile damage of a reinforced concrete square wall subjected to a centred load at $t = 0.1s$ . . . . .	188

6.47	Flow behaviour and tensile damage of a reinforced concrete square wall subjected to a centred load at $t = 0.5s$ . . . . .	189
6.48	Flow behaviour and tensile damage of a reinforced concrete square wall subjected to a centred load at $t = 1.2s$ . . . . .	190
6.49	Flow behaviour and tensile damage of a UHP-FRC square wall subjected to a centred load and incorporating COAST at $t = 0.2s$ . . . .	192
6.50	Flow behaviour and tensile damage of a UHP-FRC square wall subjected to a centred load and incorporating COAST at $t = 0.6s$ . . . .	193
6.51	Flow behaviour and tensile damage of a UHP-FRC square wall subjected to a centred load and incorporating COAST at $t = 0.8s$ . . . .	194
6.52	Flow behaviour and tensile damage of a UHP-FRC square wall subjected to a centred load and incorporating COAST at $t = 1s$ . . . . .	195
6.53	Flow behaviour and tensile damage of a UHP-FRC square wall subjected to a centred load and incorporating COAST at $t = 1.2s$ . . . .	196
6.54	Flow behaviour and tensile damage of a UHP-FRC square wall subjected to a centred load and incorporating COAST at $t = 1.8s$ . . . .	197
6.55	Flow behaviour and tensile damage of a UHP-FRC square wall subjected to a centred load and incorporating COAST at $t = 2.4s$ . . . .	198
6.56	Flow behaviour and tensile damage of a UHP-FRC square wall subjected to a centred load and incorporating COAST at $t = 3s$ . . . . .	199
6.57	Flow behaviour and tensile damage of a UHP-FRC square wall subjected to a centred load and incorporating COAST and starter bars at $t = 0.1s$ . . . . .	200
6.58	Flow behaviour and tensile damage of a UHP-FRC square wall subjected to a centred load and incorporating COAST and starter bars at $t = 0.4s$ . . . . .	201
6.59	Flow behaviour and tensile damage of a UHP-FRC square wall subjected to a centred load and incorporating COAST and starter bars at $t = 0.6s$ . . . . .	202

6.60	Flow behaviour and tensile damage of a UHP-FRC square wall subjected to a centred load and incorporating COAST and starter bars at $t = 0.8s$ . . . . .	203
6.61	Flow behaviour and tensile damage of a UHP-FRC square wall subjected to a centred load and incorporating COAST and starter bars at $t = 1s$ . . . . .	204
6.62	Tensile damage of UHP-FRC square wall incorporating COAST . . . . .	205
6.63	Tensile damage of UHP-FRC square wall incorporating COAST and starter bars . . . . .	205
6.64	Comparison of the structural response between UHP-FRC wall and UHP-FRC wall incorporating starter bars . . . . .	206
6.65	Comparison of the structural response between plain concrete wall and UHP-FRC wall . . . . .	207
6.66	Total energy of the simulation of plain concrete circular wall . . . . .	209
6.67	Total energy of the simulation of plain concrete rectangular wall . . . . .	210
6.68	Circular bund . . . . .	210
6.69	Square bund . . . . .	215
6.70	Rectangular bund . . . . .	215
A.1	Boundary conditions for alpha-oil field . . . . .	233
A.2	Boundary conditions for velocity field . . . . .	234
A.3	Boundary conditions for pressure field . . . . .	235
A.4	Boundary conditions for turbulent kinetic energy . . . . .	236
A.5	Boundary conditions for specific dissipation rate . . . . .	237
A.6	Boundary conditions for turbulent viscosity . . . . .	238
A.7	Control dictionary . . . . .	239
A.8	fvschemes dictionary . . . . .	240
A.9	fvsolution dictionary . . . . .	241
A.10	setFieldsdict dictionary . . . . .	242
B.1	Confirmation of the non-symmetry of the CDP model - email (part 1)	243
B.2	Confirmation of the non-symmetry of the CDP model - email (part 2)	244

# List of Tables

3.1	Different load cases and corresponding strain rates (CEB-FIP, 1988)	61
4.1	Effect of the separation distance (circular wall, tall tank, capacity 110%)	69
4.2	Effect of the separation distance (circular wall, tall tank, capacity 120%)	69
4.3	Effect of the separation distance (circular wall, tall tank, capacity 150%)	70
4.4	Effect of the separation distance (circular wall, tall tank, capacity 200%)	70
4.5	High collar bund wall (circular wall)	70
4.6	Effect of the height of the fluid (triangular wall, capacity 110%)	71
4.7	Effect of the height of the fluid (square wall, capacity 110%)	71
4.8	Effect of the height of the fluid (rectangular wall, capacity 110%)	71
4.9	Effect of the fluid temperature (circular wall, tall tank, capacity 110%)	72
4.10	Effect of the fluid temperature (square wall, middle tank, capacity 110%)	72
4.11	Test matrix for circular bund wall incorporating mitigation	74
4.12	Effect of COAST on non-circular bund walls	75
4.13	Partial failure tests	76
4.14	Surface tension between the fluids (Sahasrabudhe et al., 2017)	77
4.15	Physical properties of the fluids (Sahasrabudhe et al., 2017)	77
4.16	Discretisation schemes	81
4.17	Boundary conditions	82
4.18	Test matrix for FSI simulations	85
4.19	Material properties for the steel (Othman, 2016)	90

4.20	Material properties for the CDP model for plain concrete (Simulia, 2016) . . . . .	91
4.21	Material properties for UHP-FRC (Othman, 2016) . . . . .	92
5.1	Dynamic pressures and overtopping fractions of the partial failure . .	139
5.2	Common non-dimensional groups in fluid mechanics (Munson et al., 2010) . . . . .	139
6.1	Numerical results of the strain in the wall . . . . .	144
6.2	Experimental results of the strain in the wall . . . . .	145
6.3	Basic dimensions of the variables . . . . .	212

# Nomenclature

## Dimensionless Numbers

$Co$  Courant number

$Fr$  Froude number

$Ma$  Mach number

$Re$  Reynolds number

$We$  Weber number

## Greek Symbols

$\Delta\epsilon$  Element strain increment

$\Delta t$  Time step

$\Gamma$  Diffusivity

$\Gamma_{lg}$  Liquid gas interface

$\alpha$  Volume fraction

$\delta$  Dirac delta function

$\epsilon^{(m)}$  Strain within the element

$\eta$  Kolmogorov length scale

$\kappa$  Interfacial curvature

$\lambda_M$  Delimiter

$\mu$  Dynamic viscosity

$\mu_m$  Dynamic viscosity of the mixture

$\mu_t$  Eddy viscosity

$\nu$  Kinematic viscosity

$\nu_t$  Kinematic turbulent viscosity

$\omega$  Specific dissipation rate

$\bar{\epsilon}$  Virtual strain

$\bar{\sigma}$  Effective stress

$\bar{\sigma}_c$  Effective compressive stress

$\bar{\sigma}_t$  Effective tensile stress

$\phi$  Tensorial quantity  
 $\psi$  Dilation angle  
 $\rho^{(m)}$  Density of the element  
 $\rho_f$  Fluid density  
 $\rho_m$  Density of the mixture  
 $\sigma$  Stress matrix  
 $\sigma_f$  Stress tensor of the fluid  
 $\sigma_s$  Surface tension  
 $\sigma_y$  Yield stress of the material  
 $\sigma_{t0}$  Uniaxial tensile stress at failure  
 $\tau$  Kolmogorov time scale  
 $\tau_{ij}$  Reynolds stress tensor  
 $\theta$  Angle of inclination of COAST  
 $v$  Kolmogorov velocity  
 $\varepsilon$  Dissipation rate of the smallest eddies  
 $\zeta^{(m)}$  Damping property parameter  
 $\hat{\sigma}_{max}$  Maximum principle effective stress  
 $\bar{\sigma}_c(\tilde{\varepsilon}_c^{pl})$  Effective compressive cohesion stress  
 $\bar{\sigma}_t(\tilde{\varepsilon}_t^{pl})$  Effective tensile cohesion stress  
 $\sigma_i^{(m)}$  Element initial stress

### Latin Symbols

$A$  Spatial operator  
 $E$  Elastic modulus  
 $F$  Mass flux through face  $f$   
 $H$  Height of the fluid in the tank  
 $K$  Ratio of the second stress invariant on the tensile meridian to that on the compressive meridian  
 $L$  Length  
 $M$  Mass  
 $Q$  Dynamic overtopping

$S$  Effective stress deviator  
 $T$  Time  
 $U$  Velocity of the fluid flow  
 $V_P$  Control volume around point  $P$   
 $[R]$  Load vector  
 $\partial V_P$  Boundary surface of the control volume  
 $c$  Sound velocity in the medium  
 $d$  Distance between the centres of cells  $P$  and  $N$   
 $dS$  Infinitesimal surface element  
 $e$  Eccentricity  
 $g$  Gravity acceleration  
 $h$  Height of the bund wall  
 $k$  Turbulent kinetic energy  
 $l$  Length of the bund wall  
 $n$  Normal vector  
 $p$  Pressure  
 $r$  Radius of the bund wall  
 $t$  Thickness of the bund wall  
 $u$  Displacement  
 $w$  Width of the bund wall

### **Oversymbols**

$\ddot{u}_i$  Nodal acceleration  
 $\dot{u}_i$  Nodal velocity  
 $\hat{u}$  Nodal displacement  
 $\bar{u}$  Virtual displacement

### **Subscripts**

$C_s$  Damping matrix  
 $E_0$  Initial elastic stiffness  
 $E_{total}$  Total energy  
 $K_s$  Stiffness Matrix

$M_s$  Mass matrix  
 $Q_{COAST}$  Overtopping quantities when incorporating COAST  
 $Q_{MOTIF}$  Overtopping quantities when incorporating MOTIF  
 $Q_{M\&C}$  Overtopping quantities when incorporating MOTIF and COAST  
 $R_B$  Effect of the element body force  
 $R_C$  Nodal concentrated load  
 $R_I$  Effect of the element initial stresses  
 $R_S$  Effect of the element surface force  
 $S_{ij}$  Mean strain rate tensor  
 $\frac{f_{bo}}{f_{co}}$  Ratio of initial equibiaxial compressive yield stress to initial compressive yield stress  
 $d_c$  Compressive damage  
 $d_t$  Tensile damage  
 $g_b$  The gradient of the dependent variable normal to the boundary face  
 $k_d$  Number of basic dimensions  
 $l_c$  Characteristic length  
 $l_m$  Mixing length distance  
 $l_t$  Length scale  
 $l_{min}$  Smallest dimension of the element  
 $m_d$  Model  
 $n_d$  Number of variables  
 $n_s$  Scale factor  
 $n_{dof}$  Number of degrees of freedom  
 $p_d$  Prototype  
 $t_i$  Any significant time  
 $u_i$  Nodal displacement

### Superscripts

$A^*$  Spatial discretisation of  $A$   
 $B^{(m)}$  Strain displacement matrix  
 $C^{(m)}$  Constitutive law of material

$H^{(m)}$  Displacement interpolation matrix

$R_C^i$  Concentrated force

$f^B$  Body force

$f^S$  Surface force

$u'$  Fluctuating component of velocity

$u^{(m)}$  Displacement within the element  $m$

$y^+$  Non dimensionless distance from the wall

$\bar{u}^i$  Virtual displacement induced by the concentrated force

$\bar{u}^S$  Virtual displacement induced by the surface force  $f^S$

# List of Acronyms

API	American Petroleum Institute
ARIA	Analysis, Research and Information on Accidents
AST	Above-ground Storage Tanks
BASF	Baden Aniline and Soda Facto
BBC	British Broadcasting Corporation
BD	Blended Differencing
BP	British Petroleum
BPA	British Pipeline Agency
BS EN	British Standard European Norm
CA	Competent Authority
CD	Central Differencing
CDP	Concrete Damage Plasticity
CFD	Computational Fluid Dynamics
CIRIA	Construction Industry Research and Information
CLP	Classification Labelling and Packaging
COAST	Catastrophic Overtopping Alleviation of Storage Tanks
COMAH	Control of Major Accident Hazards
CSF	Continuum Surface Force
CSS	Conventional Serial Staggered
CV	Control Volume
DIF	Dynamic Increase Factor
DNS	Direct Numerical Simulation
EA	Environmental Agency
EHS	Environment and Heritage Service
eMARS	Electronic Major Accident Reporting System

EPA	Environmental Protection Agency
ESSO	Eastern States Standard Oil
EU	European Union
EVM	Eddy Viscosity Modelling
FCCU	Fluid Catalytic Cracking Unit
FDM	Finite Difference Method
FEA	Finite Element Analysis
FEM	Finite Element Method
FSI	Fluid Structure Interaction
FVM	Finite Volume Method
HSE	Health and Safety Executive
IHLS	Independent High-Level Switch
LES	Large Eddy Simulation
MAPP	Major Accident Prevention Policy
MOTIF	Mitigation of Tank Instantaneous Failure
MULES	Multidimensional Universal Limiter for Explicit Solution
NRW	National Resources Wales
NS	Navier-Stokes
OECD	Organisation for Economic Cooperation and Development
OSHA	Occupational Safety and Health Administration
OSR	Oil Storage Regulation
PDE	Partial Differential Equation
PISO	Pressure Implicit Split Operator
RANS	Reynolds-Averaged Navier-Stokes
RC	Reinforced Concrete
RSM	Reynolds Stress Modelling
SEPA	Scottish Environment Protection Agency
SPH	Smoothed Particle Hydrodynamics

SST	Shear-Stress Transport
UD	Upwind Differencing
UHP-FRC	Ultra High Performance Fibre Reinforced Concrete
UK	United Kingdom
USA	United States of America
VOF	Volume of Fluid
XFEM	Extended Finite Element Method
ZEMA	Zentrale Melde- und Auswertestelle für Störfälle und Störungen (Database on Major Accidents and Incidents in Germany)

# Chapter 1

## Introduction

### 1.1 Project background

Above-ground Storage Tanks (AST) are large vessels used to store many kinds of products such as water, waste matters, chemical and petrochemical products, etc. (Megdiche, 2013). There are many threats that can arise from the storage of hazardous materials which cause serious impacts to the environment, economy and immediate community. There have been numerous catastrophic failures of storage tanks around the world. One of the most disastrous being that which occurred at Buncefield, UK on 11<sup>th</sup> December 2005 and was deemed to be the largest explosion in Europe since the 2<sup>nd</sup> world war according to the BBC news (Ash, 2010). It was caused by overfilling due to an instrumentation failure and resulted in the injuries of 43 people, the destruction of the site, devastation estimated at £10,000,000 as well as harm to the environment (Atherton, 2008). Such catastrophic failures cannot only damage the environment but also harm the reputation of the company concerned, since environmental legislation permits courts to jail managers and directors if their negligence in applying the best practices results in pollution. An example is the imprisonment of three directors of a South Wales company because of leakage and dangerous storage of composting leachate. The first received 12 months, the second received 32 weeks and the third received 16 weeks of imprisonment apart from the unpaid hours of work and being banned from acting as directors (Walton, 2014). In addition to the reputational damage, companies are subjected to paying very high fines which according to Walton (2014), have increased significantly and can be extremely high, especially in cases where it is necessary to clean up the groundwater and the contaminated land. These liabilities might be compounded by the insurance

costs that are likely to rise for companies responsible for failure of their facilities. As a way to protect their reputations, companies are asked to apply the best practices and comply with the appropriate regulations.

In the UK, there are various environmental agencies that work on compliance with the regulations to ensure the prevention of pollution. These include the Environment Agency (EA) for England, National Resources Wales (NRW), Environment and Heritage Service (EHS) for Northern Ireland, Scottish Environment Protection Agency (SEPA) for Scotland and the Health and Safety Executive (HSE). These agencies are known as Competent Authorities (CA) or Regulators, they have statutory duties to enforce the regulations relevant to the protection of the environment. In the UK, businesses whose activities are related to the storage of any hazardous products need to comply with the Control of Major Accident Hazards (COMAH) which is an instrument aiming at the prevention of major accidents and reducing the consequences for the population and the environment (Walton, 2014). They came into force in the UK in 1999 (Ash, 2010) and were recently amended after the SEVESO III Directive came into force replacing the SEVESO II on 1<sup>st</sup> June 2015. SEVESO Directives are the main EU legislation dealing with the control of accidents arising from the storage of dangerous substances (HSE, 2015*a*). The main changes from SEVESO II to SEVESO III is that the list of substances have been reclassified, a requirement is put on co-operation by the authorities in testing of external emergency plans as well as the need to inform people who are likely to be affected following a major accident, etc. COMAH regulations regard the risk to the environment as severe as that to public. It applies mainly to industries that store chemical and petrochemical substances, but also other businesses that store fuel, alcoholic spirit and businesses that manufacture or store explosives. In general, COMAH regulations apply where a specific threshold of hazardous substance is exceeded. Another set of regulations that applies in England is the Oil Storage Regulations (OSR) that require providing secure containment facilities to prevent the oil from escaping to the environment (Walton, 2014).

Primary containments are storage facilities that are in direct contact with the in-

ventory. They can take the form of storage tanks, vessels and associated pipework. They have to be designed and maintained properly to ensure the safe storage of the material during the life time of the facility. In many storage sites where potentially polluting materials are handled, the primary containment is surrounded by a secondary containment referred to as a bund wall. This is for the purpose of containing any spillage, should the primary containment fails. A bund wall is a facility that consists of a wall and base, which is structurally independent from the primary containment. The bund walls are commonly constructed from earth, brickworks, reinforced concrete and in some old facilities, they are made from plain concrete. Concerning their capacities, the adopted practice in the UK industries is that a bund wall has to hold 110% of the capacity of the storage tank in case of individual bunding or 25% of the total capacity of the storage tanks if two tanks or more are provided within the same bund wall, whichever is greater (Ash, 2010, Walton, 2014). The 10% margin is considered to contain the firefighting agents and rainwater and prevent the overtopping caused by the catastrophic failure of the storage tank or induced by a wind wave. The 25% rule is adopted on the basis that it is less probable that more than one tank will fail at the same time. In Ash (2010) and Walton (2014), it is recommended that the capacity has to be increased up to 185% in cases of environmentally sensitive areas. However, these rules proved to be inadequate in the wake of catastrophic failure (Atherton, 2008, Ash, 2010). The bund shape must be as simple as possible and it is a good practice to limit its height to 1.5m to allow for an easy ingress and egress for maintenance or in case of accident. As an additional means of mitigation, a tertiary containment can be provided in the form of lagoons and site drainage to minimise the consequences of the failure of storage tanks and bund walls.

Bund walls in the UK are designed to the BS EN 1992-3:2006, which is based on BS 8007:1987, where the structure is only designed to withstand the hydrostatic pressure which makes it vulnerable to dynamic pressures that arise in the wake of catastrophic failure. This is compounded with the fact that the existing installations are old and located in the proximity of rivers and the sea, which increases

the risk of corrosion. Previous work carried out by Atherton (2008) proved that dynamic pressures may be as high as 16 times the hydrostatic pressures at the base of the bund wall. Even if the bund wall does not fail, the 110% capacity which is mostly adopted by the industry, proved to be ineffective as substantial losses of containment have been recorded in the wake of catastrophic failures. The problem of reducing the overtopping quantities has been addressed by Ash (2010) by suggesting to incorporate two different techniques of mitigation:

- Mitigation of Tank Instantaneous Failure (MOTIF): It is a baffle inserted inside the storage tank.
- Catastrophic Overtopping Alleviation of Storage Tanks (COAST): It is a deflector fitted at the top of the bund wall.

Ash (2010) demonstrated that the overtopping quantities could be reduced to 98% when both of the mitigation techniques were combined together. The method of investigation followed by Ash (2010) was based on experimentation and numerical methods via the use of Computational Fluid Dynamics (CFD). A discrepancy was reported in the CFD results against experimental results, which makes it necessary to revise the computational approach. Additionally, incorporating COAST adds weight to the structure which might compromise its structural integrity.

Atherton (2008) research was undertaken at Liverpool John Moores University (LJMU) following an agreement with HSE to investigate the losses incurred in the wake of catastrophic failure and the accompanying dynamic pressures. Research on the same topic continued with Ash (2010) to reduce the amount of losses by incorporating the aforementioned mitigation techniques. Both of those researchers established the baseline of this research for studying the performance of the bund walls under the effects of dynamic pressures when the mitigation techniques are incorporated.

The novelty of this research lies in studying the performance of bund walls under impact loading and proposing a new design allowing to reduce the damage incurred. The outcomes of this project will allow to provide a guidance on the optimum configuration of the bund wall allowing to reduce the losses in stored material along

with the damage to the structure. There is no previous research that studied the structural integrity of the bund wall which makes this research novel.

## 1.2 Research aim and objectives

The aim of this research is to investigate computationally and experimentally, the performance of the bund wall under the impact load following the catastrophic failure of a vertical above-ground storage tank and to enhance its design. Design considerations include reducing the bund wall overtopping quantities by incorporating the mitigation techniques and proposing an appropriate design that reduces the damage to the structure. In order to fulfil this aim, several objectives need to be achieved. The objectives of this thesis are as follows:

- To study the catastrophic failure of the above-ground storage tank by means of CFD in order to quantify the overtopping quantities and dynamic pressures.
- To validate the results obtained against experimental results.
- To investigate the effect of incorporating the mitigation measures on the overtopping quantities and dynamic pressures and to optimise the appropriate mitigation technique.
- To assess the performance of the current bund walls in terms of their structural integrity by using Fluid Structure Interaction (FSI) analysis and to validate the results corresponding to a flat wall against experimental results.
- To propose a new design of the bund wall and compare its performance against the current installations.
- To perform a preliminary dimensional analysis study which can be used to propose design rules for the purpose of predicting the performance of the structure at full scale.

## 1.3 Thesis outline

The remainder of this thesis is organised as follows:

**Chapter 2** presents a history of catastrophic failures of storage tanks due to accidental releases and natural disasters around the world. It also details the current regulations in force for the design of bund walls in the UK. Additionally, it reviews the previous research work relevant to the present investigation and it highlights the motivation behind the current research.

**Chapter 3** details the different approaches used to solve this problem. Firstly, it presents the CFD method by outlining the mathematical and numerical modelling approaches. Then, it thoroughly details the Finite Element Analysis (FEA) and FSI approaches. Additionally, it presents the behaviour of the materials at high strain rates, particularly for the Ultra High Performance Fibre Reinforced Concrete (UHP-FRC), as it constitutes the material adopted for the new design of the bund wall. Finally, it outlines the dimensional analysis method.

**Chapter 4** describes the methodology of the CFD, FEA and FSI simulations by detailing the modelling assumptions and the test matrix. It also outlines the experimental tests for validation purposes.

**Chapter 5** presents and discusses the CFD results for the standard configurations without mitigation techniques and incorporating mitigation techniques along with the results of partial failures. The comparison against the experimental results is also presented.

**Chapter 6** examines the performance of the current bund wall systems through coupling the CFD and FEA simulations. It also presents the performance of the new design over the current design.

**Chapter 7** summarises the key findings that are presented in this thesis and provides recommendations for future work.

# Chapter 2

## Literature review

### 2.1 Introduction

Storage tanks contain large volumes of hazardous and flammable substances that can pose a high risk if an accident occurs and immediate measures fail to reduce the extent of the failure. Over previous years, there have been many catastrophic failures of storage tanks around the world that resulted in severe consequences for human health, the environment and the economy. Regulatory bodies, engineering societies and associations such as American Petroleum Institute (API), HSE and the Construction Industry Research and Information Association (CIRIA) commission research projects and publish reports on this matter to increase the awareness within the community and to learn lessons from previous failures. There are many databases in existence that aim to disseminate reports on failures and investigations to improve the mitigation of potential consequences. These include the Electronic Major Accident Reporting System (eMARS) into which all EU member states must report failure events, the ARIA database that reports feedback on technological accidents in France, ZEMA which is the database on Major Accidents and Incidents in Germany, the U.S. Chemical Safety Board and the Japanese Failure knowledge Database. This chapter aims to analyse the modes of collapses of above-ground storage tanks, the root causes of such failures and their consequences. A review of the literature on the recent collapses and on the behaviour of bund walls, where the information is available, is also presented along with the regulations in existence in the UK. This chapter also illustrates the relevant previous research works on the bund walls and highlights the need for proposing a new design of the bund wall.

## 2.2 History of major incidents

### 2.2.1 Modes of collapse, causes and consequences

According to the Occupational Safety and Health Administration (OSHA), an atmospheric tank is an outside storage area that contains substances at pressures ranging from the atmospheric pressure to 3,447 Pa. There are many modes of a sudden failure of these tanks: collapse, implosion and explosion. A collapse of a storage tank consists of a rupture of its walls and roof releasing its contents as a result of an inadequate design, a deterioration of the tank over time or simply because of converting the facility to store a material inappropriate for the capabilities of the initial design. The hazard is exacerbated if the escaped material is hazardous and flammable or if it causes other tanks to fail. An implosion occurs when the tank is exposed to a vacuum which causes the tank to crumple. This mode of failure is not typically associated with a loss of containment because usually the implosion takes place when the tank is empty. Contrary to the implosion, an explosion occurs due to the fact that the tank is subjected to overpressure, it can be caused equally by the explosion of the flammable material being stored (Schmidt, 2017).

There are many causes that can trigger the failure of storage tanks. Chang and Lin (2006) conducted a study where 242 accidents of storage tanks were investigated over a period of 40 years. The study revealed that 33% of the accidents were caused by lightning, 30% were attributed to human errors while other factors consisted of crack propagation, equipment failure, sabotage, etc.

- Natural disasters: Some countries experience extreme climatic conditions or geological phenomena such as earthquakes and hurricanes. For instance, the east side of USA is a focal region of coastal storms and hurricanes while the west side sits on the junction of two tectonic plates, which makes it a potential area of earthquakes. In the wake of Hurricane Katrina that hit the Gulf Coast, many sudden catastrophic failures occurred. There have been many catastrophic failures due to earthquakes such as in Alaska, USA in 1964, and three major failures in Japan: a huge fire ignited as a result of sparks during

an earthquake at Niigata, Japan in 1964, a release of a large quantity of oil due to crack propagation at Shiogama, Japan in 1978 and the damage of 29 tanks at Hokkaido, Japan in 2003 (Chang and Lin, 2006).

- **Lightning:** Two modes of failure of storage tanks following lightning were identified in Chang and Lin (2006). The first mode is a direct strike which has a zone of radius between 1 and 10m. The second mode is due to the secondary effect such as the bound charge, the earth currents and the electromagnetic pulses. A dozen tank failures among the 80 lightning-related tank failures occurred because they were located in the direct striking zone area. The risk of secondary effect of lightning is far greater. The storm cells produce a charge on the surface around the surface under the cell which spreads between 15 and 150km<sup>2</sup>. According to Ash (2010), lightning accounts for 61% of all accidents that were induced by natural disasters.
- **Maintenance errors:** The maintenance period is considered as one of the most dangerous times for a storage facility especially if hot work is involved, such as welding. Out of the 242 failures investigated by Chang and Lin (2006), 18 failures were caused by welding. A fire started at Thessaloniki, Greece in 1986 as flammable vapours were ignited by a cutting torch. The fire lasted for 7 days and destroyed 10 tanks storing crude oil and caused 5 deaths. Mechanical friction that occurs during the maintenance is another cause of failure. Mechanical friction can generate sparks because of cleaning or grinding operations. For example, 40 workers were killed in a New York gas plant while they were cleaning an empty tank (Chang and Lin, 2006).
- **Operational errors:** These include overfilling, overpressure and mistakes committed by operators. Overfilling might happen if valves fail to close when the capacity of the tank is attained. The situation is exacerbated if the stored material is flammable. Such a scenario occurred in Buncefield, UK in 2005 where a fire was ignited on the site because a tank was overfilled. Exposing the tank to an overpressure can cause its explosion. Overpressure was responsible for

7% of 28 major tank failures over a period ranging from 1997-2001 (Chang and Lin, 2006).

- Equipment failures: These include the failure of roofs, valves, vents, etc. (Chang and Lin, 2006). Valve failure was responsible in the case of the Buncefield oil storage depot incident. Recently, during Hurricane Harvey that hit Texas, many oil storage depots and refineries reported that floating roof storage tanks were damaged due to the huge quantities of water that accumulated on the top of their roofs, which caused them to sink (Blum, 2017).
- Cracks and corrosion: These are considered as main factors that threaten the safety of the tank. According to Chang and Lin (2006) study, 17 out of 242 tanks failed as a result of cracks and corrosion. They usually occur due to the deterioration of the tank over the years being exposed to harsh climatic conditions, such as very low temperatures during the winter, seismic motions or rain water. Corrosion and crack propagation can emanate from poor inspection and maintenance, especially for the welds. Defective welds were the cause of many tank failures, such as the spillage of 400m<sup>3</sup> of light crude oil from one of the tanks of Eastern States Standard Oil (ESSO) petroleum refinery at Fawley, Hampshire in 1999 due to a defective weld at the base of the tank (HSE, 2001).

The consequences of the sudden failures of storage tanks are very severe. Failures have impacts on the environment, human health and the economy. Catastrophic failures are usually associated with intense aftereffects unless strict preventive measures are taken.

- Impacts on the environment: In a study conducted by Gyenes and Wood (2014) on the impacts of major accidents of storage tanks on the environment, it has been shown that 86 out of 687 major accidents occurring between 1986 and 2013 in the EU and Organisation for Economic Cooperation and Development (OECD) countries had serious effects on the environment. Threats to the environment cover pollution of rivers, sea, soil, air, etc. It was demonstrated in this study that 56% of the accidents were near water resources. In

27 accidents, the releases escaped to rivers, and in 6 cases, the releases escaped directly to the sea while for 19 cases, the escaped materials flowed to the drainage systems and then to the rivers and sea. The contamination of rivers and sea can affect the daily lives of human beings, as they are the main sources to provide drinking water, fish and recreational areas. For example, in the aftermath of a sudden failure of a storage tank in Floreffe, USA in 1988, large quantities of fuel entered the Monongahela River, resulting in the death of 11,000 fish and 2,000 birds as well as limiting the supplies of drinking water (Atherton, 2008). Alternatively, the spillage can pollute the soil. Gyenes and Wood (2014) reported that 15 cases involved releases to soil which can kill the vegetation or pollute the water table. Another mode of pollution, is the contamination of air associated with fires and explosions and the release of toxic vapours. According to Gyenes and Wood (2014), 8 accidents were associated with air pollution. In a failure occurring in Lithuania in 1989 resulting in a fire ignition, large quantities of ammonia were evaporated resulting in 10 deaths due to the inhalation of ammonia gas (Atherton, 2008).

- Impacts on human beings: The impacts on the environment can have implications for the immediate community by contaminating the air, the water, fish and food. Moreover, the accidents can cause a disruption of the livelihood of the people living in the affected area. In some cases, there were orders of emergency evacuation of people and closure of local infrastructure such as motorways, hospitals and schools (Atherton, 2008). Additionally, some accidents involved the death and injury of operators at the time of the failure, having impacts on their families.
- Impacts on the economy: The losses in some accidents were deemed very high and had major impacts on the economy. For example, during the failure of a storage tank in Buncefield, UK in 2005, losses were estimated at £10,000,000 in stored material. This is apart from the fact that the facility needed to be shut down during the accident along with the additional cleaning cost which added to the incurred losses (Atherton, 2008).

## **2.2.2 Incidents caused by natural disasters**

### **Houston, USA, 17<sup>th</sup> August 2017 - 2<sup>nd</sup> September 2017**

During the 2017 Atlantic Hurricane season, Houston was hit by Hurricane Harvey that caused significant damage to the city, particularly to the storage facilities. The Houston area is a hub of chemical plants, refineries, storage terminals and oil production sites. It has more than 1,000 storage tanks with 400 employing floating roofs that are supposed to float up and down on the top of the liquid to reduce the emissions. The technology of floating roofs proved to be inadequate as many tanks ruptured due to the huge accumulated quantities of water which caused the roofs to flip on their sides. At the Valero Energy Houston refinery, one floating roof tank collapsed releasing more than 235,000 pounds (106,594 Kg) of toxic vapours into the atmosphere (Blum, 2017). Spills were also recorded at different companies. For example, at Baden Aniline and Soda Facto (BASF) which is the second largest producer of chemical products in North America, tanks overflowed releasing chemicals in a containment dyke which itself overflowed to the surrounding ground due to the storm water. At ExxonMobil Beaumont oil refinery, oil spilled over a nearby road after overfilling a 3m levee (Mufson, 2017).

### **USA Gulf Coast, 2005**

In 2005, the Gulf Coast of the United States was hit by two Hurricanes, Katrina and Rita, which caused huge losses in petroleum products estimated at 7.5 million gallons (28,390m<sup>3</sup>) by the Environment Protection Agency (EPA) including five major spills of more than 100,000 gallons (378m<sup>3</sup>) and 134 spills of less than 100,000 gallons (378m<sup>3</sup>) (Copper, 2006). According to a study by Godoy (2007) in which the performance of storage tanks during the hurricanes was investigated, 50% of the U.S daily production of oil and 20-25% of gas was affected. Additionally, 6 refineries went out of service in Louisiana and Mississippi during Hurricane Katrina and 16 refineries had to be shut down during Hurricane Rita in Texas and Louisiana. In the aftermath of Hurricane Katrina, the wind reached a speed of 200 km/h which caused the tanks to fail in the following two modes. In the first mode, tanks buckled under the effect of the wind and in the second mode, tanks were dislodged and

moved away from their original positions, particularly those which were empty or not totally filled. Some other tanks failed due to the effect of flooding such as in the Bass Enterprises Facility in Cox Bay, where two tanks were dislodged from their foundations releasing 3.3 million gallons ( $12,492\text{m}^3$ ) to the surrounding environment. In Chalmette Town, that sat in the path of the hurricane, over 1 million US gallons ( $3,785\text{m}^3$ ) of oil were discharged from the Murphy Meraux refinery, which is the largest one in the United States. This was due to the failure of the levees along the Mississippi River overwhelming the refinery with up to 4m height of water. One above-ground tank was lifted and dislodged from its foundation. The lost material impacted more than 1,800 homes in the surrounding area located in a 1 mile radius, nearby canals and Murphy's tank farm containment area. This resulted in cleaning up costs and the disruption of the lives of the people (Godoy, 2007, Copper, 2006). Lessons learnt from Hurricane Katrina and the precautions that were taken for the refineries in Texas and Louisiana, reduced the extent of the damage for the tanks during Hurricane Rita that landed in Texas on 24<sup>th</sup> September 2005. Only minor to a moderate level of damage was reported because of loss of insulation and roof damage.

#### **Alaska, USA, 27<sup>th</sup> March 1964**

The earthquake that struck Alaska in 1964 was the strongest in the history of the USA and the second strongest worldwide, with a magnitude of 9.2. The effect of the earthquake reached other states such as California and Oregon (Leith, 2014). Many tanks across Alaska exhibited damage, most of these tanks belonged to oil companies and were designed to standards that did not account for the forces generated by the earthquake. Many of the tanks owned by the Union Oil Company, a major petroleum explorer in the last century, collapsed in the city of Whittier, resulting in the release of combustible substances and the ignition of a fire that lasted for three days. Additionally, seven tanks collapsed in Anchorage releasing combustible materials and three tanks in California ruptured resulting in the escape of 750,000 US gallons ( $2,839\text{m}^3$ ) of aviation fuel. At that time, there were no dykes or bund walls in effect in Alaska and seismic prone areas in the USA (National Research

Council, 1968).

### **2.2.3 Incidents caused by accidental releases**

#### **Superior, Wisconsin, USA, 26<sup>th</sup> April 2018**

An explosion occurred at Husky refinery located in Superior, Wisconsin while its Fluid Catalytic Cracking Unit (FCCU) was shutting down for periodic maintenance. A nearby above-ground storage tank was struck by a piece of debris from the explosion which caused it to become punctured and to release 15,000 barrels (2,454m<sup>3</sup>) of its content into the refinery. Two hours later, the released asphalt ignited resulting in a huge fire. To date, the root cause of the explosion is still unclear and the investigation is still ongoing (as of November 2018). In terms of consequences, 36 people had to undergo medical treatment including eleven injuries (U.S. Chemical Safety and Hazard Investigation Board, 2018). Additionally, a state of emergency was declared in Douglas County as well as the evacuation of Superior County (Dellinger, 2018).

#### **Aabenraa, Denmark, 2011**

A tank storing a fish sludge collapsed suddenly in Aabenraa in 2011 releasing 6,000 tons (5,443 tonnes) of product which itself produced a wave of 14m height. The bulk of material escaped the bund wall and hit the trees and the parked cars until it reached a residential area and a harbour. Other tanks located in the same bunded area sustained damage with one of them storing soya bean oil also reported to be leaking. Fortunately, there were no recorded casualties and no serious damage to the environment, as fish sludge is not classified as hazardous material. However, cleaning up efforts had to be undertaken to replace the topsoil of the affected area (Hedlund et al., 2015).

#### **Chesapeake, Virginia, USA, 12<sup>th</sup> November 2008**

On 12<sup>th</sup> November 2008, a tank storing liquid fertiliser owned by Allied Terminals, Inc failed catastrophically. The ruptured tank released 2 million US gallons (7,571 m<sup>3</sup>) of material which overtopped the secondary containment in the form of an earthen dyke within a few seconds. The tank split vertically prior to reaching the

maximum safe fill height of 27.01 feet (8.23m). An investigation into the causes of the catastrophic failure revealed that the tank ruptured because of a defective weld. The tank was originally built in 1929 to store petroleum products. It was constructed from overlapping riveted plates. In 2006, Allied modified the tank by replacing the riveted joints by welded joints to increase the capacity of the tank. Allied did not ensure that the modifications to the tanks were carried out by a qualified welder as per the American Petroleum Institute (API) 653 requirements. Additionally, API 653 requires verification of the weldability by conducting spot radiography, which was not fulfilled. Also, Allied lacked safety procedures for work on tanks that are filled for the first time. Following the failure, the escaped fertiliser overwhelmed a neighbouring residential area forcing them to evacuate for several days and to leave their homes weeks later to allow for the repair of their properties. At least 200,000 US gallons (757m<sup>3</sup>) of the liquid could not be recovered after escaping to the southern branch of the Elizabeth River. In terms of injuries, at the time of failure, a welder and his helper were sealing leaking rivets on the tank. The welder who was standing in the lift basket was impacted by the lift mechanism and the helper was pinned to the ground after being hit by the tank stairs. They were both submerged under the liquid wave but fortunately they were rescued by employees from a neighbouring business (U.S. Chemical Safety and Hazard Investigation Board, 2009).

#### **Sløvåg, Norway, 24<sup>th</sup> May 2007**

On 24<sup>th</sup> May 2007, a tank owned by the Vest Tank Company exploded resulting in the destruction of the remaining tanks in the farm. The facility included 17 tanks distributed into three farms. The tank farm that included the exploded tank was used to store, treat and recover liquids including coker gasoline. The tank farm had five tanks which were surrounded by a bund wall. The tank explosion commenced with the rupture in the weld between the base and the wall which caused the shell to be ejected towards the north eastern corner of the farm and the roof of the tank was pushed even further as shown in Figure 2.1. Subsequently, the remaining four tanks in the farm collapsed and part of the bund wall was damaged. Additionally,

two lorries outside the bunded area were completely burnt out. Witnesses described the event as akin to the launching of a space shuttle. Some of the employees were thrown on the ground and others, who were at the company buildings escaped quickly after flying objects entered the roof and the walls shook. Fortunately, there were no casualties, but two employees sought medical treatment. An investigation into the potential causes of the explosion revealed that the accident occurred after a flammable mixture was ignited in the tank or in the air filter (Skjold et al., 2008).



Figure 2.1: Collapse of the tanks of Vest Tank Company<sup>1</sup>(Skjold et al., 2008)

### **Ambès, France, 12<sup>th</sup> January 2007**

At a depot for oil and petroleum products located in Ambès, France, a tank failed suddenly. The tank dated back to 1958 and had a floating roof. On 11<sup>th</sup> January, a leak was detected which required the tank to be drained. However, before performing this task, the tank failed suddenly releasing 12,000m<sup>3</sup> within a few seconds. The tank farm was surrounded by an earthen dyke which was able to withstand the surge of the crude oil. However, 2,000m<sup>3</sup> escaped to the ground and nearby roads. The failure was due to the corrosion at the base of the tank. An inspection that was conducted less than one year prior to the failure of the tank, indicated that the thickness was degraded between 20% and 50% at the central part and between 20% and 80% on the periphery. The consequences of this failure were deemed to be very significant, especially in terms of environmental and economic consequences, and the quantity of dangerous material released. The material released was estimated

---

<sup>1</sup>Permission to reuse this image has been granted by Trygve Skjold

at 22% of the upper SEVESO thresholds of 50,000 tonnes. Fortunately, there was no direct impact on human health and there were no reported casualties. However, residents in the surrounding area had to be evacuated within 7 hours of the failure. In terms of the environmental consequences, the death of a few birds and coypu was reported, and 50m<sup>3</sup> of oil polluted 2km of ditches and was able to reach the water table. Oil spills were observed 20km away from the site and in the Dordogne River. The level of pollution intensified to spread onto 40km of the riverbanks of the Garonne, Dordogne and Gironde. Following the spill, the operator had to perform cleaning up efforts that lasted until June 2009, including soil excavation and water table treatment. The economic losses were huge, estimated at over 50 millions Euros, as crude oil extraction had to be suspended (ARIA, 2009).

### **Hertfordshire, UK, 11<sup>th</sup> December 2005**

Huge quantities of petrol overflowed from a tank that belonged to the Buncefield oil storage depot after an instrumentation failure triggered an overfilling of the tank resulting in a giant explosion. The faulty tank belonged to Hertfordshire Oil Storage LTD (HOSL), that was using the depot along with the British Pipeline Agency Ltd (BPA) and British Petroleum (BP) Oil UK Ltd. All of these sites were classified as “top-tier” according to the COMAH Regulations. The filling operation started during the night of 10<sup>th</sup> December. The tank was fitted with two means of control: a gauge that permits monitoring of the filling operation and an Independent High-Level Switch (IHLS) that is meant to close the valves in case the liquid reaches the maximum fill height. Both of these forms of control were inoperable, failing to inform the operator in the control room that overfilling occurred. Ultimately, large quantities of petrol escaped the tank from the top. Both the bund wall and the catchment area failed to contain the escaped liquid as shown in Figure 2.2, which ended up by entering the groundwater. This initiated the explosion which was the largest experienced in the UK. The fire swept over 20 adjacent tanks and lasted for five days. It was estimated that 250,000 litres of petrol escaped the tank by the time the explosion took place. Large quantities of fire-fighting agents and water were used to extinguish the fire. The bund wall behaved badly at the level

of joints and pipe penetrations allowed the petrol, fire water and foam to leak out. The tertiary containment provided was not designed to handle large quantities of releases. Eventually, the discharged mixture of materials flowed to a nearby road. The consequences of this major failure were deemed to be considerable. Over 40 people were injured and around 2,000 people had to be evacuated from the nearby residential area. The loss of material was estimated at £10,000,000 in addition to the disruption caused to the surrounding businesses and the closure of two motorways. The environmental impact was not very significant. Although, pollutants entered an aquifer, the drinking water supplies were not affected (HSE, 2011, Atherton, 2008).

The image originally presented here cannot be made freely available via LJMU E-Theses Collection because of 'copyright'. The image was sourced from: <http://www.hse.gov.uk/comah/buncefield/buncefield-report.pdf>.

Figure 2.2: Rupture of the bund wall of the Buncefield oil storage depot

### **Helsingborg, Sweden, 4<sup>th</sup> February 2005**

A tank storing sulphuric acid at Kemira Kemi industrial plant in Helsingborg, Sweden failed catastrophically releasing 8,900m<sup>3</sup>. Near the tank, there was a water pipe with a diameter of 600mm and a nominal pressure of 6 bar which transported cooling water from the sea to the facilities of the industrial plant. In the early morning of 4<sup>th</sup> February, a low pressure was observed in the pipeline, which meant water was leaking through the pipe wall. The water jet was very powerful and caused the liquefaction of the earth on which the tank was founded. After one hour, a hole appeared near the bottom of the tank releasing its content within 4 minutes. The sulphuric acid was mixed with salt water contaminating an area of 100,000m<sup>2</sup>. Following that, the pressure in the tank dropped to a negative level causing the tank to implode and the roof to be extensively damaged. The released sulphuric

acid reacted violently with the chloride ions of the salt water to form hydrogen chloride. A cloud of gas and aerosols spread over 10km away from the failure location. The majority of the escaped material flowed to the harbour. The tank was located within a bund wall of 0.6m height and a volume of 3,100m<sup>3</sup> along with two other tanks. There is no information available on the behaviour of the bund wall, but most likely that the bund wall remained intact as the sulphuric acid jet created a hole 7m deep in the ground. At the time of the event, there were eight people on site. Four people had to run away and four others were picked up by a pilot boat. Six people received medical treatment and people living nearby were asked to stay indoors, while keeping windows and doors closed. In terms of environmental consequences, the sulphuric acid remained in the bottom of the harbour over three weeks after the initial accident had been neutralised. A test of the soil layer showed that the acid reached the groundwater level and greatly lowered its pH. A low pH in the ground can dissolve heavy metals from minerals and soil. Following the failure, a remediation program was started by Kemira Kemi to reduce the environmental effects (Swedish Accident Investigation Board, 2008).

### **Rotterdam, Holland, 16<sup>th</sup> January 2003**

A tank failed catastrophically while it was filling with ortho-cresol releasing 1,700 tonnes. The cause of the failure is attributed to corrosion of the steam coil of the tank which resulted in the steam pressure to increase to 7 bar. This created pressure and turbulence waves, which caused the tank to fail at one of the welds. As a result, the tank turned on its side and released its contents within a few seconds spreading over 3 hectares and forming a vapour cloud that drifted towards a neighbouring urban area. The site was surrounded by an earthen dyke but the latter was unable to retain the large wave, which flowed at a high velocity towards the pump room. The failure was rated badly concerning the quantities of the dangerous material released. It caused disruption to the neighbouring companies which had to stop their activities. The road and rail traffic had to be interrupted and people were advised to stay indoors. Following the failure, 6 storage tanks had to be dismantled and the site had to be cleaned up (ARIA, 2006).

## **Delaware City, USA, 17<sup>th</sup> July 2001**

A tank at Motiva Enterprises LLC, Delaware City refinery failed catastrophically from roof to shell after it exploded releasing its entire contents of sulphuric acid of 264,000 US gallons (999m<sup>3</sup>). The explosion caused an adjacent tank to lose its contents and several tanks to leak for several weeks. In total, 1.1 million gallons (4,164m<sup>3</sup>) was lost and 99,000 gallons (375m<sup>3</sup>) found its way to the Delaware River. The accident happened while a crew of contractors was repairing gratings on a cat-walk. The failure was attributed to many causes. The tank experienced localised corrosion and some of the holes were not repaired. One hole was discovered in the shell but instead of repairing it, the level of the liquid was lowered under the level of the hole. Also, the carbon dioxide inerting system and the conservation vent installed were poorly designed. These systems are installed to prevent the light hydrocarbons in the acid from evaporating and creating a flammable atmosphere that can ignite in the presence of oxygen. The explosion is believed to have initiated because of sparks generated by hot work, which ignited the flammable vapours. The site was surrounded by a bund wall of 180 feet (55m) long by 130 feet (40m) wide by 5 feet (1.5m) tall which was only designed to resist hydrostatic pressures. The acid flowed out of the banded area to the ground and the nearby streets and part of it entered the river which resulted in the death of 2,500 fish and 250 crabs. In terms of injuries, there was one person killed whose body was found only on 18<sup>th</sup> of September and there were 8 people injured who suffered burning eyes and lungs, acid burns and nausea (U.S. Chemical Safety and Hazard Investigation Board, 2002).

## **2.3 Current requirements**

In the UK, there exists a number of standards and pieces of legislation that regulate and control activities related to the bulk storage industries in order to ensure the safety of the operations and the mitigation of the related hazards. The current Eurocode applied for the design of bund walls is BS EN 1992-3:2006 Design of concrete structures, liquid retaining and containing structures. The pieces of legislation

currently in force are the SEVESO III Directive and COMAH Regulations.

### **2.3.1 Code of practice**

The current BS EN 1992-3:2006 - Eurocode 2 replaced the BS 8007:1987 in 2006. It is designated to the design of retaining structures, bulk storage containers, buildings, etc. Neither of these two standards is specific to the design of bund walls nor do they consider the effect of the hydrodynamic pressures that arise from the catastrophic failure of the primary containment.

### **2.3.2 Legislation**

#### **2.3.2.1 SEVESO III Directive**

The SEVESO III Directive is the principal legislation of the European Union relating to the control of major accident hazards. SEVESO III came into force on 1<sup>st</sup> June 2015 replacing SEVESO II. The main changes strengthen some areas in relation to safety and include:

- The list of the substances was updated in line with (Classification, Labelling and Packaging) CLP regulation. This results in some companies moving from non-SEVESO to SEVESO status or moving from lower-tier to upper-tier. The status is determined by the quantities and the class of materials stored.
- Some of the companies whose status has changed need to update their safety reports. A company that is moving to a lower-tier must provide a Major Accident Prevention Policy (MAPP) and a company that is moving to an upper-tier must provide the competent authority with a full SEVESO report and update at least every five years.
- There is more emphasis to inspection with upper-tier sites subjected to more frequent inspections.
- A requirement is put on the co-operation between the appropriate authorities to test external emergency plans.

- The information related to the activities of the companies has to be made available electronically to the public and kept up to date in line with the Aarhus Convention on public information. The information has to be made available by each company through “non-technical summary” documents. There is also a requirement on the participation of the public in decision making and their access to justice (HSE, 2015*b*).

### **2.3.2.2 COMAH Regulations**

The SEVESO III is implemented in the UK through the COMAH Regulations which came into force on 1<sup>st</sup> June 2015 replacing COMAH 1999. It applies mainly to the chemical industry, but also some other industries that handle explosives and dangerous substances if the quantity exceeds the threshold specified in the regulations. The competent authorities in the UK who are in charge of implementing the COMAH Regulations are the HSE and the EA in England and Wales and the HSE and the Scottish EPA in Scotland (HSE, 2015*a*).

## **2.4 Previous work**

### **2.4.1 Clark et al (2001)**

Clark et al. (2001) conducted a study on the effectiveness of secondary containments for the purpose of risk assessment of major hazard sites. The list of secondary containment systems covered in this study includes bunds, buildings, shelters and double skinned vessels. The performance of secondary containments used in the industry was assessed by visiting five sites within the UK. The sites were selected due to the materials stored being toxic and flammable and implementing secondary containments. The bund walls were assessed in terms of the material of construction, drainage issues, bunding of pumps, the overtopping issues, the availability of measures to minimise the evaporation, etc. Most of the containments were constructed from poured concrete, bricks and specialist concrete to reduce the heat transfer. Some overtopping issues were noticed in one site that employs low bund

which were ineffective to prevent dynamic overtopping and spigot flow. Clark et al. (2001) reviewed 46 major accidents for a period of 10-15 years occurring throughout the world and the effectiveness of the performance of secondary containment was assessed in terms of containing the released materials. In one third of the reviewed accidents, there were no secondary containment systems provided. In one half of the accidents, there was an issue with the design of the secondary containment. Clark et al. (2001) conducted calculations to assess the effect of secondary containment. The following equation was proposed for dynamic overtopping

$$Q = e^{-p\frac{h}{H}}, \quad (2.1)$$

where  $p = 3.89, 2.43$  or  $2.28$  for a vertical bund wall, a bund wall inclined outwards at 60 degrees from the horizontal or a bund wall inclined outwards at 30 degrees from the horizontal,  $h$  is the height of the bund wall and  $H$  is the height of fluid in the tank (Clark et al., 2001).

#### **2.4.2 Atherton (2008)**

Atherton (2008) investigated the problem of catastrophic (axisymmetric) and partial (asymmetric) failures of storage tanks experimentally using a test facility constructed to the scale of 1:30. Hundreds of tests were conducted to quantify the losses incurred in the wake of failure as well as the dynamic pressures exerted on the bund wall. The catastrophic or total failure of the storage tank was modelled by releasing a tank quadrant suddenly allowing water to escape rapidly. The partial failures were modelled by considering slots and orifices which replicated cracks in the shell of the tank or a valve/pipe connection failure, releasing the fluid directionally through the gap. The research covered a range of bund geometries (triangular, square and rectangular), four bund capacities covering 110%, 120%, 150%, 200% by varying the bund height and the separation distance between the tank and the bund wall. Three groups of tanks, based on the ratio of the tank radius to the fluid height were investigated adopting ratios of 0.5, 1.0 and 2.5 which correspond to tall, middle and squat tanks, respectively.

Atherton (2008) derived empirical equations from the vast amount of data collected.

For overtopping, the equation is

$$Q = Ae^{-B\frac{h}{H}}, \quad (2.2)$$

and for dynamic pressures, the equation is

$$Dyn/Stat_{base} = Ce^{-D\frac{h}{H}}, \quad (2.3)$$

where  $h$  is the height of the bund wall and  $H$  is the height of fluid in the tank.

These equations have the same form for the axisymmetric and asymmetric failures for both orifice and slot but with different ranges of validity and different  $A$ ,  $B$ ,  $C$  and  $D$  constants that depend on the type of the tank and the bund.

Atherton (2008) demonstrated that for bunds of 110% capacity, overtopping losses of 70% were obtained in case of catastrophic failure and the dynamic pressures were in excess of 16 times the hydrostatic pressure. These values are deemed to be high and cause concern to the operators in terms of the quantities of material lost and the structural integrity of the bund wall in the wake of catastrophic failure (Atherton, 2008).

### 2.4.3 Ash (2010)

Ash (2010) addressed the effect of mitigation on overtopping losses and dynamic pressures for axisymmetric and asymmetric failures using experimental and computational approaches. The mitigation measures incorporated were MOTIF and COAST. MOTIF is implemented by adding a baffle inside the tank of a height of one third of the fluid height, while COAST is implemented by fitting a baffle at the top of the bund wall. Ash (2010) investigated the effect of the incorporation of MOTIF only, COAST only and MOTIF and COAST combined. Empirical equations for overtopping quantities were derived for both axisymmetric and asymmetric failures.

For MOTIF, the equation of overtopping is

$$Q_{Motif} = A_M e^{-B_M \frac{h}{H}}, \quad (2.4)$$

where the constants  $A_M$  and  $B_M$  allow the calculations of losses of axisymmetric and asymmetric failures for different types of tank and different angles of inclination.

For COAST, the equation of overtopping is

$$Q_{COAST} = A_C e^{-B_C \frac{h}{H}}, \quad (2.5)$$

where  $A_C$  and  $B_C$  allow the calculation of losses for vertical bund wall for cases where COAST is incorporated into the height of the bund and as a retrofit. Incorporating COAST into the height of the wall does not alter the capacity from the 110% capacity and adding COAST as a retrofit increases its capacity.

For COAST and MOTIF combined, the equation is

$$Q_{M\&C} = A_{M\&C} e^{-B_{M\&C} \frac{h}{H}}, \quad (2.6)$$

where  $A_{M\&C}$  and  $B_{M\&C}$  allow the calculation of losses for a vertical bund wall for both cases of incorporating COAST in the height of bund wall and as a retrofit.

Using MOTIF allows a reduction in losses between 73% and 80%, 60% and 73%, 34% and 55% for squat, middle and tall tanks, respectively, when using a vertical bund wall under the total failure. The inclusion of COAST allowed a reduction between 15% and 60% in case where the capacity remains at 110% and 21% and 74% in case where COAST is incorporated as retrofit. Combining COAST and MOTIF allows a considerable reduction, varying between 70% and 98% for the range of configurations considered.

Ash (2010) examined this problem numerically via the use of CFD, the results obtained from the simulations showed very high variability against experimental results in terms of dynamic pressures for all mitigation techniques.

## 2.5 Need for a new design

There are many publications by governmental agencies and associations that highlight the inadequacy of the current bund walls to retain the escaped materials in the wake of a catastrophic failure and emphasise the need to take the dynamic effect of the tidal wave into account in the design process. Examples of publications include Secondary Containment Systems (Environmental Containment Systems, 2012) by the New Zealand Environmental Protection Authority, CIRIA C736 Containment Systems for the Prevention of Pollution (Walton, 2014). In the CIRIA C736 report,

the dynamic loads include the hydrodynamic load of the wave of liquid hitting the bund wall and the impact of debris of the ruptured tanks on the walls. It is suggested to provide a freeboard which is an increased wall height to cater for the effects of wind and waves. CIRIA C736 provides good practice and recommendations in the UK on the best practices but it does not mandate the operators to comply with their recommendations. In the COMAH Regulations, there is an increased emphasis on the safety, but no explicit requirement, to act on the necessity of designing a bund wall capable of withstanding the dynamic load, is given. This tends to be the case in the USA, according to safety expert Frank Lees who states “It has been common to design bunds for the hydrostatic load of the liquid in the tank, but not for the dynamic load” (U.S. Chemical Safety and Hazard Investigation Board, 2002). Additionally, there is no dedicated standard for the design of bund walls, however the currently applied BS EN 1992-3:2006 - Eurocode 2 takes the static pressure only into consideration.

The study of Ash (2010) revealed a high discrepancy between CFD results and experimental results in terms of dynamic pressures and overtopping losses, which necessitates reviewing the methodology adopted and the software utilised, especially for the dynamic pressures which are important to quantify accurately in order to predict the realistic behaviour of the bund wall under the impact of fluid flow. Additionally, as mentioned in the recommendations of Ash (2010), incorporating COAST increases the overturning moment which might threaten the structural stability of the bund wall. Taking all of aforementioned state of the art research into consideration, it is necessary to propose a new design of bund wall capable of providing the required level of safety.

## **2.6 Summary**

This chapter presented a number of examples of major accidents throughout the world, which aims to provide the scope of this project and the motivation behind it. Despite regulations and best practices applied, the failure of storage tanks is still a problem of huge concern, since the regulations are not designed to cope with all

circumstances. A review of the recent failures demonstrated that the consequences are severe and bund walls are not adequately designed to mitigate the effects of major collapses. Atherton (2008) studied the dynamic pressures exerted on the bund wall in the wake of catastrophic failure of storage tanks and the related overtopping quantities. Subsequently, Ash (2010) investigated the effect of incorporating mitigation measures on minimising the losses in material. However, none of these two researches or any other research work have attempted to study the structural behaviour of the bund wall under dynamic loading. As a result, this work proposes to investigate the behaviour of bund walls based on the previous works and major accidents that confirm their inadequacy in the case of catastrophic failures compounded with the fact that regulations in the UK put emphasis on the safety and inspection. Numerical analysis is utilised to study the behaviour of bund walls for the purpose of proposing a new design of the wall which allows to provide a guidance on the efficient construction of the bund wall. The methodology is based on FSI approach in which CFD and FEA codes are coupled, therefore a review of the different numerical approaches is needed.

# Chapter 3

## Different approaches

### 3.1 Introduction

Numerical and experimental approaches were utilised to investigate the behaviour of bund walls in this research project. The software sets utilised were OpenFoam blueCFD-Core 2016, OpenFoam 17.06 for CFD, Abaqus 2017 for FEA and MpCCI 4.5.2 for FSI. Reasons behind using these software sets are given in the following chapter. This chapter gives a general overview of the numerical approaches and some code specifications.

### 3.2 Physical and numerical modelling

Real world engineering problems are solved by many methods including analytical, experimental and numerical approaches. Analytical methods are only suited to simple problems that allow simplifications in the governing equations. However, engineering problems often involve complicated physics that needs to be taken into consideration in the modelling process. Experimental approaches have been used for many centuries and continue to be used to date, whilst they have many limitations, the method continues to be used for different classes of problems. Getting experimental data from the full scale industrial processes is usually difficult because of the operating conditions involving high temperature, pressures, hazardous materials, etc. Alternatively, investigators have recourse to laboratory tests, which are bound to certain scales or safety rules. Pilot scale studies are usually conducted at a small scale, then scaling laws are applied to predict the behaviour of the system under investigation at full scale. For some problems, these scaling laws are based on many simplifications which make them less able to account for all physics for

the prediction of a faithful behaviour of the system at full scale, this is apart from the fact that certain parameters cannot be scaled such as gravity and friction. Additionally, the instrumentation utilised might be expensive or not accurate enough. The experiment itself can be expensive, time consuming or simply not achievable in addition to that many experiments will be needed to conduct in order to account for variability. An alternative approach is to have recourse to numerical modelling (Rusche, 2002). Computational mechanics is an evolving branch of engineering that makes use of computers to solve problems by describing them with models that can be solved computationally. It can solve a wide class of problems such as fluid, structural, electromechanical problems, etc. The three main methods of discretisation are the Finite Difference Method (FDM), the Finite Volume Method (FVM) which is the most widely used method for fluid mechanics problems and the Finite Element Method (FEM) which solves material science, solid and structural mechanics problems (Hirsch, 2007).

## **3.3 Computational Fluid Dynamics (CFD)**

### **3.3.1 Mathematical Modelling**

The mathematical modelling is the description of the underlying physics of a specific problem into a set of partial differential equations. Navier-Stokes (NS) equations, a mass conservation equation and appropriate boundary conditions constitute a sufficient description of an incompressible fluid flow problem (Jasak, 1996). If a high Mach number is considered, an additional complexity appears and the fluid flow should be treated as compressible. A third equation must be added to account for the compressibility which is the energy equation. The Mach number is defined as  $Ma = \frac{U}{c}$ , where  $U$  is the velocity of the fluid flow and  $c$  is the sound velocity in the medium. A threshold of  $Ma = 0.2$  is considered to differentiate between incompressible and compressible fluid flows of gas. For a fluid flow of gas, if  $Ma \leq 0.2$ , the fluid flow is considered incompressible and compressible if  $Ma > 0.2$  (Hirsch, 2007). Another aspect modelled is the type of the fluid involved, whether it is

Newtonian or non-Newtonian. For Newtonian fluid, the relationship between the stress and strain is linear and described in terms of a constant kinematic viscosity  $\nu$ . Additionally, the turbulence of the fluid flow needs to be accounted for in the modelling (Hirsch, 2007). It is assumed that the behaviour of the fluid flow after the collapse of a storage tank is incompressible, turbulent, involving Newtonian fluids and falling under the type of multiphase flows. The governing equations of this type of flow are given in the following sections.

### 3.3.1.1 Governing equations of fluid dynamics

The fundamental governing equations of fluid dynamics problems are given by the continuity (conservation of mass), momentum (Navier-Stokes) and energy equations which are derived from the fundamental physical principles stating that for a given system, its mass, momentum and energy are conserved (Anderson, 1995). For an incompressible flow, the continuity and the Navier-Stokes equations are sufficient to model the problem.

The conservation of mass equations is

$$\frac{\partial \rho_f}{\partial t} + \nabla \cdot (\rho_f U) = 0, \quad (3.1)$$

and the conservation of momentum equation is

$$\frac{\partial \rho_f U}{\partial t} + \nabla \cdot (\rho_f U U) = \rho_f g + \nabla \cdot \sigma_f, \quad (3.2)$$

where  $\rho_f$  is the fluid density,  $U$  is the velocity field,  $\sigma_f$  is the stress tensor and  $g$  is the gravity acceleration.

The Newton's law of viscosity for Newtonian fluid is

$$\sigma_f = -(p + \frac{2}{3}\mu \nabla \cdot U)I + \mu[\nabla U + (\nabla U^T)], \quad (3.3)$$

where  $p$  is the pressure and  $\mu$  is the dynamic viscosity.

Combining the constitutive relation of a Newtonian fluid with the governing equations gives a closed system of partial differential equations. For an incompressible fluid flow and an isothermal fluid, the governing equations are further simplified (Jasak, 1996):

$$\nabla \cdot (\rho_f U) = 0 \quad (3.4)$$

$$\frac{\partial \rho_f U}{\partial t} + \nabla \cdot (\rho_f U U) = \rho_f g - \nabla p + \mu \nabla^2 U, \quad (3.5)$$

where

- $\frac{\partial \rho_f U}{\partial t}$  is the unsteady term called temporal acceleration, it appears as a first order derivative in time.

- $\nabla \cdot (\rho_f U U)$  is the convective term, it appears as a first order derivative in space. The convection term is complex and source of turbulence, vorticity and shocks.

- $\rho_f g$  represents the body force due to gravity.

- $-\nabla p$  is the pressure gradient due to thermodynamics pressure.

- $\mu \nabla^2 U$  represents the viscous diffusion. It appears as second order derivative term (Boston University, 2012a).

The Navier-Stokes equations are non-linear, second order partial differential equations. The unknowns are the fluid pressure and three components of velocity. Together with the conservation of mass equation, the system of equations is very complex and has few known solutions in case of simplified equations. The solution of these equations is obtained by the means of CFD.

### 3.3.1.2 Governing equations of two-phase flow

The free surface flow problems are encountered in many applications such as ship hydrodynamics, motion of river and seas, bubbly flows, etc. (Yue et al., 2003). For these types of flow, it is necessary to include the surface tension forces in the conservation of momentum equation. These forces act at the interface of the different phases of the flow. The fluid flow arising from the catastrophic failure of a storage tank falls under the class of multiphase flows. It is assumed that the only fluids involved in the modelling are the initially stored liquid and the air with the assumption that air is not trapped as in bubbly flows. Therefore, this is a two-phase flow problem.

There are many numerical approaches to solve for free surface problems such as surface tracking methods, moving mesh methods and volume tracking methods. In the volume tracking methods, the interface between the different fluids is marked by an indicator function (volume fraction, level set, phase field) or massless particles.

The Volume of Fluid (VOF) approach falls under the volume tracking method and is extensively used to model a multiphase flow problem (Heyns and Oxtoby, 2014). It is based on considering an indicator function ( $\alpha$ ) which represents the volume fraction of the fluids in the cell grid. If  $\alpha$  is the volume fraction of the liquid, then  $\alpha = 1$  for a cell occupied by the liquid,  $\alpha = 0$  for a cell occupied by the gas and  $0 < \alpha < 1$  if the cell is occupied by the liquid and the gas. The VOF is based on constructing an advection equation for the volume fraction that describes the evolution of the free surface, it reads

$$\frac{\partial \alpha}{\partial t} + \nabla \cdot (\alpha U) = 0. \quad (3.6)$$

By accounting for the surface tension, the Navier- Stokes equation becomes

$$\frac{\partial \rho_m U}{\partial t} + \nabla \cdot (\rho_m U U) = \rho_m g - \nabla p + \mu_m \nabla^2 U + \int_{\Gamma_{lg}} \sigma_s \kappa \delta(x - x_s) n d\Gamma_{lg}(x_s), \quad (3.7)$$

where  $\sigma_s$  is the surface tension,  $\kappa$  is the interfacial curvature,  $\delta(x - x_s)$  is the 3D Dirac delta function,  $n$  is the normal vector to the surface and  $\Gamma_{lg}$  is the liquid-gas interface. The viscosity  $\mu_m$  and the density  $\rho_m$  are those corresponding to the mixture of the two phases and given by

$$\rho_m = \alpha \rho_1 + (1 - \alpha) \rho_2 \quad (3.8)$$

and

$$\mu_m = \alpha \mu_1 + (1 - \alpha) \mu_2, \quad (3.9)$$

where  $\rho_1$ ,  $\rho_2$ ,  $\mu_1$  and  $\mu_2$  are the densities and the dynamic viscosities of the liquid and the gas, respectively (Deshpande et al., 2012).

### 3.3.1.3 Turbulence Modelling

Most of the flows of practical engineering interest are turbulent. Examples include flows past automobiles, airplanes, rockets, flows in geophysical applications such as river current and even in the human body. For example, for a defective heart valve, the blood flow in the arteries and veins becomes turbulent. In a turbulent flow, the fluid motion exhibits three dimensional, unsteady, rotational and irregular fluctuations. The turbulence develops as an instability of a laminar flow. The

likelihood of a flow to be laminar, transitional or turbulent is measured by the dimensionless Reynolds number  $Re$ , which is equal to the ratio of the inertial forces to the viscous forces. A laminar flow is controlled by the viscous diffusion of vorticity and momentum while for a turbulent flow, the fluid inertia overcomes the viscous stresses hence the Reynolds number becomes larger (Wilcox, 2006). Turbulence is characterised by a continuous spectrum of scales that range from the largest to the smallest. The largest scale is the integral length scale in which eddies are limited by the size of the system under consideration. The unsteady flow behaviour causes these eddies to break to smaller eddies, this cascade process continues to occur until the smallest eddies dissipate into heat through the action of molecular viscosity, hence turbulent flows are of dissipative nature. The smallest scale is called the Kolmogorov scale. Kolmogorov derived the following scales of length  $\eta$ , time  $\tau$  and velocity  $v$  (McNaughton, 2013),

$$\eta = \left(\frac{\nu^3}{\varepsilon}\right)^{\frac{1}{4}}, \quad (3.10)$$

$$\tau = \left(\frac{\nu}{\varepsilon}\right)^{\frac{1}{2}}, \quad (3.11)$$

$$v = (\nu\varepsilon)^{\frac{1}{4}}, \quad (3.12)$$

where  $\varepsilon$  is the dissipation rate of the smallest eddies.

There are several numerical approaches to solve a turbulent flow. The first approach is the Direct Numerical Simulation (DNS) in which the governing equations are integrated over the whole range of turbulence scales. This approach is very demanding in terms of computation power which makes it unsuitable for engineering problems. The second approach is the Large Eddy Simulation (LES). It uses a spatial filter to distinguish between the different scales. The flow is resolved for the large scales whilst the small scales are modelled. The reason behind modelling the small scales lies in the fact that they are homogeneous and isotropic, hence easy to model. The third approach is the Reynolds-Averaged Navier-Stokes (RANS) models which are based on a statistical approach by separating the velocity into mean and fluctuating components (Jasak, 1996), the velocity reads:

$$U = \bar{U} + u', \quad (3.13)$$

where  $\bar{U}$  is the mean component and  $u'$  is the fluctuating component.

The averaging procedure obeys the following rules:

$$\bar{U} \equiv U \quad (3.14)$$

$$\bar{u'} = 0 \quad (3.15)$$

$$\overline{(V + v')(U + u')} = VU + \overline{v'u'} \quad (3.16)$$

By applying the averaging rules, the averaged governing equations of an incompressible fluid flow are

$$\frac{\partial U_i}{\partial x_i} = 0, \quad (3.17)$$

$$\frac{\partial(\rho_f U_i)}{\partial t} + \frac{\partial(\rho_f U_j U_i)}{\partial x_j} = -\frac{\partial p}{\partial x_i} + \frac{\partial}{\partial x_j} (2\mu S_{ij} - \overline{\rho_f u'_i u'_j}), \quad (3.18)$$

$$S_{ij} = \frac{1}{2} \left( \frac{\partial U_i}{\partial x_j} + \frac{\partial U_j}{\partial x_i} \right). \quad (3.19)$$

The quantity  $\tau_{ij} = -\overline{\rho_f u'_i u'_j}$  is called the Reynolds stress tensor. The obtained system of equations is indeterminate, therefore in order to close it, further modelling is required. There are two approaches for modelling. The first one is the Reynolds Stress Modelling (RSM) in which the transport equations of the Reynolds stress tensor are formulated and solved. The second approach is the Eddy Viscosity Modelling (EVM), which is the most popular one and based on prescribing a relationship between the Reynolds stress and mean velocity gradient (Jasak, 1996). Boussinesq (1877) proposed the eddy viscosity concept that mimics the molecular gradient-diffusion process by describing the Reynolds stress tensor as a product of eddy viscosity and mean strain rate tensor according to the following relationships:

$$\tau_{ij} = 2\mu_t S_{ij} - \frac{2}{3} \rho_f k \delta_{ij}, \quad (3.20)$$

$$k = \frac{1}{2} \overline{u'_i u'_i} \quad (3.21)$$

where  $\mu_t$  is the eddy viscosity,  $S_{ij}$  is the mean strain-rate tensor and  $k$  is the turbulent kinetic energy. The question now is how to evaluate the eddy viscosity. Models for determining the eddy viscosity are classified according to the number of transport equations. The zero-equation model is also called the algebraic model. An example of the class of zero-equation models is the mixing-length hypothesis of

Prandtl (1925), which is based on the assumption that eddy viscosity is the product of mixing-length distance  $l_m$  and the velocity gradient. The one-equation model is based on estimating  $\mu_t$  by resolving the transport equation of the turbulent kinetic energy  $k$ . The turbulent viscosity is prescribed according to

$$\mu_t = \rho_f k^{\frac{1}{2}} l_t, \quad (3.22)$$

where  $l_t$  is a length scale that must be chosen (McNaughton, 2013). The two-equations model is the most popular method for engineering applications and based on solving two transport equations for the turbulent kinetic energy  $k$  and the dissipation rate  $\varepsilon$  giving rise to  $k - \varepsilon$  model which was proposed by Jones and Launder (1972) in both low Reynolds and high Reynolds versions. Launder and Sharma (1974) proposed a model with retuned coefficients referred to as the Standard  $k - \varepsilon$  model. The high Reynolds version is the most widely used, the corresponding kinematic turbulent viscosity is calculated using

$$\nu_t = C_\mu \frac{k^2}{\varepsilon}, \quad (3.23)$$

the transport equation for the turbulence kinetic energy is

$$\frac{\partial k}{\partial t} + U_j \frac{\partial k}{\partial x_j} = \tau_{ij} \frac{\partial U_i}{\partial x_j} - \varepsilon + \frac{\partial}{\partial x_j} \left[ \left( \nu + \frac{\nu_t}{\sigma_k} \right) \frac{\partial k}{\partial x_j} \right], \quad (3.24)$$

and the transport equation for the dissipation rate

$$\frac{\partial \varepsilon}{\partial t} + U_j \frac{\partial \varepsilon}{\partial x_j} = C_{\varepsilon_1} \frac{\varepsilon}{k} \tau_{ij} \frac{\partial U_i}{\partial x_j} - C_{\varepsilon_2} \frac{\varepsilon^2}{k} + \frac{\partial}{\partial x_j} \left[ \left( \nu + \frac{\nu_t}{\sigma_\varepsilon} \right) \frac{\partial \varepsilon}{\partial x_j} \right], \quad (3.25)$$

with  $C_{\varepsilon_1} = 1.44$ ,  $C_{\varepsilon_2} = 1.92$ ,  $C_\mu = 0.09$ ,  $\sigma_k = 1$  and  $\sigma_\varepsilon = 1.3$  (Wilcox, 2006).

The  $k - \omega$  model of Wilcox (1988) uses the specific dissipation rate  $\omega \sim \frac{\varepsilon}{k}$ , the kinematic turbulent viscosity is

$$\nu_t = \frac{k}{\omega}. \quad (3.26)$$

The turbulent kinetic energy is

$$\frac{\partial(\rho_f k)}{\partial t} + \frac{\partial}{\partial x_j} (\rho_f U_j k) = P^{(k)} - \beta^* k \omega + \frac{\partial}{\partial x_j} \left[ \left( \mu + \frac{\mu_t}{\sigma_k} \right) \frac{\partial k}{\partial x_j} \right], \quad (3.27)$$

and the specific dissipation rate equation is

$$\frac{\partial(\rho_f \omega)}{\partial t} + \frac{\partial}{\partial x_j} (\rho_f U_j \omega) = \alpha \frac{\omega}{k} P^{(k)} - \beta \omega^2 + \frac{\partial}{\partial x_j} \left[ \left( \mu + \frac{\mu_t}{\sigma_\omega} \right) \frac{\partial \omega}{\partial x_j} \right], \quad (3.28)$$

where

$$P^{(k)} = \mu_t \frac{\partial U_i}{\partial x_j} \left( \frac{\partial U_i}{\partial x_j} + \frac{\partial U_j}{\partial x_i} \right) - \frac{2}{3} \rho_f k \delta_{ij} \frac{\partial U_i}{\partial x_j}, \quad (3.29)$$

with the coefficients used in the model are  $\alpha = 0.555$ ,  $\beta = 0.075$ ,  $\beta^* = 0.09$ ,  $\sigma_k = 2$  and  $\sigma_\omega = 2$  (Morgan, 2012, McNaughton, 2013, Wilcox, 2006).

A comparison between  $k-\varepsilon$  and  $k-\omega$  shows that the former does not allow to capture the flow behaviour of turbulent boundary layer up to separation and over-predicts the shear stress in adverse pressure gradients while the  $k-\omega$  is better at predicting the flow with adverse pressure in the near wall. However,  $k-\omega$  exhibits a sensitivity to the values of  $\omega$  in the freestream outside the boundary layer, which causes a poor performance. To overcome the shortcomings of these two models, Menter (1994) proposed to combine them, which resulted in the Shear-Stress Transport ( $k-\omega$ -SST) model (Menter et al., 2003, McNaughton, 2013). Blending functions are used to change from the  $k-\omega$  inside the boundary layer to  $k-\varepsilon$  away from the surface Menter et al. (2003).

The physics of turbulence near the wall is different from other regions of the flow and usually is of highest interest to predict quantities such as pressure drops, wall shear stress, drag on bodies, etc. The velocity gradients are the largest in the near wall-region because the velocity changes from non-slip condition (zero velocity) that results from the viscous nature of the fluid to the free stream value, hence the production is increased near the wall. The near wall region is subdivided in three regions:

- viscous sub-layer:  $0 < y^+ \leq 5$ , the viscous effects are of more importance and the turbulence is negligible. The viscous velocity varies linearly with the non-dimensionless distance  $y^+$  from the wall and is

$$U^+ = y^+. \quad (3.30)$$

- buffer layer:  $5 < y^+ \leq 30$ , both viscous effects and turbulence are of importance. The maximum turbulence production occurs in the buffer layer at  $y^+ = 12$ .

- inertial sub-layer:  $30 < y^+ \leq 200$ , the turbulence is more important in this region. This region is also called logarithmic (log) region since the velocity varies logarithmically with the non-dimensional distance from the wall according to the following velocity profile

$$U^+ = \frac{1}{\kappa} \ln y^+ + B, \quad (3.31)$$

where  $\kappa = 0.41$ ,  $B = 5.25$ ,  $U^+ = \frac{U}{u_\tau}$ ,  $y^+ = \frac{u_\tau y}{\nu}$ ,  $u_\tau = \sqrt{\frac{\tau_\omega}{\rho_f}}$ .  $y^+$ ,  $u_\tau$  and  $\tau_\omega$  are the wall normal coordinate, the friction velocity and wall shear stress, respectively.

In order to predict the wall behaviour, the flow must be resolved up to the wall by applying a very fine mesh in such a way the first node is inside the viscous sub-layer. This approach necessitates the use of Low Reynolds number (LRN) models and is quite demanding in terms of computing resources. Another approach is to use the wall functions to compensate for the existence of the wall but at the expense of losing a significant amount of information. This approach uses High Reynolds Number (HRN) models (Bredberg, 2000).

### 3.3.2 Numerical Modelling

The numerical modelling of fluid problems is based on the discretisation of the governing equations over a solution domain. By discretisation, it is meant that continuum quantities are approximated into discrete quantities at some predetermined locations in space and time (Rusche, 2002, Jasak, 1996). The finite Volume Method is the most widely used method in CFD. It gives flexibility in terms of the mesh used over the Finite Difference Method since it allows the use of an unstructured mesh that fits complex geometries. The method uses integral formulation of the conservation laws which is more appropriate for problems involving shock and discontinuity. The reason behind this is that in order to obtain the integral formulation there is no need to assume a smoothness in the solution unlike in the finite difference method which is based on the assumption of the continuity of the solution to obtain differential equations of the governing equations (Boston University, 2012b).

### 3.3.2.1 Discretisation of the solution domain

The solution domain includes the time and space domains. The time discretisation is required when solving for transient flows. It is carried out by dividing the total time of simulation into time steps  $\Delta t$ . The time step can be constant throughout the simulation time or changing depending on some conditions computed during the simulation. The discretisation of space consists of dividing the solution domain into a number of cells called also Control Volumes (CV) forming a computational mesh. The cells need to fill the domain and they cannot overlap. Each cell is bounded by a number of faces which can be either internal or coinciding with the boundaries of the domain. In OpenFOAM, there is no limit on the number of faces bounding each cell which allows the use of an unstructured mesh. There are two types of cells: cell-centred where the dependent variables are stored at the centroid of the cell and cell-vertex where the dependent variables are stored at the vertices of the cell. OpenFOAM uses principally the cell-centred scheme (Greenshields, 2015).

### 3.3.2.2 Discretisation of the transport equation

The standard transport equation of a tensorial quantity  $\phi$  is

$$\underbrace{\frac{\partial \rho_f \phi}{\partial t}}_{\text{temporal derivative}} + \underbrace{\nabla \cdot (\rho_f U \phi)}_{\text{convection term}} = \underbrace{\nabla \cdot (\rho_f \Gamma \nabla \phi)}_{\text{diffusion term}} + \underbrace{S_\phi(\phi)}_{\text{source term}}, \quad (3.32)$$

where  $\Gamma$  is the diffusivity (Jasak, 1996).

It should be noted that for flows with more complex physics, other terms appear in the governing equation. The standard transport equation is merely used to explain how temporal and spatial terms are discretised and the way FVM works. The transport equation is of second order since the diffusion term includes the second spatial derivative of  $\phi$ , therefore, in order to obtain a good accuracy, the order of discretisation needs to be second order or higher.

The Taylor expansion of a function  $u(x)$  around a point  $x_i$  is

$$u(x) = u(x_i) + (x - x_i) \frac{\partial u}{\partial x} \Big|_i + \frac{(x - x_i)^2}{2!} \frac{\partial^2 u}{\partial x^2} \Big|_i + \dots + \frac{(x - x_i)^n}{n!} \frac{\partial^n u}{\partial x^n} \Big|_i + \dots \quad (3.33)$$

If  $\frac{\partial u}{\partial x}|_i$  is approximated in this way

$$\frac{\partial u}{\partial x}|_i = \frac{u_{i+1} - u_i}{x_{i+1} - x_i} - \underbrace{\frac{x_{i+1} - x_i}{2!} \frac{\partial^2 u}{\partial x^2}|_i - \frac{(x_{i+1} - x_i)^2}{3!} \frac{\partial^3 u}{\partial x^3}|_i}_{\text{truncation error: neglected terms}} - h.o.t, \quad (3.34)$$

the first term in the truncation error scales with  $x_{i+1} - x_i$ , therefore the discretisation scheme is of first order. Similarly, for a second order scheme, the first term in the truncation error scales with  $(x_{i+1} - x_i)^2$ .

The Finite Volume Method requires that the integral conservation law is satisfied on each control volume  $V_P$  around the point  $P$ ,

$$\int_t^{t+\Delta t} \left[ \frac{\partial}{\partial t} \int_{V_P} \rho_f \phi dV + \int_{V_P} \nabla \cdot (\rho_f U \phi) dV - \int_{V_P} \nabla \cdot (\rho_f \Gamma \nabla \phi) dV \right] dt = \int_t^{t+\Delta t} \left( \int_{V_P} S_\phi(\phi) dV \right) dt. \quad (3.35)$$

### 1. Discretisation of spatial terms

The Gauss theorem is used for the discretisation of spatial terms to convert the volume integrals to surface integrals, hence the following identities are used,

$$\int_{V_P} \nabla \cdot a dV = \oint_{\partial V_P} dS \cdot a, \quad (3.36)$$

$$\int_{V_P} \nabla \phi dV = \oint_{\partial V_P} dS \phi \quad (3.37)$$

and

$$\int_{V_P} \nabla a dV = \oint_{\partial V_P} dS a, \quad (3.38)$$

where  $\partial V_P$  is the bounding surface of the control volume,  $dS$  is an infinitesimal surface element,  $\phi$  is a general scalar property and  $a$  is a general vector property (Greenshields, 2015, Jasak, 1996).

- Convection term (Greenshields, 2015)

The convection term is discretised by integrating it over a control volume and transforming it into a surface integral using Gauss theorem as follows,

$$\begin{aligned} \int_{V_P} \nabla \cdot (\rho_f U \phi) dV &= \int_S dS \cdot (\rho_f U \phi) = \\ &= \sum_f S_f \cdot (\rho_f U)_f \phi_f = \sum_f F \phi_f, \end{aligned} \quad (3.39)$$

where  $F = S_f \cdot (\rho_f U)_f$  is the mass flux through the face  $f$  and  $\phi_f$  needs to be evaluated at the face  $f$  using one of these interpolation schemes:

**Central differencing (CD):** It is second-order but it gives unbounded solution.  $\phi_f$  is given by

$$\phi_f = f_x \phi_P + (1 - f_x) \phi_N, \quad (3.40)$$

where  $f_x = \frac{|x_f - x_N|}{|x_f - x_N| + |x_f - x_P|}$ ,  $P$  and  $N$  are the centres of the cell of interest and the neighbouring cell, respectively.

**Upwind differencing (UD):** It is only first order accurate but ensures the boundedness of the solution. It determines  $\phi_f$  from the direction of the flow as follows:

$$\phi_f = \begin{cases} \phi_f = \phi_P, & \text{for } F \geq 0. \\ \phi_f = \phi_N, & \text{for } F < 0. \end{cases} \quad (3.41)$$

**Blended differencing (BD):** It combines UD and CD to preserve the boundedness of the solution and provides a reasonable degree of accuracy.  $\phi_f$  is given by

$$\phi_f = (1 - \gamma)(\phi_f)_{UD} + \gamma(\phi_f)_{CD}, \quad (3.42)$$

where  $0 \leq \gamma \leq 1$ .

- Diffusion term (Greenshields, 2015)

The diffusion term is discretised in a similar way as the convection term, it is given by

$$\begin{aligned} \int_{V_P} \nabla \cdot (\rho_f \Gamma \nabla \phi) dV &= \int_S dS \cdot (\rho_f \Gamma \nabla \phi) = \\ \sum_f S_f \cdot (\rho_f \Gamma \nabla \phi)_f &= \sum_f (\rho \Gamma_{\phi_f})_f S_f \cdot (\nabla \phi)_f, \end{aligned} \quad (3.43)$$

where

$$S_f \cdot (\nabla \phi)_f = |S| \frac{\phi_N - \phi_P}{|d|}, \quad (3.44)$$

and  $d$  is the distance between the centres of cells  $P$  and  $N$ . In case of non-orthogonal meshes, a correction term must be used. More details on the non-orthogonal correction is found in (Jasak, 1996).

- Source term (Greenshields, 2015)

Any term  $S_\phi$  that can not be written in the form of diffusion or convection terms is treated as a source term. It represents the rate of production/ destruction per unit volume (Rusche, 2002). The source term is integrated over the control volume and linearised as follows,

$$\int_{V_P} S_\phi dV = S_\phi V_P. \quad (3.45)$$

## 2. Temporal discretisation (Greenshields, 2015)

To simplify the PDE in its integral form, all spatial terms will be denoted as  $A\phi$  where  $A$  is any spatial operator. The integral conservation law becomes

$$\int_t^{t+\Delta t} \left[ \frac{\partial}{\partial t} \int_{V_P} \rho_f \phi dV + \int_{V_P} A\phi dV \right] dt = 0. \quad (3.46)$$

The first term of Equation (3.46) can be discretised using Euler implicit scheme as follows by assuming that the control volumes do not change in time

$$\begin{aligned} \int_t^{t+\Delta t} \left[ \frac{\partial}{\partial t} \int_{V_P} \rho_f \phi dV \right] dt &= \int_t^{t+\Delta t} \frac{(\rho_f \phi V_P)^n - (\rho_f \phi V_P)^0}{\Delta t} dt \\ &= \frac{\rho_f V_P \phi^n - \rho_f V_P \phi^0}{\Delta t} \Delta t, \end{aligned} \quad (3.47)$$

where  $\phi^n = \phi(t + \Delta t)$  and  $\phi^0 = \phi(t)$ .

The second term of Equation (3.46) can be discretised using three different schemes where  $A^*$  represents the spatial discretisation of  $A$ :

**Euler implicit:**

$$\int_t^{t+\Delta t} \left[ \int_{V_P} A\phi dV \right] dt = A^* \phi^n \Delta t. \quad (3.48)$$

This scheme uses the values of  $\phi^n$  at the current time step. It is first order accurate in time, unconditionally stable and ensures boundedness.

**Explicit:**

$$\int_t^{t+\Delta t} \left[ \int_{V_P} A\phi dV \right] dt = A^* \phi^0 \Delta t. \quad (3.49)$$

This scheme uses the old values of  $\phi^0$ . It is first order accurate in time, but unstable if the Courant number  $Co$  is greater than 1, where  $Co = \frac{U \Delta t}{\Delta x}$  and  $U$  is the velocity field.

**Crank Nicolson:**

$$\int_t^{t+\Delta t} \left[ \int_{V_P} A\phi dV \right] dt = A^* \left( \frac{\phi^n + \phi^0}{2} \right) \Delta t. \quad (3.50)$$

This scheme uses the mean of the current values  $\phi^n$  and old values  $\phi^0$ . This scheme is second order in time, unconditionally stable, but does not ensure boundedness.

The discretisation procedure converts the PDE into linear algebraic equations for each control volume that can be written in a generic form

$$a_P \phi_P^n + \sum_N a_N \phi_N^n = R_P. \quad (3.51)$$

The equations corresponding to all control volumes can be written in a matrix form as:

$$[A][\phi] = [R], \quad (3.52)$$

where  $[A]$  is a square matrix that includes  $a_P$  in the diagonal and  $a_N$  off the diagonal,  $[\phi]$  is a column vector of the dependent variable and  $[R]$  is the source vector. The system of algebraic equations is solved iteratively by starting with an initial guess until some tolerance is satisfied.

### 3.3.2.3 Implementation of boundary conditions

Boundary conditions need to be specified on the boundary faces in order to completely set up the problem. Boundary conditions can be divided into two categories (Greenshields, 2015):

- **Dirichlet:** The value of the dependent variable  $\phi$  is prescribed on the boundary face, hence it is called fixed value. The value of the dependent variable at the boundary  $\phi_b$  is directly substituted in the discretised equation where the boundary values are needed, e.g. for the convection term ( $\phi = \phi_b$ ). For the terms that require the gradient  $(\nabla\phi)_f$  such as the diffusion term, the gradient is calculated as follows

$$S \cdot \nabla_f \phi = |S_f| \frac{\phi_b - \phi_P}{|d|}. \quad (3.53)$$

- **Von Neumann:** The gradient of the dependent variable normal to the boundary face  $g_b$  is prescribed, hence it is called fixed gradient.  $g_b$  is directly substituted for terms that require the face gradient as follows

$$S \cdot \nabla_f \phi = |S| g_b. \quad (3.54)$$

For terms that require the value of  $\phi$ , the value at the face is interpolated in this way

$$\phi_b = \phi_P + |d|g_b. \quad (3.55)$$

#### 3.3.2.4 Solution procedure

The solution procedure implemented in OpenFoam to solve transient fluid flow problems is the Pressure-Implicit Split Operator (PISO). PISO operates in the following way:

1. Set initial guess to all fields.
2. Solve the momentum equation using the guessed pressure field to get the values of the velocity. This step is called momentum predictor. This step is optional in OpenFoam.
3. Convert the continuity equation into a pressure equation.
4. Solve the pressure equation and calculate the conservative fluxes by using the values of the predicted velocities and satisfying the continuity equation.
5. Correct the velocity using available values of fluxes, pressure fields.
6. Check for convergence, if the process has not converged start a new iteration from step 2 through step 6.

After each iteration, other equations such as turbulence models are solved using the updated velocities and fluxes (Morgan, 2012, Jasak, 1996).

#### 3.3.2.5 Solution Procedure for two-phase flow

In order to solve for a two-phase flow in OpenFOAM, the advection equation of the phase fraction needs to be solved first and then the momentum equation is solved through the PISO algorithm. OpenFOAM uses the Multidimensional Universal Limiter for Explicit Solution (MULES) method in the discretisation process to maintain the boundedness of the phase fraction (Greenshields, 2018) and the

Continuum Surface Force (CSF) for the surface tension term. The discretisation of the phase fraction and the surface tension term are first given and the solution procedure of the tow phase flow is then presented.

- Discretisation of the phase fraction equation

The integral form of the advection equation of the phase fraction reads:

$$\int_{V_P} \frac{\partial \alpha}{\partial t} dV + \int_{\partial V_P} \alpha U \cdot n dS = 0. \quad (3.56)$$

In OpenFOAM, the convection term is modified according to the MULES method, therefore, equation 3.56 in discretised form becomes

$$\frac{\alpha^{n+1} - \alpha^n}{\Delta t} = -\frac{1}{|V_P|} \sum_{f \in \partial V_P} (F_u + \lambda_M F_c)^n, \quad (3.57)$$

where

$$F_u = U_f \cdot S_f \cdot \alpha_f \quad (3.58)$$

and

$$F_c = U_f \cdot S_f \alpha_f + \underbrace{U_{rf} \cdot S_{rf} \alpha_{rf} (1 - \alpha)_{rf}}_{\text{interfacial compression flux}} - F_u. \quad (3.59)$$

$\lambda_M$  is a delimiter that is equal to one in the interface and zero away from it (Deshpande et al., 2012).

- A volume reformulation of the surface tension

The surface tension in equation 3.7 is problematic to implement because it is non-zero only at the interface. A method to overcome this problem is to convert the surface force to a volume force over a small region surrounding the interface using CSF proposed by Brackbill et al. (1992). A volume integral of the surface tension term becomes (Deshpande et al., 2012)

$$\int_{\Gamma_{lg} \cap V_P} \sigma_s \kappa n d\Gamma_{lg}(x_s) = \int_{V_P} \sigma_s \kappa \nabla \alpha dV_P \quad (3.60)$$

and the local interfacial curvature  $\kappa$  is evaluated from

$$\kappa = -\nabla \cdot n = -\nabla \cdot \left( \frac{\nabla \alpha}{|\nabla \alpha|} \right). \quad (3.61)$$

- Solution procedure of two-phase flow

A two-phase flow problem is solved in OpenFOAM as follows (Lopes, 2013):

1. Set all variables to their initial values.
2. Compute the Courant number and adjust the time step.
3. Solve the phase fraction equation using the fluxes from the previous time step and calculate the density and viscosity using the new  $\alpha$  values.
4. Compute the normal vector  $n$  and the local interfacial curvature  $k$ .
5. Go through the PISO algorithm until convergence is reached.

#### 3.3.2.6 Source of errors

The source of errors that can accompany a numerical solution can be divided into three groups (Jasak, 1996, Rusche, 2002)

- **Modelling errors:** They are the difference between the actual problem and the mathematical model. The mathematical model needs to include the most relevant underlying physics of the problem. Simplifications are usually made to obtain a solution more easily, but it is important that these simplifications do not alter the solution.
- **Discretisation errors:** They are further divided into two other categories; the first category is related to the discretisation of the solution domain. Hence, the more control volumes and time steps on which the solution is sought, the better the accuracy obtained, but this is at the expense of the computation time. The second category is related to the method of the discretisation of the equations. A higher order scheme yields a better accuracy but increases the cost of the solution.
- **Iteration convergence errors:** The system of equations is solved iteratively. These errors can be reduced by choosing tighter solver tolerances.

## 3.4 Finite Element Analysis (FEA)

In a design process of new products, designers need to build models and subject them to loads that mimic the operating conditions under which a given system is

working. This task is tedious and time consuming, alternatively the use of FEA is very popular to design new products and analyse their behaviours. The roots of FEA date back to the early 1960's for the analysis of specific structures, mainly in the civil and aerospace engineering industries. The method is mainly applied to solid and structural mechanics to quantify stresses, strains and displacements, but can be used equally in other classes of problems such as fluid dynamics, electromagnetic, etc. (Bathe, 2014). The standard formulation of a finite element solution of solids is typically a displacement-based method. The principle of virtual work is the main feature of FEA that allows the determination of the element stiffness matrix. It states that for a body to stay in equilibrium, while it is subjected to a small virtual displacement, the total internal virtual work must equalise the total external virtual work:

$$\int_V \bar{\epsilon}^T \sigma dV = \int_V \bar{u}^T f^B dV + \int_S \bar{u}^{ST} f^S dS + \sum_i \bar{u}^i R_C^i, \quad (3.62)$$

where  $\bar{\epsilon}$  are the virtual strains,  $\sigma$  are the stresses,  $\bar{u}^T$ ,  $\bar{u}^S$  and  $\bar{u}^i$  are the virtual displacements induced by the body forces  $f^B$ , surface forces  $f^S$  and concentrated forces  $R_C^i$ , respectively.

In a finite element analysis, the displacement within each element is a function of the nodal displacements. It is determined as follows,

$$u^{(m)}(x, y, z) = H^{(m)}(x, y, z)\hat{u}, \quad (3.63)$$

where  $u^{(m)}$  is the displacement within the element  $m$ ,  $H^{(m)}$  is the displacement interpolation matrix and  $\hat{u}$  is nodal displacement vector. The strains are determined from the displacements using

$$\epsilon^{(m)}(x, y, z) = B^{(m)}(x, y, z)\hat{u}, \quad (3.64)$$

where  $B^{(m)}$  is the strain displacement matrix obtained by differentiating the matrix  $H^{(m)}$ . The stresses are calculated from the strains and the material law using

$$\sigma^{(m)} = C^{(m)}\epsilon^{(m)} + \sigma_i^{(m)}, \quad (3.65)$$

where  $C^{(m)}$  is the constitutive law of the material and  $\sigma_i^{(m)}$  are the element initial stresses.

By applying equation 3.62 to each element of the mesh and summing the equilibrium equations, the following equation is obtained:

$$\begin{aligned} \sum_m \int_{V^{(m)}} \bar{\epsilon}^{(m)T} \sigma^{(m)} dV^{(m)} &= \sum_m \int_{V^{(m)}} \bar{u}^{(m)T} f^{B(m)} dV^{(m)} \\ &+ \sum_m \int_{S_1^{(m)}, \dots, S_q^{(m)}} \bar{u}^{S(m)T} f^{S(m)} dS^{(m)} + \sum_i \bar{u}^i R_C^i \end{aligned} \quad (3.66)$$

where  $m = 1, 2, \dots, k$  with  $k$  being the number of elements and  $S_1^{(m)}, \dots, S_q^{(m)}$  are the element surfaces that belong to the surface of the body.

The virtual displacements and strains are obtained in a similar way as for the true displacements and strains. Consequently, the displacements are

$$\bar{u}^{(m)}(x, y, z) = H^{(m)}(x, y, z) \bar{\hat{u}}, \quad (3.67)$$

and the strains are

$$\bar{\epsilon}^{(m)}(x, y, z) = B^{(m)}(x, y, z) \bar{\hat{u}}. \quad (3.68)$$

By substituting equations 3.65, 3.67 and 3.68 into equation 3.66, the equilibrium equation of the whole system becomes

$$\begin{aligned} \bar{\hat{u}}^T \left[ \sum_m \int_{V^{(m)}} B^{(m)T} C^{(m)} B^{(m)} dV^{(m)} \right] \hat{u} &= \bar{\hat{u}}^T \left[ \left\{ \sum_m \int_{V^{(m)}} H^{(m)T} f^{B(m)} dV^{(m)} \right\} \right. \\ &+ \left. \left\{ \sum_m \int_{S_1^{(m)}, \dots, S_q^{(m)}} H^{S(m)T} f^{S(m)} dS^{(m)} \right\} - \left\{ \sum_m \int_{V^{(m)}} B^{(m)T} \sigma_i^{(m)} dV^{(m)} \right\} + R_c \right]. \end{aligned} \quad (3.69)$$

In order to obtain the equations of the unknown nodal displacements from equation 3.69, the principle of virtual displacement is applied  $n_{dof}$  times ( $n_{dof}$  is the number of degrees of freedom) by imposing unit virtual displacements to all components of  $\bar{\hat{u}}$ . In the first application  $\bar{\hat{u}} = e_1$ , in the second application  $\bar{\hat{u}} = e_2$  until in the  $n_{dof}^{th}$  application  $\bar{\hat{u}} = e_{n_{dof}}$ , where  $e_i$  is the unit displacement vector with  $i = 1, 2, \dots, n_{dof}$ . The obtained equations are written in a matrix form

$$K_s u = R, \quad (3.70)$$

where  $u = \hat{u}$ ,

$K_s$  is the stiffness matrix

$$K_s = \sum_m \int_{V^{(m)}} B^{(m)T} C^{(m)} B^{(m)} dV^{(m)}, \quad (3.71)$$

and  $R$  is the load vector

$$R = R_B + R_S - R_I + R_C. \quad (3.72)$$

$R_B$  is the effect of the elements body force

$$R_B = \sum_m \int_{V^{(m)}} H^{(m)T} f^{B(m)} dV^{(m)}, \quad (3.73)$$

$R_S$  is the effect of the elements surface force

$$R_S = \sum_m \int_{S_1^{(m)}, \dots, S_q^{(m)}} H^{S(m)T} f^{S(m)} dS^{(m)}, \quad (3.74)$$

$R_I$  is the effect of the elements initial stresses

$$R_I = \sum_m \int_{V^{(m)}} B^{(m)T} \sigma_i^{(m)} dV^{(m)}, \quad (3.75)$$

and  $R_C$  is the nodal concentrated load.

In the case where the loads are rapidly applied to the system and the dissipation of the energy is accounted for, the equilibrium equation becomes

$$M_s \ddot{u} + C_s \dot{u} + K_s u = R, \quad (3.76)$$

where  $M_s$  is the mass matrix

$$M_s = \sum_m \int_{V^{(m)}} \rho^{(m)} H^{(m)T} H^{(m)} dV^{(m)}, \quad (3.77)$$

and  $C_s$  is the damping matrix

$$C_s = \sum_m \int_{V^{(m)}} \zeta^{(m)} H^{(m)T} H^{(m)} dV^{(m)}, \quad (3.78)$$

with  $\rho^{(m)}$  is the density of the element and  $\zeta^{(m)}$  is the damping property parameter.

It should be noted that in practice  $C_s$  matrix is constructed from the mass matrix and stiffness matrix. For more details, the reader should refer to Bathe (2014).

There are many commercial software types used for FEA. The leading software used in research and industry is Abaqus which offers a variety of products. To simulate dynamic problems in which direct integration of the equations of motions of the system need to be performed, Abaqus offers two products (Simulia, 2016):

- Implicit dynamic analysis: It uses implicit operators to integrate the equations of motion, this implies that the integration operator matrix must be inverted and a set of non-linear equilibrium equations must be solved in each time increment within a certain tolerance. This integration scheme is unconditionally stable thus allowing the use of large time increments, however each iteration is expensive. This type of analysis is suited for applications involving non-linearity, contact and moderate energy dissipation.
- Explicit dynamic analysis: It uses the central-difference scheme to integrate the equations of motion. The nodal velocities and displacements are determined from the nodal quantities that are known at the beginning of the time increment as follows:

$$\ddot{u}_i = [M_s]^{-1}(P_{(i)} - I_{(i)}) \quad (3.79)$$

The central difference operator is used to determine the velocities and displacements from the following equations:

$$\dot{u}_{i+\frac{1}{2}} = \dot{u}_{i-\frac{1}{2}} + \frac{\Delta t_{i+1} + \Delta t_i}{2} \ddot{u}_i, \quad (3.80)$$

$$u_{i+1} = u_i + \Delta t_{i+1} \dot{u}_{i+\frac{1}{2}}. \quad (3.81)$$

Then, the stresses are computed from the constitutive equation of the material,

$$\sigma_{i+1} = C(\sigma, \Delta\epsilon), \quad (3.82)$$

where,  $\ddot{u}_i$ ,  $\dot{u}$  and  $u$  are the nodal accelerations, velocities and displacements respectively,  $[M_s]$  is the mass matrix,  $P_{(i)}$  is the external applied forces,  $I_{(i)}$  is the internal forces of the system,  $\Delta\epsilon$  is the element strain increment and  $\sigma_{i+1}$  is the stress matrix.

The explicit integration of equations of motions uses a lumped mass matrix because its inverse is simple to calculate and does not require any iteration nor tangent stiffness matrix to be formed. The internal force vector is assembled from the contribution of each element which makes it cheaper than the dynamic implicit procedure. This comes at the expense of stability as the central difference scheme is conditionally stable. To overcome this problem, Abaqus

adjusts the time step automatically to ensure stability. The maximum time step that can be used for an analysis is

$$\Delta t = \frac{l_{min}}{c_s}, \quad (3.83)$$

where  $l_{min}$  is the smallest dimension of an element across the mesh and  $c_s$  is the propagation wave speed calculated from

$$c_s = \sqrt{\frac{E}{\rho_m}}, \quad (3.84)$$

with  $E$  is the elastic modulus and  $\rho_m$  is the density of the material (Simulia, 2016).

It is a good practice to check the total energy ( $E_{total}$ ) of the system to verify the stability of the results. Abaqus specifies that the variation of the total energy needs to be within 1% to accept the stability of the results (Othman, 2016).

Abaqus explicit solver is suited to problems that involve short dynamic response time and for the analysis of events involving discontinuities such as impact, blast load and material degradation such as cracking of concrete. Conversely, it may not be possible to obtain an efficient solution for this class of problems when using the dynamic/implicit solver (Othman, 2016). Therefore, the explicit solver is used for the structural analysis of the bund wall, as the latter is subjected to an impact load of the fluid flow following the catastrophic failure of the storage tank and the concrete exhibits damage due to cracking.

### 3.4.1 Load application analysis procedure

#### 3.4.1.1 Impact loading types

Impact loads can be classified into two categories: hard and soft impacts. In hard impacts, the deformations in the impactor are negligible, therefore it is not needed to take account of them in the analysis of the target. Whilst, in soft impact, both the impactor and target undergo deformations and require to be considered in the analysis (Othman, 2016). Impact loads can be further categorised into low and

high velocity impacts. Previous researches investigated the behaviour of Reinforced Concrete (RC) under hard impact with high velocity ranging between 40m/s and 300m/s. According to CEB-FIP (1988), civil engineering structures are most commonly subjected to low velocity impacts. It is assumed that the bund wall is subjected to soft impact of low velocity.

#### **3.4.1.2 Different techniques for impact load modelling**

Most of the available research in the literature focuses on studying structures under hard impacts. In order to model hard impact in Abaqus, the impactor is modelled at a very close position to the target and is given an initial impact velocity. This technique is not appropriate to model the impact of the fluid flow on the bund wall as the fluid is deformable and the velocity is not known. Alternatively, the impact load can be fed to Abaqus as an input. This requires the prior knowledge of the load profile and particularly for this problem, the bund wall is subjected to different pressure values at the same time, i.e. the fluid flow might impact the wall in some regions of the wall before it reaches the rest of it. Another way to model the soft impact is through the use of Smoothed Particle Hydrodynamics (SPH) which is a meshless technique that replaces the fluid by a set of particles (Sasson et al., 2016). The drawback of this method is that the deformations that occur in both the structure and the fluid and their influence on each other is not accounted for. As a result, a realistic way that mimics the loading mode is needed and the influence of the deformations of the structure on the fluid and vice versa needs to be accounted for, particularly in the case of using ductile materials.

#### **3.4.2 Geometric modelling**

The choice of element type is a basic step in the finite element modelling. Abaqus provides a range of element types designed for various analyses. An element is characterised by its family, degrees of freedom, number of nodes, formulation and integration. For the family of the 3D stress, the explicit solver provides hexahedral, wedge and tetrahedral elements. For this problem, C3D8R elements shown in figure

3.1 were used because they were found efficient to model impact problems (Othman, 2016, Shakir, 2017). The use of the brick elements is favoured over the use of the shell elements to reflect the through thickness deformation of the bund wall.

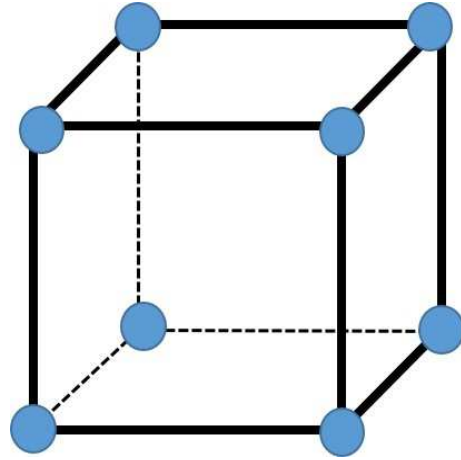


Figure 3.1: C3D8R element

C3D8R is a first order eight nodes element with reduced integration and hourglass control. The first order elements have only nodes on the corners while the second order elements contain nodes in the middle as well. Abaqus explicit adopts only first order interpolation for this element while it offers the reduced and full integration techniques. The reduced integration technique uses fewer integration points than the full integration technique. Using linear interpolation with reduced integration was shown to be more efficient than using the full integration to model problems with large distortions and was used for most of the studies involving impact loading (Belytschko et al., 2013). The hourglass control is activated automatically to prevent the spurious deformation mode of the finite element.

The rebars in Abaqus can be either modelled as three dimensional solid elements which increase the computation time or by simply embedding them in the concrete. This implies that the rebars are tied to the concrete. The benefit of the embedded technique is that the nodes of the rebars elements do not need to coincide with the nodes of the brick elements.

### 3.4.3 Material modelling

The models available in Abaqus to model the concrete are Concrete Smeared Cracking, cracking model for concrete and Concrete Damage Plasticity (CDP). The first model is only available in Abaqus/Standard and permits modelling of problems where concrete is subjected to monotonic load at low confining pressure. The second model is only available in Abaqus/Explicit and allows modelling of brittle materials and cases where the behaviour of the structure is dominated by tensile cracking. This model assumes that the behaviour of concrete is linear elastic. The third model is available in both Abaqus/Standard and Abaqus/Explicit and it is suitable to model structures subjected to dynamic loading, which is the case for this research problem. Furthermore, it does not assume a linearity in the compressive behaviour of the concrete, which allows a more realistic modelling (Simulia, 2016). Additionally, this model has been used by many researchers to model the Ultra High Performance Fibre Reinforced Concrete (UHP-FRC) which is the material adopted for the new design of the bund wall. For all these reasons, CDP is the adopted material model to model the plain concrete, the reinforced concrete and UHP-FRC. This section presents a brief description of the CDP model in conjunction with the plasticity model for the steel, the properties of UHP-FRC and the material behaviour at high strain rate which need to be taken into consideration even for structures subjected to low velocity according to Othman (2016). Strain rate effects are not as significant as in case of extreme loading such as blast and explosion but for a better modelling of the structure, they need to be accounted for.

#### 3.4.3.1 Concrete Damage Plasticity model

The CDP model is based on the concept of isotropic damaged elasticity along with isotropic tensile and compressive plasticity. It considers that the failure mechanisms are tensile cracking and compressive crushing. The model was developed initially by Lubliner et al. (1989) for monotonic loading and developed later by Lee and Fenves (1998) to include dynamic loading. To define the elastic behaviour, the model requires the values of elastic modulus and Poisson's ratio. To define the plastic

behaviour, a yield function, a plastic flow rule and a hardening law in the form of uniaxial tension and compression stress behaviours are required. Additionally, the degradation of the stiffness can be defined (Simulia, 2016).

### Yield function

The yield function is used to determine if the material responds purely elastically at a particular state of stress, temperature, etc. The CDP model uses the following function

$$F = \frac{1}{1 - \alpha}(\bar{q} - 3\alpha\bar{p} + \beta(\tilde{\epsilon}^{pl})\langle\hat{\sigma}_{max}\rangle - \gamma\langle-\hat{\sigma}_{max}\rangle) - \bar{\sigma}_c(\tilde{\epsilon}_c^{pl}) = 0, \quad (3.85)$$

where

$$\bar{p} = -\frac{1}{3}trace(\bar{\sigma}), \quad (3.86)$$

$$\bar{q} = \sqrt{\frac{3}{2}(\bar{S} : \bar{S})}, \quad (3.87)$$

$$\alpha = \frac{(\frac{f_{bo}}{f_{co}}) - 1}{2(\frac{f_{bo}}{f_{co}}) - 1}; 0 \leq \alpha \leq 0.5, \quad (3.88)$$

$$\beta = \frac{\bar{\sigma}_c(\tilde{\epsilon}_c^{pl})}{\bar{\sigma}_t(\tilde{\epsilon}_t^{pl})}(1 - \alpha) - (1 + \alpha), \quad (3.89)$$

and

$$\gamma = \frac{3(1 - K)}{2K - 1}. \quad (3.90)$$

With

$\bar{\sigma}$  is the effective stress,

$\bar{S}$  is the effective stress deviator,

$\hat{\sigma}_{max}$  is the maximum principle effective stress,

$\bar{\sigma}_t(\tilde{\epsilon}_t^{pl})$  is the effective tensile cohesion stress,

$\bar{\sigma}_c(\tilde{\epsilon}_c^{pl})$  is the effective compressive cohesion stress,

$\frac{f_{bo}}{f_{co}}$  is the ratio of initial equibiaxial compressive yield stress to initial compressive yield stress, the default value in Abaqus is 1.16, and

$K$  is the ratio of the second stress invariant on the tensile meridian to that on the compressive meridian, the default value is 0.66 (Simulia, 2016).

### Plastic flow

The flow rule defines the inelastic deformation that occurs in the material. The

CDP model assumes the non-associated plastic flow, which means that the material stiffness matrix is nonsymmetric. The flow potential,  $G$  for this model is the Drucker-Prager hyperbolic function which reads

$$G = \sqrt{(e\sigma_{t0} \tan\psi)^2 + \bar{q}^2} - \bar{p} \tan\psi, \quad (3.91)$$

where,

$\psi$  is the dilation angle

$e$  is the eccentricity, the default value in Abaqus is 0.1.

$\sigma_{t0}$  is the uniaxial tensile stress at failure determined from the tension stiffening data.

The material model in Abaqus needs to be calibrated with  $\frac{f_{bo}}{f_{co}}$ ,  $K$ ,  $\psi$ ,  $e$ , in addition to a viscosity parameter to overcome convergence difficulties, its default value is 0 (Simulia, 2016).

### **Uniaxial tension and compression stress behaviour**

The uniaxial tensile and compressive behaviours are depicted in Figure 3.2. Under uniaxial tension, the stress-strain curve is characterised by a linear branch until the failure stress  $\sigma_{t0}$  is reached. Beyond the failure stress, the response is characterised by a softening regime representing the formation of micro-cracks. Under uniaxial compression, the response of concrete is composed of three branches. In the first branch, the material exhibits a linear response until  $\sigma_{c0}$  is reached. In the second branch, the plastic regime is characterised by a hardening behaviour until the ultimate stress  $\sigma_{cu}$ . Beyond that point, in the third branch, the response of the material exhibits a softening regime.

The image originally presented here cannot be made freely available via LJMU E-Theses Collection because of 'copyright'. The image was sourced from: Simulia (2016), Abaqus analysis user guide <http://130.149.89.49:2080/v2016/books/usb/default.htm>.

The image originally presented here cannot be made freely available via LJMU E-Theses Collection because of 'copyright'. The image was sourced from: Simulia (2016), Abaqus analysis user guide <http://130.149.89.49:2080/v2016/books/usb/default.htm>.

(a) Tensile behaviour

(b) Compressive behaviour

Figure 3.2: Uniaxial stress-strain curves in CDP model (Simulia, 2016)

The model assumes that when the concrete is unloaded from any point in the softening stress-strain curve, the elastic stiffness is degraded which is characterised by two parameters, a tensile damage parameter  $d_t$  and a compressive damage parameter  $d_c$ . The stress-strain relations under uniaxial tensile and compressive loading of a material with an initial elastic stiffness  $E_0$  become:

$$\sigma_t = (1 - d_t)E_0(\epsilon_t - \tilde{\epsilon}_t^{pl}), \quad (3.92)$$

$$\sigma_c = (1 - d_c)E_0(\epsilon_c - \tilde{\epsilon}_c^{pl}). \quad (3.93)$$

The damage parameters can be calculated from

$$d_t = 1 - \frac{\sigma_t}{\bar{\sigma}_t}, \quad (3.94)$$

$$d_c = 1 - \frac{\sigma_c}{\bar{\sigma}_c}. \quad (3.95)$$

$\bar{\sigma}_t$  and  $\bar{\sigma}_c$  are the effective tensile and compressive stresses calculated from

$$\bar{\sigma}_t = E_0(\epsilon_t - \tilde{\epsilon}_t^{pl}) \quad (3.96)$$

$$\bar{\sigma}_c = E_0(\epsilon_c - \tilde{\epsilon}_c^{pl}). \quad (3.97)$$

### 3.4.3.2 Steel reinforcement constitutive model

To model the steel reinforcement, the classical metal plasticity model has been used, which assumes that the behaviour of steel in compression and tension is the same.

The model uses the Mises yield surface to define isotropic yielding. The values of the uniaxial stress-strain curve need to be entered into Abaqus in order to define the Mises yield surface.

### **3.5 Ultra High Performance Fibre Reinforced Concrete UHP-FRC**

UHP-FRC is a relatively new construction material that is known for its enhanced mechanical and durability properties. The history of its first development dates back to the 1930's with Eugene Freyssinet who proved that pressing high strength concrete during setting could enhance its compressive strength. Subsequent investigations during the 1970's considered increasing the mechanical properties of concrete by reducing its porosity using vacuum mixing and high pressure at high temperature. During the 1980's, improvement in the density has been achieved through the use of superplasticisers and pozzolanic admixtures such as silica fume, however this resulted in a very brittle concrete. The last improvement was during the 1990's and proposed to add fibres to enhance the concrete ductility, which led to what is known today as UHP-FRC. Many types of fibres can be used such as steel, glass, carbon, etc. However, steel fibres are the most used in UHP-FRC. UHP-FRC is mainly composed of cement, fine aggregate, supplementary cementitious materials such as silica fume, superplasticiser and water. The material has been used in many civil engineering structures. A footbridge in Sherbrooke, Canada was the first structure to be built from UHP-FRC in 1997. Additionally, it is used in many highway bridges and offshore structures, to name but a few (Hassan, 2013). The material is known for its good performance under impact loading (Hassan, 2013, Othman, 2016, Eide and Hisdal, 2012). It was reported that UHP-FRC was used in the stabilisation of a sea wall in Reunion Island in France (Hassan, 2013). Furthermore, due to its compact matrix, it can resist the penetration of liquid, gas and aggressive agents. As a result, UHP-FRC is a good candidate to be used for the construction of the bund wall to resist the impact of the fluid flow, even in the case of small spillage, the material can be retained in the banded area. The principles of UHP-FRC as

well as its mechanical behaviour are further detailed in the following subsections.

### **3.5.1 Principle of UHP-FRC**

The basic principles of UHP-FRC consist in developing a more homogeneous and denser material than concrete, with a better microstructure and ductility. These principles can be detailed as follows:

**Homogeneity:** Eliminating the coarse aggregates and replacing them with fine aggregates with a size no more than 2.5mm according to JSCE (2008) enhances its homogeneity which results in reducing the number of voids and microcracks (Acker and Behloul, 2004).

**Packing density:** The use of fine sand, cement and fine grained supplementary cementitious material that can fill the voids results in a dense mixture. Additionally, the use of low water-cement ratio ranging between 0.2 to 0.25 maintains the small spacing of the cement grains which contributes to increasing the density of the material. Lowering the water-cement ratio can cause workability issues which is overcome by the use of superplasticisers (Hassan, 2013, Othman, 2016).

**Microstructure:** The microstructure of UHP-FRC can be enhanced by applying pressures and heat treatment (Hassan, 2013).

**Ductility:** The addition of fibres enhances significantly the ductility and the tensile properties (Hassan, 2013).

### **3.5.2 Mechanical properties of UHP-FRC under low strain rate**

UHP-FRC exhibits better mechanical properties than those of a normal concrete. However, the most important feature of UHP-FRC is the significant improvement in its tensile behaviour (Eide and Hisdal, 2012).

#### **3.5.2.1 Compressive behaviour**

The compressive behaviour of UHP-FRC is characterised by the compressive strength, modulus of elasticity, Poisson's ratio and a significant post-peak ductility. Figure 3.3

depicts the stress-strain curve of UHP-FRC compared to high strength concrete. It has been reported that more than 150 MPa in compressive strength can be achieved (Richard and Cheyrezy, 1994, Acker and Behloul, 2004, Graybeal, 2005, Yang et al., 2009). UHP-FRC is characterised by high modulus of elasticity ranging between 45 and 60 GPa. Compared to high strength concrete, the modulus of elasticity and compressive strength are slightly higher but the main improvement in the compressive behaviour lies in the significant post-peak ductility. The Poisson's ratio is slightly higher than Poisson's ratio of normal strength and high strength concrete. A value of 0.2 can be adopted for UHP-FRC according to BFUP and AFGC (2002) but higher values reaching 0.25 can be achieved (Dugat et al., 1996, Voo et al., 2003).

The image originally presented here cannot be made freely available via LJMU E-Theses Collection because of 'copyright'. The image was sourced from: Fehling, E., Leutbecher, T. and Bunje, K. (2004), Design relevant properties of hardened ultra high performance concrete, in 'Int. Symp. on Ultra High Performance Concrete', Vol. 1, pp. 327-338.

Figure 3.3: Typical compressive behaviour of UHP-FRC (Fehling et al., 2004)

### 3.5.2.2 Tensile behaviour

Figure 3.4 shows the tensile behaviour of UHP-FRC. The stress-strain curve is characterised by a linear response up to the tensile strength of the matrix. Then, the response exhibits a strain hardening phase that corresponds to the appearance of non-continuous micro-cracks in the cementitious paste. At this stage, the tensile stress and deformations keep increasing until reaching the tensile strength of the material. Beyond that point, one macrocrack develops which corresponds to a strain softening stage (Hassan, 2013). The tensile strength of UHP-FRC ranges between 8 and 15 MPa according to Chanvillard and Rigaud (2003).

The image originally presented here cannot be made freely available via LJMU E-Theses Collection because of 'copyright'. The image was sourced from: Fehling, E., Leutbecher, T. and Bunje, K. (2004), Design relevant properties of hardened ultra high performance concrete, in 'Int. Symp. on Ultra High Performance Concrete', Vol. 1, pp. 327-338.

Figure 3.4: Typical tensile behaviour of UHP-FRC (Fehling et al., 2004)

### 3.5.2.3 Fracture behaviour

The fracture energy is the amount of energy required to open a unit area of crack (Simulia, 2016). Figure 3.5 depicts the fracture energy of UHP-FRC. It is calculated as the area under the strain hardening and softening branches. The fracture energy ranges between 14,000 and 40,000 N/m compared to 100 and 160 N/m for normal strength concrete and high strength concrete, respectively (Othman, 2016).

The image originally presented here cannot be made freely available via LJMU E-Theses Collection because of 'copyright'. The image was sourced from: Othman, H. A. B. (2016), Performance of ultra-high performance bre reinforced concrete plates under impact loads, PhD thesis, Ryerson University.

Figure 3.5: Fracture energy of UHP-FRC (Othman, 2016)

## 3.6 Material behaviour at high strain

In general, materials subjected to high strain rates exhibit an enhancement in their mechanical properties. The degree of the increase in the dynamic properties depends

on the strain rate which itself depends on the load case. Different load cases and the corresponding strain rates are indicated in Table 3.1.

Table 3.1: Different load cases and corresponding strain rates (CEB-FIP, 1988)

<b>Load case</b>	<b>Strain rate (<math>s^{-1}</math>)</b>
Traffic	$10^{-6} - 10^{-4}$
Gas explosions	$5 \times 10^{-5} - 5 \times 10^{-4}$
Earthquake	$5 \times 10^{-3} - 5 \times 10^{-1}$
Pile driving	$10^{-2} - 10^0$
Aircraft impact	$5 \times 10^{-2} - 2 \times 10^0$
Hard impact	$10^0 - 5 \times 10^1$
Hypervelocity impact	$10^2 - 10^6$

A method to take into account the increase in dynamic properties is through the Dynamic Increase Factor (DIF) which is the ratio of the dynamic to static strength. When subjected to high load rate, the concrete exhibits an increase in its strength, strain capacity and fracture energy (Banthia et al., 1989). Similarly, the mechanical properties of steel reinforcement are also enhanced with a more significant improvement in the yield stress than the ultimate stress (Asprone et al., 2009). It was shown in Othman (2016) that UHP-FRC is less strain sensitive than higher strength concrete. In Abaqus, the strain rate can be accounted for by giving the tabular input of the enhanced stresses as a function of inelastic strains.

### 3.7 Fluid Structure Interaction (FSI)

Fluid Structure Interaction (FSI) is the act of modelling a multi-physics problem involving a fluid and structural sub-domains, where the fluid flow causes the deformation of a solid structure, which in turn causes the boundary conditions of the fluid problem to change (Raja, 2012). FSI history dates back to the late 1970's with an extensive research related to the aerospace field (Campbell, 2010). However, the applications of FSI include other fields such as the study of parachutes (Tezduyar et al.,

2008), bridges, offshore structures, storage tanks, aircraft (Ross, 2006), biomedical applications for example investigating arterial blood flow (Figuroa et al., 2006), lung modelling (Wall and Rabczuk, 2008), etc.

### 3.7.1 Types of approach

There are two approaches to solve an FSI problem, namely the monolithic and the partitioned approaches. In the monolithic approach, the whole fluid and structure system is described in one combined system by the same primitive variables. The system of governing equations is then solved using the same scheme. This approach gives accurate numerical results. However, it needs highly specialised software. Furthermore, a single time step is used which might not be appropriate for some problems. Similarly, the use of a single mesh for both domains might affect the quality of the mesh of one domain if it needs refined mesh quality on some region, usually for the fluid domain. On the other hand, the partitioned approach solves the discretised governing equations of each domain separately and exchanges information at the interface. This approach permits the use of different software and the modelling can be done by different experts. Furthermore, the meshes can be of different resolutions. This comes at the expense of the stability of the solution due to the small errors (Campbell, 2010, Sicklinger, 2014).

### 3.7.2 MpCCI workflow

MpCCI is a commonly referenced software. MpCCI supports only the partitioned approach, which in its terminology is called the weak coupling. Coupling can be unidirectional or bidirectional. MpCCI supports two coupling schemes which are the Gauss-Seidel and the Jacobin algorithms corresponding to serial and parallel schemes. The Gauss Seidel is commonly referred to as the Conventional Serial Staggered (CSS) (Campbell, 2010) in which code 1 computes for one time step, sends the data to code 2. The latter, solves the governing equation for one time step and sends the data back to code 1 as shown in Figure 3.6. The drawback of this serial scheme is that it leads to an increase of the overall run time. In a parallel

scheme as shown in Figure 3.7, both codes are solving the equations at the same time which eliminates the dependency of one code on the other.

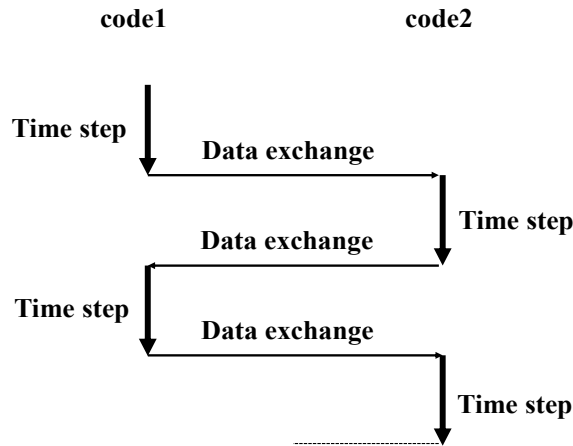


Figure 3.6: Serial coupling

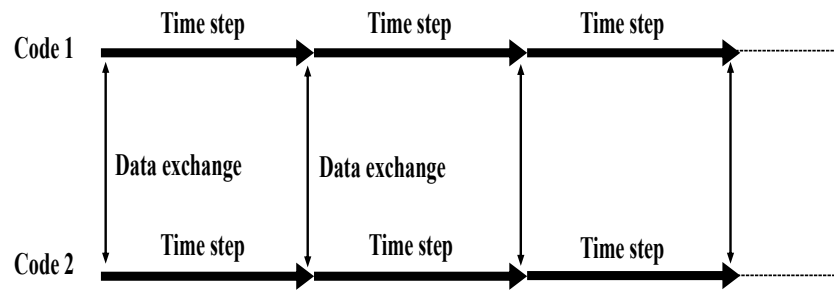


Figure 3.7: Parallel coupling

Furthermore, MpCCI adopts within each scheme two types of coupling: the explicit coupling and the implicit coupling. In the explicit coupling, the data sets are exchanged just once during each time step which results in stability issues. In the implicit coupling known also as iterative coupling, iterations are required within each time step and data sets are exchanged between codes after each iteration. This coupling algorithm ensures the stability of the solution but the inner iterations are expensive. The iterative coupling is used when the interaction is strong usually for FSI problems involving incompressible fluid and a low density solid (Fraunhofer, 2018).

In order to transfer the data at the interface, MpCCI first performs an association operation in which each element from one domain is associated to a partner element

from the other domain and then it performs interpolation in which quantities need to be transferred to the associated partner (Fraunhofer, 2018).

### 3.8 Dimensional analysis

Dimensional analysis is a method that permits the study of complex physical problems in a simpler form, i.e. more economical (Sonin, 2001). The dimensional analysis is based on the concept of similitude that implies that measurements made on a system can be used to describe the behaviour of a similar system. Usually, the measurements are made on a small scale system referred to as model to understand the behaviour of a system with a larger scale referred to as a prototype. The first step in studying a system is to decide on a specific quantity to be evaluated and on the other quantities that have effect on it. If the system has many variables, then the process of evaluating the quantity of interest will be cumbersome as this requires many experiments to be performed. An alternative way to alleviate the complexity is to use the Buckingham Pi theorem to establish a relationship between dimensionless products which reduces the number of variables. The dimensionless products are referred to as pi terms. The steps of the Buckingham Pi theorem are listed as follows (Munson et al., 2010):

1. List all the variables that are pertinent to the problem.
2. Express each variable in terms of basic dimensions, for example  $M$ ,  $L$  and  $T$  where  $M$  is the mass,  $L$  is the length and  $T$  is the time.
3. Determine the required number of pi terms by applying Buckingham Pi theorem, which says if  $n_d$  is the number of variables, and  $k_d$  is the number of the basic dimensions required to describe the variables, then  $n_d - k_d$  is the number of pi terms.
4. Select the repeating variables whose number is equal to the number of basic dimensions. Some rules need to be considered when selecting the repeating variables. First, the repeating variables do not have to include the variable to be isolated, i.e. the variable to be expressed as a function of the rest of

variables. Second, all the basic dimensions must be presented in the repeating variables. Third, a repeating variable which has the same unit as another repeating variable to a power needs not to be picked.

5. Deriving the pi terms by multiplying each of the non-repeating variables by the repeating variables raised to an exponent in such a way the combination is dimensionless.

6. Express the relationship between the pi terms in the form of

$$\Pi_1 = f(\Pi_2, \Pi_3, \dots, \Pi_{n_d-k_d}).$$

### 3.9 Summary

This chapter presented a theoretical background of the different approaches used to solve the problems encompassed in this research project. An overview of CFD, FEA and FSI techniques was given in relation to the software packages employed, which are OpenFoam, Abaqus and MpCCI. The basics of the CFD were introduced with the focus on the multiphase flow problem, as the catastrophic failure of the bund wall falls under the multiphase type of flow. Additionally, the turbulence modelling was detailed to allow an appropriate selection of the turbulence model. Furthermore, FEA presented the capabilities of Abaqus to model the concrete and the mesh options for structure modelling under impact load. Additionally, the properties of UHP-FRC were detailed as it constitutes the material adopted for the new design of the bund wall. The FSI review highlighted the state of the art of the technique and the capabilities of MpCCI. Based on this overview, the different assumptions made for the modelling will be detailed in the next chapter.

# Chapter 4

## Methodology

### 4.1 Introduction

This chapter presents the methodology followed to solve the bund wall problem for this research project based on the theoretical background outlined in the previous chapter. First, the CFD methodology is introduced by presenting the experiment, the software used, the test matrix and the assumptions made for the modelling. Then, the FEA methodology is presented in the same manner. Finally, the modelling methodology of the Fluid Structure Interaction is described by giving the different steps of coupling OpenFOAM to Abaqus.

### 4.2 Modelling methodology for the CFD

#### 4.2.1 Validation test

Within a previous research project that took place at Liverpool John Moores University, extensive experimental work was carried out to determine the overtopping fractions and the dynamic pressures at the bund wall after the catastrophic collapse of a storage tank. The experiment as depicted in Figures 4.1 and 4.2 consisted of the removal of a tank quadrant allowing olive oil to rapidly escape under the effect of gravity. The fluid flow impacts the bund wall and reaches high levels until it comes to rest. The testing was carried out to investigate the behaviour of the collapse with different capacities of bund wall, using multiple heights of fluid and various shapes of wall along with different temperatures of the fluid. The experiments were carried out at a scale of 1:30. The available experimental data of overtopping fractions and dynamic pressures were used to validate the CFD simulations.

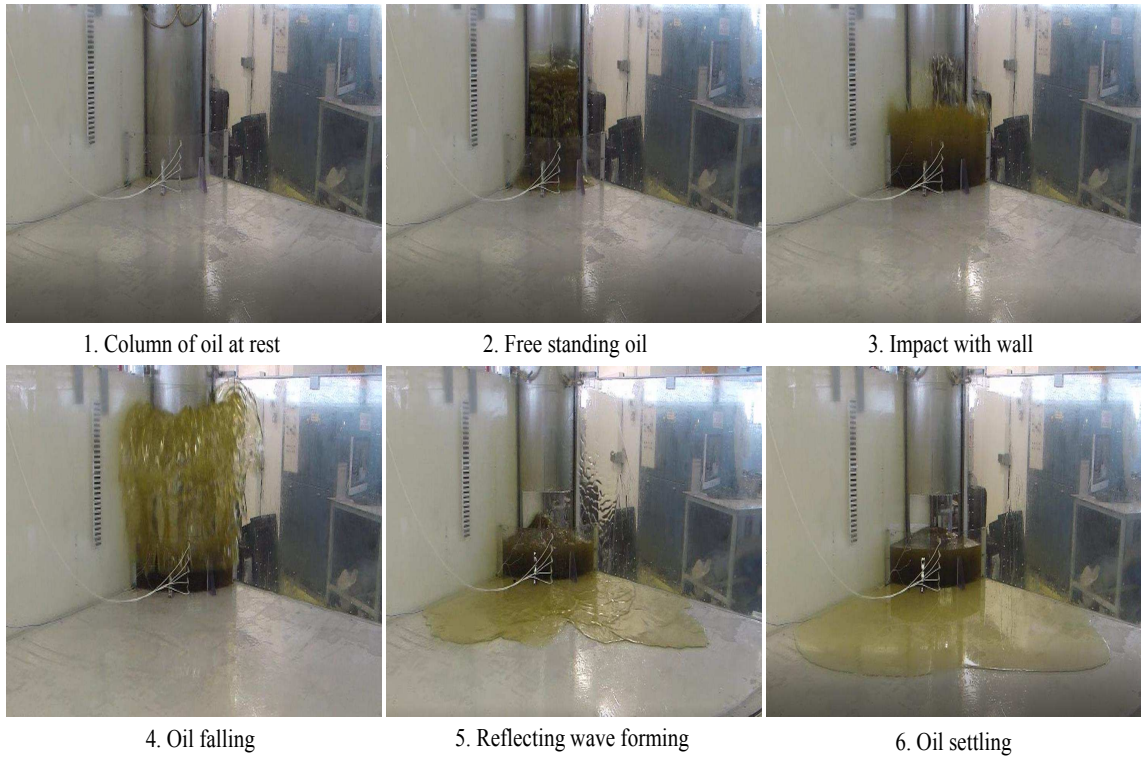


Figure 4.1: Experiment of the collapse of the storage tank - front view

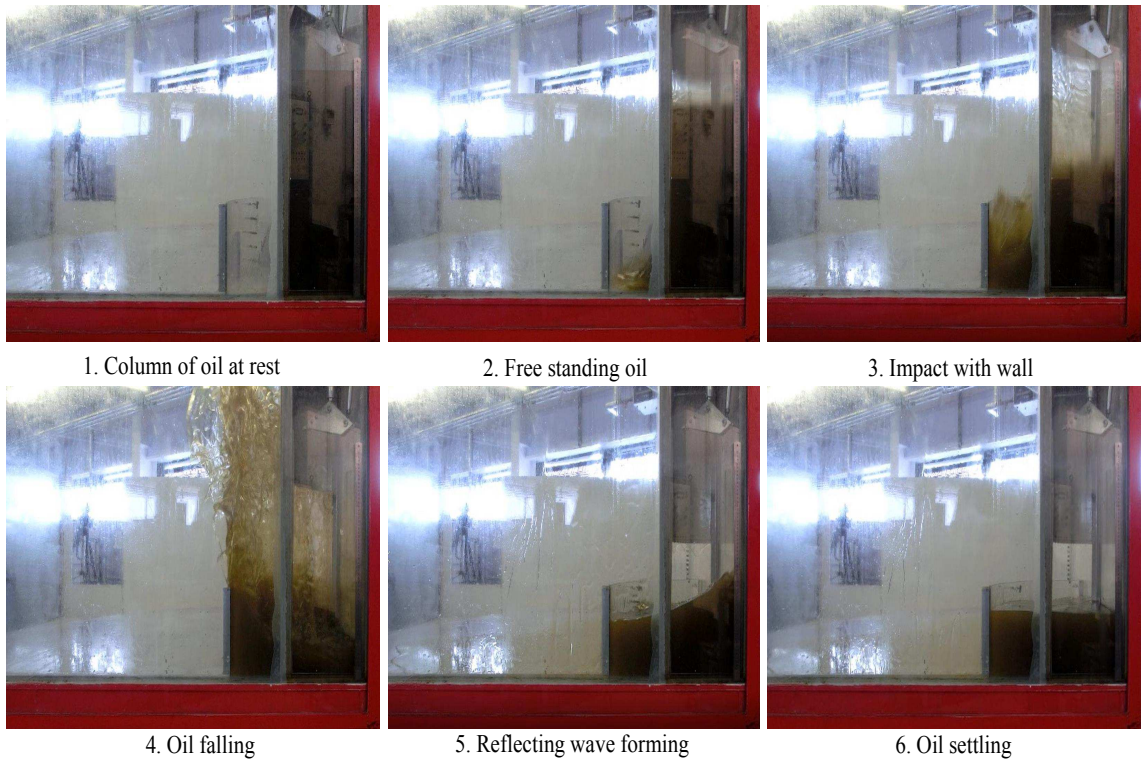


Figure 4.2: Experiment of the collapse of the storage tank - side view

### 4.2.2 Software used

OpenFOAM software was chosen for the CFD modelling due to its free availability. Additionally, OpenFOAM allows parallel processing, which decreases the simulation time. Another benefit is that OpenFOAM is an open source software, so the user is allowed to modify the algorithms to fit the needs of a specific problem. OpenFOAM was used for processing, while two other open source software packages were used for the pre and post processing which are SALOME 7.8.0 and Paraview, respectively.

### 4.2.3 Test matrix for the standard configurations

The first part of the CFD simulations consisted of simulating the collapse of a storage tank with the use of standard configurations of bund walls, which incorporate no mitigation techniques. Four different shapes of bund wall were investigated which are the circular, triangular, square and rectangular bund walls. The nomenclature of the tank and bund wall arrangements is given in Figures 4.3 and 4.4.

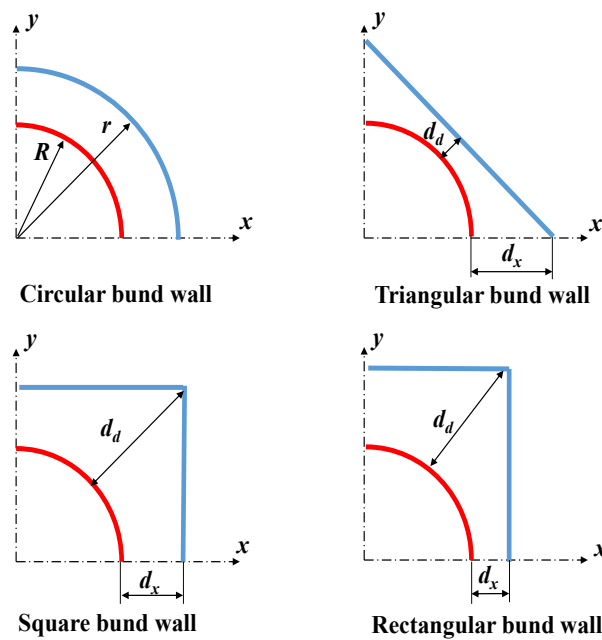


Figure 4.3: Tank and bund wall nomenclature of the different shapes

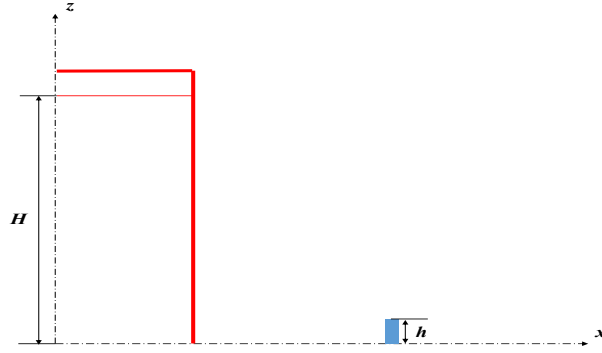


Figure 4.4: Tank and bund wall nomenclature - front view

A significant part of the simulations considered the effect of varying the capacity of the circular bund wall to cover capacities of 110%, 120%, 150% and 200%, under the same height of fluid. Additionally, for each capacity, the effect of varying the separation distance between the tank and the bund wall was studied. The test configurations and the corresponding dimensions are given in Tables 4.1, 4.2, 4.3 and 4.4.

Table 4.1: Effect of the separation distance (circular wall, tall tank, capacity 110%)

Test name	Height of the fluid $H$ (m)	Radius of the bund $r$ (m)	Height of the bund wall $h$ (m)
$F_1$	0.6	1.407	0.03
$E_1$	0.6	0.995	0.06
$D_1$	0.6	0.704	0.12
$C_1$	0.6	0.547	0.18
$B_1$	0.6	0.497	0.24

Table 4.2: Effect of the separation distance (circular wall, tall tank, capacity 120%)

Test name	Height of the fluid $H$ (m)	Radius of the bund $r$ (m)	Height of the bund wall $h$ (m)
$F_2$	0.6	1.47	0.03
$E_2$	0.6	1.039	0.06
$D_2$	0.6	0.735	0.12
$C_2$	0.6	0.6	0.18
$B_2$	0.6	0.52	0.24

Table 4.3: Effect of the separation distance (circular wall, tall tank, capacity 150%)

Test name	Height of the fluid $H$ (m)	Radius of the bund $r$ (m)	Height of the bund wall $h$ (m)
$F_3$	0.6	1.643	0.03
$E_3$	0.6	1.162	0.06
$D_3$	0.6	0.822	0.12
$C_3$	0.6	0.671	0.18
$B_3$	0.6	0.581	0.24

Table 4.4: Effect of the separation distance (circular wall, tall tank, capacity 200%)

Test name	Height of the fluid $H$ (m)	Radius of the bund $r$ (m)	Height of the bund wall $h$ (m)
$F_4$	0.6	1.897	0.03
$E_4$	0.6	1.342	0.06
$D_4$	0.6	0.949	0.12
$C_4$	0.6	0.775	0.18
$B_4$	0.6	0.671	0.24

The CFD simulations also studied the effect of using high collar bund walls, which are normally used around tanks that store hazardous substances. These simulations were performed under the same fluid height, but with different bund wall heights and separation distances as illustrated in Table 4.5.

Table 4.5: High collar bund wall (circular wall)

Test name	Height of the fluid $H$ (m)	Radius of the bund $r$ (m)	Height of the bund wall $h$ (m)
$A_1(600)$	0.6	0.315	0.6
$A_1(720)$	0.6	0.315	0.72
$A_2(600)$	0.6	0.33	0.6
$A_2(720)$	0.6	0.33	0.72
$A_3(600)$	0.6	0.36	0.6
$A_3(720)$	0.6	0.36	0.72
$A_4(600)$	0.6	0.39	0.6
$A_4(720)$	0.6	0.39	0.72

Additionally, the effect of using different shapes of bund walls was studied along with the effect of fluid height. The fluid heights investigated are 0.12m, 0.3m and 0.6m representing squat, middle and tall tanks, respectively. The shapes of bund wall

considered in addition to the circular bund walls were triangular, square and rectangular. All these cases were performed with 110% bund capacity. The respective dimensions are given in Tables 4.6, 4.7 and 4.8.

Table 4.6: Effect of the height of the fluid (triangular wall, capacity 110%)

Test name	Height of the fluid $H$ (m)	$d_x$ (m)	$d_d$ (m)	Height of the bund wall $h$ (m)
$Wall_1$ (tall tank)	0.6	0.582	0.324	0.12
$Wall_4$ (middle tank)	0.3	0.582	0.324	0.06
$Wall_7$ (squat tank)	0.12	0.947	0.582	0.012

Table 4.7: Effect of the height of the fluid (square wall, capacity 110%)

Test name	Height of the fluid $H$ (m)	$d_x$ (m)	$d_d$ (m)	Height of the bund wall $h$ (m)
$Wall_2$ (tall tank)	0.6	0.324	0.582	0.12
$Wall_5$ (middle tank)	0.3	0.324	0.582	0.06
$Wall_8$ (squat tank)	0.12	0.582	0.947	0.012

Table 4.8: Effect of the height of the fluid (rectangular wall, capacity 110%)

Test name	Height of the fluid $H$ (m)	$d_x$ (m)	$d_d$ (m)	Height of the bund wall $h$ (m)
$Wall_3$ (tall tank)	0.6	0.141	0.686	0.12
$Wall_6$ (middle tank)	0.3	0.141	0.686	0.06
$Wall_9$ (squat tank)	0.12	0.324	1.095	0.012

The final variable studied is the effect of temperature for olive oil under 20°C, 25°C and 30°C using circular and square walls. The test specifications are presented in Tables 4.9 and 4.10.

Table 4.9: Effect of the fluid temperature (circular wall, tall tank, capacity 110%)

Test name	Temperature	Height of the fluid $H$ (m)	Radius of the bund $r$ (m)	Height of the bund wall $h$ (m)
$E_1 - 20$	20°C	0.6	0.995	0.06
$E_1 - 25$	25°C	0.6	0.995	0.06
$E_1 - 30$	30°C	0.6	0.995	0.06

Table 4.10: Effect of the fluid temperature (square wall, middle tank, capacity 110%)

Test name	Temperature	Height of the fluid $H$ (m)	$d_x$ (m)	$d_d$ (m)	Height of the bund wall $h$ (m)
$Wall_5 - 20$	20°C	0.6	0.624	0.582	0.06
$Wall_5 - 25$	25°C	0.6	0.624	0.582	0.06
$Wall_5 - 30$	30°C	0.6	0.624	0.582	0.06

#### 4.2.4 Test matrix for configurations incorporating mitigation techniques

The CFD modelling of the standard configurations was followed by CFD modelling of the collapse of the storage tank with the incorporation of mitigation techniques proposed by Ash (2010). The height of MOTIF was chosen to be the same as Ash (2010) proposed after performing an optimisation study yielding an optimum height of  $H/3$  and COAST was incorporated as a retrofit to the wall with fitting a 20mm straight inwardly facing baffle. Ash (2010) used baffles inclined at 45 degrees, while in this study the angle of inclination  $\theta$  was optimised. The mitigation techniques arrangements and dimensions are given in Figures 4.5, 4.6 and 4.7.

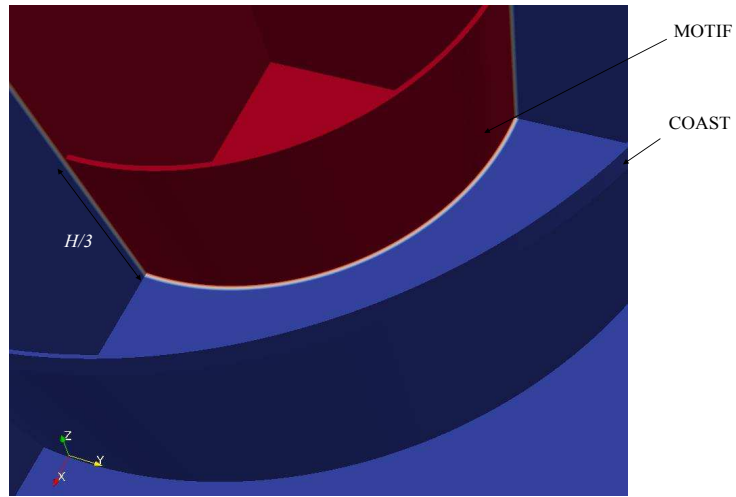


Figure 4.5: Tank and bund arrangements incorporating MOTIF and COAST

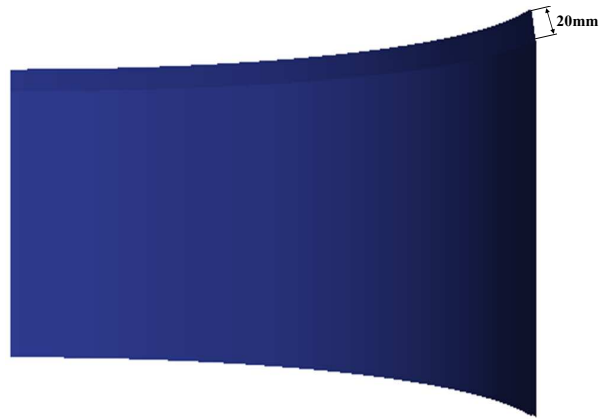


Figure 4.6: Bund wall incorporating COAST



Figure 4.7: Angle of COAST

The optimisation of the angle of inclination covered angles ranging from 10 degrees to 80 degrees with an increment of 10 degrees as given in Table 4.11, being performed

on circular configurations incorporating MOTIF and COAST. Furthermore, the performance of each mitigation measure was investigated separately and compared to the case when both MOTIF and COAST were incorporated at an angle 45 degrees. This was for the purpose of selecting the appropriate mitigation technique which allows a reduction in the dynamic pressures and overtopping quantities at a reduced cost. The optimisation study led to selecting COAST at an angle of 80 degrees. Subsequently, the effect of using COAST on bund walls with different capacities and different shapes was considered. This was to allow comparison against standard configurations, where the experimental data was available. The dimensions and the specifications of the different tests are illustrated in Tables 4.11 and 4.12.

Table 4.11: Test matrix for circular bund wall incorporating mitigation

	<b>Test name</b>	<b>Angle (degrees)</b>	<b>Capacity %</b>	<b><math>H</math> (m)</b>	<b><math>r</math> (m)</b>	<b><math>h</math> (m)</b>
Optimisation of the angle of the baffle	$M\&C_{10}$	10	110	0.6	0.497	0.24
	$M\&C_{20}$	20	110	0.6	0.497	0.24
	$M\&C_{30}$	30	110	0.6	0.497	0.24
	$M\&C_{40}$	40	110	0.6	0.497	0.24
	$M\&C_{50}$	50	110	0.6	0.497	0.24
	$M\&C_{60}$	60	110	0.6	0.497	0.24
	$M\&C_{70}$	70	110	0.6	0.497	0.24
	$M\&C_{80}$	80	110	0.6	0.497	0.24
Selection of the mitigation technique	$Motif$		110	0.6	0.497	0.24
	$C_{45}$	45	110	0.6	0.497	0.24
	$M\&C_{45}$	45	110	0.6	0.497	0.24
Effect of capacity	$C_{80} - 120\%$	80	120	0.6	0.52	0.24
	$C_{80} - 150\%$	80	150	0.6	0.581	0.24
	$C_{80} - 200\%$	80	200	0.6	0.671	0.24

Table 4.12: Effect of COAST on non-circular bund walls

Test name	Shape	$H$ (m)	$d_x$ (m)	$d_d$ (m)	$h$ (m)
$C_{80}$ – triangular	triangular	0.6	0.582	0.324	0.12
$C_{80}$ – square	square	0.6	0.324	0.582	0.12
$C_{80}$ – rectangular	rectangular	0.6	0.141	0.686	0.12

#### 4.2.5 Test matrix for the asymmetric configurations

The partial failure of storage tanks is a common problem in the industry that can be caused by the loss of integrity of a small section of the tank wall (Atherton, 2008). This work has considered a number of simulations of the partial failure by creating a rectangular aperture in the tank shell along with studying the performance of MOTIF for this mode of failure. The partial failure was investigated on the  $B_1$  test configuration with  $H = 300\text{mm}$ . The aperture specifications and dimensions were taken from Ash (2010) and are given in Figure 4.8 and Table 4.13.

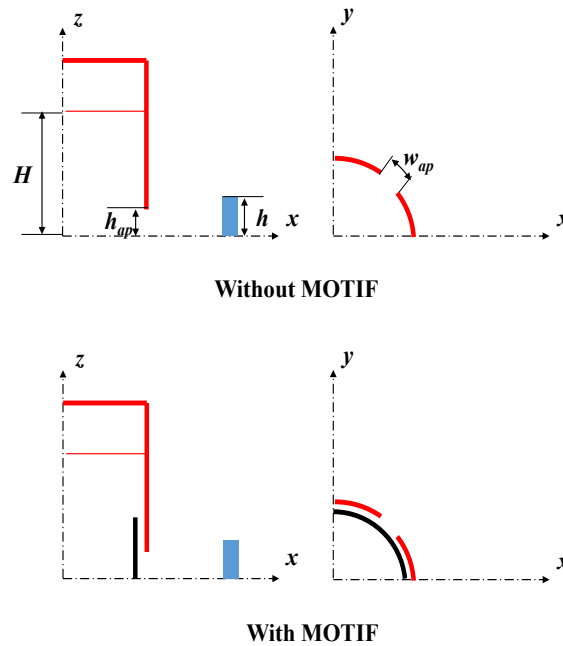


Figure 4.8: Tank and bund nomenclature for partial failure

Table 4.13: Partial failure tests

Test name	$w_{ap}$ (m)	$h_{ap}$ (m)	Mitigation
$B_1rect_1$	0.15708	0.018	unmitigated
$MB_1rect_1$	0.15708	0.018	mitigated
$B_1rect_2$	0.15708	0.054	unmitigated
$MB_1rect_2$	0.15708	0.054	mitigated
$B_1rect_3$	0.15708	0.09	unmitigated
$MB_1rect_3$	0.15708	0.09	mitigated

## 4.2.6 Mathematical model

### 4.2.6.1 Two-phase flow solver

This problem was solved in OpenFOAM using the InterFOAM solver which solves for two incompressible, isothermal immiscible fluids using the VOF method. InterFOAM uses the semi-implicit MULES for the discretisation of the phase fraction equation. Unlike the explicit MULES which requires  $Co = 0.25$ , the semi-implicit version does not require any limit on  $Co$ . However, to satisfy the requirements on temporal accuracy,  $Co$  should not exceed 1. In InterFOAM, it is difficult to use a fixed time step to satisfy the  $Co$  criteria, therefore InterFOAM uses automatic adjustment of the time step (Greenshields, 2018).

### 4.2.6.2 Turbulence model

The Shear-Stress Transport ( $k-\omega$ -SST) model in its low Reynolds version was chosen for turbulence modelling due to its ability to predict flow with adverse pressure near the wall and to avoid the sensitivity to the values of  $\omega$  outside the boundary layer.

### 4.2.6.3 Material physical properties

The physical properties needed to calibrate the material models in InterFOAM are the density and the kinematic viscosity of olive oil and air, which are considered as

Newtonian fluids. Additionally, the surface tension between olive oil and air is also required. The values of surface tension, density and kinematic viscosity for olive oil and air at the different temperatures are given in Tables 4.14 and 4.15.

Table 4.14: Surface tension between the fluids (Sahasrabudhe et al., 2017)

<b>Fluids</b>	<b>Surface tension value</b>
olive oil / air	0.03

Table 4.15: Physical properties of the fluids (Sahasrabudhe et al., 2017)

<b>Fluid</b>	<b>Temperature</b>	<b>Density <math>\rho_f</math> Kg/m<sup>3</sup></b>	<b>Kinematic viscosity <math>\nu</math> (m<sup>2</sup>/s)</b>
air	20°C	1.205	15.11 10 <sup>-6</sup>
air	25°C	1.1839	15.57 10 <sup>-6</sup>
air	30°C	1.1644	16.036 10 <sup>-6</sup>
olive oil	20°C	915.2	89.16 10 <sup>-6</sup>
olive oil	25°C	910.9	67.4 10 <sup>-6</sup>
olive oil	30°C	907.2	62.3 10 <sup>-6</sup>

## 4.2.7 Numerical model

### 4.2.7.1 Discretisation of the solution domain

The computational domain was created in Salome 7.8.0 with the same dimensions as the experimental set-up, and is depicted in Figure 4.9.

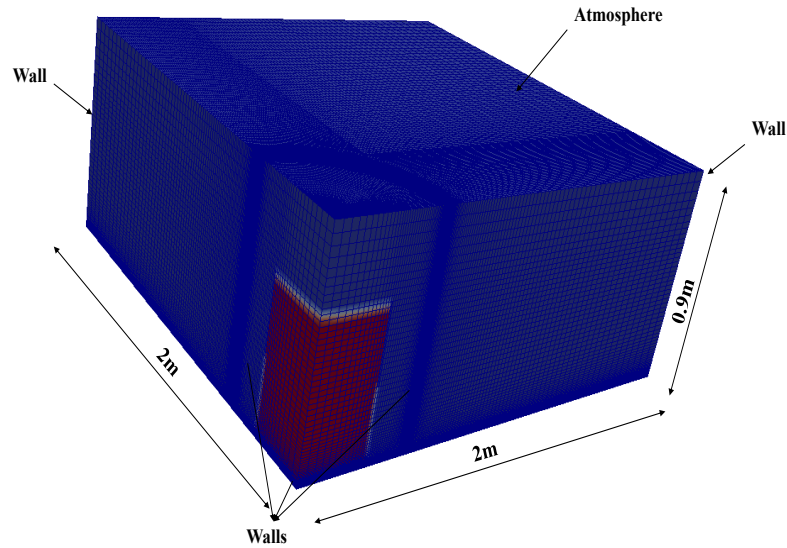


Figure 4.9: Mesh and boundary conditions of the fluid domain

The mesh was built ensuring certain rules of quality such as smoothness and aspect ratio. The mesh created is structured with hexahedral cells and a few prisms in the corner and the grid lines were aligned with the flow as much as possible. The reason behind that is that hexahedral mesh yields a more accurate solution in the case of alignment of the grid lines with the flow direction. A transition ratio of 1.2 was not exceeded to ensure a reasonable level of smoothness. Additionally, the aspect ratio was reduced as much as possible except in near wall regions, a high aspect ratio of 800 was used to reduce the cell count while satisfying the  $y^+$  condition. The height of cells near the wall were of the order of  $10^{-4}$ m. OpenFOAM allows an aspect ratio up to 1,000 and cells with high aspect ratio near the wall are commonly used to reduce the cells count and is acceptable as long as the flow is aligned with the longest side of the cell. There are other mesh quality rules such as skewness and orthogonality, etc. OpenFOAM has a utility called CheckMesh to ensure that a mesh meets the requirements before starting a simulation. All meshes were checked before running any case. The inside view of an example of a mesh is depicted in Figure 4.10.

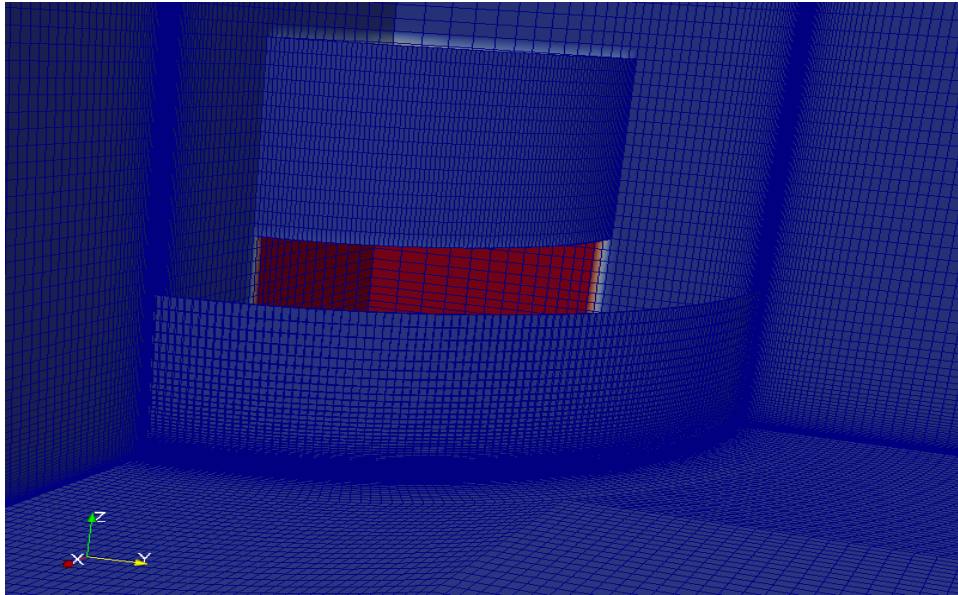


Figure 4.10: Mesh of the fluid domain - inside view

The  $y^+ = 1$  criterion was satisfied on the base and on the bund wall, which resulted in a dense mesh next to these regions as shown in Figures 4.11 and 4.12. Ultimately, the cell count ranged between 1.1 and 4.5 million cells for standard cases and up to 4.9 million cells for the cases incorporating mitigation techniques.

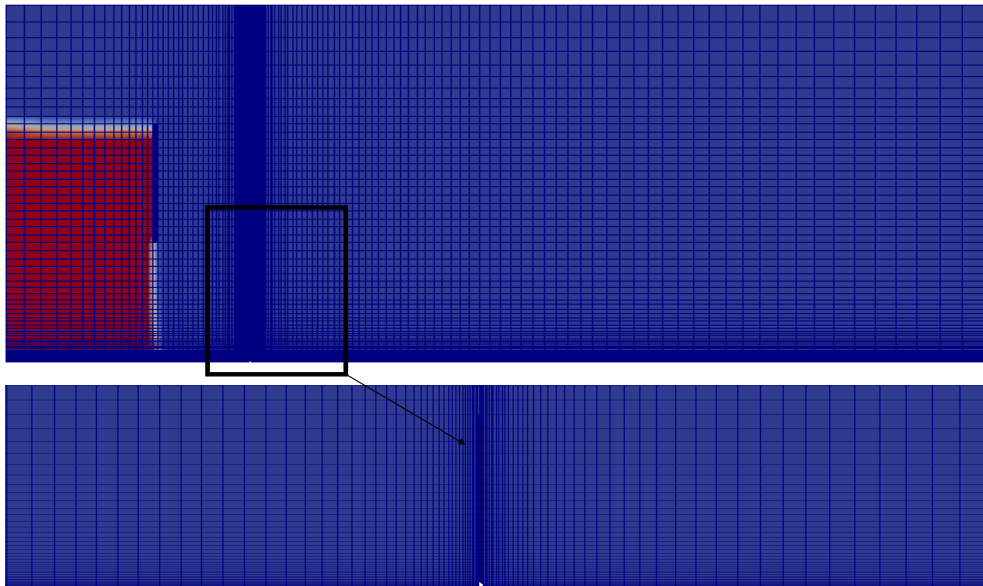


Figure 4.11: Mesh of the fluid domain - front view

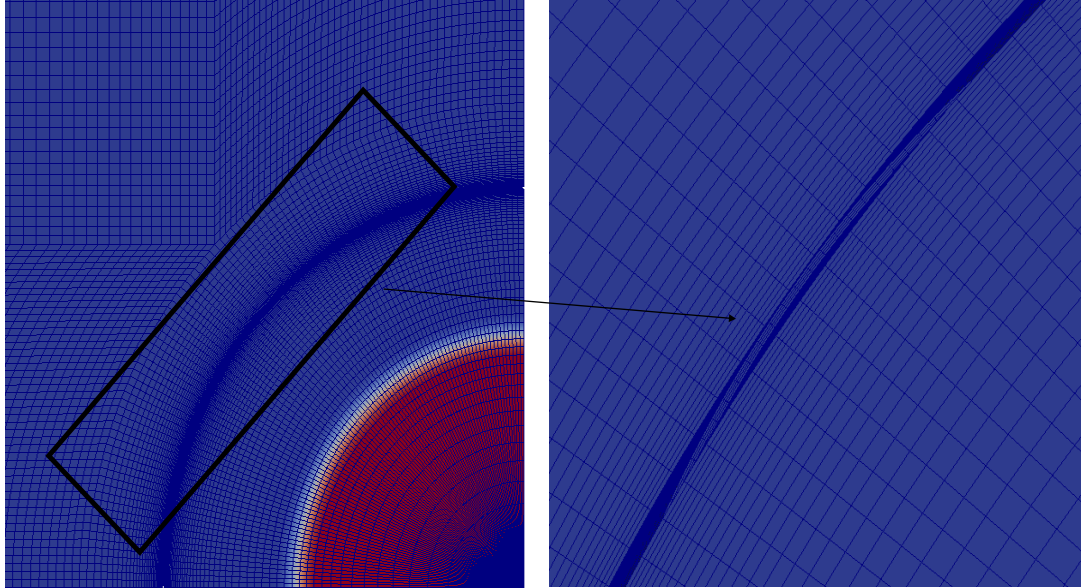


Figure 4.12: Mesh of the fluid domain - bottom view

#### 4.2.7.2 Discretisation of transport equations

The discretisation schemes of the different terms of the transport equation of the multiphase flow are summarised in Table 4.16. The default schemes proposed in OpenFOAM were adopted due to their suitability to simulate the physics, i.e. the diffusion is an isotropic phenomenon, therefore a central (linear) scheme is used for the discretisation of the diffusion term and the convection term in the N-S equation is discretised using a LinearUpwind scheme, which allows the determination of the flux from the direction of the flow.

Table 4.16: Discretisation schemes

Term		Family of discretisation scheme	Discretisation scheme	
			Discretisation scheme of volume integrals	Interpolation scheme
Temporal term		ddt schemes	-	Euler
Pressure term		grad schemes	Gauss	linear
Diffusion term		laplacian schemes	Gauss	linear corrected
Convection terms	N-S equation	div schemes	Gauss	linearUpwind
	phase fraction equation			vanLeer
	Interfacial compression flux			linear
	$k$ transport equation			upwind
	$\omega$ transport equation			upwind
	Reynolds stress term			linear

### 4.2.7.3 Boundary conditions

The boundary conditions used in this problem are depicted in Figure 4.9. They consist of walls, which are the surrounding walls and the base of the computational domain, while the top boundary of the domain is free to the atmosphere. The types of numerical boundary conditions of each computed term are given in Table 4.17. It is assumed that the walls are impermeable hence the use of the zero gradient boundary condition for the volume fraction and a fixed flux pressure set to zero for the pressure term. The velocity is considered to adhere to the walls due to viscous effects, therefore a fixed value set to zero was chosen for the velocity. For the atmosphere boundary, a combination of boundary conditions for the different

terms allows the inflow and outflow according to the internal flow (Greenshields, 2018).

Table 4.17: Boundary conditions

Variables	Wall	Atmosphere
Pressure	“fixedFluxPressure”	type “totalPressure”
Velocity	“fixedValue”	type “pressureInletOutletVelocity”
Volume fraction $\alpha$	“zeroGradient”	type “inletOutlet”
Turbulent kinetic energy $k$	“KLowReWallFunction”	type “inletOutlet”
Specific dissipation rate $\omega$	“omegaWallFunction”	type “inletOutlet”
Kinematic turbulent viscosity $\nu_t$	“nutLowReWallFunction”	type “calculated”

#### 4.2.7.4 Solution procedure

The simulations were run for 2s, which is a sufficient time for the fluid flow to settle. An adjustable time step was used with an upper limit on  $Co$  equal to 1. The PISO algorithm was used for the solution procedure as this is a transient problem. The tolerances used for the different terms are  $10^{-6}$  for the velocity, the turbulence kinetic energy  $k$  and the specific dissipation rate  $\omega$ ,  $10^{-7}$  for the pressure and  $10^{-8}$  for the phase fraction. The input files of CFD simulations are given in Appendix A.

## 4.3 Modelling methodology for the FEA

### 4.3.1 Validation test

An experiment was conducted for the purpose of validating the modelling approach of FSI. The experiment was conducted using a channel test bed already available at the Hydraulic Laboratory. It consisted of using a wall made of standard plain concrete of grade 35 N/mm<sup>2</sup> fixed at 200mm from the gate and measurement of the strain induced by the release of a water flow by means of a strain gauge and data logger. Figure 4.13 shows the experimental set-up and the instrumentation used.



Figure 4.13: Experimental set-up

The water body is of dimensions  $300\text{mm} \times 380\text{mm} \times 500\text{mm}$  with  $300\text{mm}$  is the distance between the back of the channel and the gate,  $380\text{mm}$  is the width of the channel and  $500\text{mm}$  is the height of the water body. The dimensions of the wall as well as the strain gauge position are depicted in Figure 4.14.

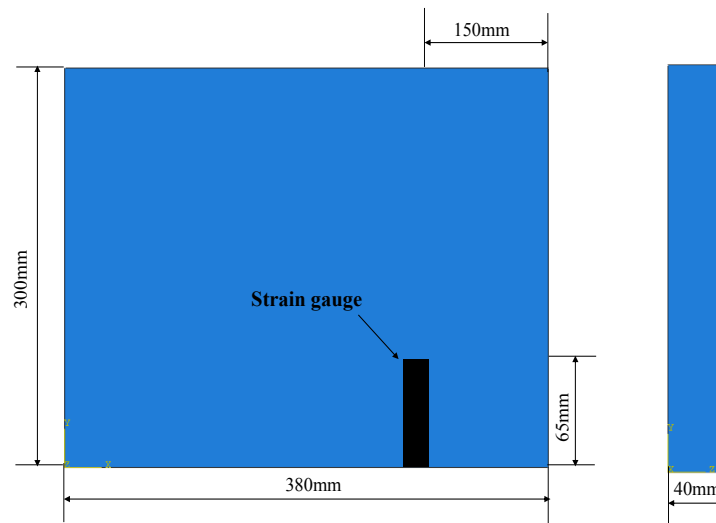


Figure 4.14: Geometry of the wall and strain gauge position

The experiment involved lifting a gate rapidly which allows the water to escape rapidly impacting the wall. Figures 4.15 and 4.16 illustrate the experiment prior to and during the impact. The strain induced was measured at the time of impact.



Figure 4.15: Experiment: prior to the release of the gate



Figure 4.16: Experiment: at the time of impact

### 4.3.2 Software used

As stated in chapter 3, Abaqus software was used for the structural mechanics modelling since it is the leading software used for research and industrial applications. Additionally, most of the research available in the literature on impact problems and the modelling of fibre reinforced concrete were carried out using Abaqus, hence it was adopted for this research.

### 4.3.3 Test matrix

Firstly, the FSI simulations considered examining the performance of the bund wall made of plain concrete. Load scaling was initially conducted on a circular bund wall to obtain the height of fluid that causes the onset of damage in the structure. The tensile damage was the parameter with which the structural integrity of the bund wall was assessed. A fluid height of 6m gave the initial appearance of damage in the circular wall. Subsequently, further FSI simulations considered the simulation of square and rectangular bund walls constructed from plain concrete subjected to the same load. The effect of asymmetric load was also investigated by creating an off-centred column of fluid which mimics the case where the fluid hits an obstacle in the banded area before impacting the wall. This is in order to compare the structural response of the bund wall under centred and off-centred loads. Additionally, the performance of a square bund wall reinforced with steel rebars according to the standard was investigated. The last set of FSI simulations investigated the performance of a square wall made of UHP-FRC and incorporating COAST. In total, this covered one simulation with the use of a wall made entirely from UHP-FRC to allow a direct comparison against a plain concrete wall and a simulation with the use of starter bars, which is a more realistic construction of the wall. Table 4.18 presents the different simulations conducted, the description of each test, the dimensions and position of the tank and the material of construction for the wall.

Table 4.18: Test matrix for FSI simulations

<b>Test name</b>	<b>Description</b>	<b><math>H</math> (m)</b>	<b><math>R</math> (m)</b>	<b>Position of the centre of the tank (m,m)</b>	<b>Material of construc- tion</b>
Circular - centred	circular bund wall with centred load	6	0.3	(0,0)	plain concrete

Circular - off-centred	circular bund wall with off-centred load	6	0.3	(0.05,0)	plain concrete
Square - centred	square bund wall with centred load	6	0.3	(0,0)	plain concrete
Square - off-centred	square bund wall with off-centred load	6	0.3	(0.05,0)	plain concrete
Rectangular - centred	rectangular bund wall with centred load	6	0.3	(0,0)	plain concrete
Rectangular - off-centred- $x$	rectangular bund wall with off-centred load along $x$ axis	6	0.3	(0.05,0)	plain concrete
Rectangular - off-centred- $y$	rectangular bund wall with off-centred load along $y$ axis	6	0.3	(0,0.05)	plain concrete

Square - RC	square bund wall with centred load	6	0.3	(0,0)	Reinforced concrete
Square - UHP-FRC	square bund wall with centred load	6	0.3	(0,0)	plain UHP-FRC incorporating COAST
Square - UHP-FRC - rebars	square bund wall with centred load	6	0.3	(0,0)	UHP-FRC with footing rebars incorporating COAST

#### 4.3.4 Development of 3D-FE model

##### 4.3.4.1 Geometric modelling, boundary conditions and mesh

The structure was fixed at the base and meshed using C3D8R element due the performance of these elements in case of impact problems as explained in chapter 3. An aspect ratio of 1 was used throughout the finite element models except in the case of incorporating COAST, the aspect ratio was violated in the corners but only for few elements. Figures 4.17 and 4.18 show the geometry and the meshed wall, respectively.

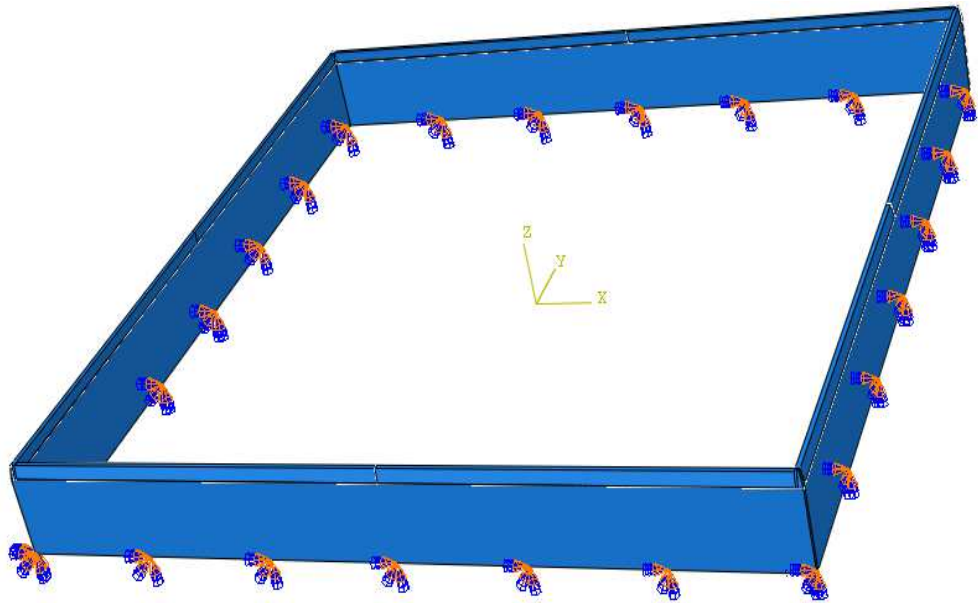


Figure 4.17: Geometry and boundary conditions of a square wall incorporating COAST

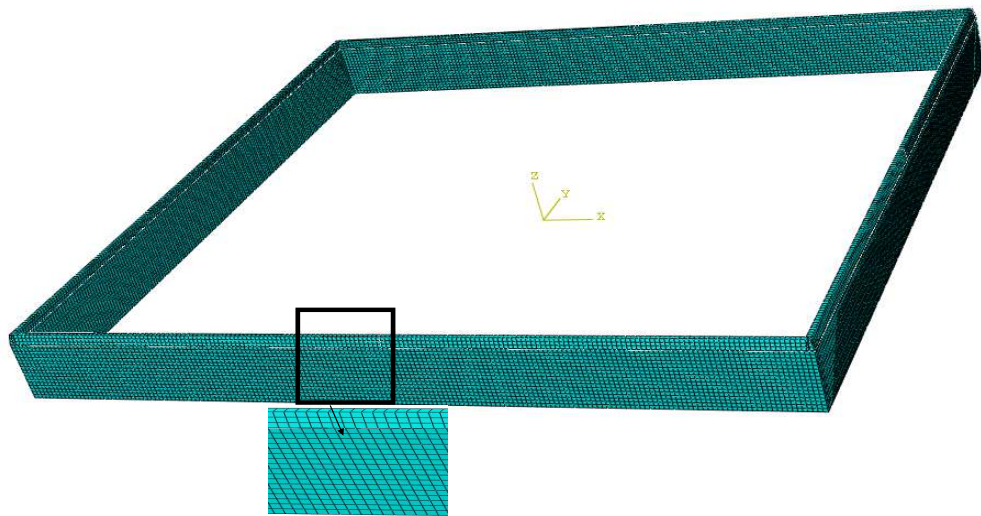


Figure 4.18: Mesh of a square wall incorporating COAST

#### 4.3.4.2 Geometric modelling of reinforced concrete wall

The wall was reinforced according to the standard BS 8007:1987. Although this standard was withdrawn and superseded by BS EN 1992-3:2006, the previous standard was used because the current bund walls in the UK are old and were designed according to the previous standard. The wall was reinforced by vertical, horizontal

and starter bars as depicted in Figure 4.19. The material of the rebars is steel of grade 460 N/mm<sup>2</sup> with a size 20M and the size of the aggregates is 20mm down. The overlap between the starter and vertical rebars is equal to 50 times the diameter of the rebars giving a length of 1m. The cover is equal to 40mm and the bar spacing is 210mm. All these dimensions are given in Figure 4.20.

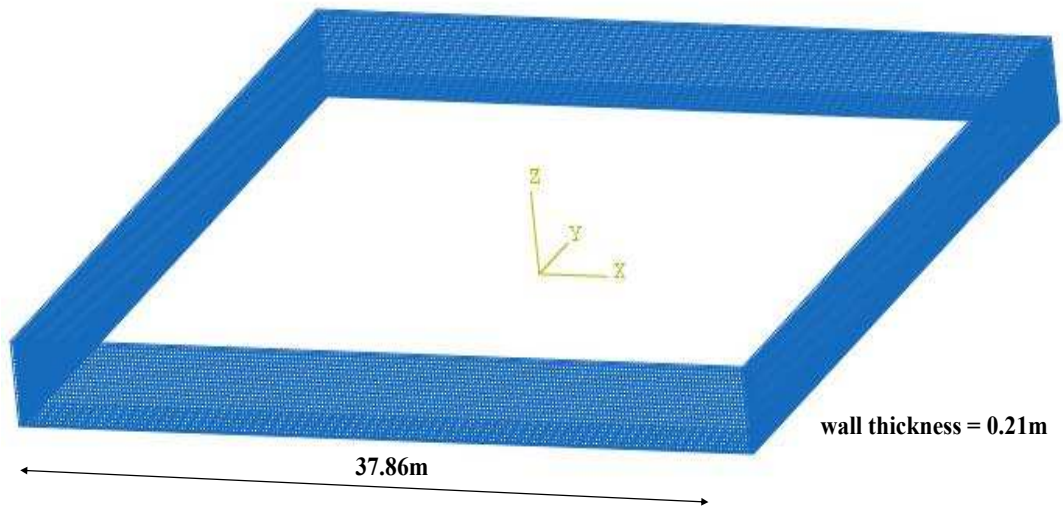


Figure 4.19: Geometric modelling of reinforced concrete wall

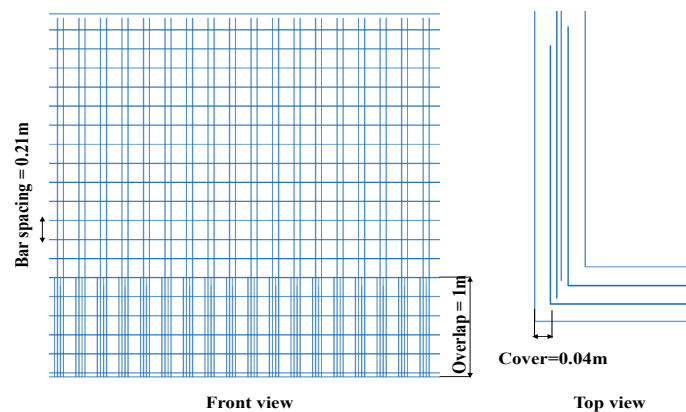


Figure 4.20: Reinforcements arrangement

#### 4.3.4.3 Material constitutive models

The material models for steel, plain concrete and UHP-FRC are given in Tables 4.19, 4.20 and 4.21 taking into consideration the strain rate effect. UHP-FRC is selected from Othman (2016), where the dynamic properties were calibrated under

a low velocity impact, which is similar to the type of impact in this problem. A maximum strain rate of  $10 \text{ s}^{-1}$  was considered. The material used is UHP-FRC Ductal<sup>®</sup> specified by Lafarge North America containing 2% of short straight steel fibres.

Table 4.19: Material properties for the steel (Othman, 2016)

Density	7,800 Kg/m <sup>3</sup>
<b>Steel elasticity</b>	
Elastic modulus (GPa)	201
Poisson's ratio	0.3
<b>Plastic behaviour of the steel</b>	
Yield stress (MPa)	Plastic strain
638.89	0
745.37	0.023367
810.19	0.040895
865.74	0.060895
893.52	0.078491
912.04	0.108383
935.19	0.125887

Table 4.20: Material properties for the CDP model for plain concrete (Simulia, 2016)

Density	2,643 Kg/m <sup>3</sup>		
<b>Concrete elasticity</b>			
Elastic modulus (GPa)	31		
Poisson's ratio	0.15		
<b>The parameters of CDP model</b>			
Dilation angle $\psi$	36.31°		
eccentricity $e$	0.1		
$\frac{f_{b0}}{f_{b0}}$	1.16		
$K$	0.667		
viscosity	0		
<b>Compressive behaviour of the concrete</b>			
Yield stress (MPa)	Inelastic strain		
13	0		
24	0.001		
<b>Tensile behaviour of the concrete</b>			
Yield stress (Pa)	Displacement (m)	Tensile damage $d_t$	Displacement (m)
2,900,000	0	0	0
1,943,930	$6.6185e^{-05}$	0.381217	$6.6185e^{-05}$
1,303,050	0.00012286	0.617107	0.00012286
873,463	0.000173427	0.763072	0.000173427
585,500	0.00022019	0.853393	0.00022019
392,472	0.000264718	0.909282	0.000264718
263,082	0.000308088	0.943865	0.000308088
176,349	0.00035105	0.965265	0.00035105
118,210	0.000394138	0.978506	0.000394138
79,238.8	0.000437744	0.9867	0.000437744
53,115.4	0.000482165	0.99177	0.000482165

Table 4.21: Material properties for UHP-FRC (Othman, 2016)

Density	2,650 Kg/m <sup>3</sup>
<b>Concrete elasticity</b>	
Elastic modulus (GPa)	48.8
Poisson's ratio	0.2
<b>The parameters of CDP model</b>	
Dilation angle $\psi$	10°
eccentricity $e$	0.1
$\frac{f_{b0}}{f_{b0}}$	1.16
$K$	0.67
viscosity	0
<b>Compressive behaviour of the concrete</b>	
Yield stress (MPa)	Inelastic strain
125.477	0
139.43	0.000481
150.1173	0.000866
161.619	0.001299
172.297	0.001684
179.698	0.00202
166.752	0.003907
154.85	0.00538
139.98	0.007138
126.203	0.008896
98.61	0.012127
<b>Tensile behaviour of the concrete</b>	
Yield stress (MPa)	Fracture energy (N/m)
11.434	21,100
<b>Concrete tension damage</b>	
Tensile damage $d_t$	Displacement (m)

0	0
0.1036	0.00023
0.21622	0.0004272
0.32432	0.0006572
0.42342	0.0008873
0.50901	0.0010845
0.59009	0.0012817
0.67117	0.0014131
0.71171	0.0020376
0.73874	0.0024977
0.78378	0.0031878
0.83333	0.0038779
0.86486	0.0045023
0.91892	0.005061
0.95495	0.0057183
0.99	0.0064413

## 4.4 Modelling methodology for the Co-simulation

### 4.4.1 Software used

MpCCI 4.5.2 software was used for the purpose of coupling OpenFOAM to Abaqus since it is a commonly referenced software. To couple InterFOAM to the explicit solver of Abaqus, a fixed time step in OpenFOAM was used because the use of an adjustable time step caused a problem to couple the two solvers. Abaqus 2017, OpenFOAM 17.06 and MpCCI 4.5.2 were installed on a computer with a Linux operating system. The computer used for the simulation has a core i7 processor.

## 4.4.2 Coupling process

The first step in the coupling process is called the Model step. It consists of choosing the coupled software and their versions, here Abaqus 2017 and Openfoam 17.06 as well as the input file for Abaqus and the case directory for OpenFOAM as depicted in Figure 4.21. The second step is called the coupling step which requires specifying the global variable, the coupled regions and the quantities transferred. The global quantity to be coupled is the time step which is sent from OpenFOAM to Abaqus. The value of the time step is 0.001s, which is believed realistic to represent the impact time. The coupling region is where the quantities are transferred. In this problem, the coupling region is the bund wall. The quantities to be transferred are NPosition and RelWallForce which represent the deformations computed by Abaqus and the pressures computed by OpenFOAM. The different stages in the coupling step are shown in Figures 4.22, 4.23, 4.24 and 4.25. The last step in the coupling process is the go step, as depicted in Figures 4.26 and 4.27. It consists of defining the coupling scheme and the initial quantity transfer along with other control parameters. The coupling algorithm is explicit transient with initial quantities transfer received by Abaqus and exchanged from OpenFOAM. The explicit transient is the only possible coupling scheme when using the explicit solver of Abaqus and is a serial coupling scheme. The sub-cycling was selected in Abaqus to allow it to sub-cycle within each time step. Furthermore, a dynamic mesh was used close to the wall in OpenFOAM to allow the coupling surface to move. Since OpenFOAM does not provide a morphing tool, the MpCCI morpher was used instead. The meshes at the interface fail to match, since the mesh from the fluid side is always more demanding in the sense that the  $y^+$  criteria must be satisfied, imposing a high aspect ratio near the base. Contrary to this, an aspect ratio of 1 was satisfied for the finite element model, which resulted in a non-matching grid. However, the coupling is still possible via the use the FSI mapper, which is a tool that can map values from one mesh to another. The MpCCI workflow is depicted in Figure 4.28, which includes the terminals of Abaqus, OpenFOAM and the MpCCI monitor showing only the coupling region.

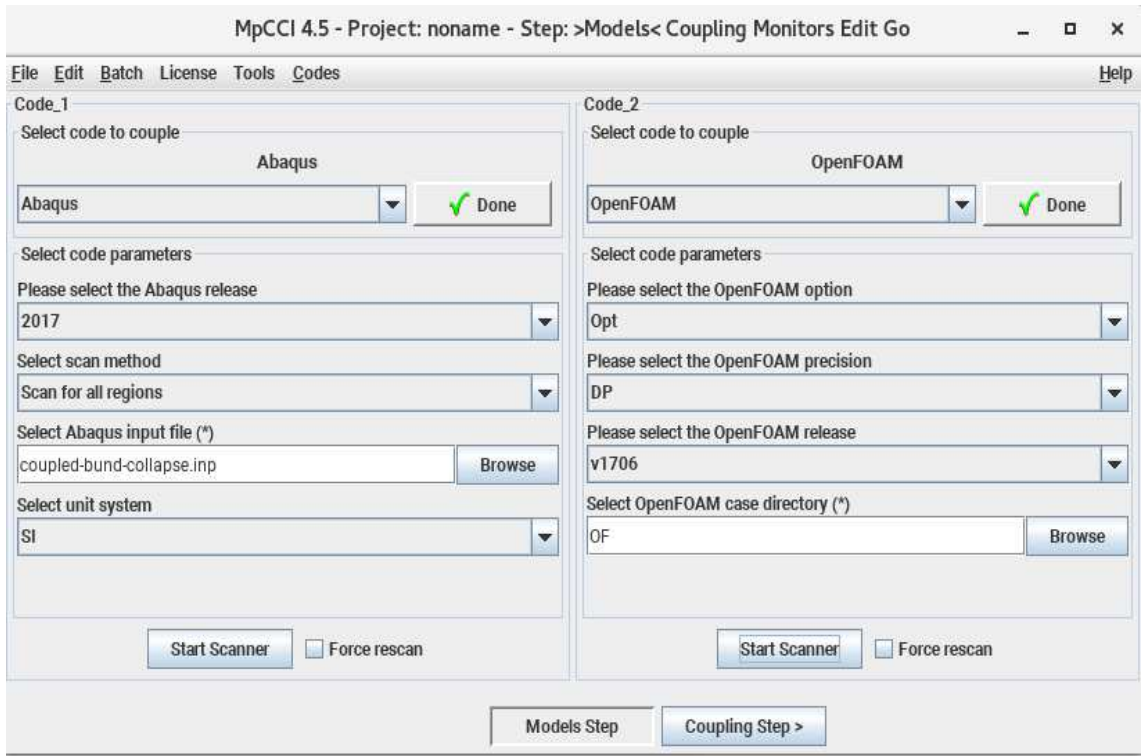


Figure 4.21: Model step

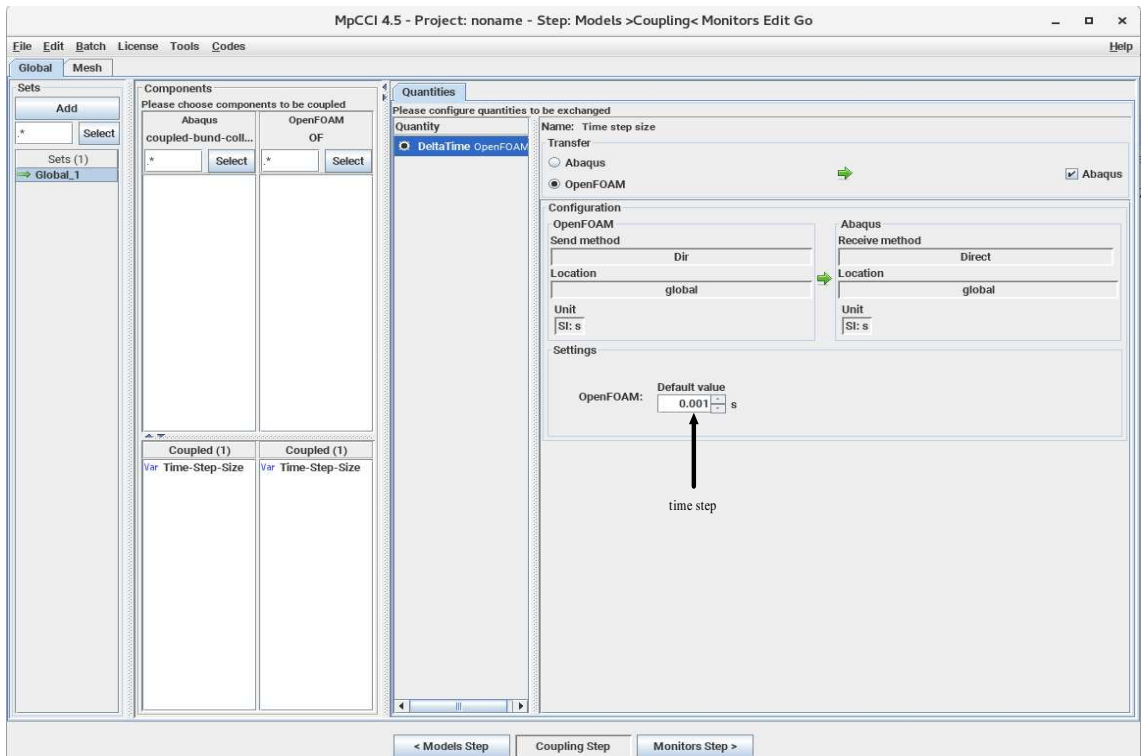


Figure 4.22: Coupling step: Global quantity

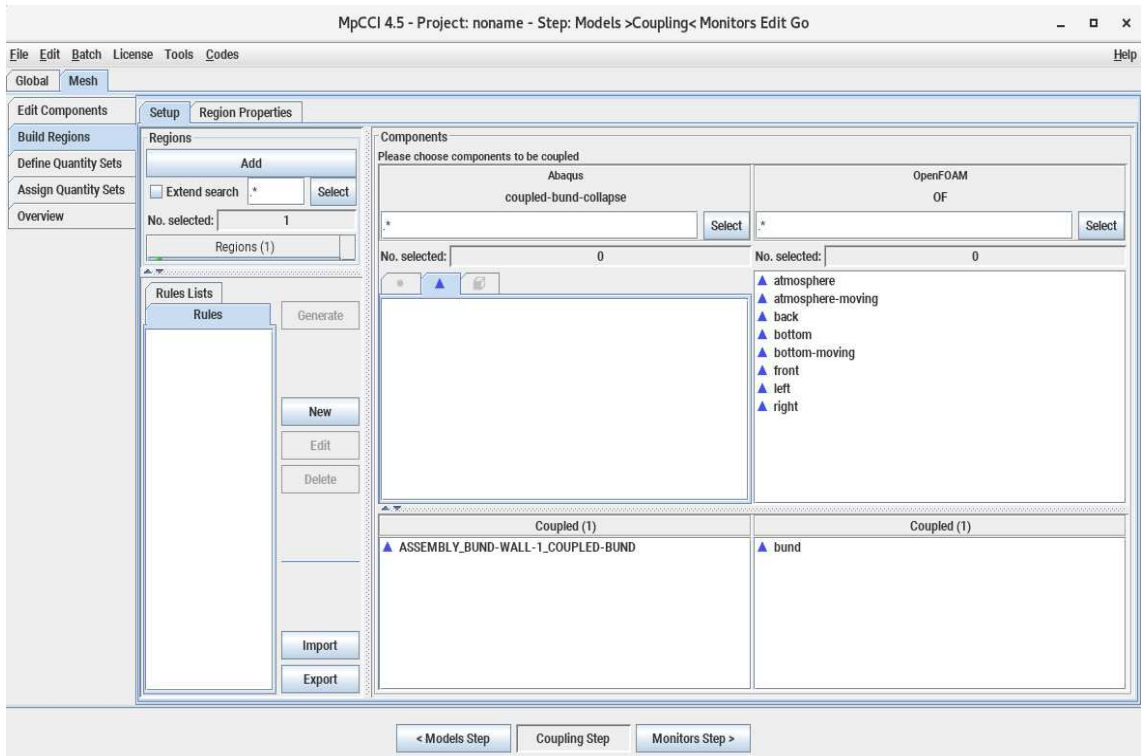


Figure 4.23: Coupling step: Build regions

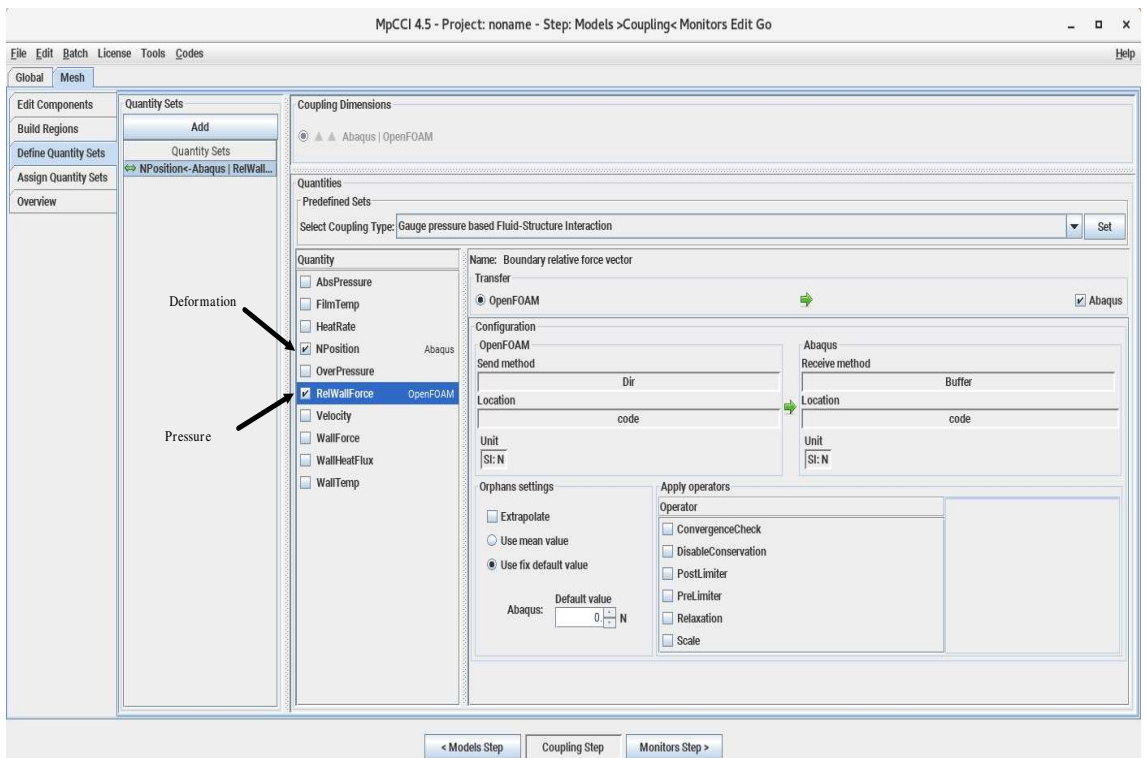


Figure 4.24: Coupling step: Define quantity sets

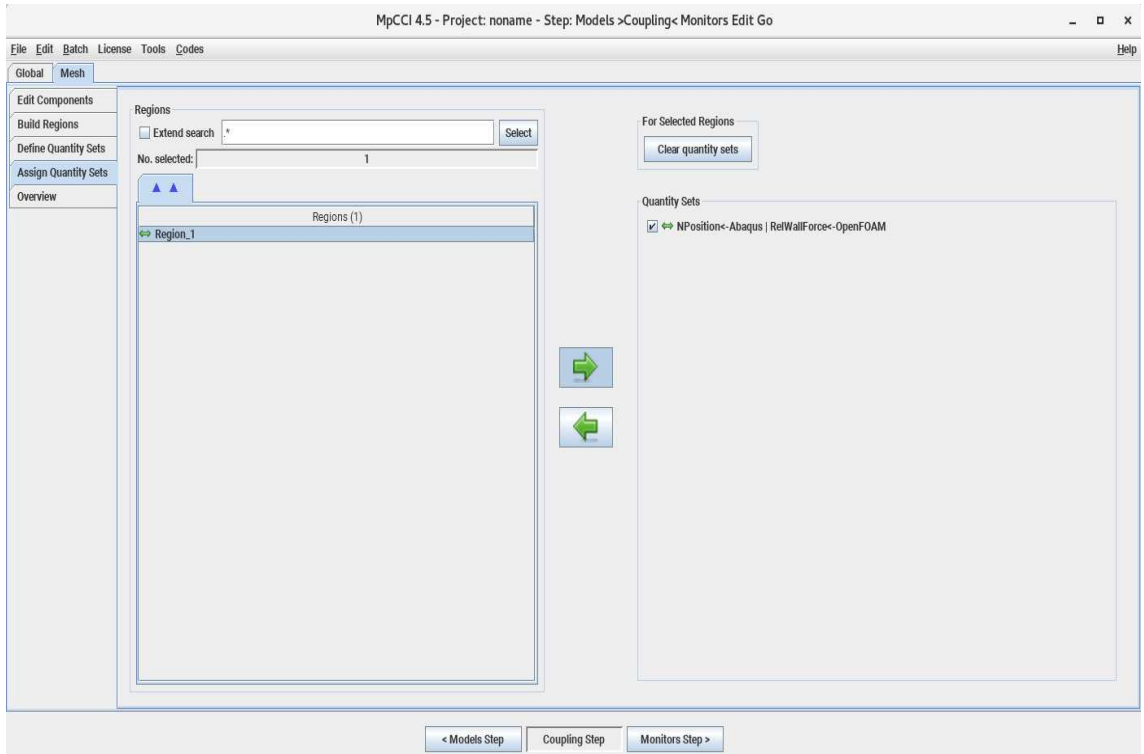


Figure 4.25: Coupling step: Assign quantity sets

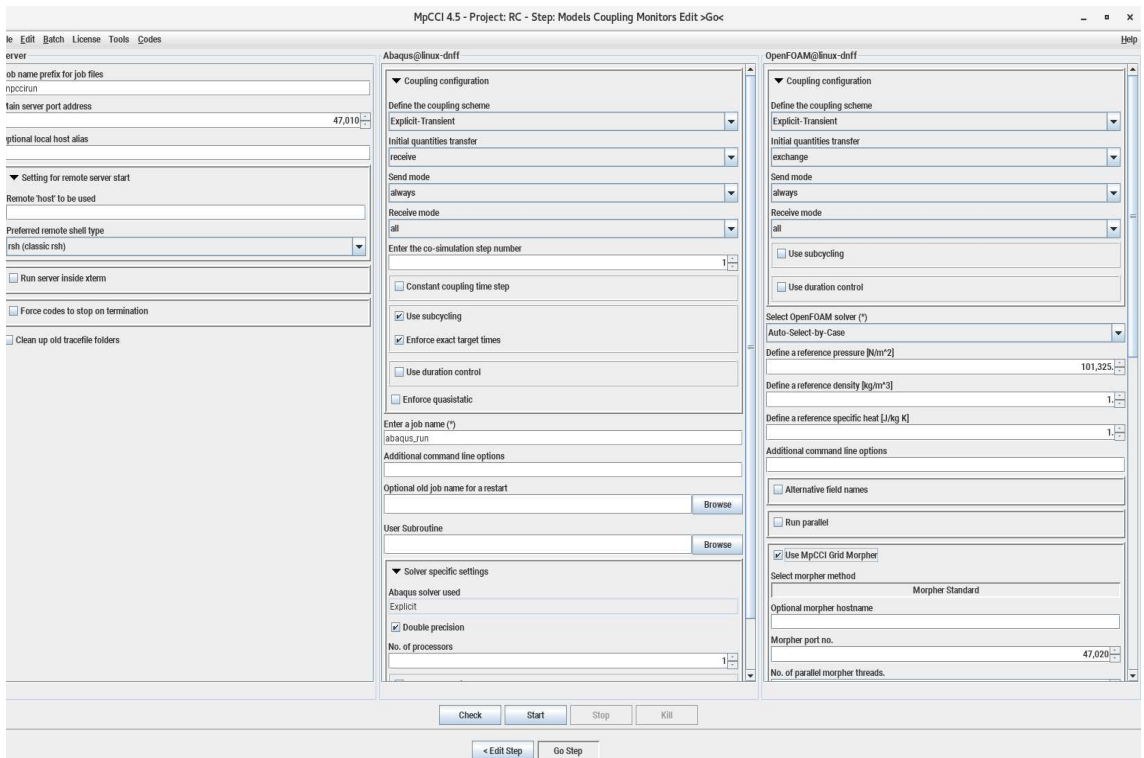


Figure 4.26: Go step

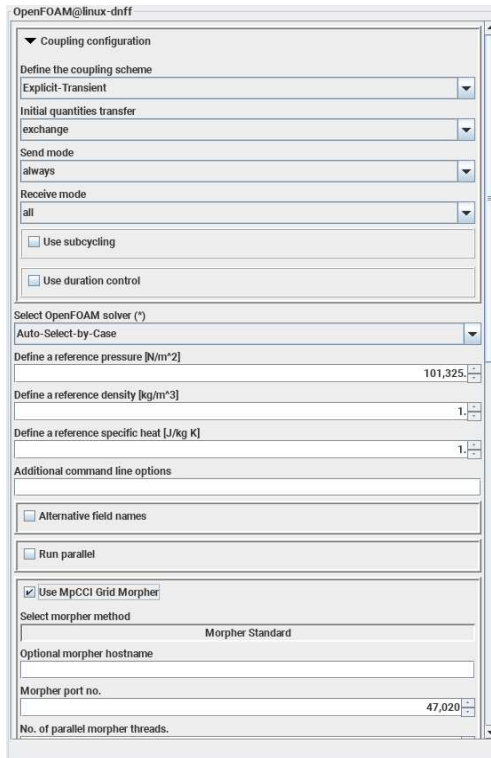


Figure 4.27: MpCCI grid morpher

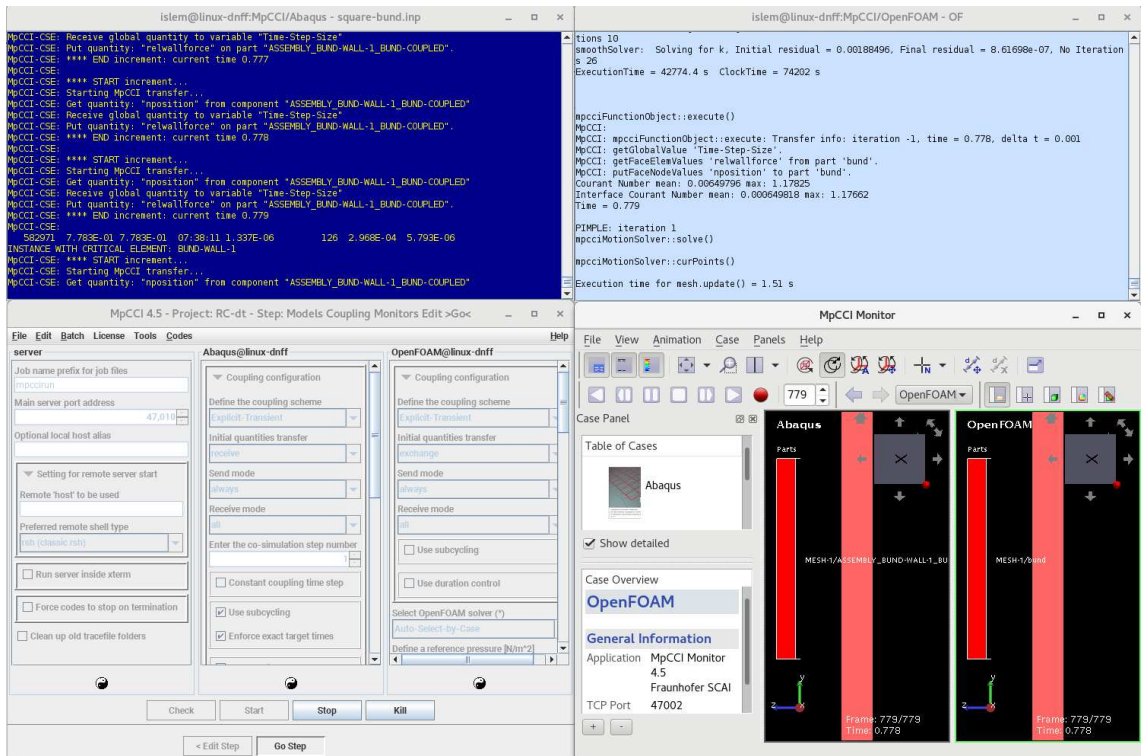


Figure 4.28: Go step: MpCCI workflow

## 4.5 Summary

This chapter presented the methodology for the use of CFD, FEA and the FSI simulations. OpenFoam blueCFD-Core 2016, OpenFAOM 17.06, Abaqus 2017 and MpCCI 4.5.2 were the software packages utilised for the modelling. It equally presented the various test configurations for CFD and FSI simulation. The extensive simulations permitted the evaluation of the performance of InterFOAM to simulate the catastrophic collapse of a storage tank and permitted the examination of the performance of the bund wall under such loads. The modelling assumptions were chosen accurately to obtain a realistic solution as far as possible. The next chapter will present the CFD results and compare them to the available experimental data in addition to further simulations to examine the performance of incorporating mitigation techniques.

# Chapter 5

## CFD results

### 5.1 Introduction

This chapter presents the CFD simulation results for the purpose of evaluating the performance of the InterFOAM solver in modelling the problem of a catastrophic collapse of a storage tank. The available experimental data of dynamic pressures and overtopping fractions were used for the validation process. The dynamic pressures at the bund wall were measured by the means of dynamic pressure transducers at specific locations, which were the centre line (CL), quarter line (QL) and end line as indicated in Figure 5.1. The overtopping fraction represents the ratio of the quantity of fluid that escapes the bunded area to the quantity of fluid that was initially in the tank. The numerical dynamic pressures were determined at the time of impact using the probe filter in the Paraview software and the overtopping fractions were calculated using the integrate variable filter in Paraview which permits the calculation of the volume occupied by olive oil outside the bunded area.

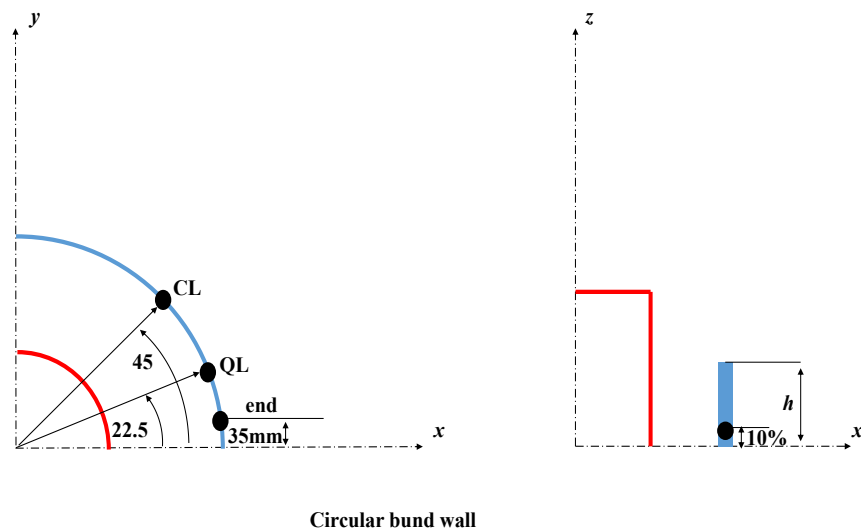


Figure 5.1: Position of the transducers along the bund wall

Extensive CFD modelling was carried out with the use of standard configurations of bund wall, mitigated configurations and the partial failure of the storage tank. In excess of 64 simulations were carried out. This chapter is divided as follows: Firstly, the experimental results are presented, then the CFD simulations of the standard configurations are given and compared against the experimental results. Subsequently, the results of the optimisation study and the effect of incorporating COAST will be discussed. Then, results of the simulation of the partial failure of a storage tank are presented. Finally, the similitude of the fluid problem is briefly introduced.

## **5.2 Experimental results for the standard cases**

### **5.2.1 Presentation and analysis of the results**

Different effects were studied throughout the experimental program namely, the effect of the separation distance between the tank and the bund wall, the effect of the capacity of the bund wall, the effect of the height of the fluid in the tank, the effect of the shape of the bund wall, the effect of high collar bund wall and the effect of the temperature of the stored material.

#### **5.2.1.1 The effect of the separation distance and capacity of the bund wall**

Figure 5.2 presents the effect of the separation distance and the capacity of the wall on both of the dynamic pressures measured at the centre line at 10% of the height of the wall along with the overtopping fractions. For each capacity, the radius and the height of the bund wall were varied as indicated in Tables 4.1, 4.2, 4.3 and 4.4. Between each set of experiments corresponding to each capacity, the heights of bund walls are chosen to be equal to allow a direct comparison. The experimental results are presented as a function of  $h/H$  along the  $x$  axis. The ratio  $h/H$  ranges between 0.05 to 0.4, a higher ratio corresponding to a smaller separation distance and vice versa.

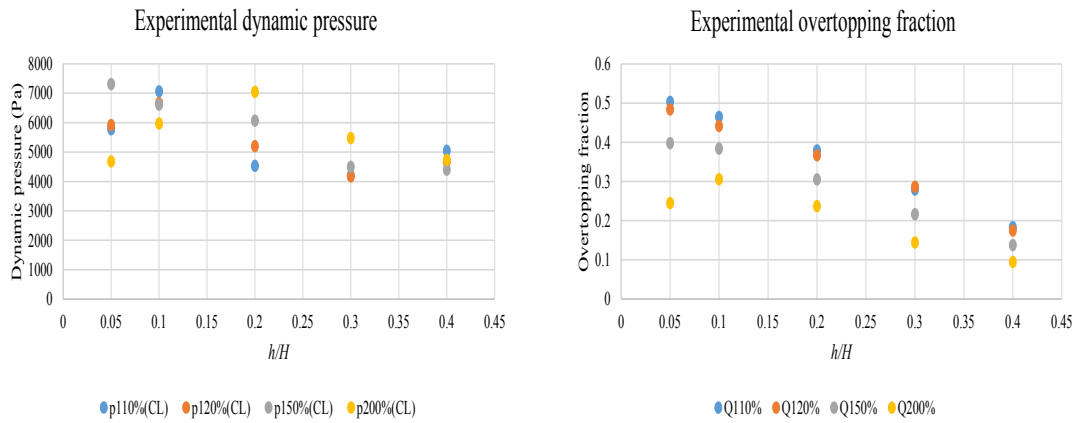


Figure 5.2: Effect of the separation distance and the capacity of the wall

### Effect of the separation distance

For each capacity, it is expected that the dynamic pressures are higher for smaller separation distances, as the velocity of the fluid flow is greater for closer walls and  $p = \frac{1}{2}\rho_f U^2$ . However, from Figure 5.2, the dynamic pressures appear to be variable and not following the expected trend. Additionally, it was noticed that between each experiment, which was repeated 5 times for repeatability, the impact times were slightly different. Furthermore, the dynamic pressures measured at the same level, e.g. at 10% from the base and at different positions covering the centre line, quarter line and end line, are expected to be equal for the circular wall as the fluid flow should impact the wall in the same manner, but variable results were noticed. The dynamic pressures are only presented at the centre line for the experimental results, while they are given for all positions in the next section for the comparison against numerical results. This variability can be attributed to the roughness of the bed of the test rig on which the flow is moving, which is different throughout the table due to wear and tear with the use of the aqua-vac in addition to other variables such as the randomness in the temperature of the oil. On the contrary, the overtopping fractions almost follow the same trend in which they decrease as  $h/H$  increases, i.e. as the wall is higher and the separation distance is lower. Although, the overtopping fractions are expected to be less for higher separation distances, as the fluid flow could settle before impacting the wall, the height of the bund wall appears to be a more influential parameter, i.e. a higher wall constructed closer to

the tank retains more quantity of fluid than a lower wall constructed further from the tank.

### **Effect of the capacity of the bund wall**

A comparison of the dynamic pressures between the different capacities at the same  $h/H$  shows a variability. A bund wall with a higher capacity should be subjected to a lower pressure as the velocity is decreasing under the effect of friction. This can only be observed for  $h/H = 0.1$ . Again, this can be attributed to the roughness of the bed of the test rig and the randomness in the temperature of the oil. Whilst, the overtopping fractions are as expected, i.e. for the same  $h/H$ , a bund wall with a higher capacity can retain more quantities of fluid than a wall with a lower capacity.

#### **5.2.1.2 The effect of high collar bund wall**

Figure 5.3 depicts the effect of the use of high collar circular bund walls on the dynamic pressures and the overtopping fractions using two walls of heights, 600mm and 720mm for various radii of the bund wall. A comparison between high collar circular bund walls and the standard circular walls indicates that the dynamic pressures are more significant for high collar bund wall, they are up to 9,000 Pa, against a maximum of 7,000 Pa for the standard walls. The reason is due to the fact that high collar bund walls are built close to the tank so there is not enough space for the fluid to escape hence applying more pressure. The dynamic pressure decreases as the radius increases for each wall as indicated in Figure 5.3. Regarding the overtopping fractions, the use of high collar bund walls allows a significant reduction, with fractions up to 2.5%, against 50% as the maximum overtopping fraction obtained for the standard walls. However, a wall of 720mm height should give less overtopping fraction than a wall of 600mm height. This was only obtained at a radius of 0.315m, while for the rest of radii, discrepancies in results were obtained. This can be caused by the roughness of the bed of the test rig and the randomness in the temperature of the oil, which are affecting the overtopping fractions unlike the standard walls, where the dynamic pressures were affected.

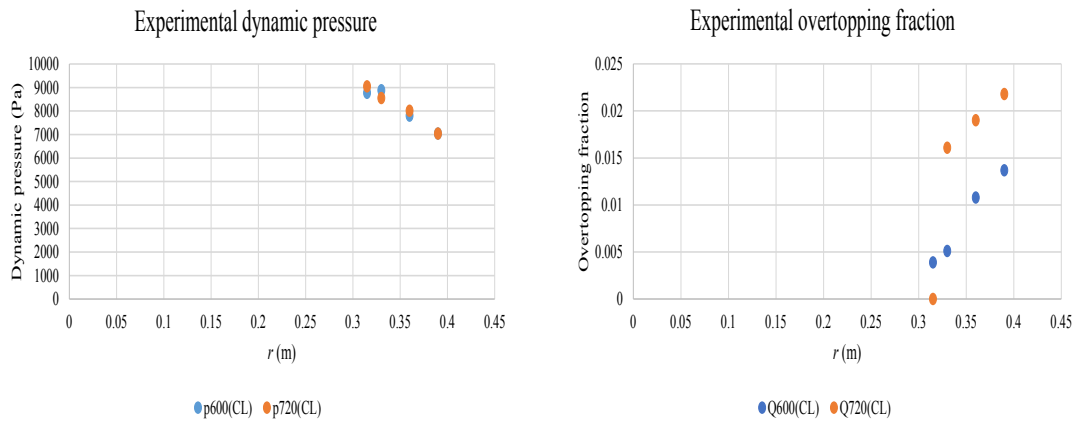


Figure 5.3: Effect of the high collar bund wall

### 5.2.1.3 The effect of the fluid height and the shape of bund wall

Figure 5.4 presents the effect of the fluid height and the shape of the bund wall on the dynamic pressures at the centre line and overtopping fractions. The experiments were conducted under three heights, 0.12m, 0.3m and 0.6m corresponding to squat, middle and tall tanks, respectively, with the use of square, rectangular and triangular walls. The experiments using circular walls were only conducted at  $H = 0.6$ m, therefore they are not included in the comparison. The experimental results are presented as a function of  $H$  along the  $x$  axis.

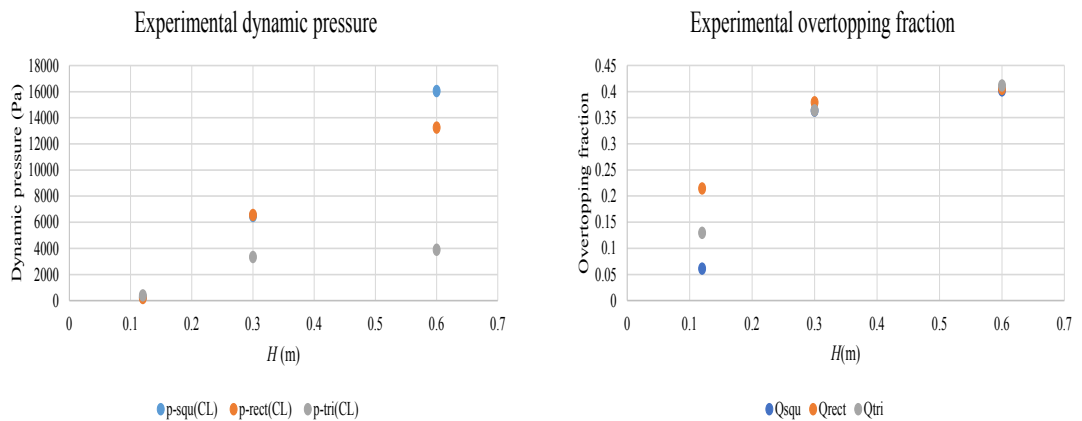


Figure 5.4: Effect of the height of fluid and shape of the wall

### **Effect of the fluid height**

A comparison of the dynamic pressures of each shape of the bund wall shows that higher pressures are obtained for taller tanks since they have more potential energy, hence more kinetic energy after the release, assuming that the energy principles are applied. This results in a higher velocity, hence more significant dynamic pressures. Similarly, this contributes in higher overtopping fractions.

### **Effect of the shape**

A comparison of the dynamic pressures between the different shapes shows that the dynamic pressure is mostly higher for the square and rectangular walls than for the triangular wall. The difference in the pressures between the three shapes is only minor for a squat tank. The dynamic pressure at the centre line for the square and rectangular walls is measured at the corner. Both of these shapes are subjected to a higher pressure due to the corner effects. The fluid is acting at the corner from many directions unlike the triangular wall, where the fluid is hitting the wall along the radial direction as shown in Figure 5.5. The corner effect is minor for the squat tank. Regarding the overtopping fractions, the square wall can retain more fluid than the other two shapes when using a squat tank. Whilst, for the middle and tall tanks, the overtopping fractions are nearly the same.

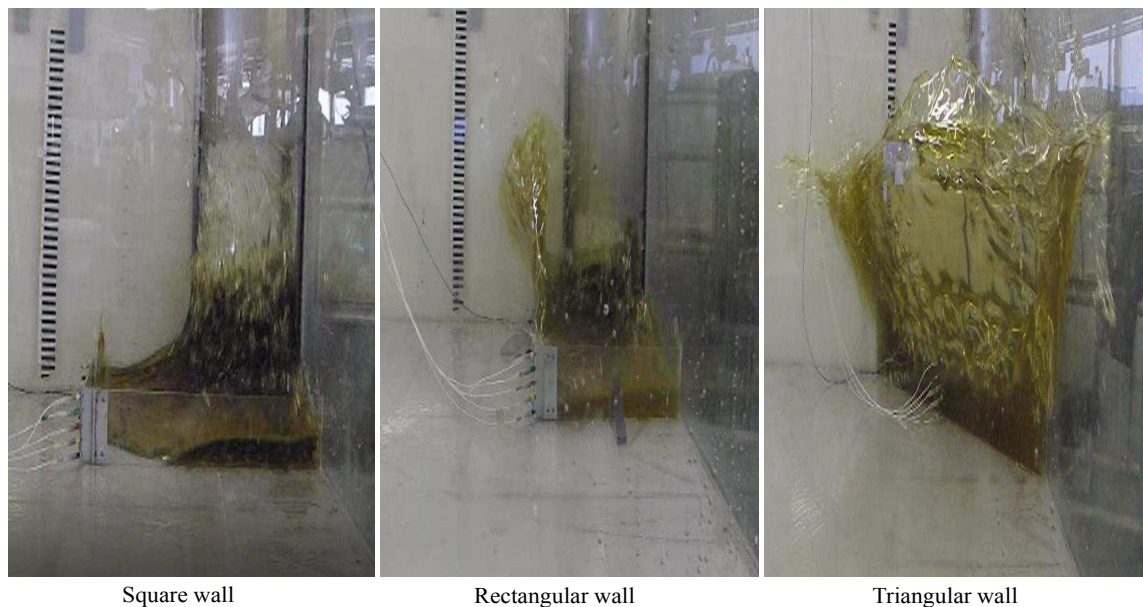


Figure 5.5: Effect of the shape of bund wall

#### 5.2.1.4 The effect of the fluid temperature

Figure 5.6 presents the overtopping fractions for circular and triangular walls as a function of the temperature. More overtopping fractions are obtained for higher temperatures because the fluid becomes less viscous as the temperature increases, hence giving greater overtopping fractions.

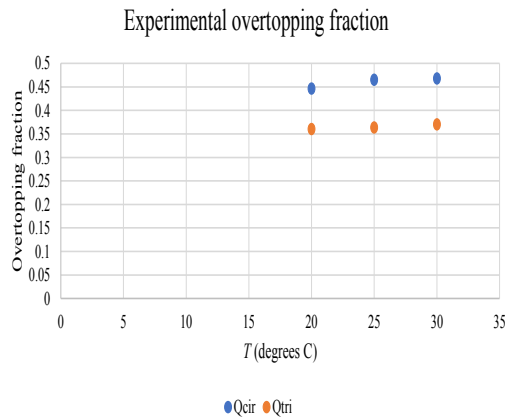


Figure 5.6: Effect of the temperature

### 5.3 CFD results for the standard cases

#### 5.3.1 Presentation and analysis of the results

The numerical results are presented in the same manner as the experimental results, i.e. the effect of the separation distance and the capacity of the bund wall is first presented, then the effect of high collar bund is given followed by the effect of the fluid height and the shape of the bund wall. Finally, the effect of the temperature is presented. The numerical results are given in terms of overtopping fractions and dynamic pressures at the centre line, quarter line and end line and compared to the experimental results.

##### 5.3.1.1 The effect of the separation distance and capacity of bund wall

Figures 5.7 and 5.8 present the flow structure corresponding to the CFD simulation and the experiment, respectively with the use of a circular bund wall. The numerical

simulation is in a close agreement with the experiment in the sense that it shows the same flow pattern, i.e. after the collapse, the flow impacts the wall, then it rises until it breaks after which, it starts falling back down. Some of the fluid returns back to the banded area and the rest escapes it until it stops.

Figures 5.9, 5.10, 5.11 and 5.12 present the numerical results compared against experimental results for circular walls of capacities, 110%, 120%, 150% and 200%. For each capacity, the pressures at the centre line and quarter line are in better agreement with the experimental results compared to the pressures at the end line. This can be due to the fact that pressures at the end line are measured near the wall and the surface tension effects between the wall and the interface have been ignored. The relative error in dynamic pressures at the end line ranges from 3% to 49%, 5% to 61%, 28% to 55%, 32% to 90% for capacities of 110%, 120%, 150% and 200%, respectively.

A comparison between the different  $h/H$  values for each capacity of the wall shows that the error in dynamic pressures mostly decreases as  $h/H$  increases, which corresponds to a decrease in separation distance. The relative error in the pressure at the centre line and the quarter line starts exceeding 10% for a radius of a bund wall equal to 0.822m which raises a question of the validity of InterFOAM for large distances. The high error obtained at great separation distances can be explained by a numerical error that accumulates as the fluid flow advances in the fluid domain. Overall, the simulation was predicting a better trend of the evolution of the pressures at all measured positions, i.e. the pressure is higher at the wall for smaller separation distances as opposed to the experiment. It was stated previously that a variability in the experimental dynamic pressures was obtained.

In terms of overtopping fractions, the simulations were successful in predicting decreasing fractions with increasing  $h/H$ . Furthermore, the error in overtopping fractions is significantly less than the error in dynamic pressures. The relative error is below 27% except for one case where it is 39%. CFD simulations underestimate the dynamic pressures for most of the cases, while they overestimate the overtopping fractions with few exceptions.

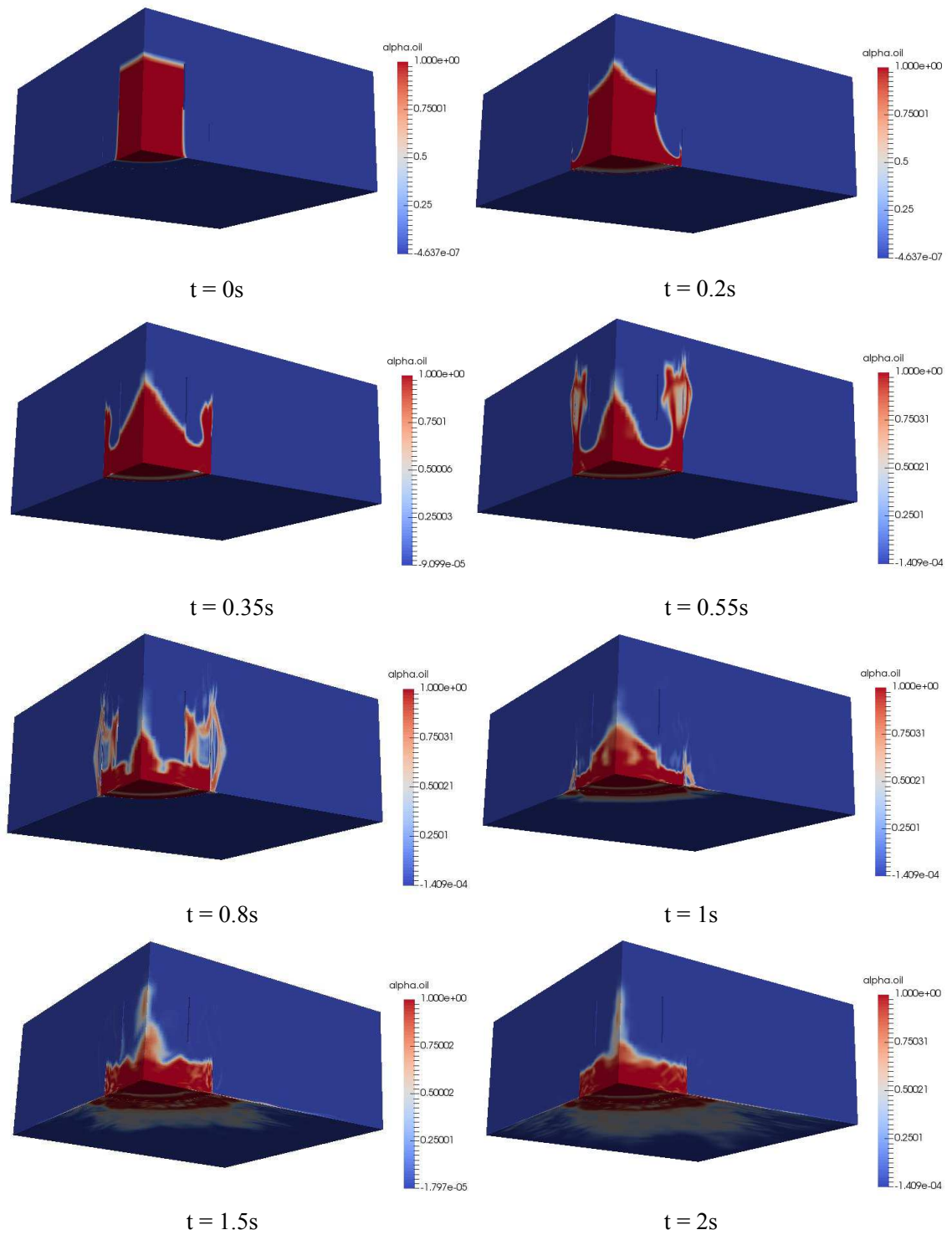


Figure 5.7: Flow structure corresponding to a standard configuration - test  $B_1$  (circular wall)



t = 0s



t = 0.2s



t = 0.35s



t = 0.55s



t = 0.8s



t = 1s



t = 1.5s



t = 2s

Figure 5.8: Experimental flow structure corresponding to a standard configuration - test  $B_1$  (circular wall)

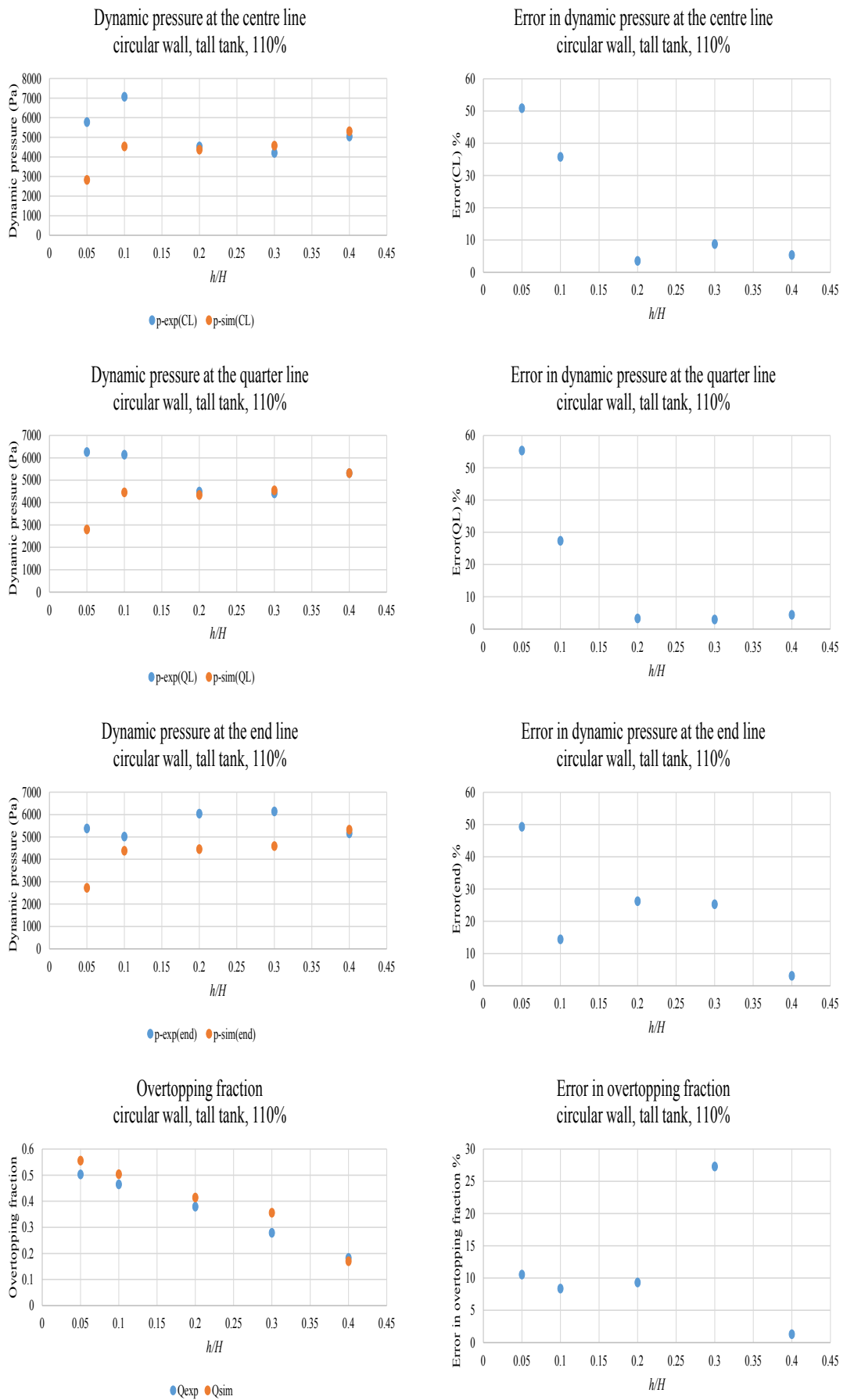


Figure 5.9: Effect of the separation distance (circular wall, tall tank, capacity 110%)

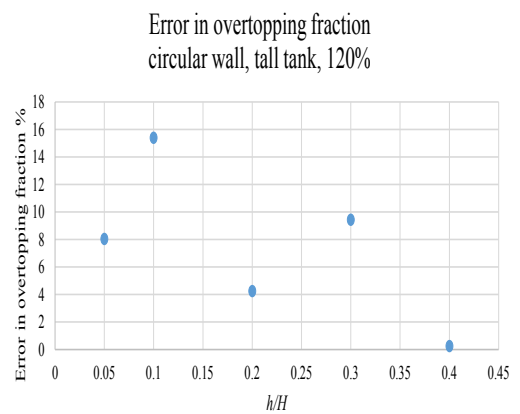
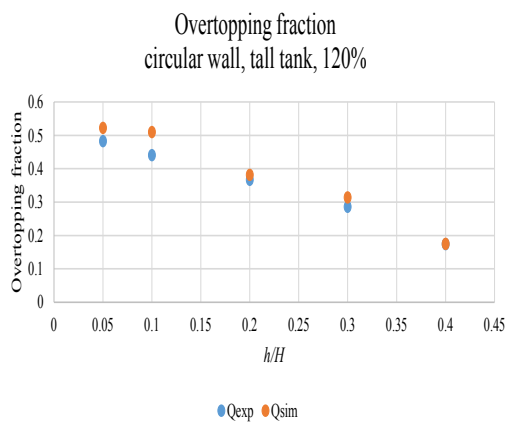
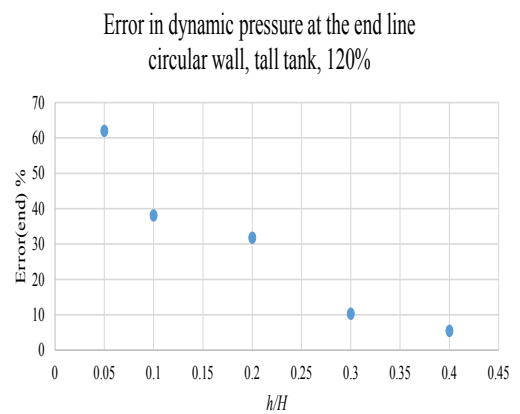
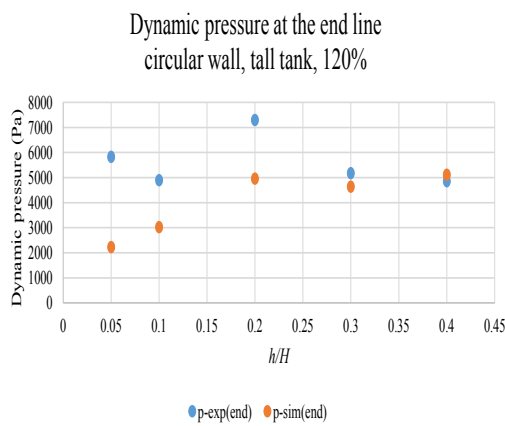
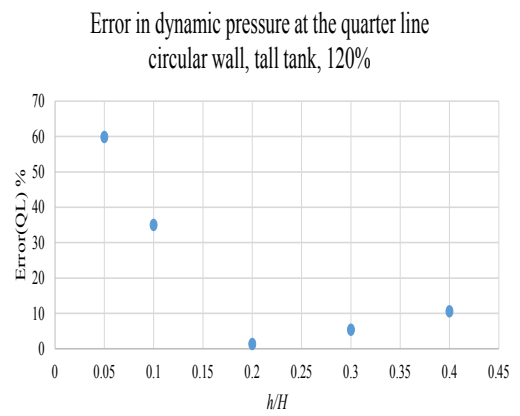
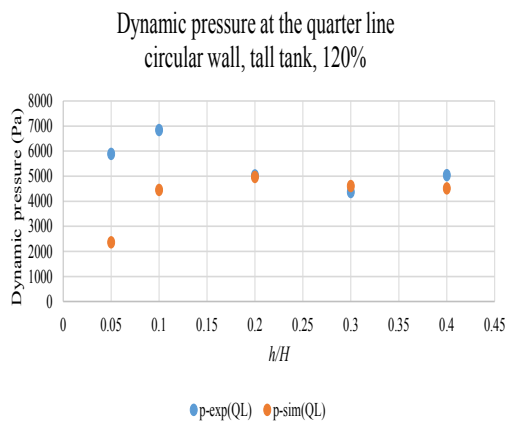
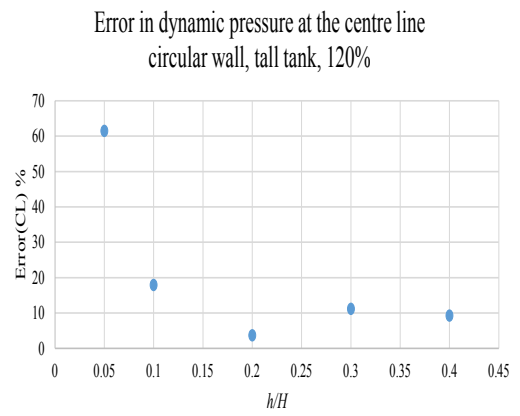
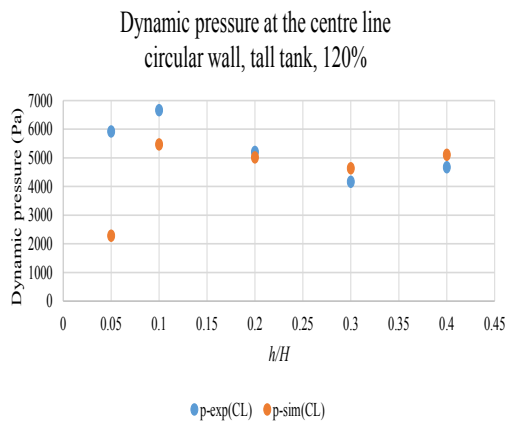


Figure 5.10: Effect of the separation distance (circular wall, tall tank, capacity 120%)

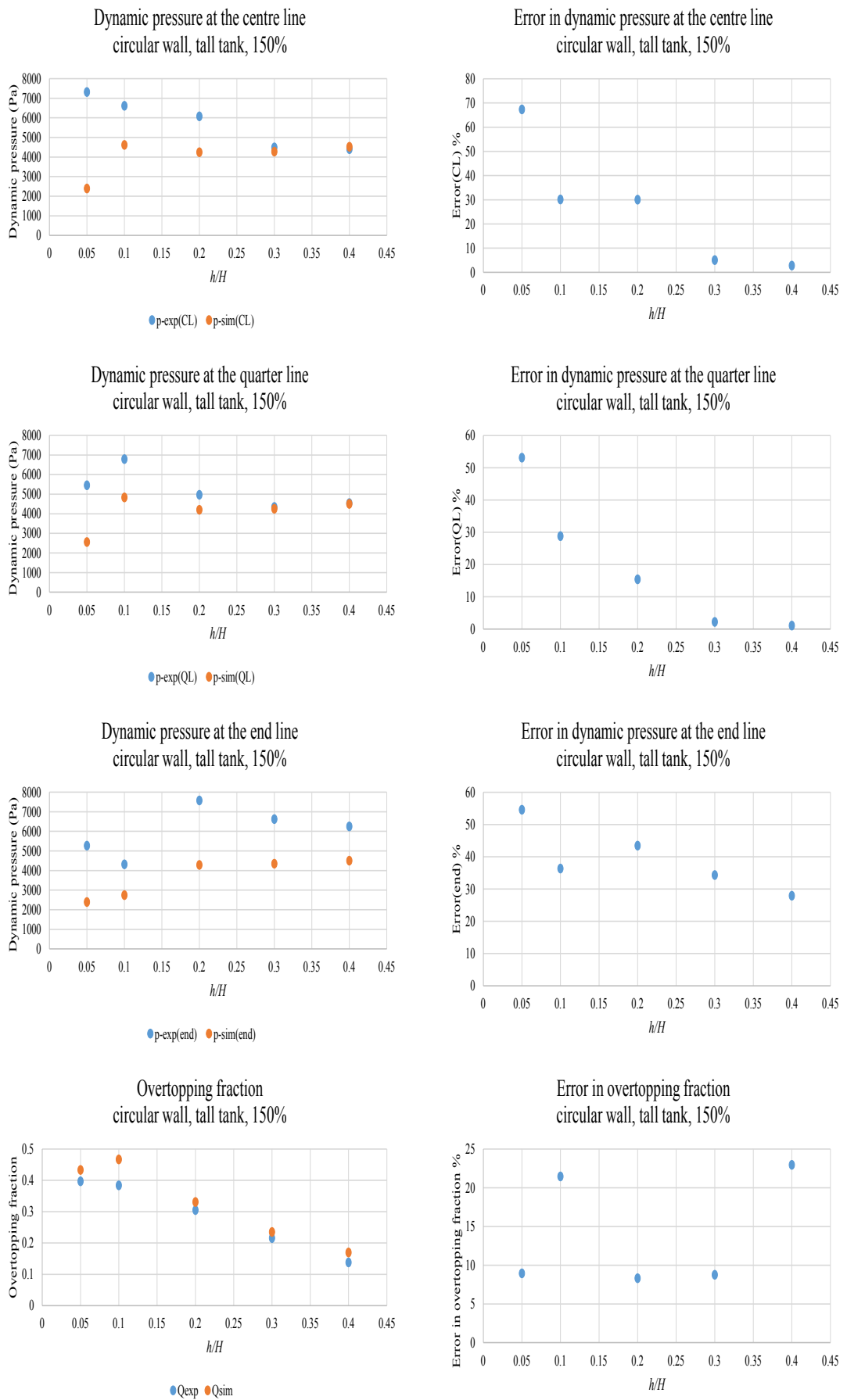


Figure 5.11: Effect of the separation distance (circular wall, tall tank, capacity 150%)

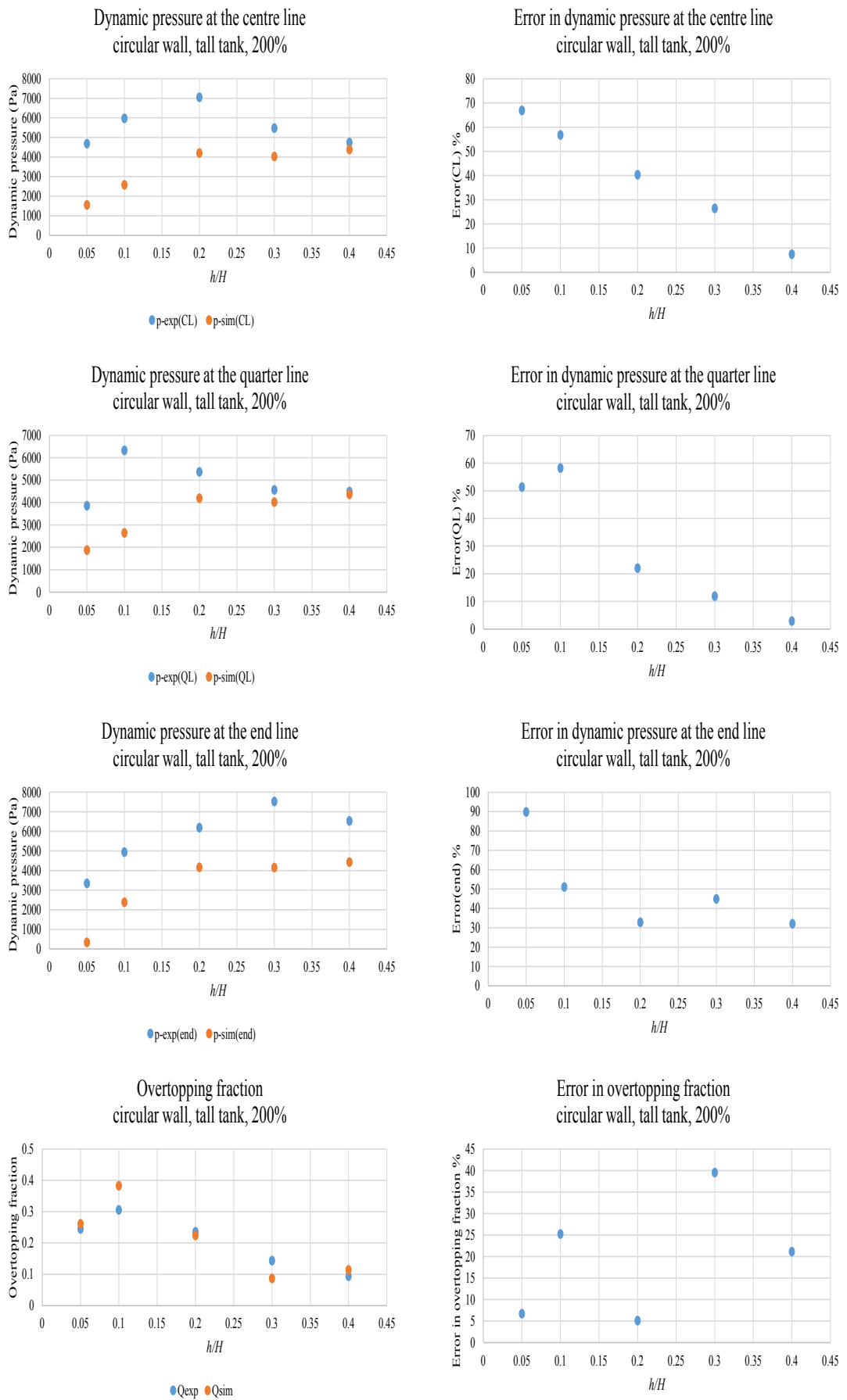


Figure 5.12: Effect of the separation distance (circular wall, tall tank, capacity 200%)

### 5.3.1.2 The effect of high collar bund wall

Figures 5.13 and 5.14 present the numerical results of dynamic pressures and overtopping fractions for bund walls of heights 600mm and 720mm, respectively. Unlike the standard walls, the relative error in dynamic pressures is decreasing with increasing separation distances. The relative error is above 50% for a separation distance of 15mm and a wall of 600mm high. This again raises the question of the validity of InterFoam for small separation distances. This can be attributed to the very narrow space that does not let the fluid flow move. Overall, for separation distances of 30mm, 60mm, 90mm, a reasonable error was obtained ranging from 9% to 31%. The simulations were reasonably successful in the prediction that overtopping fractions increase with increasing separation distances. Although the relative error is as high as 99% for some cases, these values are expected because the overtopping fractions are very small and the relative error is computed as follows

$$\text{Relative error} = \frac{Q_{sim} - Q_{exp}}{Q_{exp}}. \quad (5.1)$$

This implies that even if the difference between the values of overtopping fractions obtained from the experiment and CFD is small, if it is divided by a small value, a high relative error will be obtained.

All the overtopping fractions obtained from the simulations are very small which gives a confidence in the solver for this type of walls. Furthermore, a comparison of the overtopping fractions between the walls of heights 600mm and 720mm at the same radius  $r$  shows that the simulations were better than the experiment in predicting that a higher wall can retain more quantities of fluid. CFD mostly underestimates the values of dynamic pressures and overtopping fractions for high collar bunds, unlike the standard circular configurations, where dynamic pressures are underestimated and overtopping fractions are overestimated.

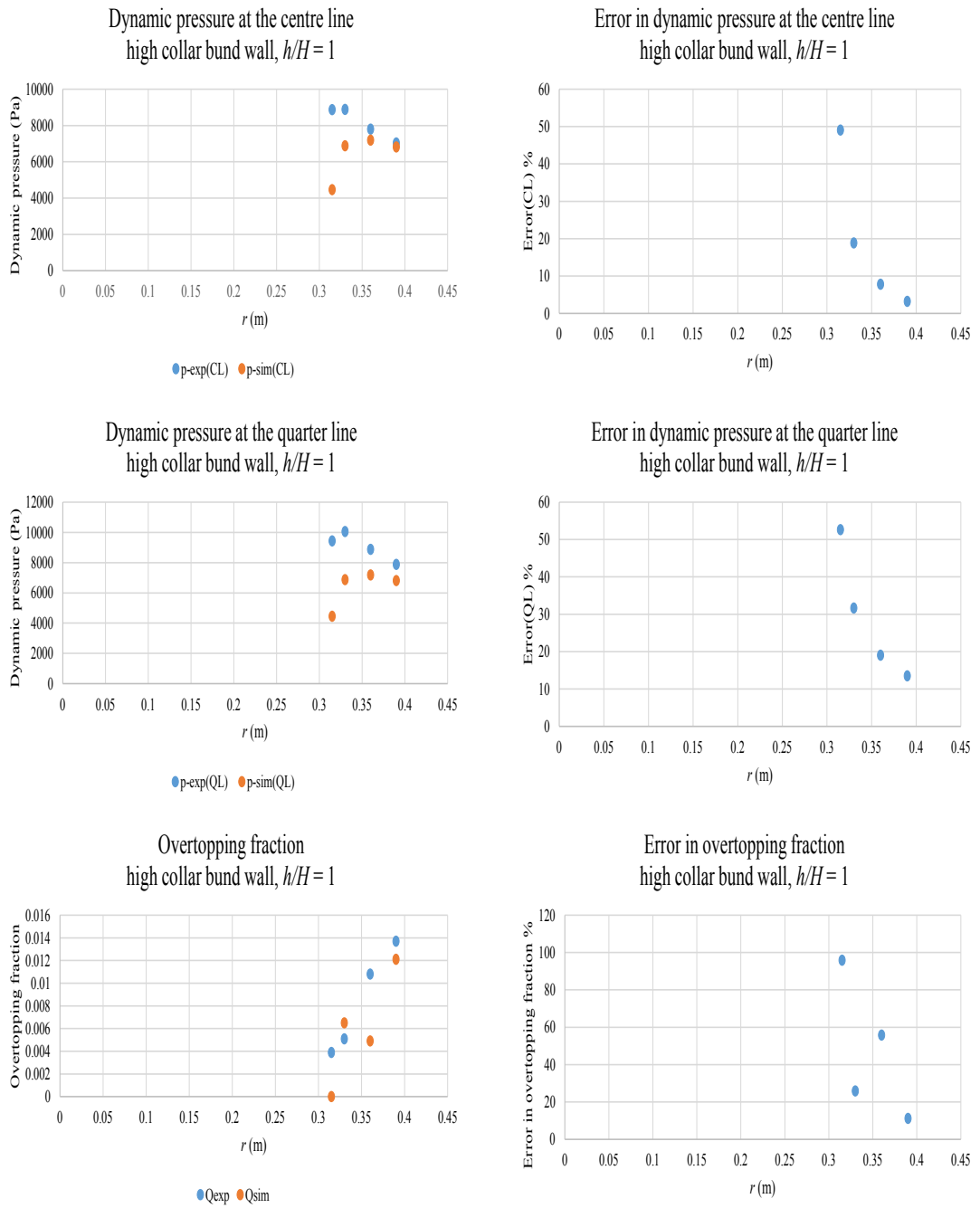


Figure 5.13: High collar bund wall,  $h/H = 1$

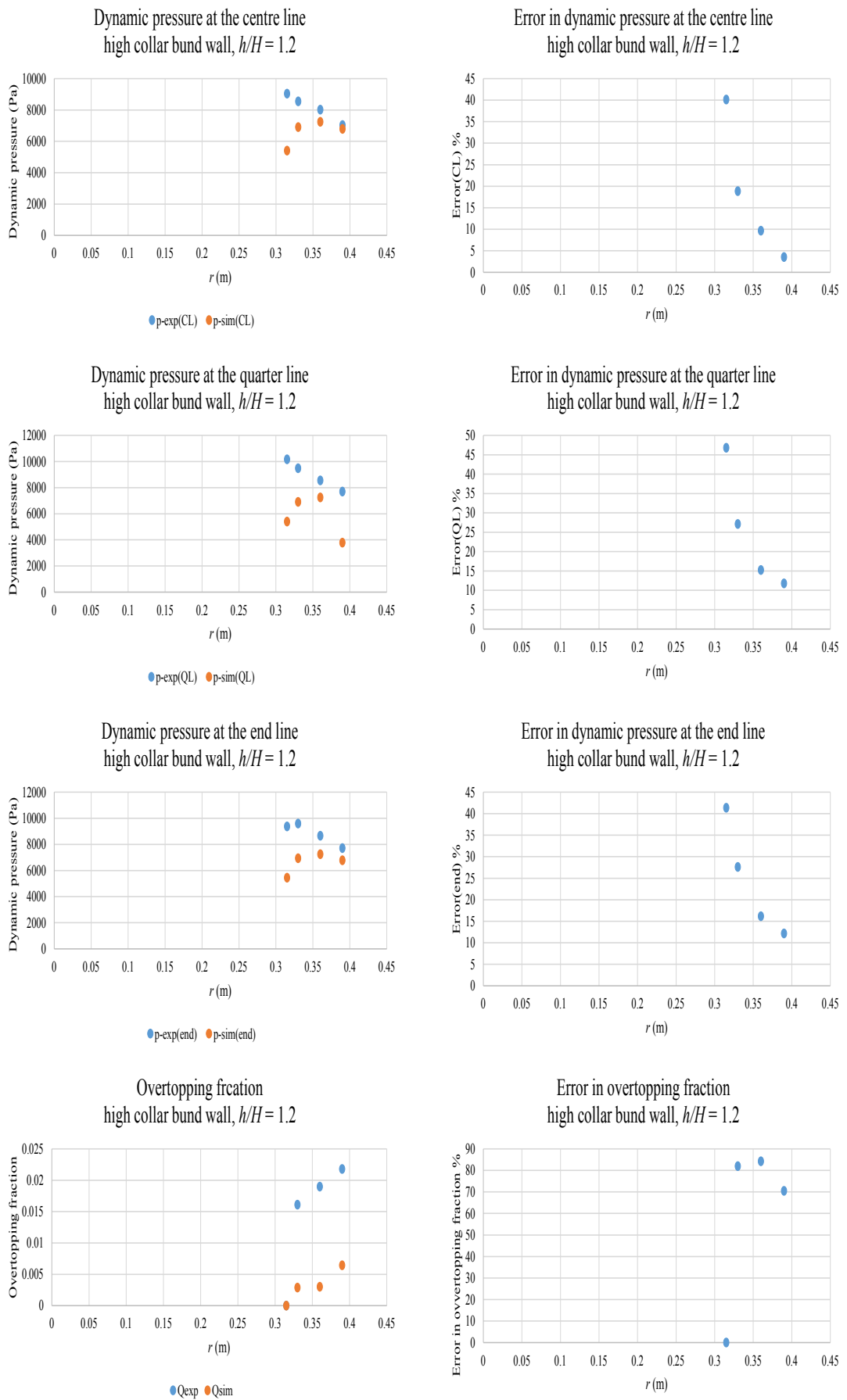


Figure 5.14: High collar bund wall,  $h/H = 1.2$

### 5.3.1.3 The effect of the fluid height and shape of bund wall

#### Triangular bund wall

Figure 5.15 and 5.16 present the numerical and experimental flow structure using a triangular bund wall. The simulation was able to predict the flow structure well. The fluid, initially at rest, collapses under the effect of gravity. The fluid flow first impacts the wall in its middle, then in the corners. The fluid flow gains height until it breaks, with a quantity returning back to the banded area and the rest of it flowing outside the bund. Most of the fluid that escapes the bund moves next to the surrounding walls of the test rig, with a little of it spreading in the middle of the bed of the test rig, this behaviour was predicted by CFD modelling.

Figure 5.17 presents the numerical results of dynamic pressures measured at the centre line, quarter line and end line along with overtopping fractions with respect to the fluid height  $H$ . The simulations were able to predict a similar trend of the evolution of the pressures, i.e. the dynamic pressure increases as  $H$  increases at all positions. The relative error does not seem to depend on  $H$  as there is no constant trend that the error is following as  $H$  is increasing. Overall, the relative error is below a reasonable limit for most of the measured pressures which is 25% with few exceptions.

Regarding the overtopping fractions, the simulations could predict that a higher level of fluid produces more overtopping quantities. The numerical results are in a better correlation with the experimental results at higher values of  $H$  corresponding to middle and tall tanks with a relative error within 12%. Similarly to the circular standard configurations, the dynamic pressures are mostly overestimated, while the overtopping fractions are underestimated.

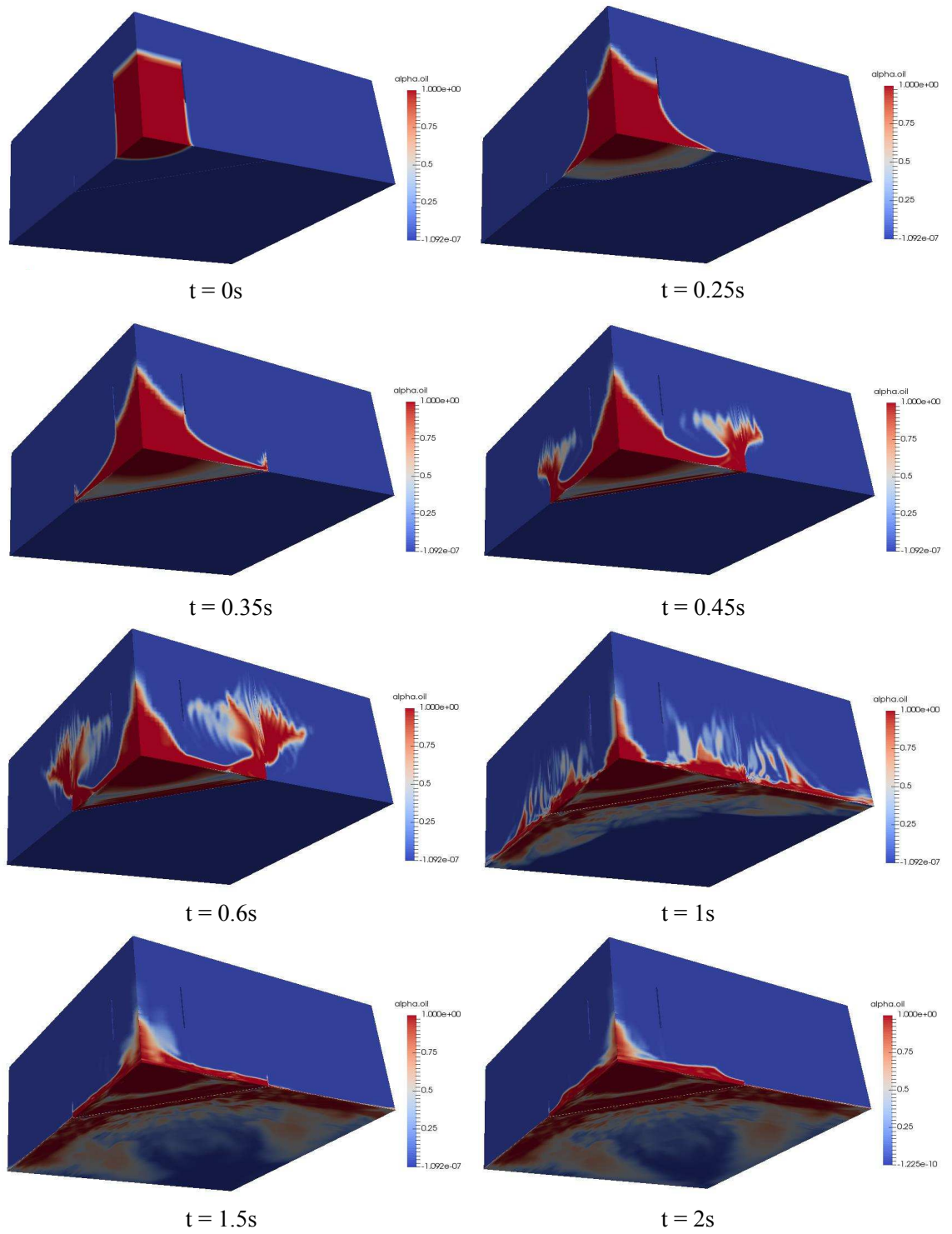


Figure 5.15: Flow structure corresponding to a standard configuration - test  $Wall_1$  (triangular wall)



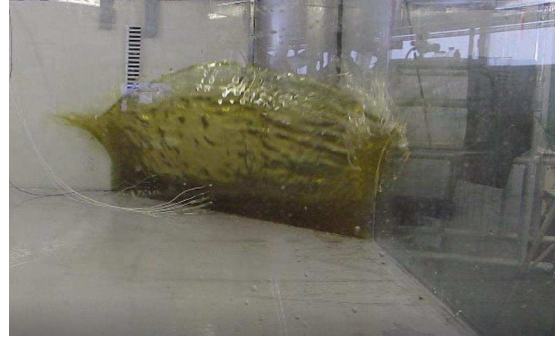
t = 0s



t = 0.25s



t = 0.35s



t = 0.45s



t = 0.6s



t = 1s



t = 1.5s



t = 2s

Figure 5.16: Experimental flow structure corresponding to a standard configuration - test  $Wall_1$  (triangular wall)

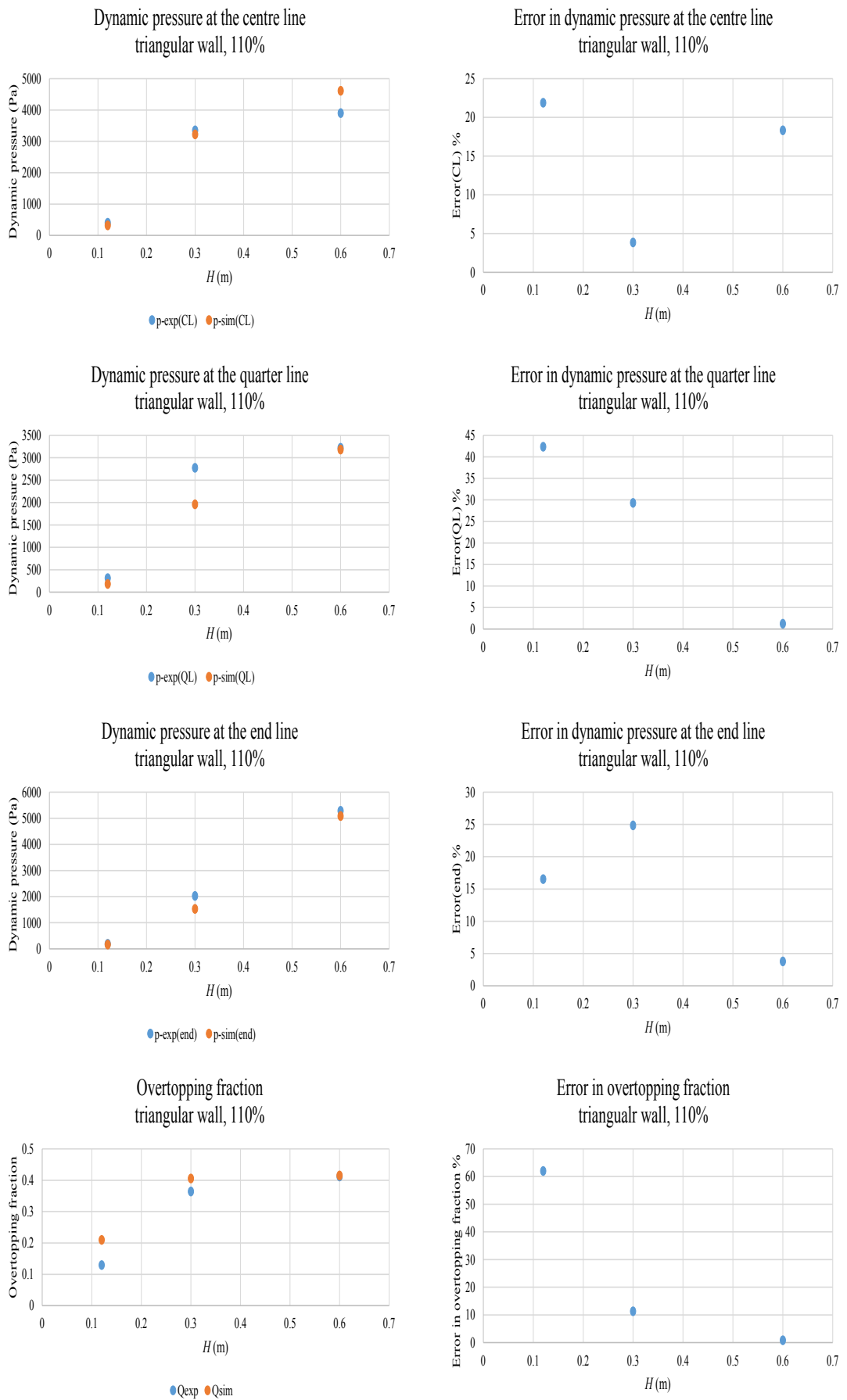


Figure 5.17: Effect of the height of the fluid (triangular wall, capacity 110%)

## Square bund wall

Figures 5.18 and 5.19 present the numerical simulation and the experimental results of the collapse of a quadrant of a storage tank using a square bund wall. As with the use of circular and triangular bund walls, the simulation was able to predict a similar flow structure as the experimental one. The fluid initially at rest, collapses under the action of gravity. The fluid hits the wall at first along its sides after which it hits the corner. At the same time as the fluid hits the corner, the fluid that already impacted the walls gains height until it breaks and falls down. The quantity that escapes the banded area spreads mostly in front of the corner with very little moving close to the surrounding walls. This flow structure is well predicted as compared with the experiment.

Figure 5.20 represents the numerical results of dynamic pressures and overtopping fractions compared to the experimental results. For the square wall, the pressures at the centre and the quarter lines are measured at the corner and the middle of the side of the wall, respectively. The simulation results are following the same trend as the experimental ones, for which the pressure is increasing with greater heights of fluid. Although the relative error in the dynamic pressure is high at some locations, the simulation is considered to yield reasonable results, as most of the errors are within 40% with few exceptions.

Regarding the overtopping fractions, the simulations predicted the increase in the lost material with the respect to the height. The error in overtopping fractions for the squat tank is 243%, which is considerably high due to the fact that the quantities lost are very minor, only 6%, which results in high relative error. For the middle and tall tanks, good correlations were obtained.

By comparing the performance of the solver for the prediction of dynamic pressures and overtopping fractions, InterFOAM always overestimates the dynamic pressures at all positions, while the overtopping fractions are always underestimated.

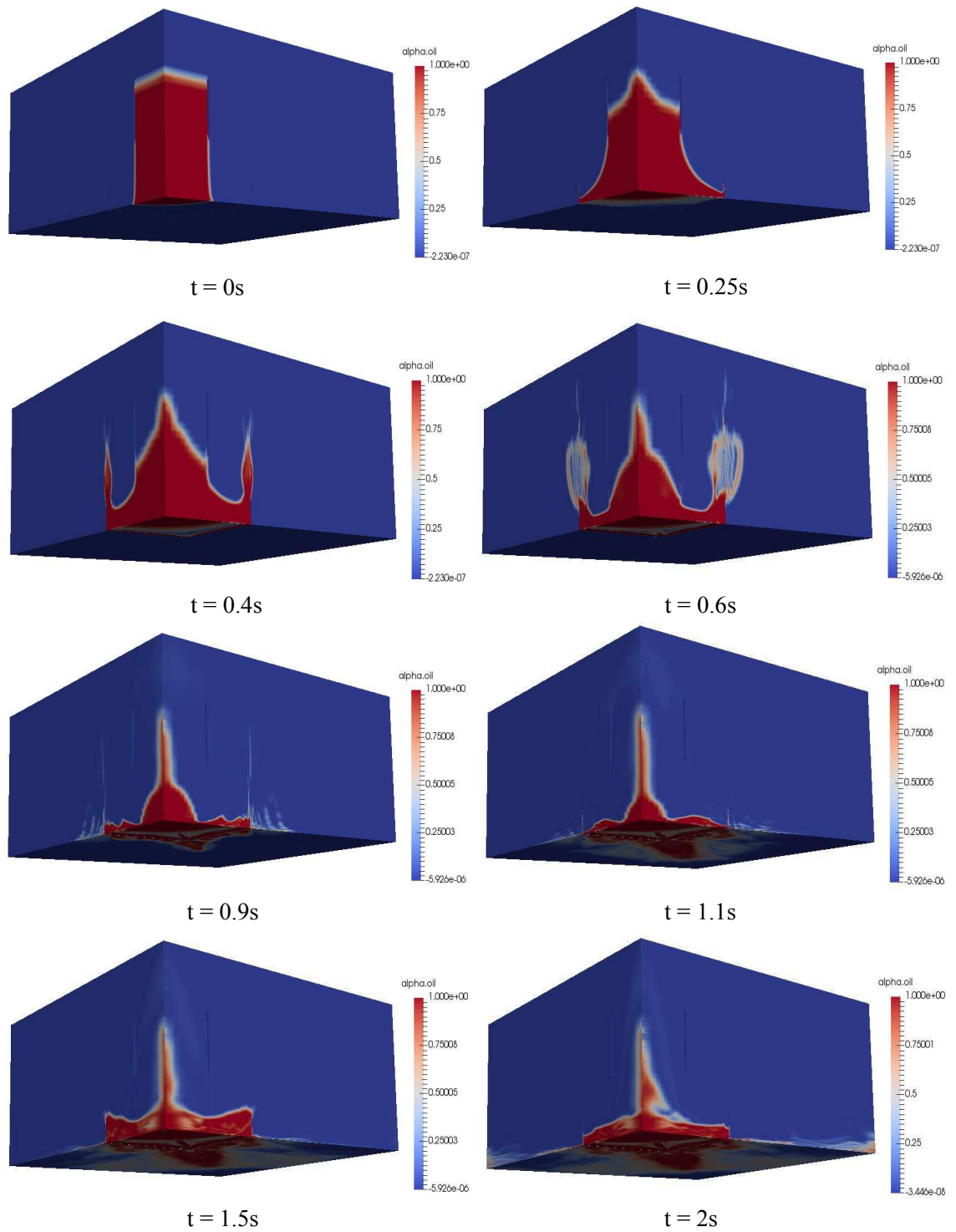
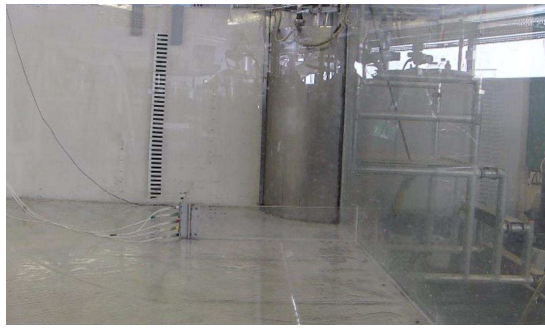


Figure 5.18: Flow structure corresponding to a standard configuration - test  $Wall_2$  (square wall)



t = 0s



t = 0.25s



t = 0.4s



t = 0.6s



t = 0.9s



t = 1.1s



t = 1.5s



t = 2s

Figure 5.19: Experimental flow structure corresponding to a standard configuration - test  $Wall_2$  (square wall)

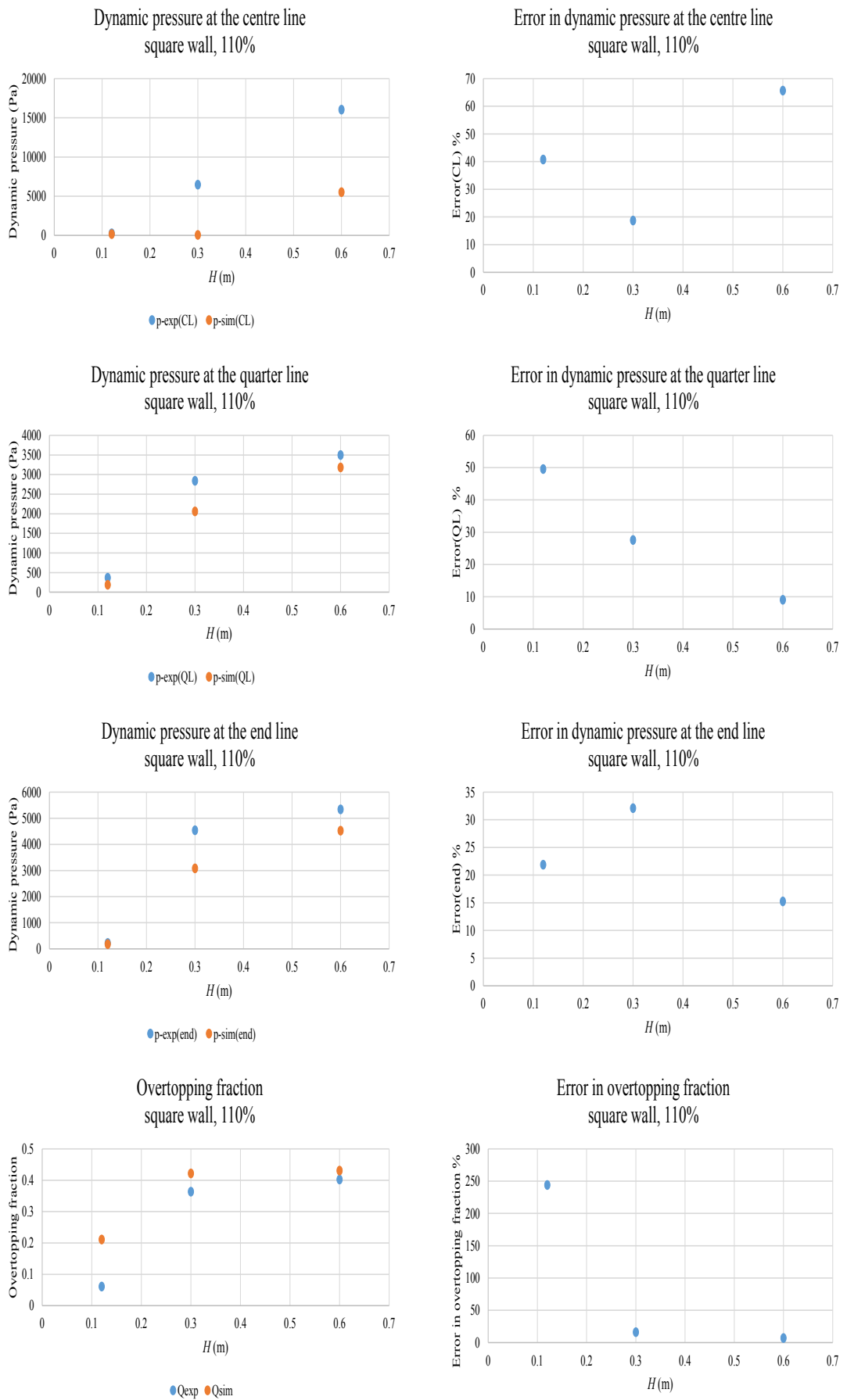


Figure 5.20: Effect of the height of the fluid (square wall, capacity 110%)

## **Rectangular bund wall**

Figures 5.21 and 5.22 depict the collapse of a quadrant of a storage tank using a rectangular bund wall corresponding to the CFD simulation and the experiment, respectively. The simulation gives a close prediction of the actual flow pattern. Upon the collapse, the fluid flow hits the closest side of the bund wall, after which it gains height and it breaks. At around the same time when the fluid rises, the second side of the wall undergoes the impact of the fluid. The fluid then escapes and spreads in all the outer area of the bund wall.

Similarly to the square wall, the pressures at the centre and the quarter lines are measured at the corner and the middle of the longest side of the wall, respectively. CFD was successful in the prediction of increasing dynamic pressures with increasing heights. The simulations were able to predict close values of dynamic pressures to the experimental ones, where the error is close to 0% at some positions, while at one position, the error is as high as 78%. The high errors obtained could be related to the mesh quality, where the mesh lines are not aligned with the flow direction. For the rectangular wall, the flow direction is more complex than the other three shapes, which makes it hard to create a mesh aligned with the flow throughout all the simulation time.

Regarding the overtopping fractions, the simulation produces a similar trend as compared to the experimental results. Very good correlations were obtained for the middle and tall tanks. As for previous simulations, the dynamic pressures are mostly under-predicted, while the overtopping fractions are over-predicted.

The simulations using a triangular bund wall produced better results compared to the square and rectangular bund walls for dynamic pressures. The relative errors obtained in the case of using a triangular wall were all below 29%, except in one case where it is 49%. However, for the square and rectangular shapes, errors reached more than 50%. This could be related to the mesh alignment with the fluid flow. The fluid flow structure obtained using the triangular wall exhibits a similar pattern to the flow in the case of using a circular bund wall in the sense that they both follow a radial direction. This makes a radial mesh similar to the one created in Figure 4.12

a good choice for the mesh orientation. Regarding the overtopping fractions, the simulations gave the best results using a rectangular bund wall over the triangular and the square bund walls.

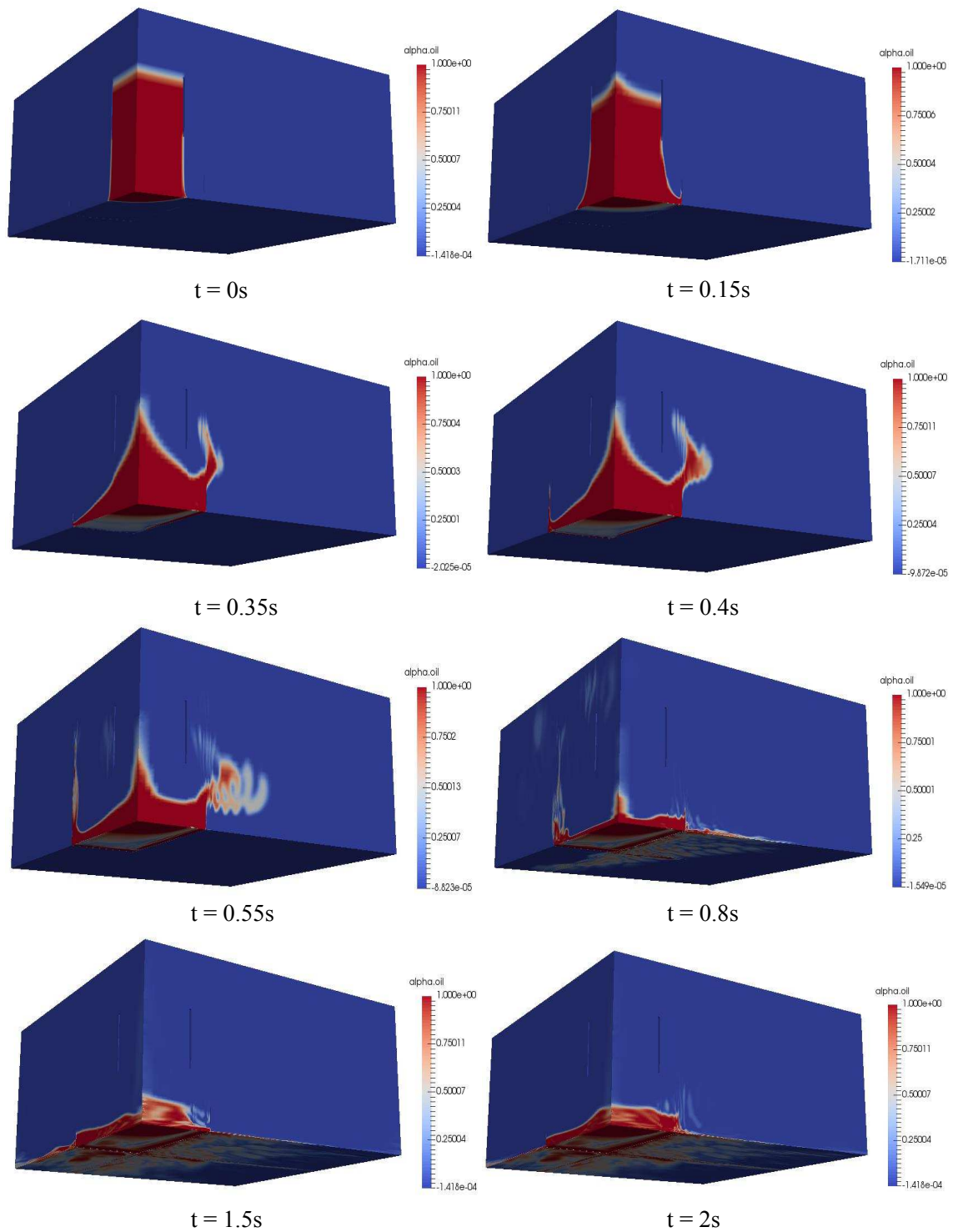
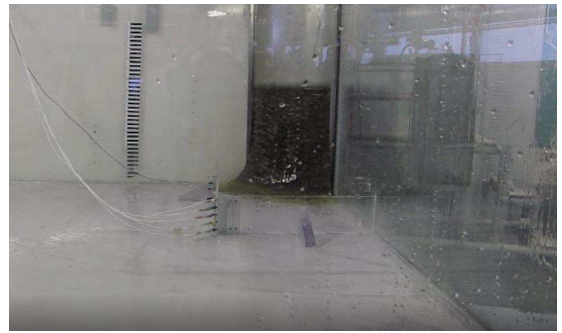


Figure 5.21: Flow structure corresponding to a standard configuration - test  $Wall_3$  (rectangular wall)



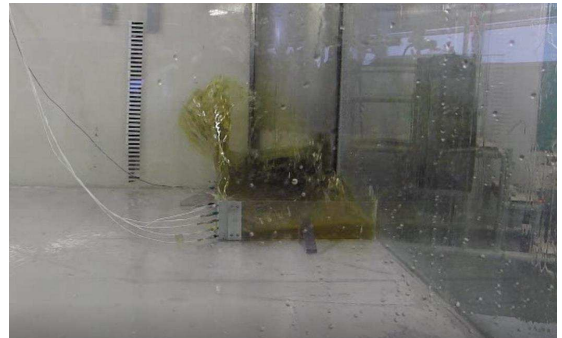
t = 0s



t = 0.15s



t = 0.35s



t = 0.4s



t = 0.55s



t = 0.8s



t = 1.5s



t = 2s

Figure 5.22: Experimental flow structure corresponding to a standard configuration - test  $Wall_3$  (rectangular wall)

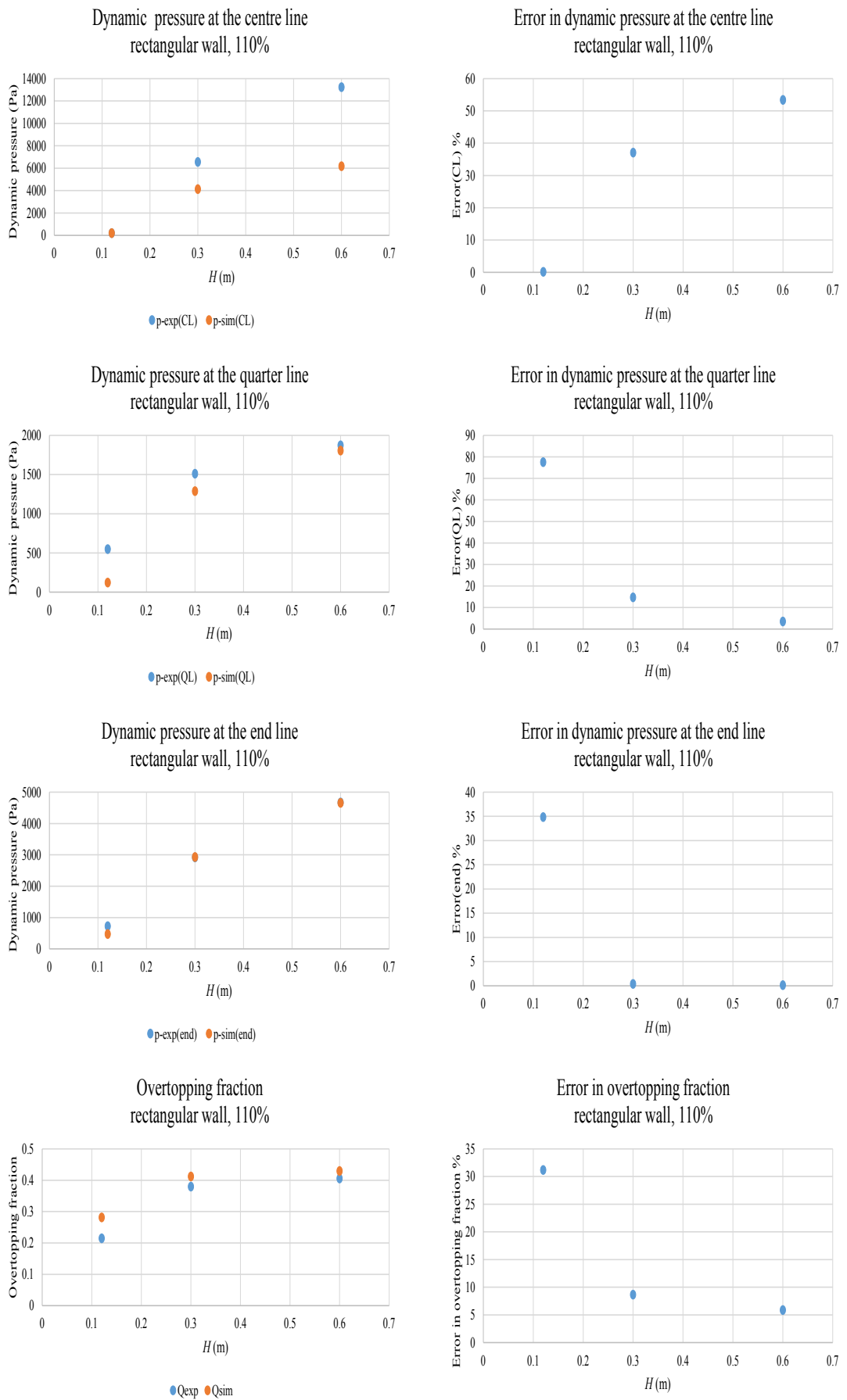


Figure 5.23: Effect of the height of the fluid (rectangular wall, capacity 110%)

### 5.3.1.4 The effect of the fluid temperature

Figures 5.24 and 5.25 present the effect of the temperature of the fluid on the overtopping fractions using circular and square walls. Overall, CFD was able to predict that overtopping fractions increase with increasing temperatures except at 25 degrees for a circular wall, where the overtopping fraction was overestimated. The variation in experimental overtopping quantities corresponding to 20 degrees and 25 degrees is 2%. This small variation could not be captured by the simulation. The relative error in the overtopping fractions can be deemed acceptable.

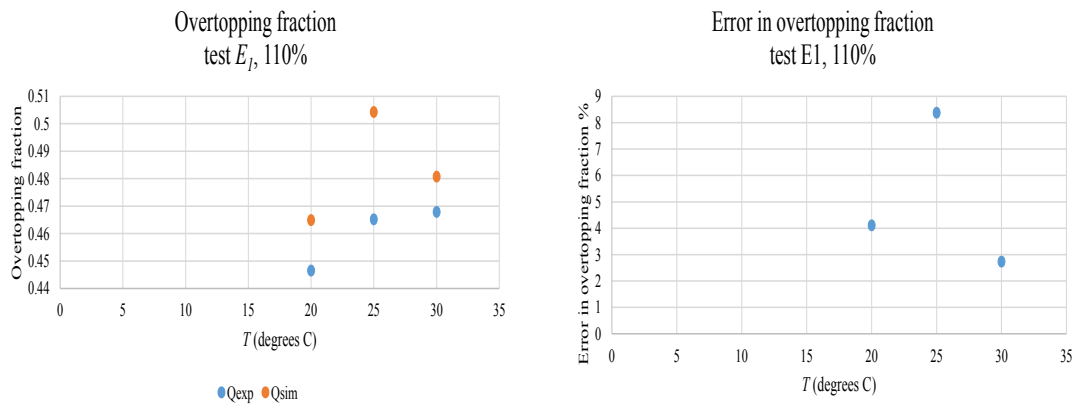


Figure 5.24: Effect of the temperature of the fluid (circular wall, tall tank, capacity 110%)

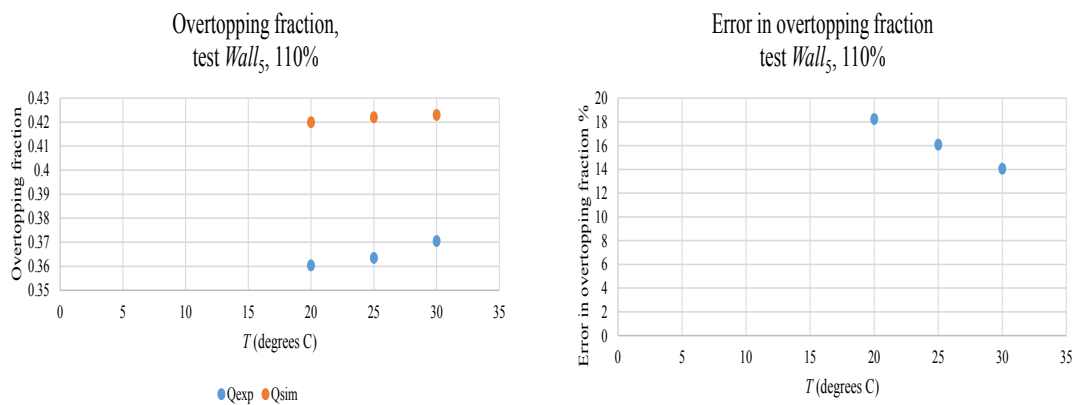


Figure 5.25: Effect of the temperature of the fluid (square wall, tall tank, capacity 110%)

### 5.3.2 Critical appraisal of InterFOAM

The solver is assessed in the following way:

- if  $0 \leq \text{relative error} \leq 15\%$ , then the simulation is good.
- if  $15\% < \text{relative error} \leq 50\%$ , then the simulation is average.
- if  $50\% < \text{relative error}$ , then the simulation is weak.

InterFOAM was able to predict good results of dynamic pressure at 38.53%, average results at 43.12% and weak results at 18.34% for the centre line, quarter line and end line. For overtopping fractions, InterFoam yielded good predictions at 58.53%, average predictions at 21.95% and weak predictions at 19.51%.

Ash (2010) conducted CFD simulations on standard configurations using STAR-CD software. The investigation was limited to only 8 simulations. Direct comparison against Ash (2010) results is impossible because water was used instead of olive oil and only a squat tank using a circular bund wall was simulated. The results produced indicated a huge discrepancy against the experimental results for the dynamic pressures since up to 1,089% in relative error was obtained. However, the overtopping fractions were reasonably predicted with a maximum error of 11.92%. Ash (2010) reported a problem of a variability in dynamic pressures that accentuates as the separation distance increases, which is a similar problem obtained using InterFOAM. This seems to be a problem related to the algorithms used to solve a multiphase flow problem.

## 5.4 CFD results for standard cases incorporating mitigation techniques

### 5.4.1 Presentation and analysis of the results

After gaining confidence in the InterFOAM solver and testing its capability for different ranges of separation distances, capacities, fluid heights, bund shapes and temperatures, a configuration that gave good results for overtopping fraction and

dynamic pressures has been selected for the optimisation of mitigation techniques. Test  $B_1$  was selected, which uses a tall tank, a circular bund wall located at 0.497m from the centre of the tank and a capacity of 110%. The relative error obtained from this test was below 5% for both dynamic pressures and overtopping fraction. Ash (2010) investigated the use of COAST at an angle of 45 degrees while in this research COAST with angles ranging from 10 to 80 degrees were studied. The incorporation of MOTIF and COAST combined together was used for the optimisation of the angle because Ash (2010) demonstrated that when using a combination, the reduction in overtopping fractions varied between 70% and 95% across the range modelled, including square and circular walls and middle tank arrangements.

Figure 5.26 depicts the results of dynamic pressures and overtopping fractions corresponding to different angles of COAST. The dynamic pressures shown are measured at the centre line, they tend to decrease with increasing angles. Similarly, the overtopping fractions decrease with an increasing angle, but at an angle 60 degrees and beyond, they become nearly constant. The angle 80 degrees was selected for subsequent simulations because it gave the lowest overtopping fraction and lowest dynamic pressure. The reduction in overtopping fraction compared to the experimental fraction is equal to 18.5%.

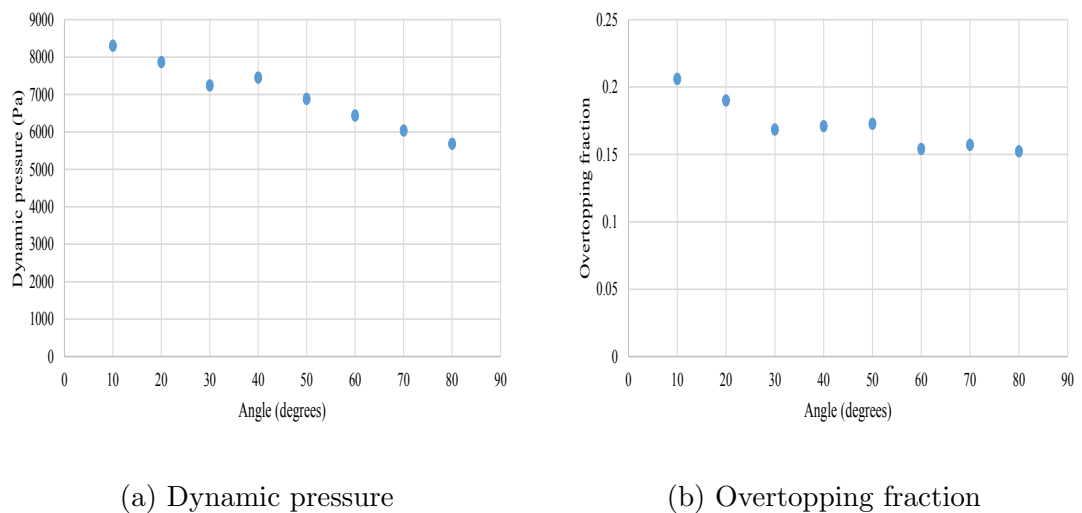


Figure 5.26: Optimisation of the angle of COAST

However, the dynamic pressure indicates an increase of 15% compared to the ex-

perimental dynamic pressure obtained from the standard configuration, this can be attributed to the level of turbulence that increases when the fluid hits MOTIF. Furthermore, the location where the maximum pressure is obtained is near the top of the wall as shown in Figure 5.27. This is opposed to the case of standard configurations where the maximum pressure is at the base of the wall. This can affect the structural integrity of the wall as the overturning moment increases.

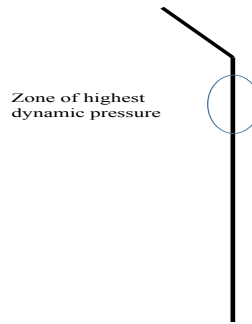


Figure 5.27: Zone of the highest dynamic pressure

Therefore, the combination of MOTIF and COAST was questioned on whether MOTIF is really beneficial, especially that it adds to the cost of construction. For this, three CFD simulations were conducted on a circular wall, where the angle of COAST is 45 degrees. The three simulations correspond to the use of MOTIF only, MOTIF and COAST combined together and COAST only, as depicted in Figures 5.28, 5.29 and 5.30, respectively. By comparing the flow behaviours, it is noticed that whenever MOTIF is incorporated, the flow pattern becomes different from the standard cases and the configuration incorporating only COAST. Figure 5.31 shows a comparison between the different mitigation techniques in terms of dynamic pressures measured at the centre line along with overtopping fractions. The dynamic pressure is the lowest in case of using only COAST and the overtopping fraction is significantly reduced. Incorporating COAST produces overtopping fraction of 2.5% compared to 17% for COAST and MOTIF combined together. The reduction in overtopping fraction compared to the standard case with the use of COAST only is 86%, therefore COAST only is adopted for subsequent simulations.

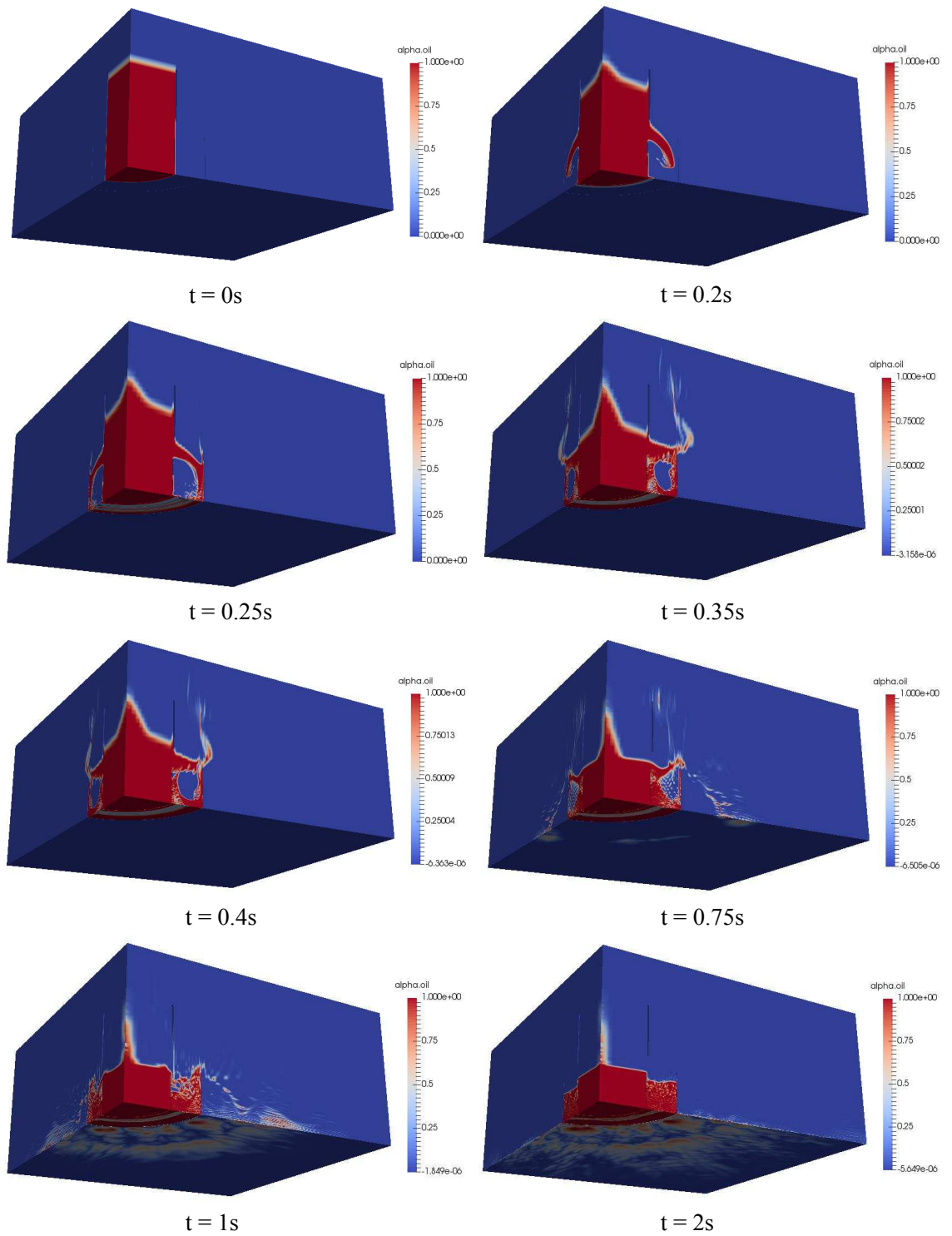


Figure 5.28: Flow structure corresponding to a configuration incorporating MOTIF

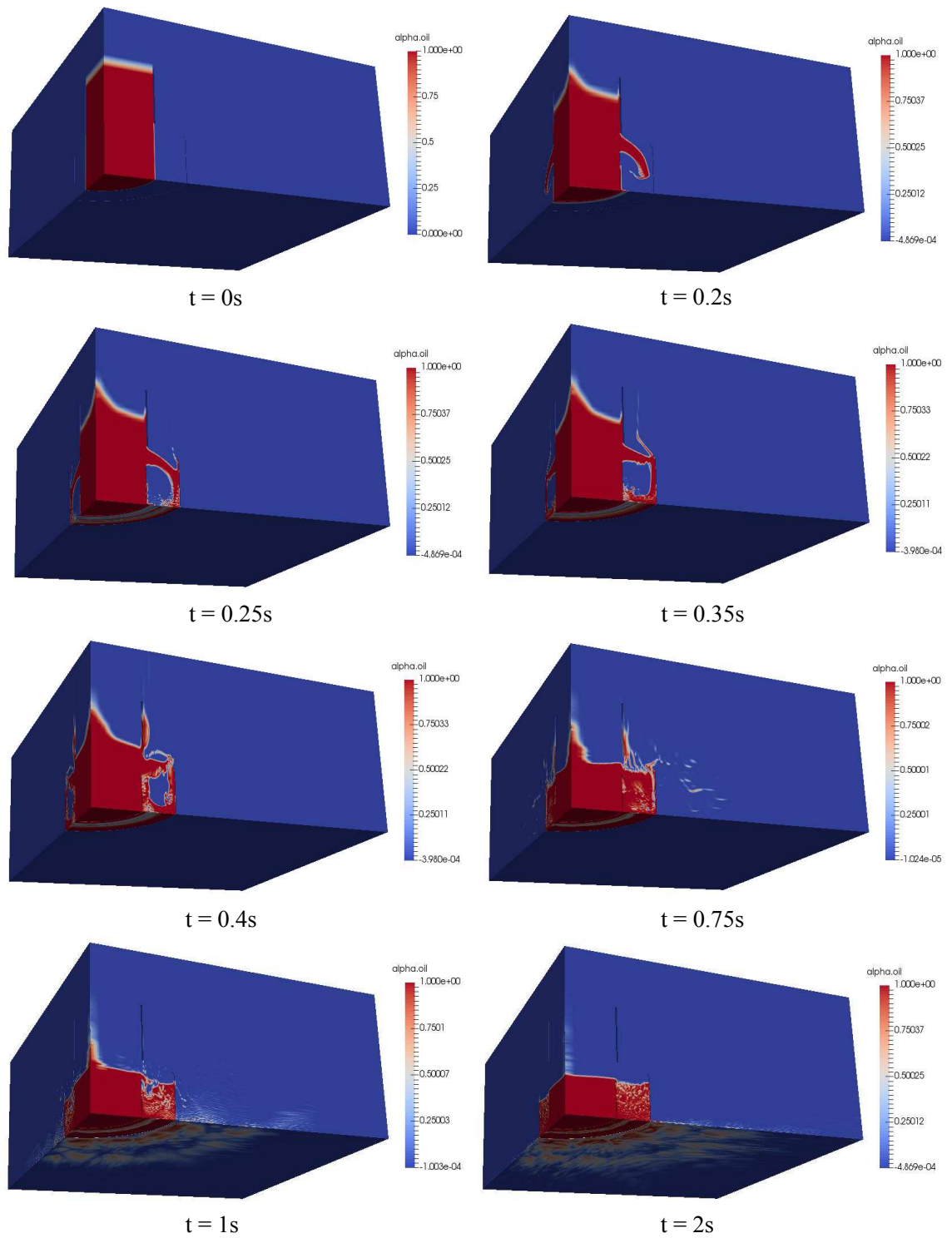


Figure 5.29: Flow structure corresponding to a configuration incorporating MOTIF and COAST

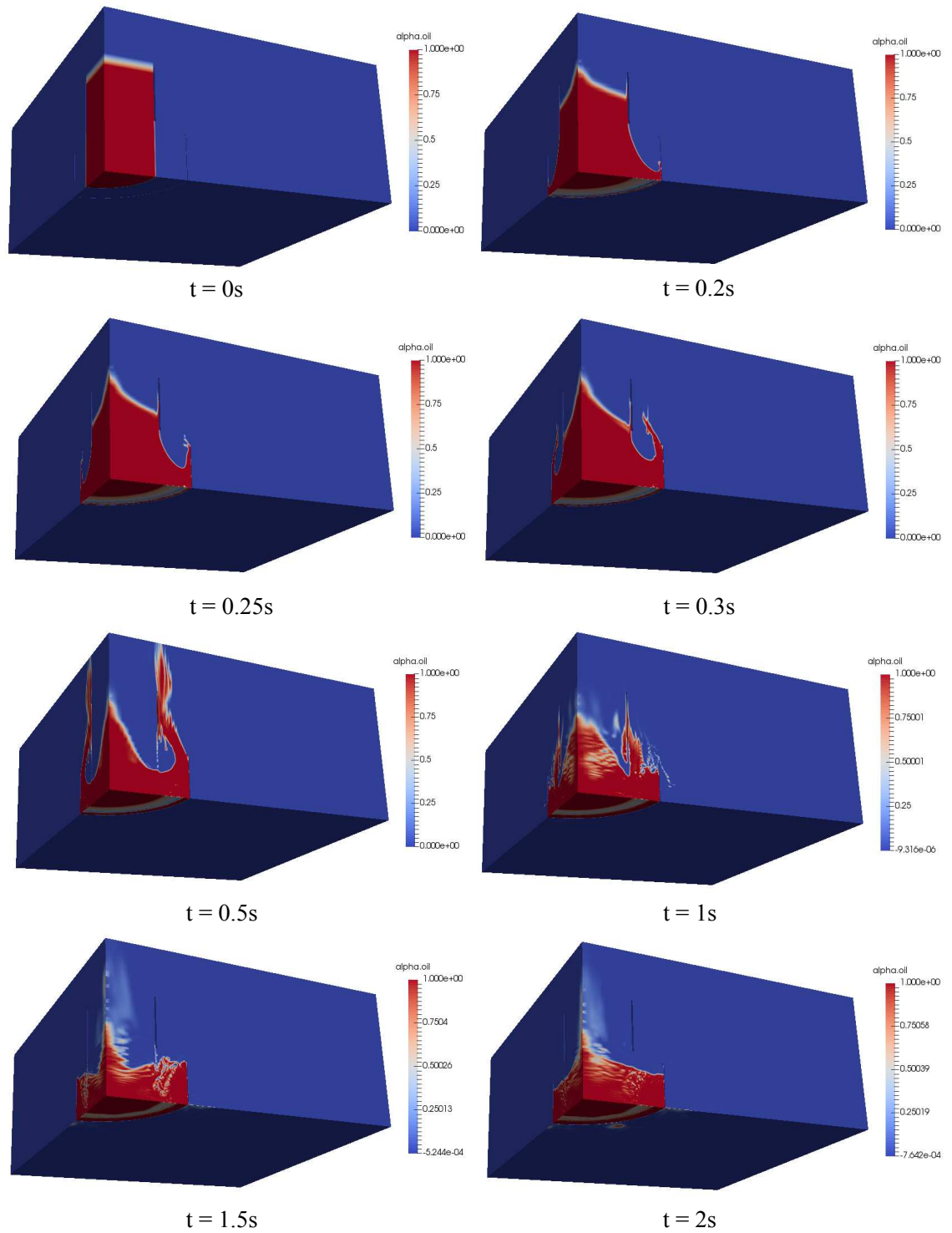


Figure 5.30: Flow structure corresponding to a configuration incorporating COAST

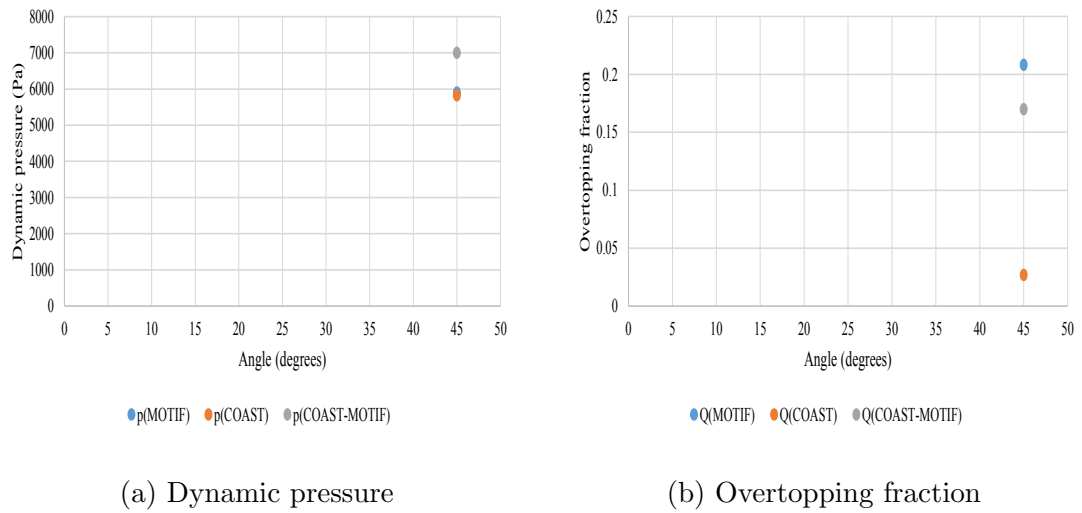


Figure 5.31: Selection of the mitigation technique

#### 5.4.1.1 The effect of COAST on the capacity and shapes of the bund wall

Figures 5.32 and 5.33 present the effect of incorporating COAST on different capacities and different shapes of the bund wall, respectively, by comparing them to the experimental results of the standard configurations. With different capacities, the dynamic pressures in the case of incorporating COAST appear to be greater than the experimental pressures of standard cases. Theoretically, COAST does not change the dynamic pressures as the flow structure is similar at the instant of the initial impact with the wall, the dissimilarity in the pressures is merely related to numerical error. However, the overtopping fractions are significantly reduced. Generally, COAST conserves the same trend of the variation of overtopping fraction with the capacity. The reduction in overtopping fractions varies from 93% to 98% for the different capacities. Regarding the reduction in overtopping fractions corresponding to different shapes of bund wall, COAST permits reductions of 93%, 35%, 10% and 34% for circular, square, rectangular and triangular bund walls of capacity 110%, respectively.

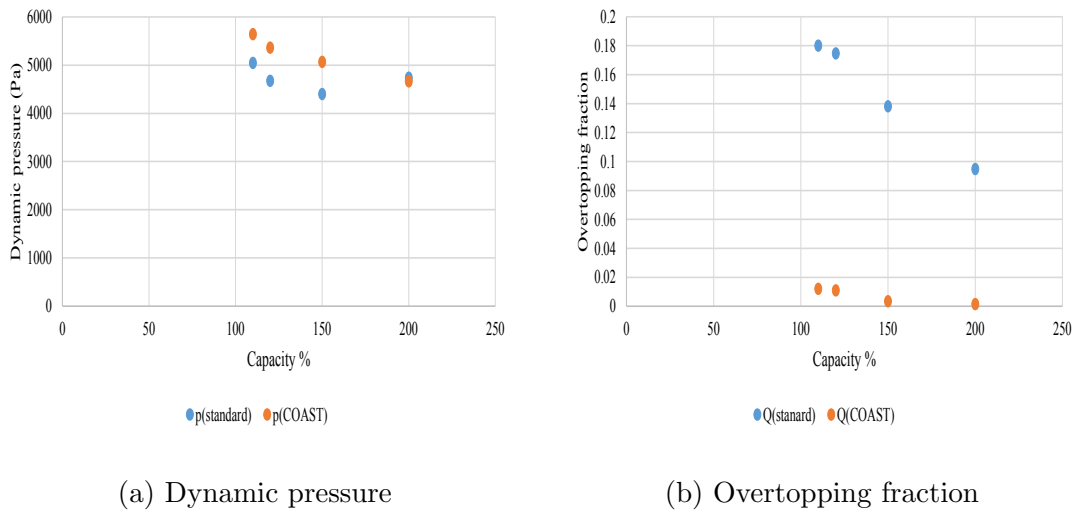


Figure 5.32: Effect of COAST with different capacities of the bund wall

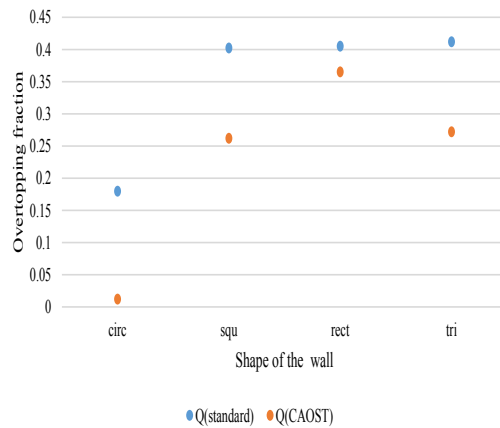


Figure 5.33: Effect of COAST on the overtopping fraction for different shapes of the bund wall

## 5.5 CFD results for the partial failure cases

### 5.5.1 Presentation and analysis of the results

The problem of partial failure was also studied with few simulations to investigate the performance of MOTIF. Unlike the case of total failure, MOTIF does not change the flow structure because it is constrained to escape the tank through the aperture. MOTIF performance consists in delaying the impact time as indicated in Figure 5.34, reducing the dynamic pressures and overtopping fractions as shown in table

5.1. The reduction in overtopping fractions is 94.56%, 99.24% and 99.91% using  $MB_{1rect_1}$ ,  $MB_{2rect_2}$  and  $MB_{3rect_3}$ , respectively.

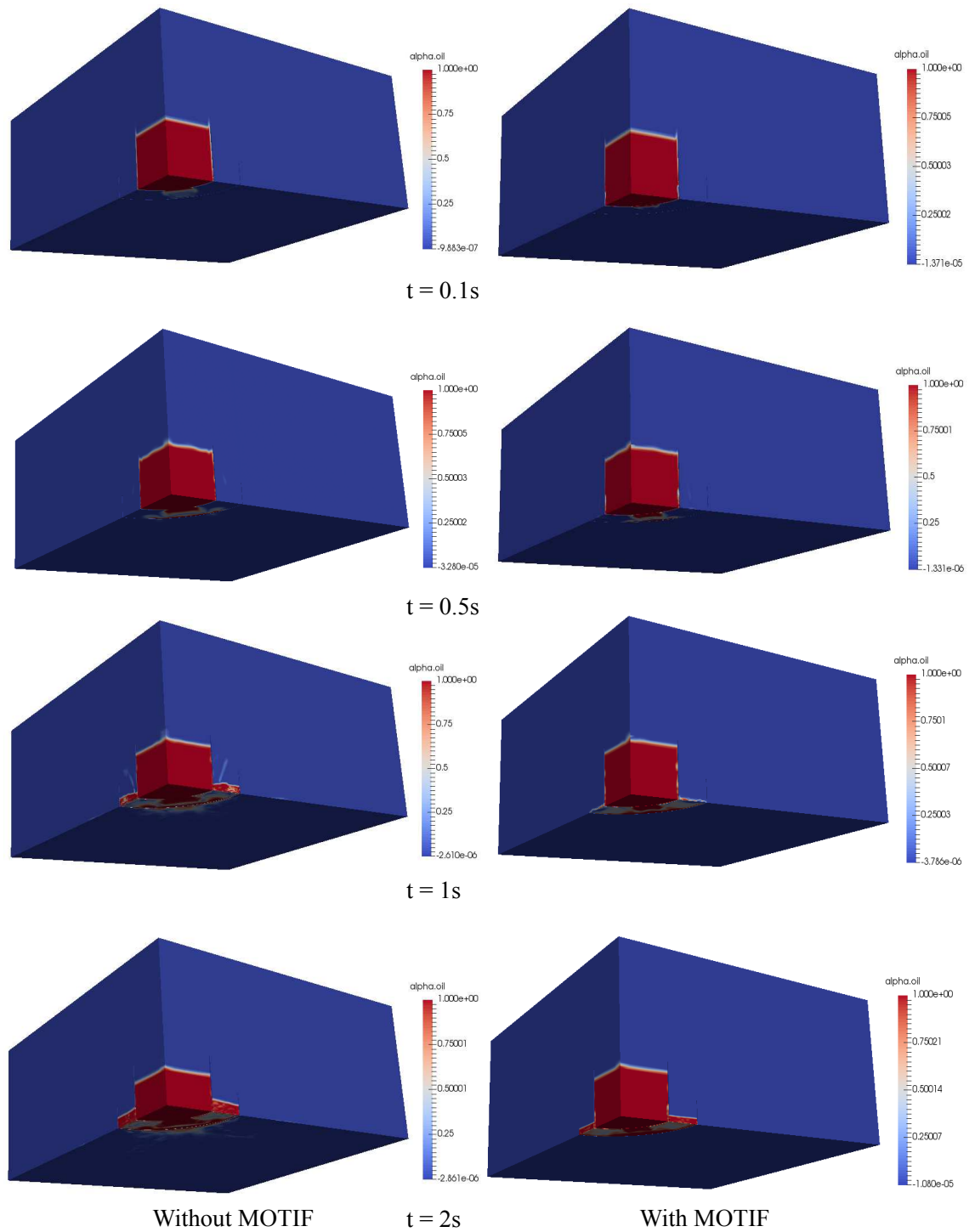


Figure 5.34: Flow structure corresponding to a partial failure of a tank

Table 5.1: Dynamic pressures and overtopping fractions of the partial failure

Test name	Dynamic pressure at centre line (Pa)	Dynamic pressure at quarter line (Pa)	Overtopping fraction
$B_1rect_1$	685.734	383.141	0.01046
$MB_1rect_1$	469.173	133.911	0.0000569
$B_1rect_2$	769.67	752.101	0.1431
$MB_1rect_2$	460.235	233.543	0.0010799
$B_1rect_3$	711.243	752.487	0.1729
$MB_1rect_3$	628.863	297.43	0.0001541

## 5.6 Similitude of fluid model

Some of the common non-dimensional groups in fluid mechanics are given in table 5.2.

Table 5.2: Common non-dimensional groups in fluid mechanics (Munson et al., 2010)

Dimensionless group	Name	Interpretation	Types of application
$\frac{\rho_f U l_c}{\mu}$	Reynolds number, $Re$	$\frac{\text{inertia force}}{\text{viscous force}}$	All types of flow
$\frac{U}{\sqrt{g l_c}}$	Froude number, $Fr$	$\frac{\text{inertia force}}{\text{gravitational force}}$	Free surface flow e.g. flow of water around ships flow through rivers or open conduits
$\frac{U}{c}$	Mach number, $Ma$	$\frac{\text{inertia force}}{\text{compressibility force}}$	Flows where compressibility of the fluid is important
$\frac{\rho_f U^2 l_c}{\sigma}$	Weber number, $We$	$\frac{\text{inertia force}}{\text{surface tension force}}$	Flows where surface tension is important e.g. flows of thin films of liquid the formation of droplet or bubbles

It is assumed that during the release of the fluid, the gravitational forces are important. Therefore, the two relevant numbers to this problem are the Froude and Reynolds numbers. By equating these two dimensional numbers between the model

and prototype, it is possible to predict the behaviour of the problem at the full scale.

$$\left(\frac{\rho U l_c}{\mu}\right)_{m_d} = \left(\frac{\rho U l_c}{\mu}\right)_{p_d} \quad (5.2)$$

$$\left(\frac{U}{\sqrt{g l_c}}\right)_{m_d} = \left(\frac{U}{\sqrt{g l_c}}\right)_{p_d}, \quad (5.3)$$

where,  $m_d$  refers to the model and  $p_d$  refers to the prototype.

## 5.7 Summary

This chapter presented an empirical and numerical study on the catastrophic failure of a storage tank. The capacity of the bund wall, the separation distance, the height of the wall, the shapes of the bund walls, the height and the temperature of the fluid were investigated through an extensive investigational program. The main findings are summarised as follows:

- Overtopping fractions decrease as the separation distance decreases implying an increase of the wall height.
- Overtopping fractions decrease with an increasing capacity of the bund wall.
- A variability of pressures was obtained in the study of the effect of capacity and separation distance.
- A significant reduction in the overtopping fractions was achieved with the use of high collar bund walls that are normally constructed around tanks storing hazardous materials, this is accompanied by an increase in dynamic pressures.
- Both the dynamic pressures and overtopping fractions increase with increasing fluid heights.
- For square and rectangular bund walls, there is an increase in dynamic pressures at the corners.
- Higher values of overtopping fractions are obtained with increased temperatures of the fluid.

The experiments constitute a baseline for the evaluation of the performance of the InterFOAM solver. Extensive CFD simulations were conducted and the outcomes showed that InterFOAM was better in the prediction of overtopping fractions than the dynamic pressures. Generally, the solver was able to predict acceptable values of dynamic pressures compared to Ash (2010) results. Dynamic pressures tend to be variant as the separation distance increases, which questions the validity of the solver for large distances. The CFD simulations of the standard configurations were then followed by an optimisation study to select the optimum mitigation technique. COAST with an inclination of 80 degrees achieved lower dynamic pressures and a significant reduction in overtopping fraction. The effect of incorporating COAST on bund walls with different capacities and shapes was then studied and a reduction of up to 93% was achieved using a circular bund wall. Additionally, the problem of the partial failure of storage tank was studied with the incorporation of MOTIF, which allowed a reduction in the overtopping fractions to up to 99.99%. Finally, the similitude of the fluid model was briefly described.

# Chapter 6

## FEA results

### 6.1 Introduction

This chapter presents the results of FSI simulations. The modelling approach was first validated against the experiment using a plain concrete wall. Then, the simulations of bund walls with different configurations and materials were conducted. CFD models were selected on the basis of reducing the separation distance between the tank and the wall to minimise the numerical errors. The configurations simulated include circular, square and rectangular walls subjected to centred and off-centred loading and made from plain concrete, reinforced concrete and UHP-FRC. The ultimate purpose of these simulations is to investigate the performance of UHP-FRC over the use of plain and reinforced concrete.

### 6.2 Validation of the FSI simulation

The experiment was conducted by allowing water to escape rapidly. Some spillage occurred prior to the release of the gate, which was modelled in the CFD simulation as indicated in Figure 6.1 depicting the flow structure in terms of the phase fraction.

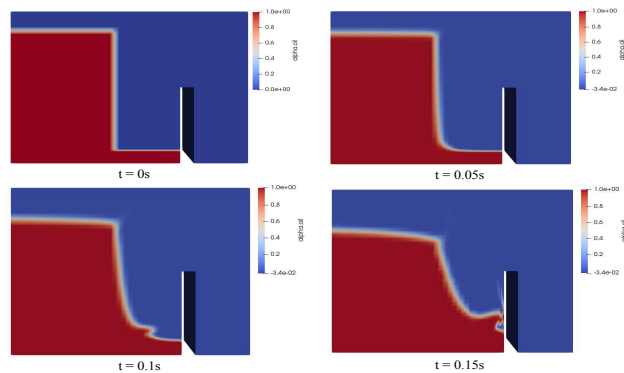


Figure 6.1: Flow structure of the water release

Figure 6.2 depicts the numerical pressure field induced by the water on the wall. At  $t = 0.15\text{s}$ , the water flow impacts the wall and applies dynamic pressures in the range of 8,000 Pa.

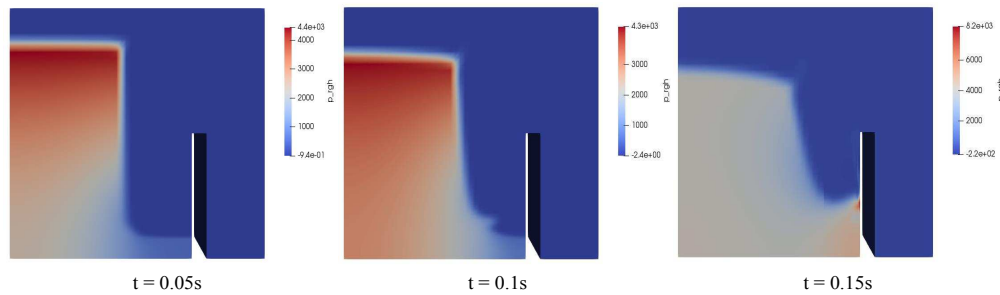


Figure 6.2: Pressure field of the water flow

Figure 6.3 presents the linear strain field in the wall induced by the pressures of water. It is expected that the strain distribution should be symmetrical and decreasing from the bottom to the top of the wall, but Figure 6.3 shows a different distribution of the strain. This can be attributed to two reasons. The first reason is that the CFD simulation itself does not give a symmetry in the results as indicated in Figure 6.4. The second reason is that the meshes for the CFD and FEA models are non-matching, so the mapping process from the CFD model to the FEA model can cause unequal pressure values at positions where they should be the same.

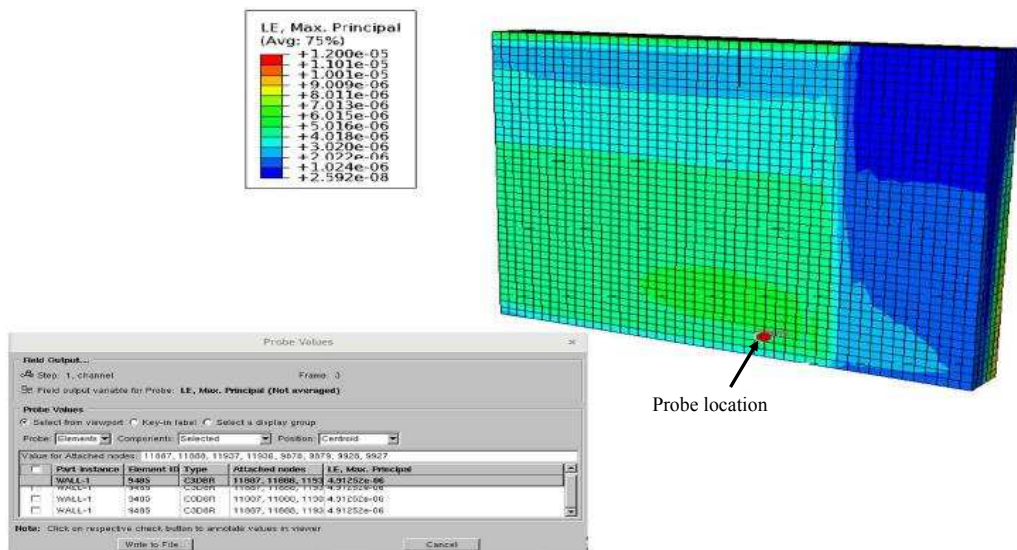


Figure 6.3: Numerical results of the strain in the wall

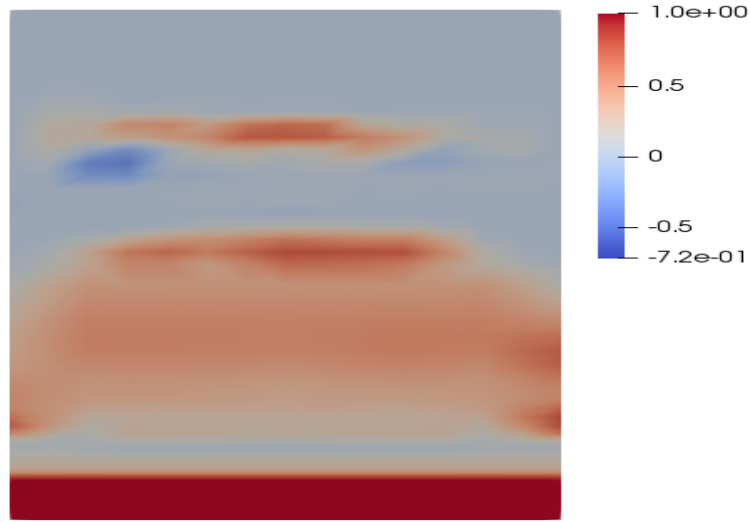


Figure 6.4: Non symmetry in the flow structure

FSI simulations were repeated three times using different element sizes until an insignificant change in the result was obtained. The element lengths corresponding to the different simulations are 8mm, 4mm and 2mm, respectively. The strain was measured using a probe tool in Abaqus at the specified location as shown in Figure 6.3. The results of the strain are given in Table 6.1.

Table 6.1: Numerical results of the strain in the wall

Simulation number	Strain value	time of impact (s)
1 (8mm)	$4.97 \times 10^{-6}$	0.15
2 (4mm)	$3.59 \times 10^{-6}$	0.15
3 (2mm)	$3 \times 10^{-6}$	0.15

The results of the strain obtained from the FSI simulations are compared against the experimental results. The experiment was conducted five times for repeatability. The strain values measured by the strain gauge are shown in Figure 6.5 and Table 6.2. A good correlation is obtained with a relative error equal to 11.76%.

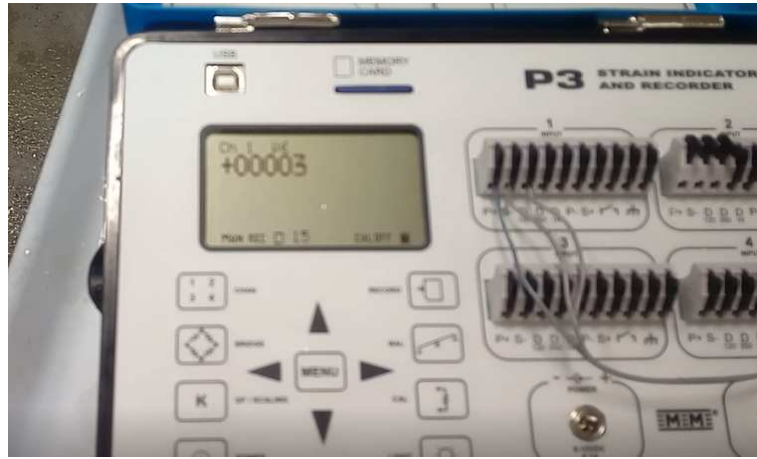


Figure 6.5: Experimental results of the strain

Table 6.2: Experimental results of the strain in the wall

Test number	Strain value
1	$4 \times 10^{-6}$
2	$3 \times 10^{-6}$
3	$3 \times 10^{-6}$
4	$5 \times 10^{-6}$
5	$2 \times 10^{-6}$
Average	$3.4 \times 10^{-6}$

### 6.3 Presentation and analysis of the results

The FSI simulations are presented below. Firstly, the plain concrete bund wall behaviour with circular, square and rectangular shapes, subjected to centred and off-centred loads is presented and discussed. Then, the performance of a reinforced concrete wall is given. Finally, results of the response of a square wall made of UHP-FRC and incorporating COAST is presented and compared to a plain concrete standard wall.

The CDP model gives non symmetrical distribution of the tensile damage on the whole structure when subjected to a symmetric load as depicted in Figure 6.6. This raises a question about the performance of this material model. The asymmetry in

the results was discussed with DS SIMULIA Abaqus which confirmed that the CDP model gives asymmetry in the results for cases where a symmetry is expected, as indicated in figures B.1 and B.2 (Appendix B). This required the simulation of the whole structure, even for cases where both of the load and geometry are symmetrical for the purpose of determining the tensile damage more precisely.

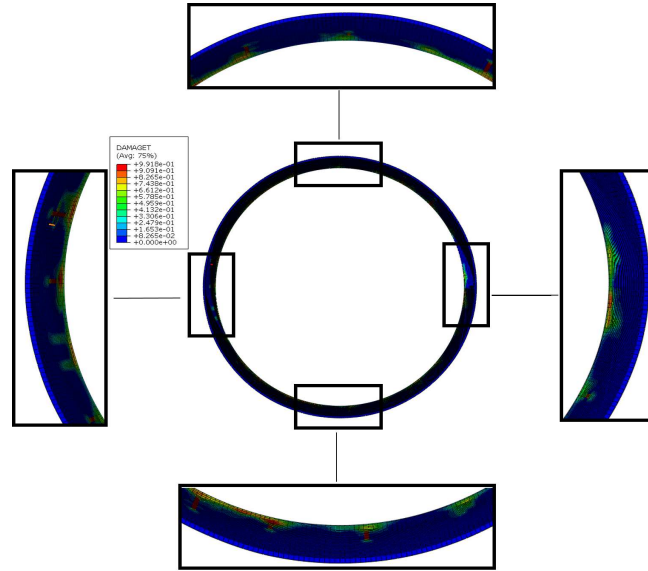


Figure 6.6: Non symmetric distribution of tensile damage

### 6.3.1 Simulation results of the plain concrete wall

#### 6.3.1.1 Simulation results of the circular wall

Figures 6.7, 6.8, 6.9, 6.10, 6.11 and 6.12 present the tensile damage of a circular bund wall made of plain concrete and subjected to a centred load at different instants. In each figure, the flow structure and the pressures applied to the wall are also included. The wall starts exhibiting damage at  $t = 1s$  and remains constant until the end of the simulation ( $t = 2s$ ). The tensile damage occurs all through the wall. Figures 6.13, 6.14, 6.15, 6.16, 6.17 and 6.18 present the structural response of the wall in the case where it is subjected to an off-centred load. Unlike the previous case, the damage is occurring only in some regions of the wall. The side of the wall that is first impacted by the fluid exhibits more damage than other regions. The maximum tensile damage caused increases slightly after the first instant when it appeared, and remains constant until the end of the simulation.

## Circular wall subjected to a centred load

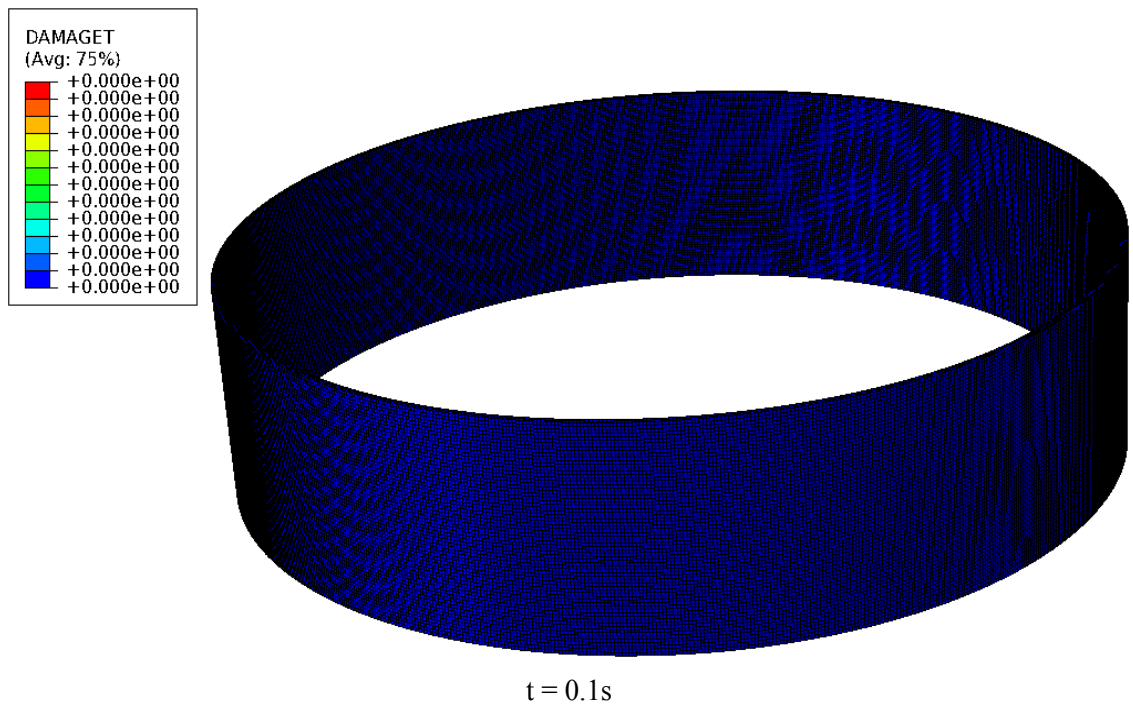
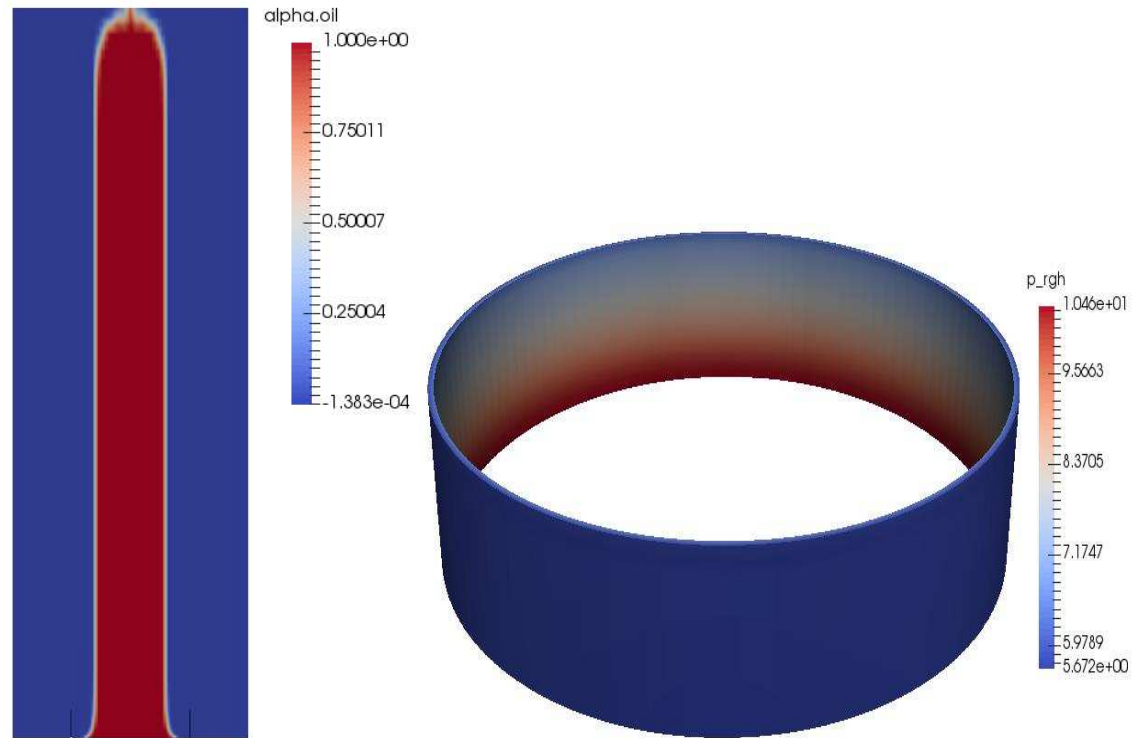


Figure 6.7: Flow behaviour and tensile damage of a plain concrete circular wall subjected to a centred load at  $t = 0.1s$



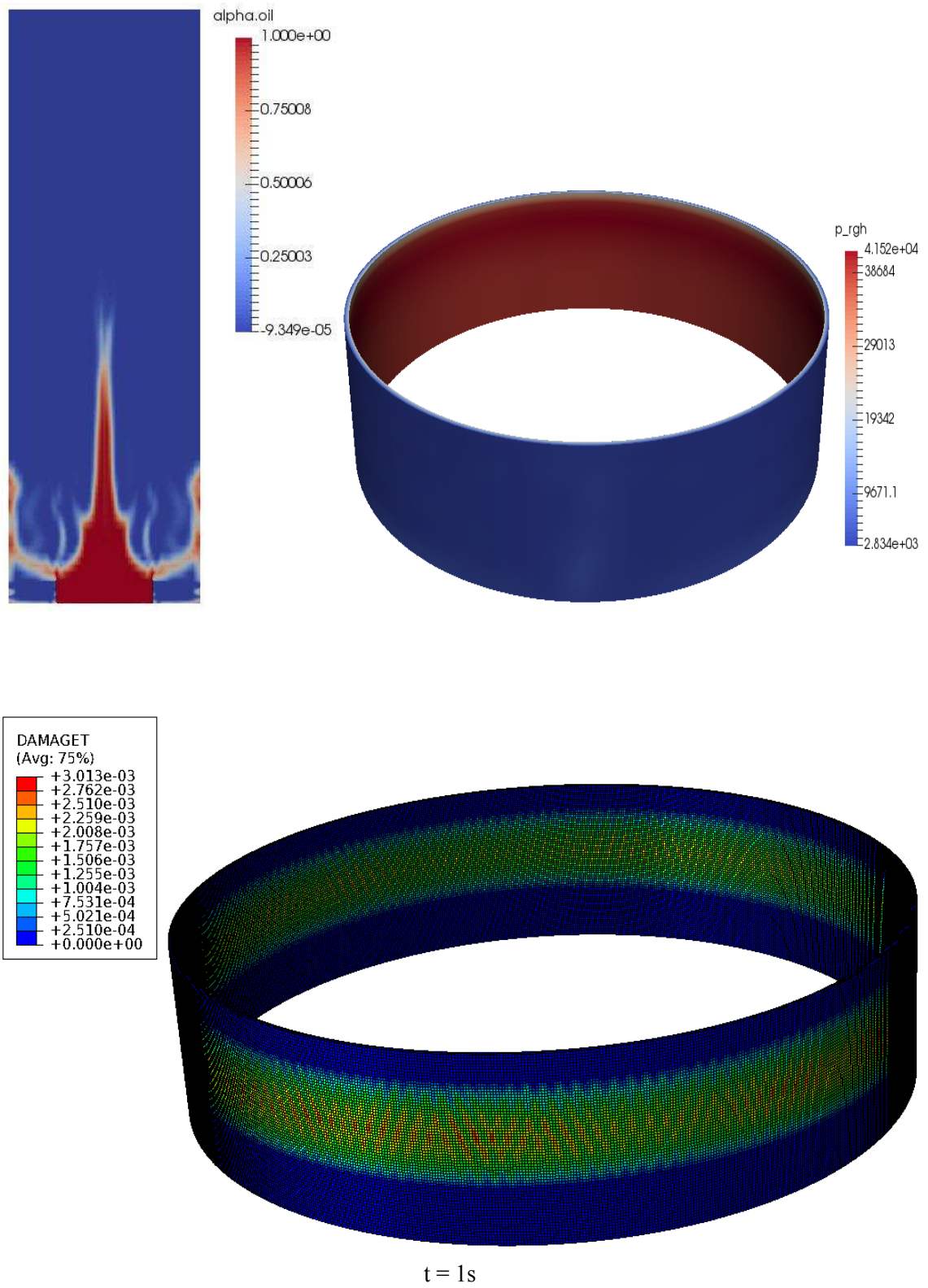


Figure 6.9: Flow behaviour and tensile damage of a plain concrete circular wall subjected to a centred load at  $t = 1s$

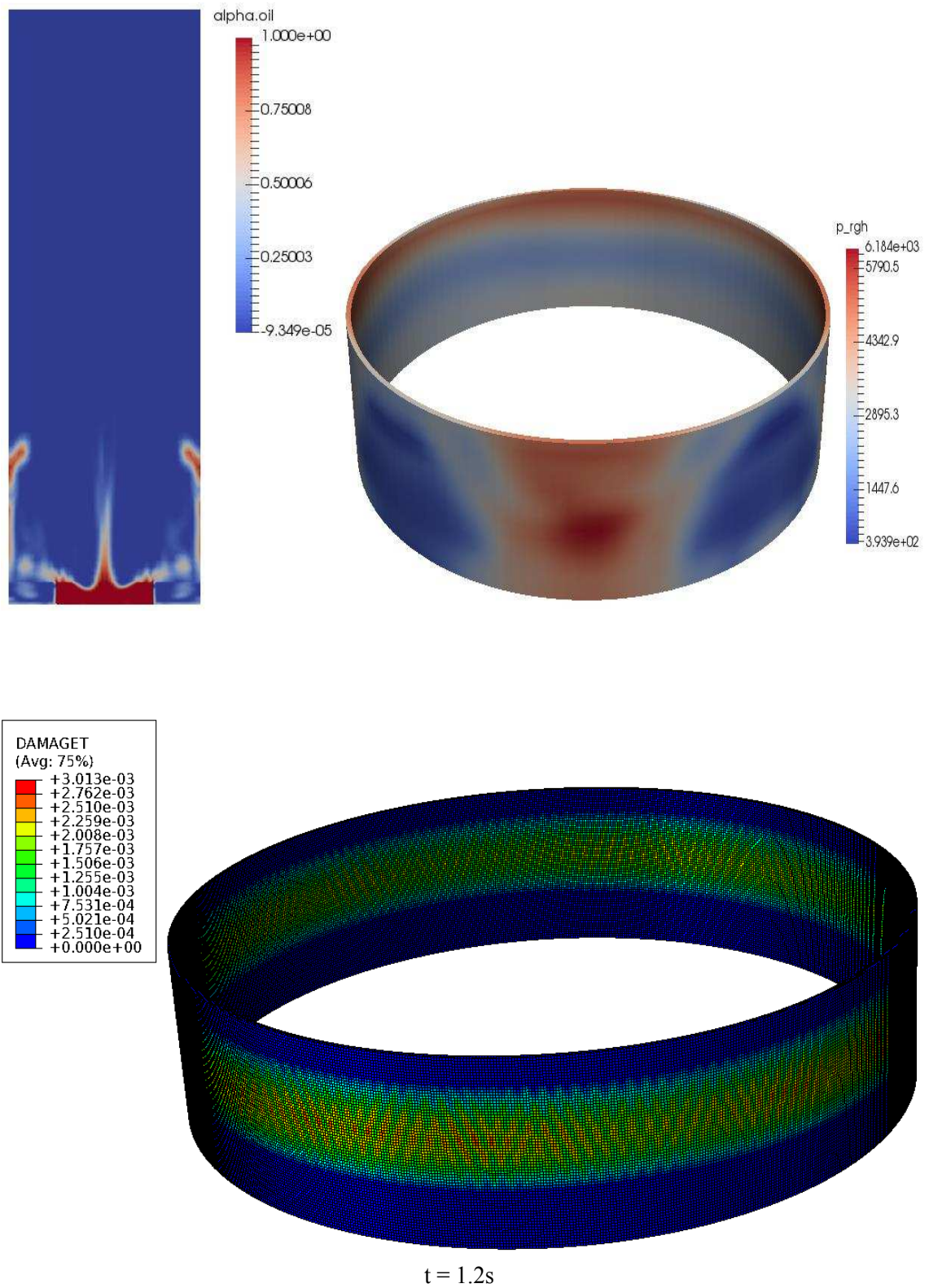


Figure 6.10: Flow behaviour and tensile damage of a plain concrete circular wall subjected to a centred load at  $t = 1.2s$

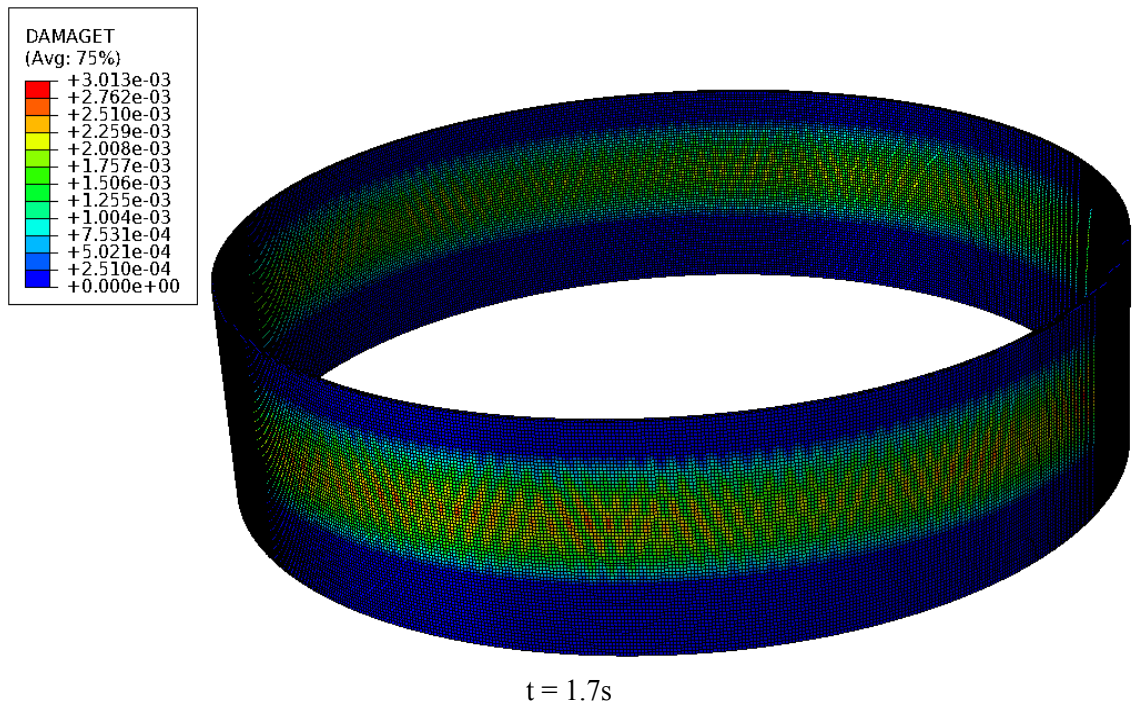
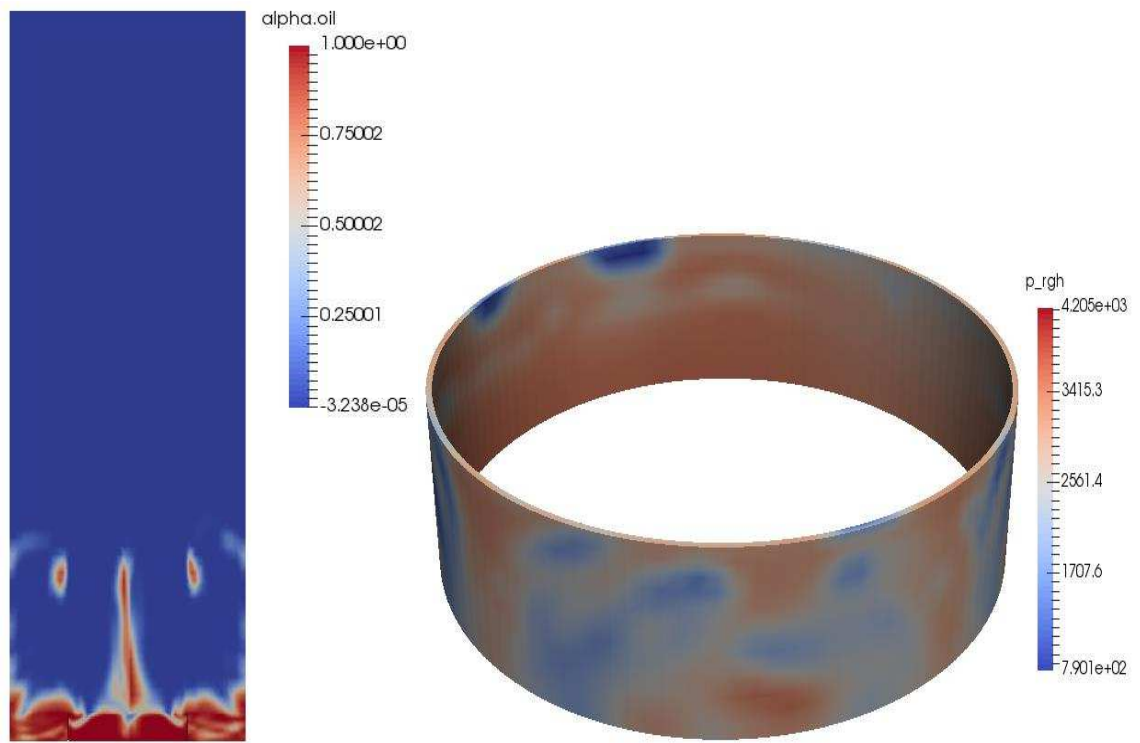


Figure 6.11: Flow behaviour and tensile damage of a plain concrete circular wall subjected to a centred load at  $t = 1.7s$

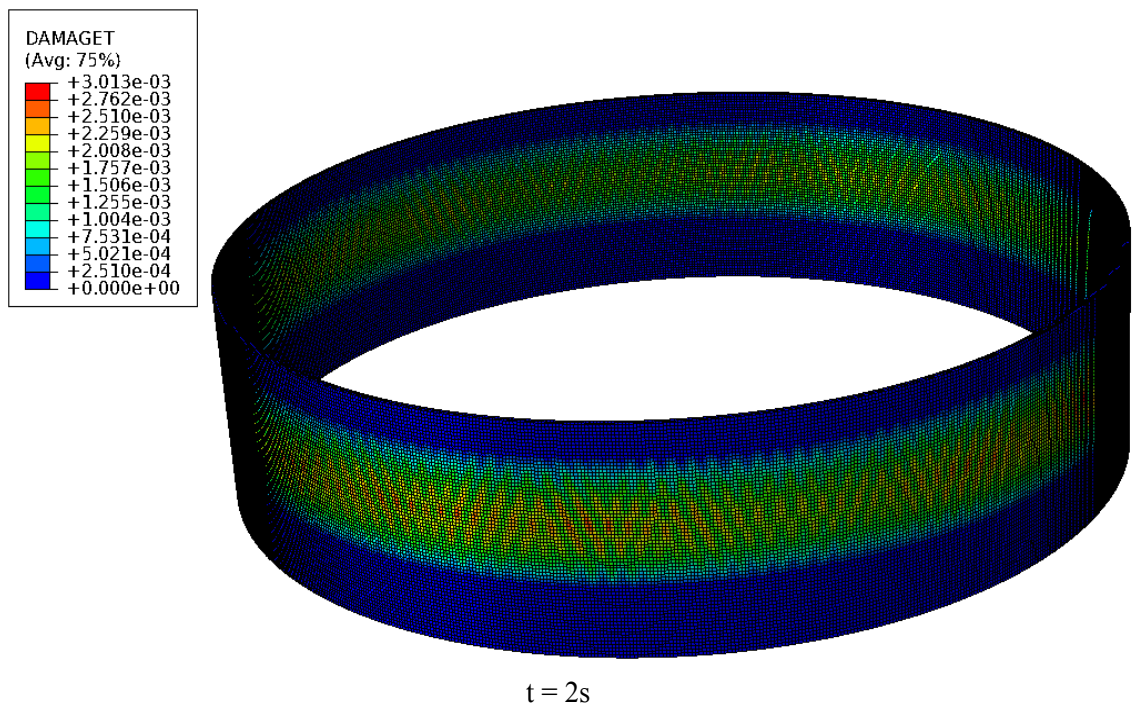
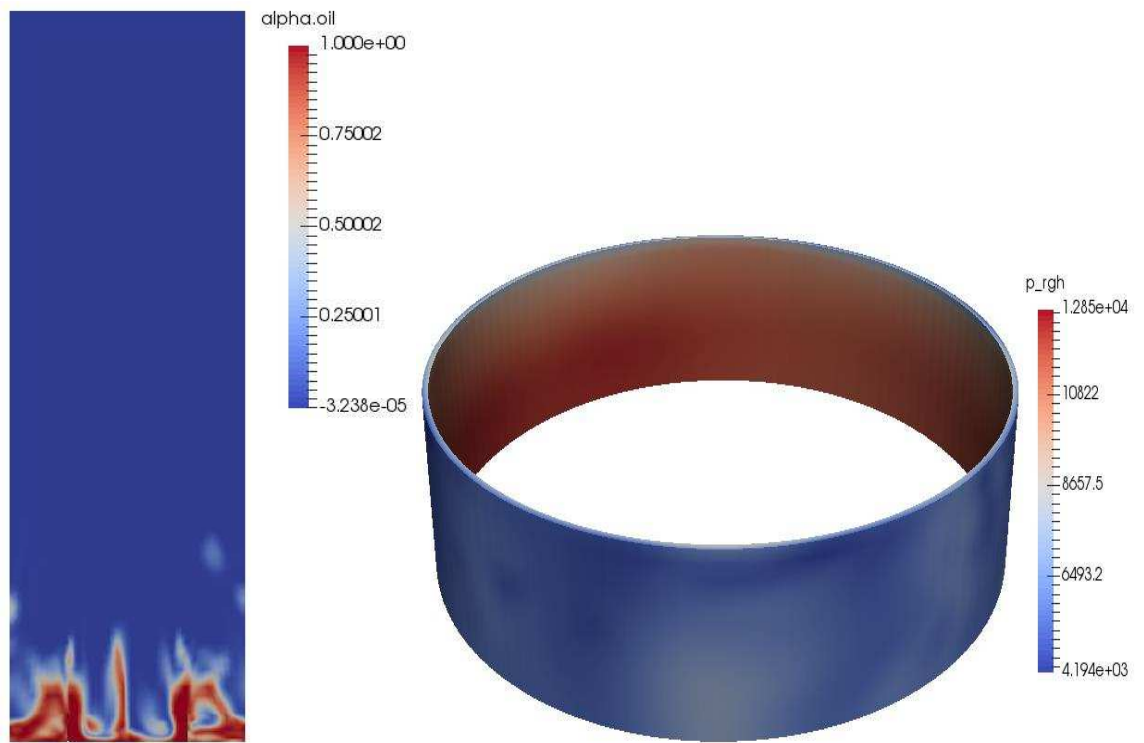


Figure 6.12: Flow behaviour and tensile damage of a plain concrete circular wall subjected to a centred load at  $t = 2s$

## Circular wall subjected to an off-centred load

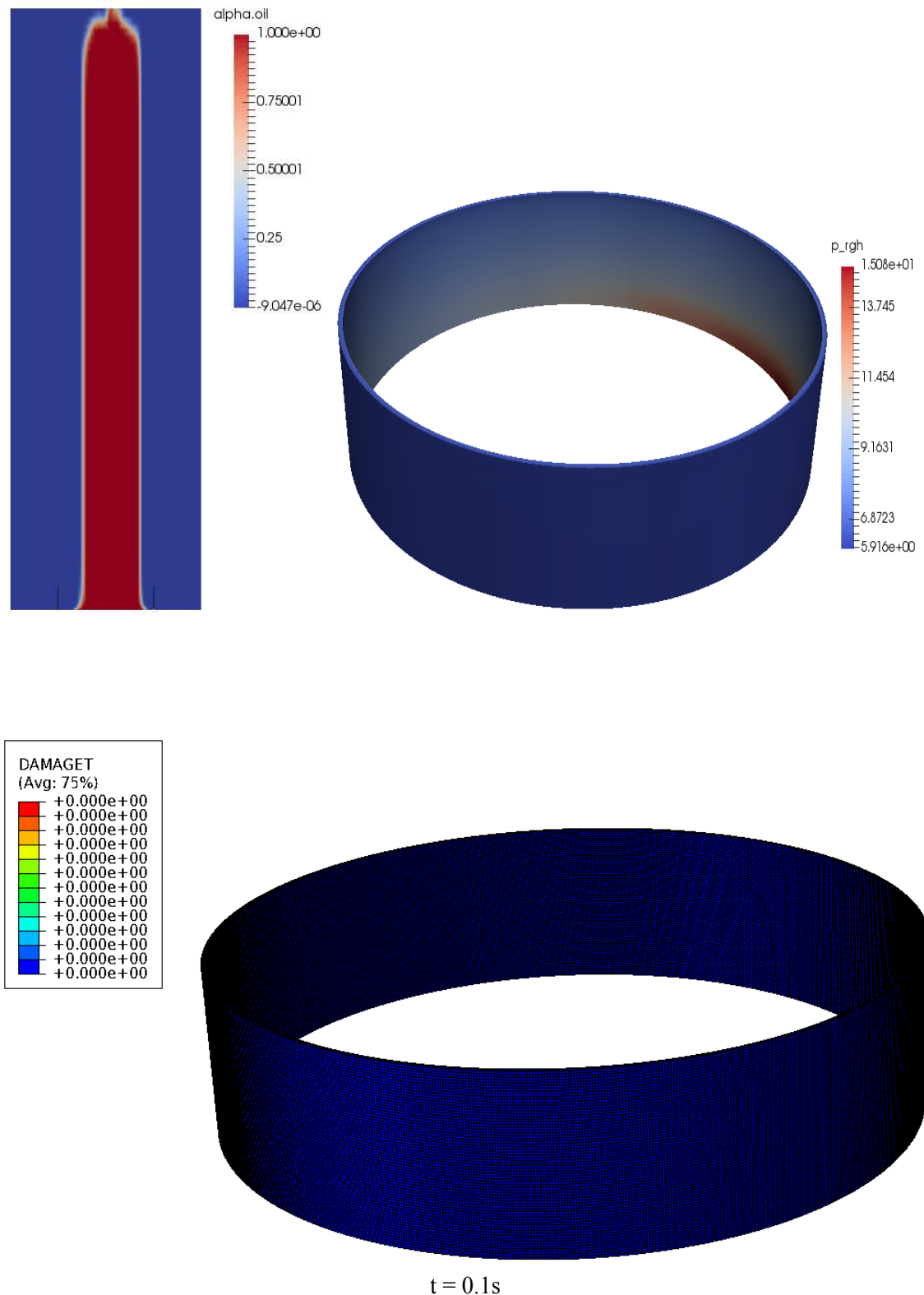


Figure 6.13: Flow behaviour and tensile damage of a plain concrete circular wall subjected to an off-centred load at  $t = 0.1s$

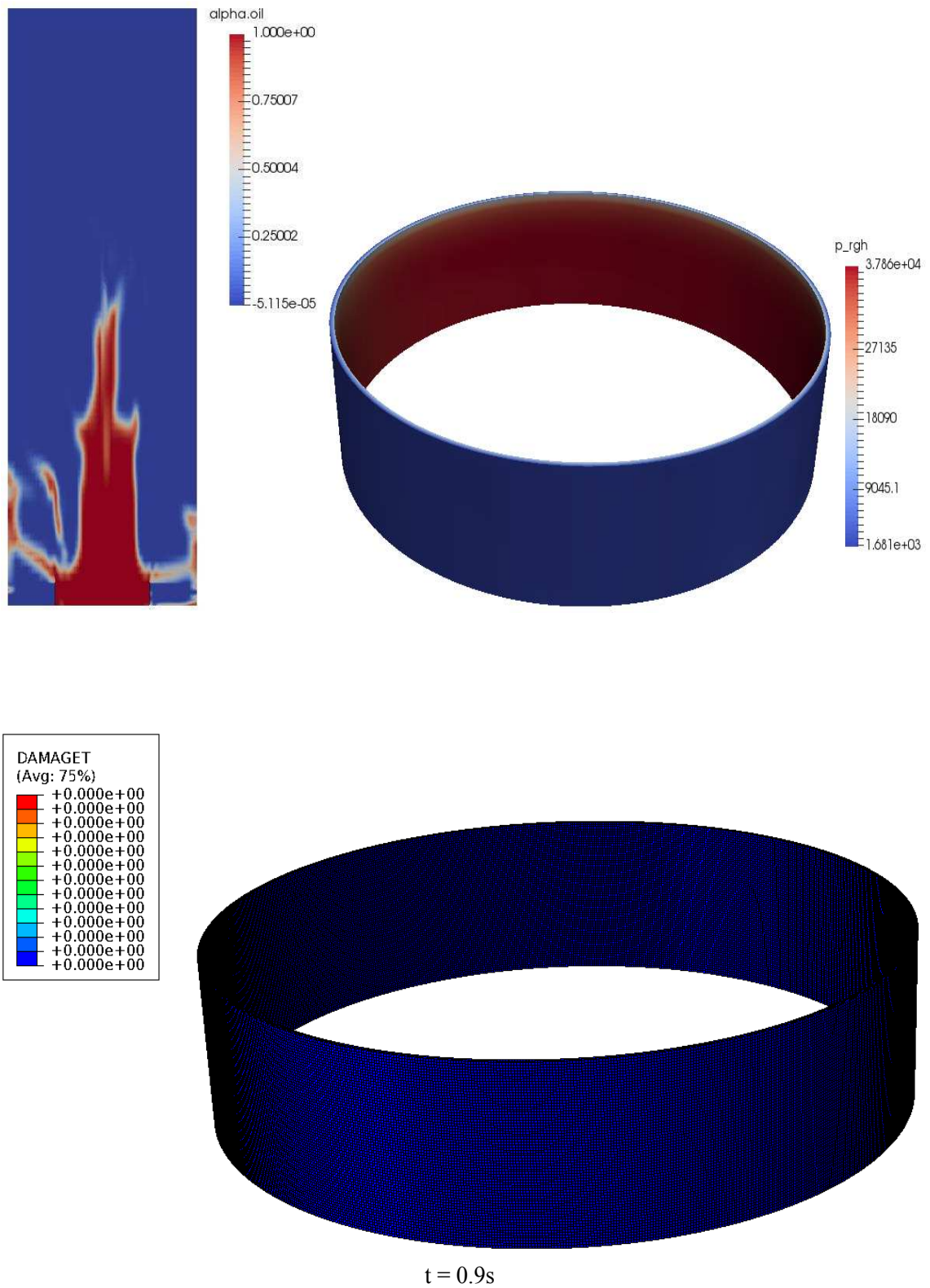


Figure 6.14: Flow behaviour and tensile damage of a plain concrete circular wall subjected to an off-centred load at  $t = 0.9s$

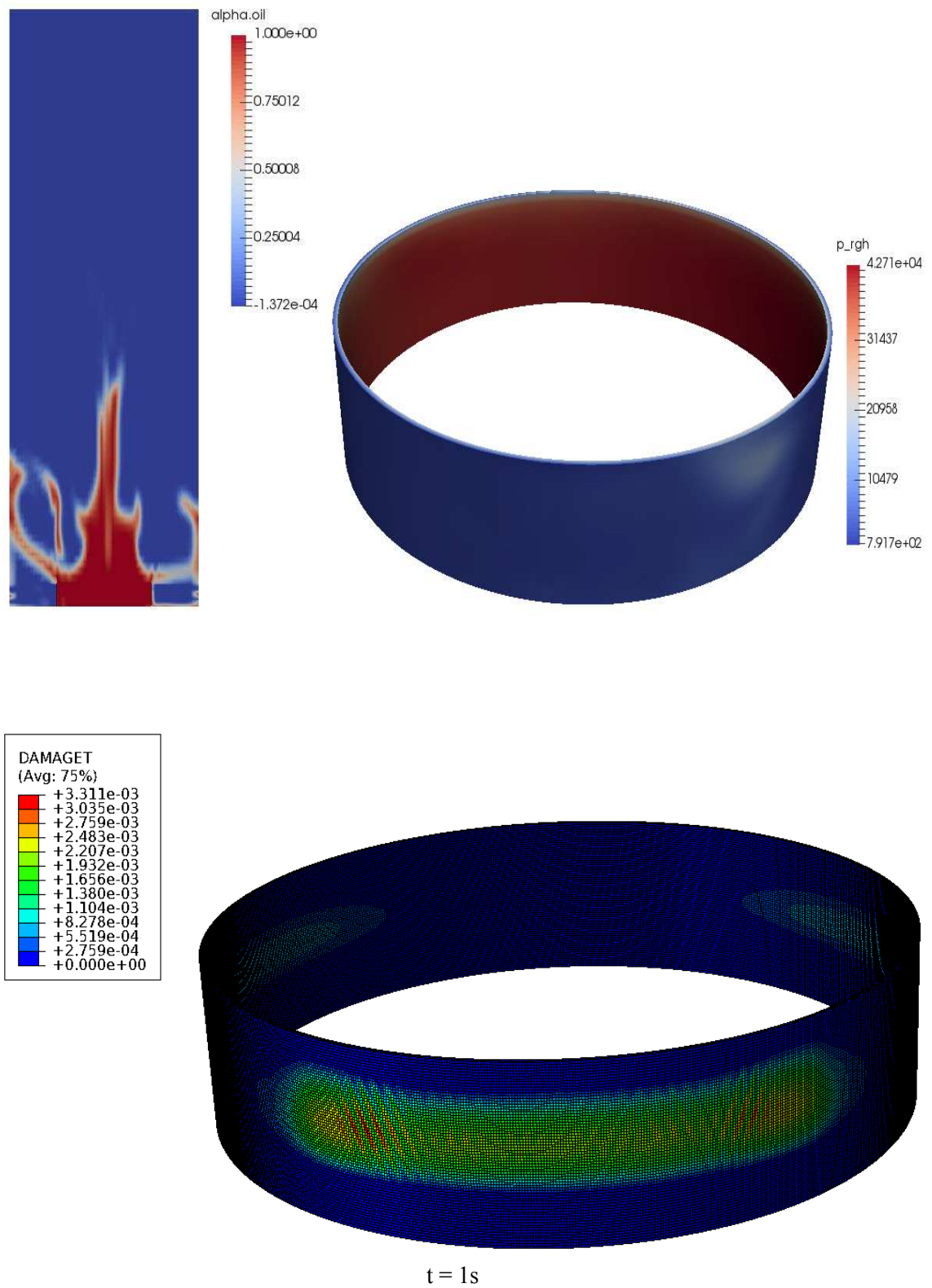


Figure 6.15: Flow behaviour and tensile damage of a plain concrete circular wall subjected to an off-centred load at  $t = 1s$

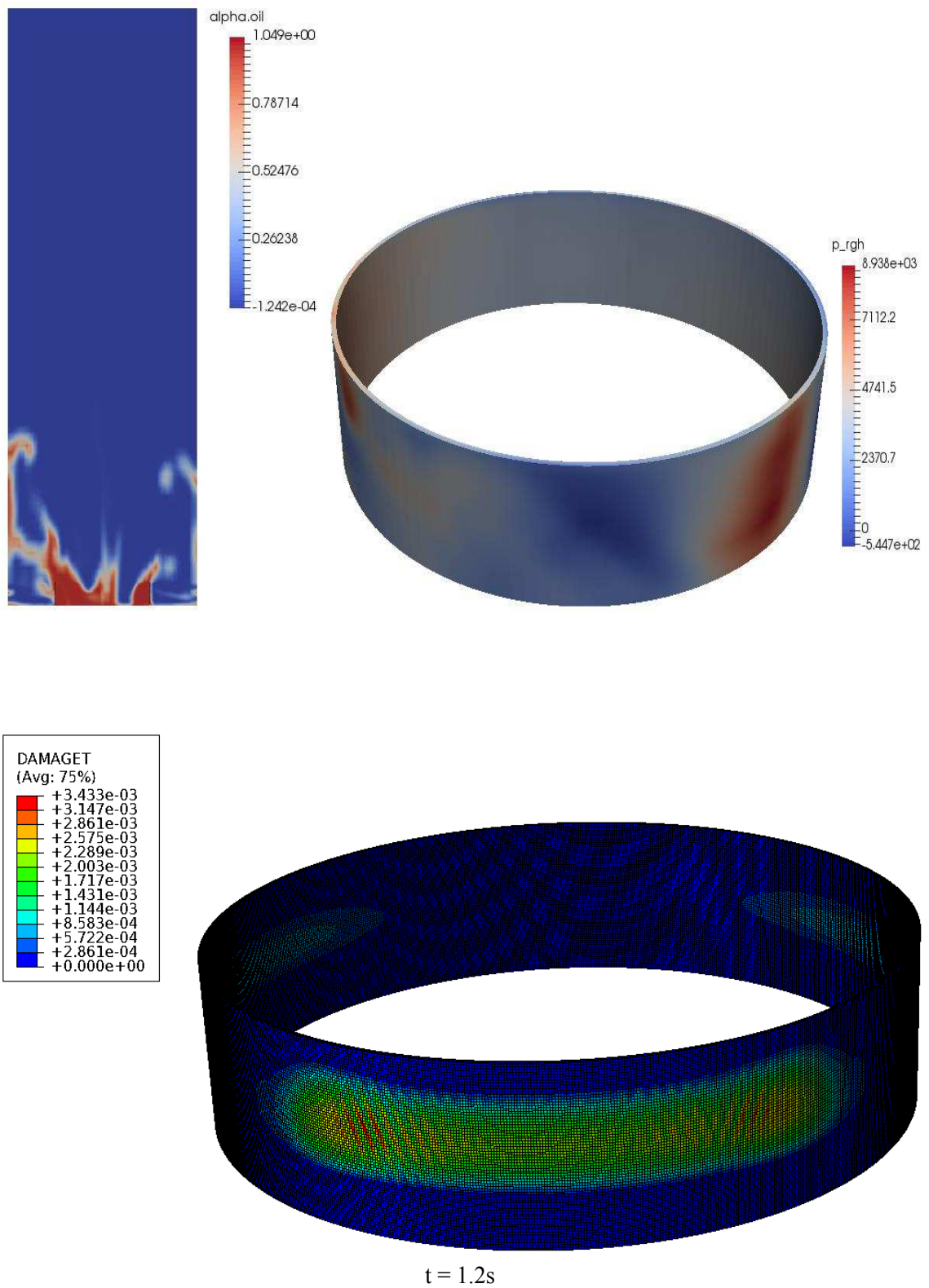


Figure 6.16: Flow behaviour and tensile damage of a plain concrete circular wall subjected to an off-centred load at  $t = 1.2s$

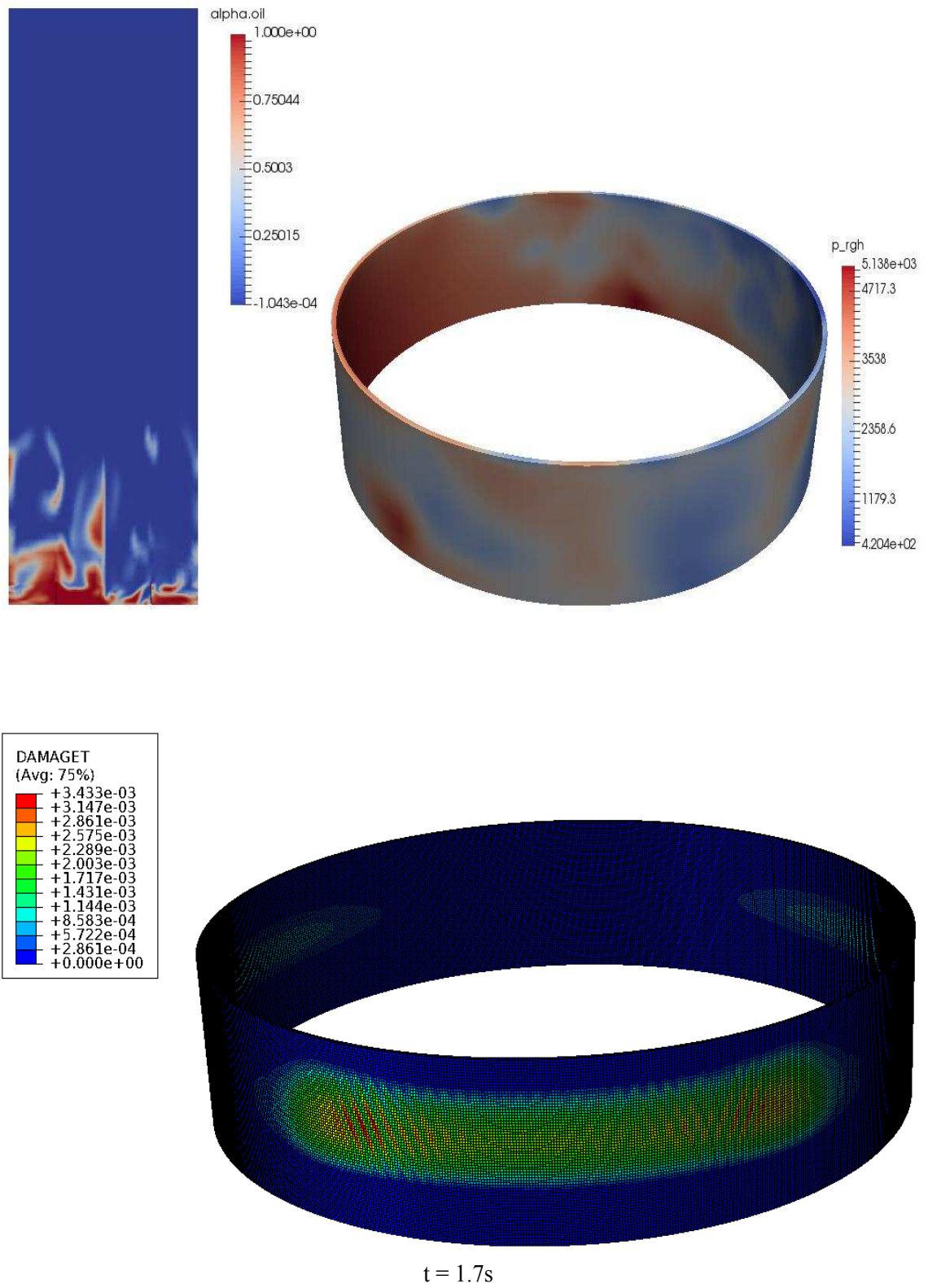


Figure 6.17: Flow behaviour and tensile damage of a plain concrete circular wall subjected to an off-centred load at  $t = 1.7s$

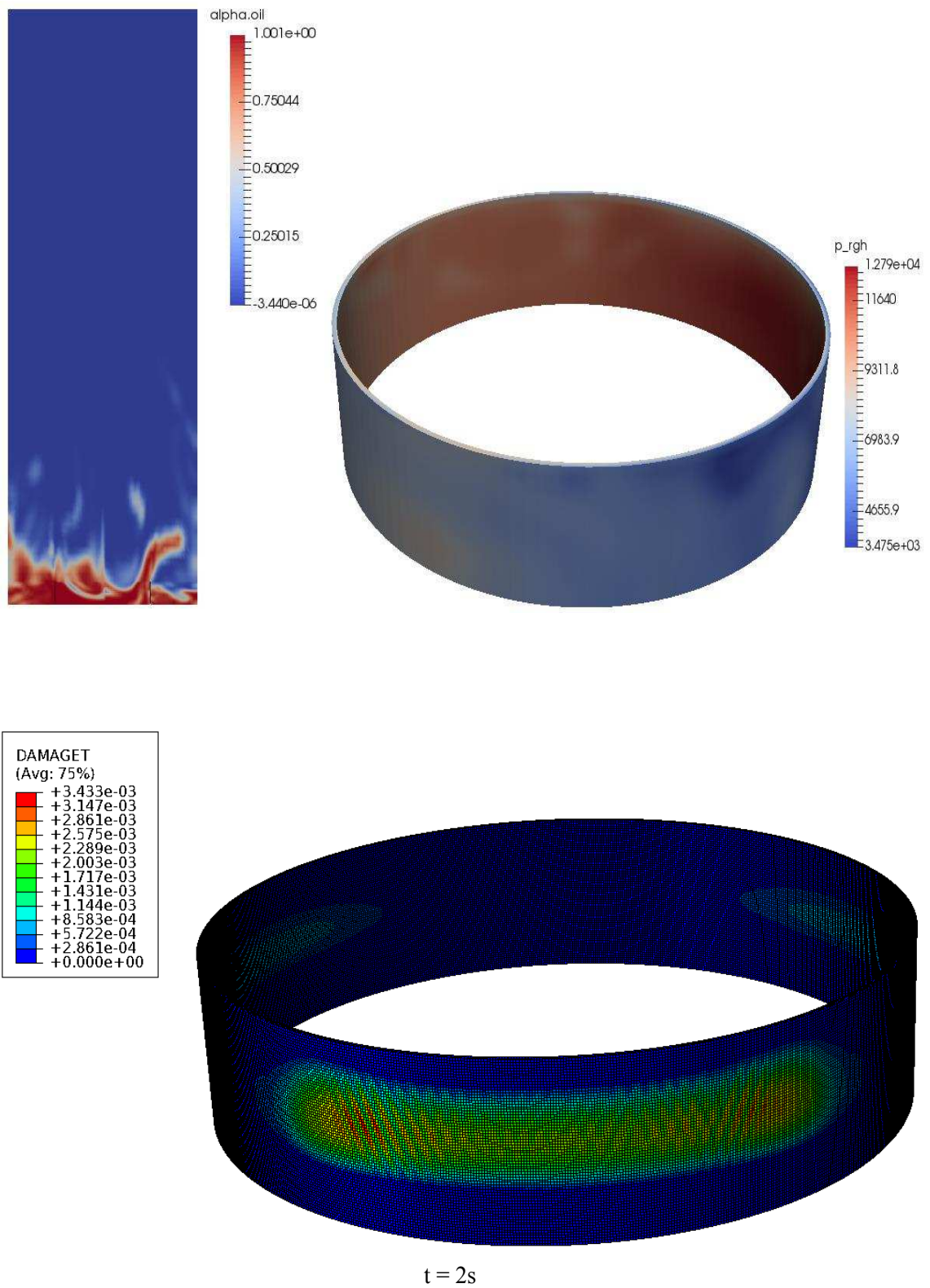


Figure 6.18: Flow behaviour and tensile damage of a plain concrete circular wall subjected to an off-centred load at  $t = 2s$

### 6.3.1.2 Comparison of the behaviour of a circular wall subjected to a centred and an off-centred loads

Figure 6.19 presents a comparison in the tensile damage corresponding to a circular wall subjected to a centred and an off-centred loads. The off-centred load causes more tensile damage than a centred load. This increase is only minor and equal to 14%, but can rise more significantly if the tank is closer to the wall.

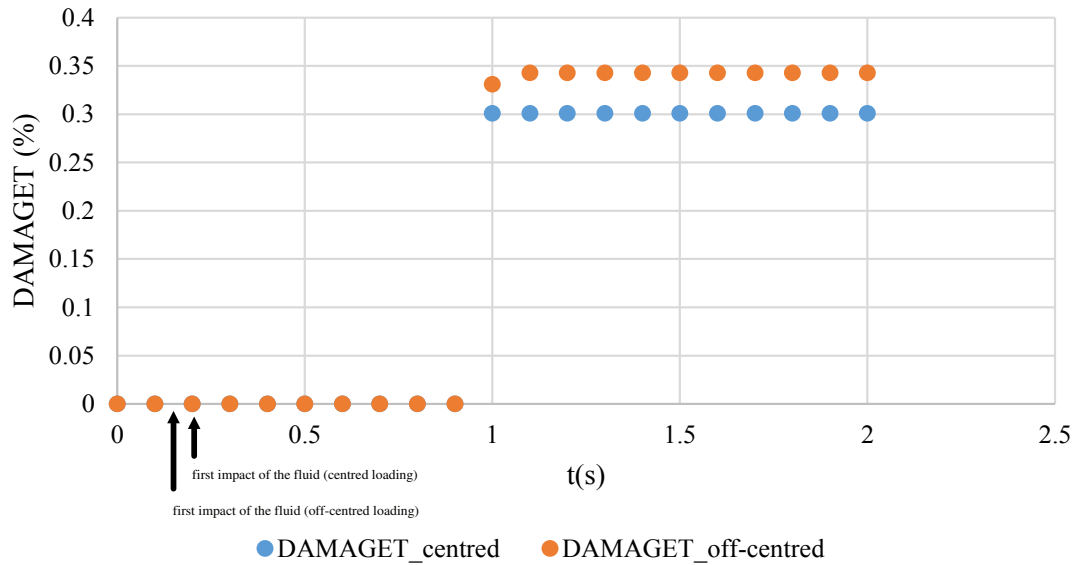


Figure 6.19: Comparison of the structural response of a plain concrete circular wall under a centred and an off-centred loads

### 6.3.1.3 Simulations results of the square wall

Figures 6.20, 6.21, 6.22, and 6.23 present the simulation results of a square wall made of plain concrete and subjected to a centred load. The damage appears first at  $t = 0.4s$  at the base of the four sides of the wall with a maximum value of 1.43%, then increases quickly towards the corners until a complete failure occurs corresponding to 99% of tensile damage at 0.653s. Figures 6.24, 6.25, 6.26 and 6.27 present the structural response of a square bund wall subjected to an off-centred load. More tensile damage occurs in the side of the wall closest to the tank. Similarly to the previous case, cracks represented in terms of tensile damage propagate to the corners of the wall until a complete failure occurs at 0.6393s.

## Square wall subjected to a centred load

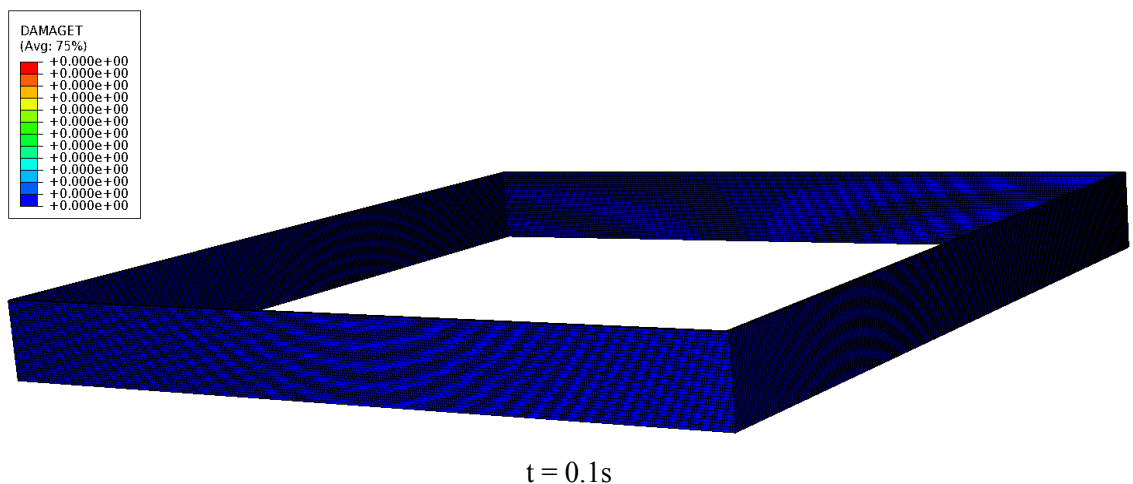
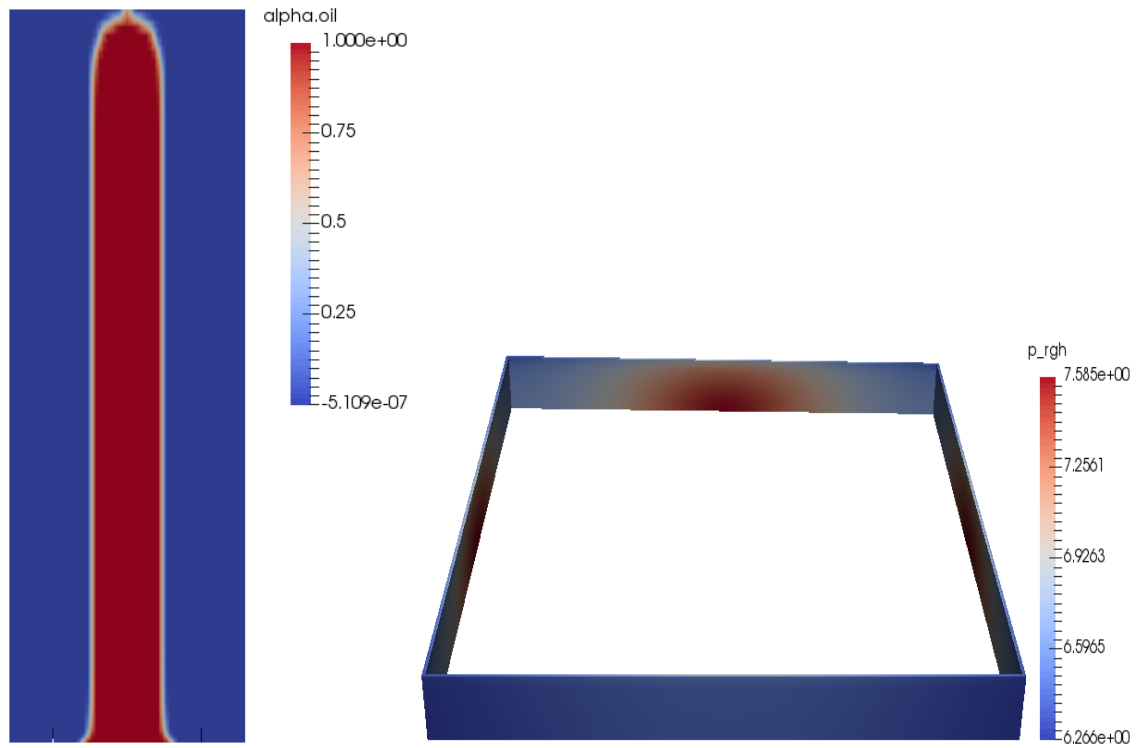


Figure 6.20: Flow behaviour and tensile damage of a plain concrete square wall subjected to a centred load at  $t = 0.1s$

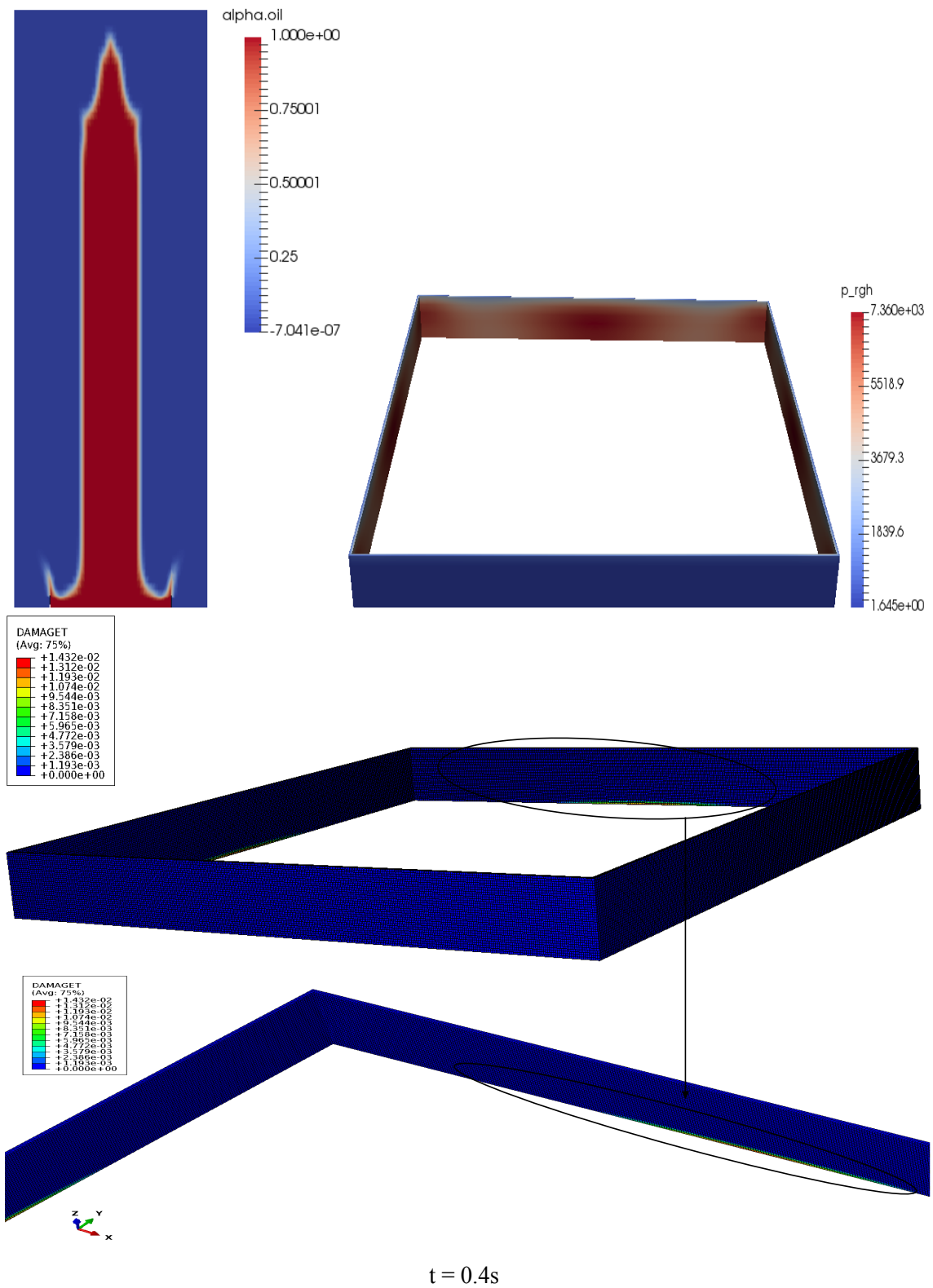


Figure 6.21: Flow behaviour and tensile damage of a plain concrete square wall subjected to a centred load at  $t = 0.4s$

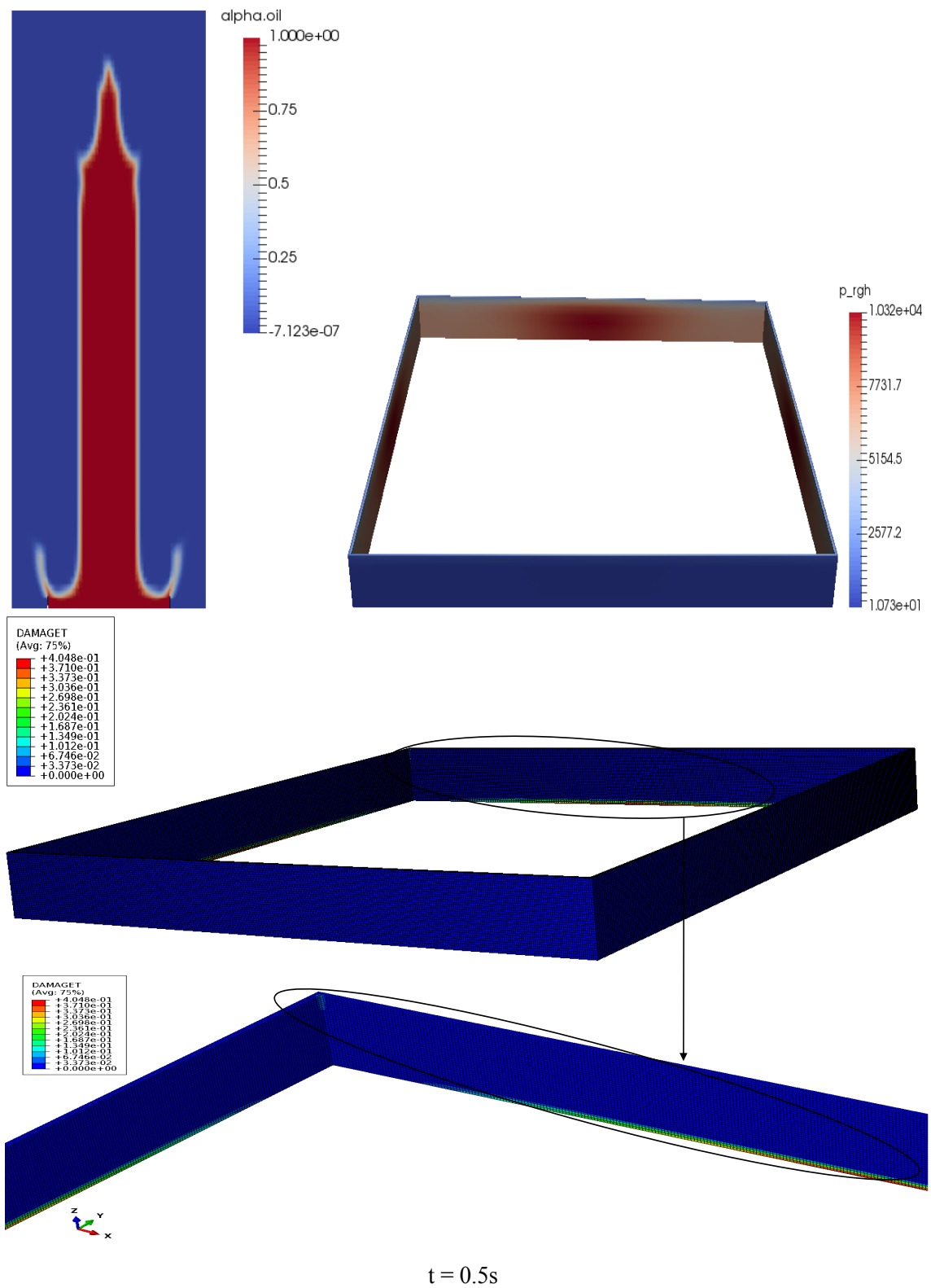


Figure 6.22: Flow behaviour and tensile damage of a plain concrete square wall subjected to a centred load at  $t = 0.5s$

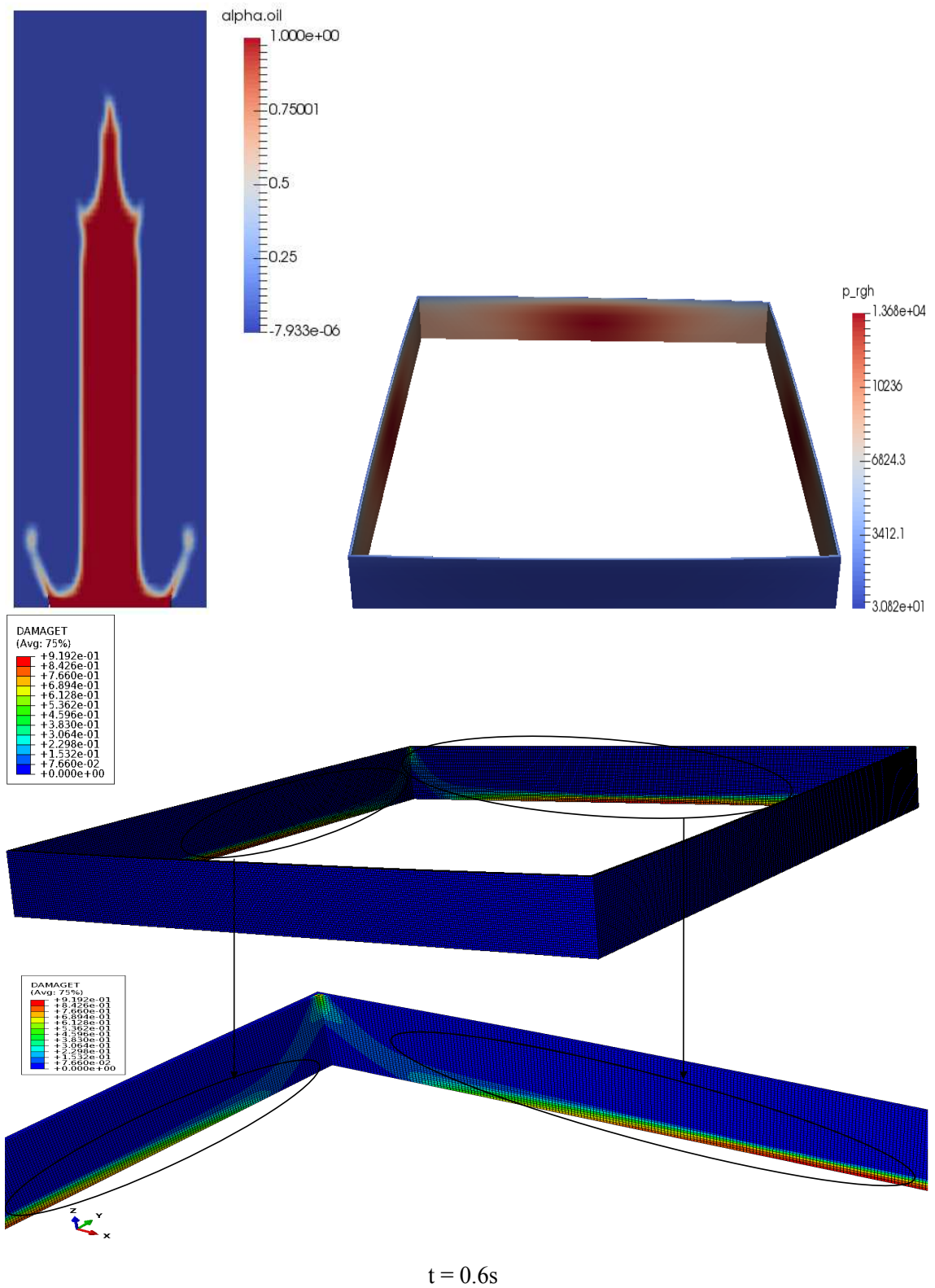


Figure 6.23: Flow behaviour and tensile damage of a plain concrete square wall subjected to a centred load at  $t = 0.6s$

## Square wall subjected to an off-centred load

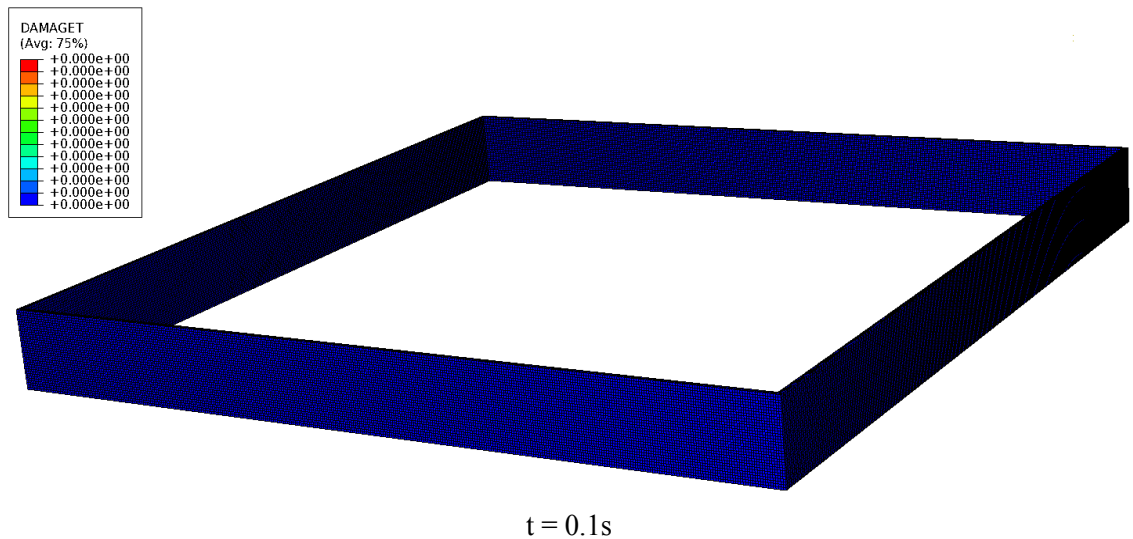
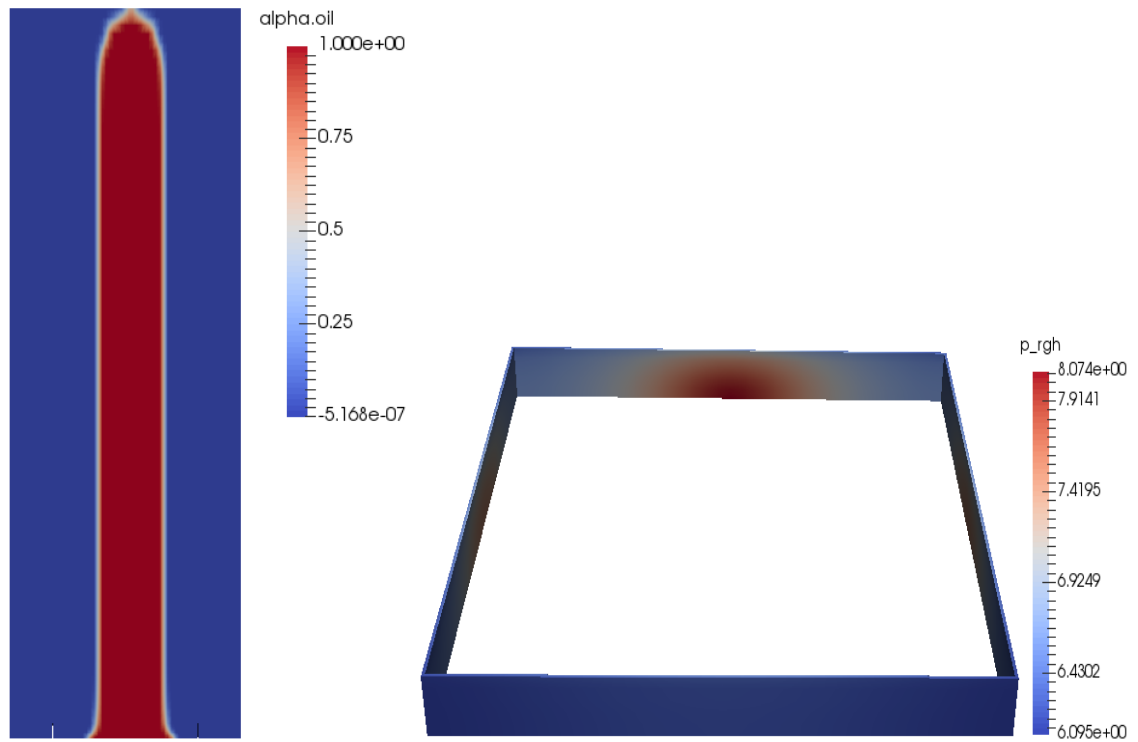


Figure 6.24: Flow behaviour and tensile damage of a plain concrete square wall subjected to an off-centred load at  $t = 0.1s$

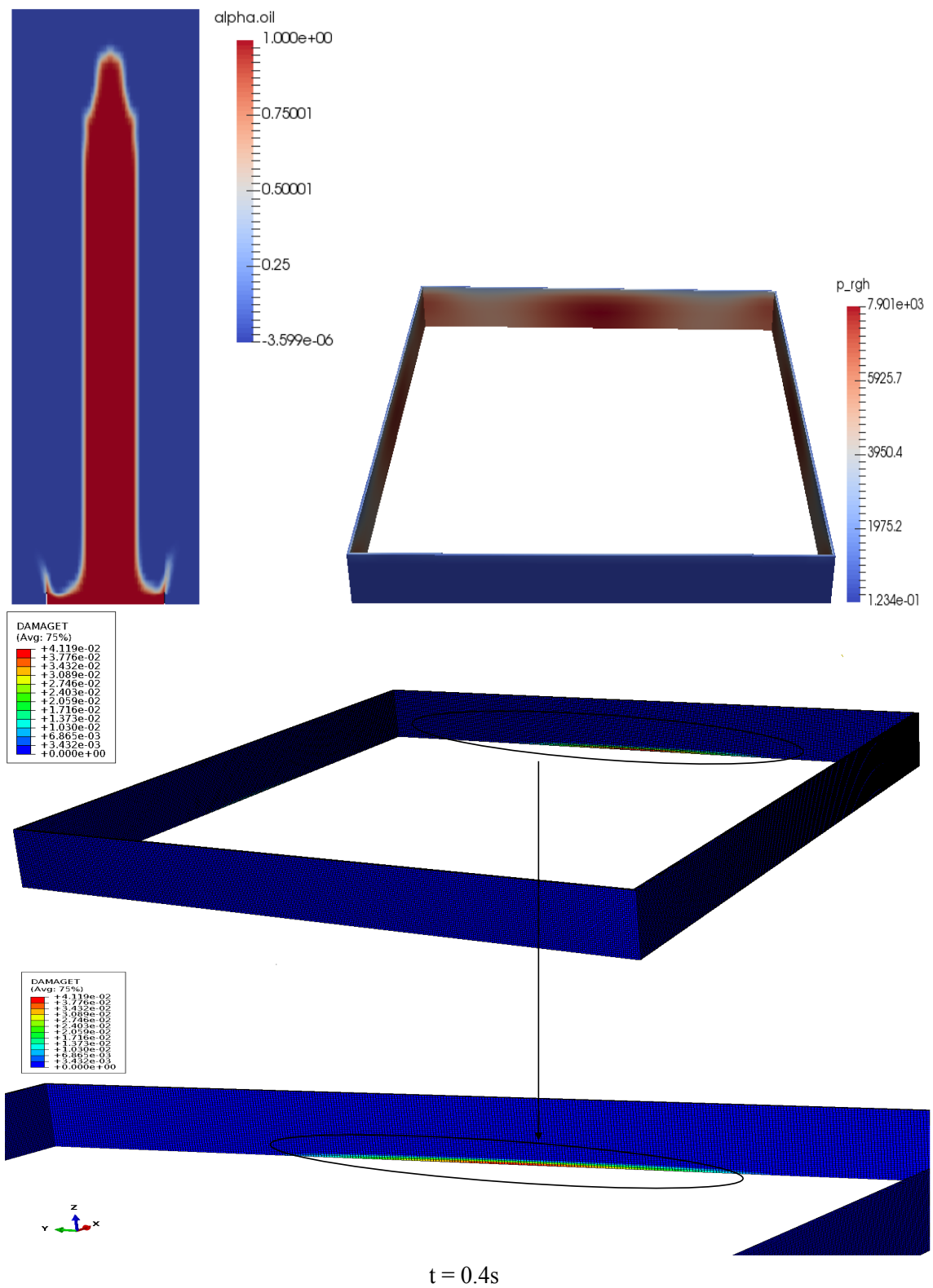


Figure 6.25: Flow behaviour and tensile damage of a plain concrete square wall subjected to an off-centred load at  $t = 0.4s$

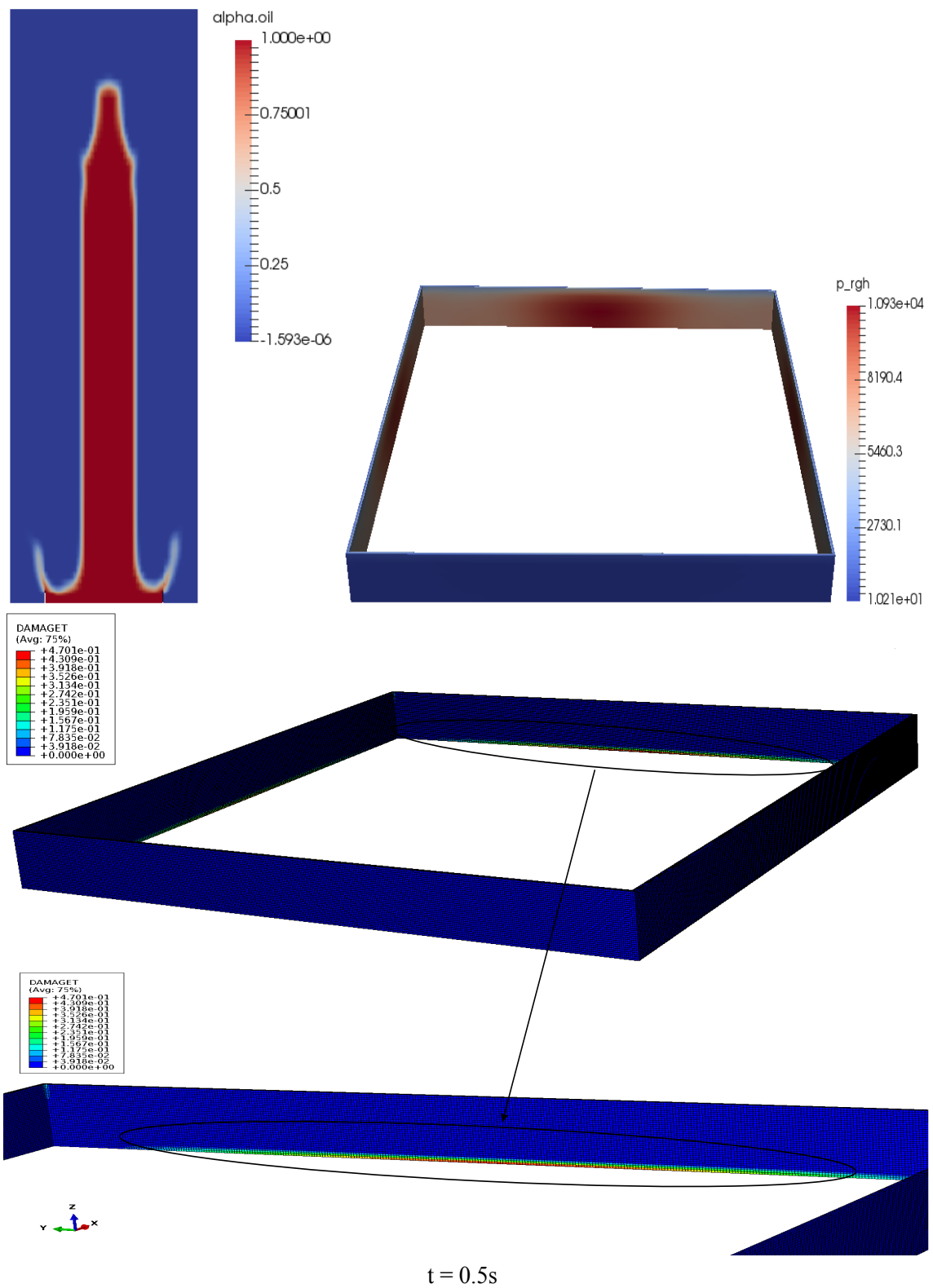


Figure 6.26: Flow behaviour and tensile damage of a plain concrete square wall subjected to an off-centred load at  $t = 0.5s$

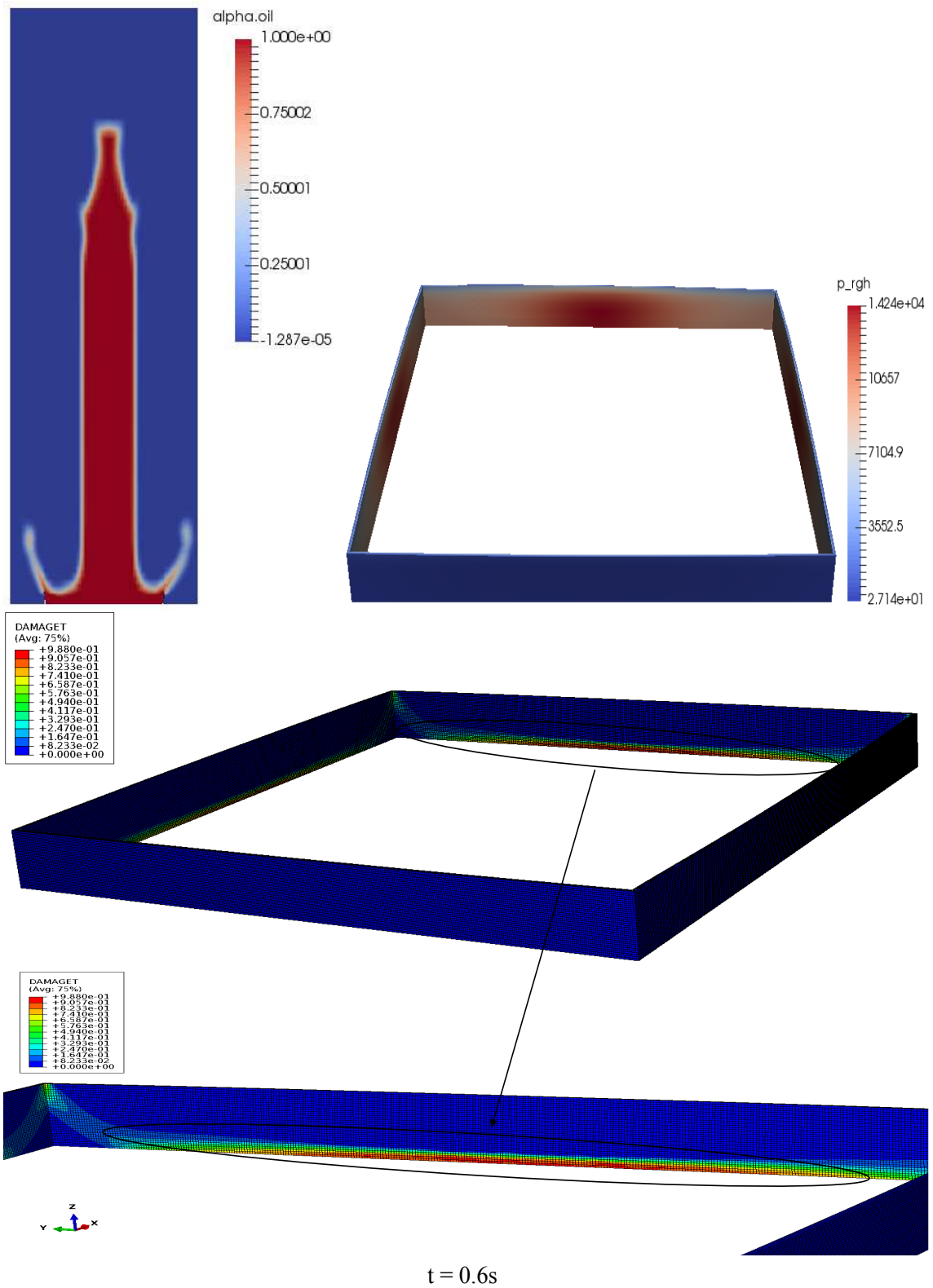


Figure 6.27: Flow behaviour and tensile damage of a plain concrete square wall subjected to an off-centred load at  $t = 0.6s$

### 6.3.1.4 Comparison of the behaviour of a square wall subjected to a centred and an off-centred loads

Figure 6.28 shows a comparison in the tensile damage corresponding to a square bund wall subjected to a centred and an off-centred loads. Similar to the circular wall, an off-centred load causes a slightly higher tensile damage than a centred load as well as an earlier failure of the wall. This can be attributed to the fact that only one side is subjected to the initial impact, which makes it act as a flat wall while the other sides do not contribute to withstanding the applied pressure. By the time the fluid hits the other sides, the side already impacted is getting subjected to more pressure than the three other sides. This non uniformity of the load distribution throughout the structure results in a wall of a reduced structural integrity. At  $t = 0.6s$ , the increase in the damage between the centred and the off-centred loads is equal to 7.78%. Even though the difference here is minor, the damage can increase more significantly with a greater magnitude of eccentricity of the load.

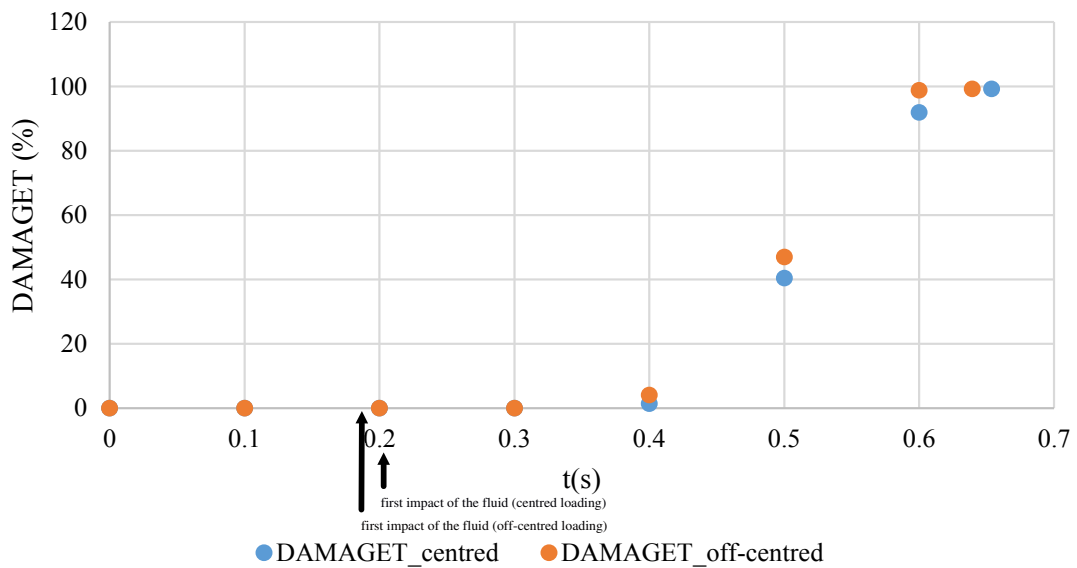


Figure 6.28: Comparison of the structural response of a plain concrete square wall under a centred and an off-centred loads

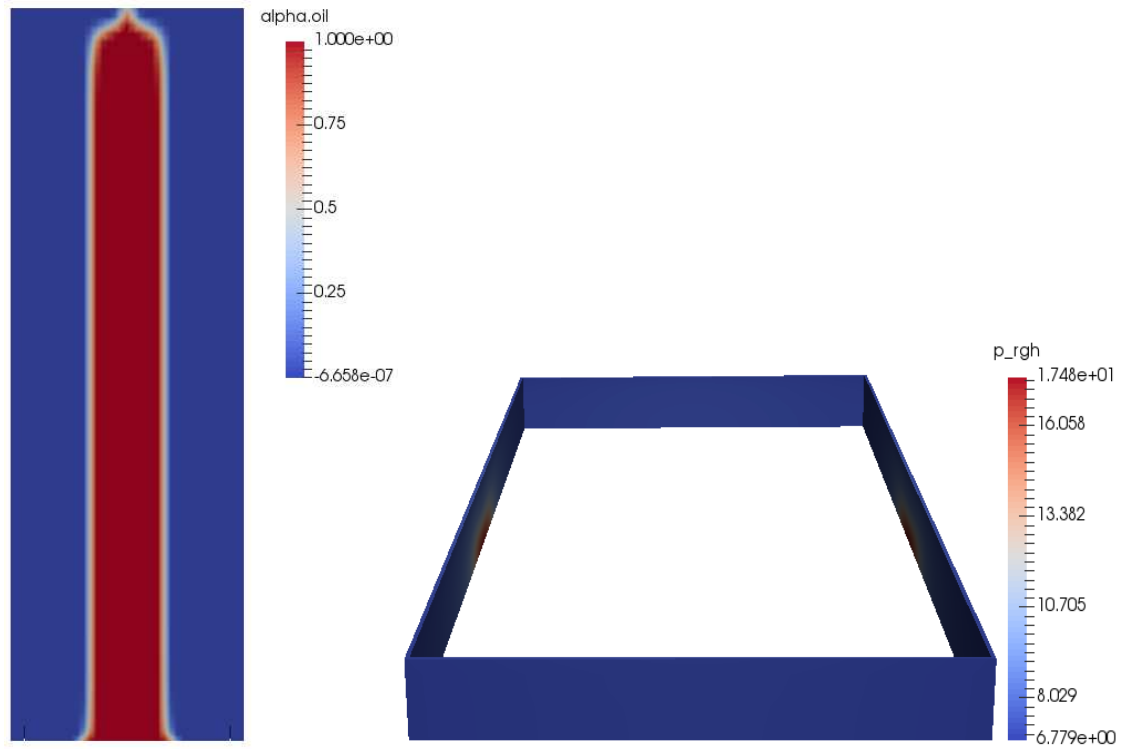
### 6.3.1.5 Simulation results of the rectangular wall

Figures 6.29, 6.30, 6.31, 6.32 and 6.33 present the simulation results corresponding to a rectangular wall subjected to a centred load. The fluid hits first at the longest sides of the bund wall, which are in this case the closest to the tank. The cracks appear first at  $t = 0.4\text{s}$  and propagate quickly towards the corners and the upper edges of the longest sides. The total failure occurs at  $t = 0.6074\text{s}$ .

Figures 6.34, 6.35, 6.36, 6.37 and 6.38 present the simulation results of a rectangular wall subjected to an off-centred load along the  $x$  axis. The side of the wall (A) depicted in Figure 6.34 sits closer to the wall. At  $t = 0.3\text{s}$ , very minor damage starts appearing through the side (A). The cracks start propagating until the wall fails completely at  $t = 0.5946\text{s}$ . It is clearly shown that the side (A) of the wall undergoes more deformations as indicated in Figure 6.38 because the load is not distributed equally between the two long sides of the wall. By the time the side opposite to (A) starts exhibiting damage, the side (A) has already undergone significant damage, which induces an earlier total failure of the wall.

Figures 6.39, 6.40, 6.41, 6.42 and 6.43 present the simulation results of a rectangular bund wall subjected to an off-centred load along the  $y$  axis. The load in this case is off-centred towards one of the two short sides of the wall denoted as side (B) as shown in Figure 6.39. Nevertheless, the longest sides still undergo the tensile damage because they are closer to the tank than the short sides. The crack pattern is similar to the case of a centred load, where both of the sides exhibit the same amount of damage as indicated in Figure 6.43. A total failure occurs at  $t = 0.619\text{s}$ .

## Rectangular wall subjected to a centred load



t = 0.1s

Figure 6.29: Flow behaviour and tensile damage of a plain concrete rectangular wall subjected to a centred load at t = 0.1s

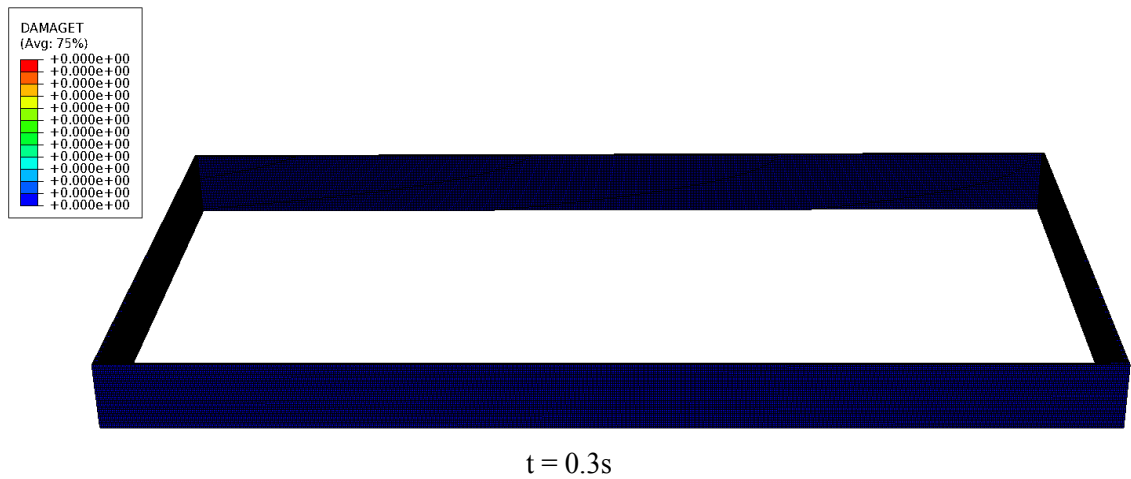
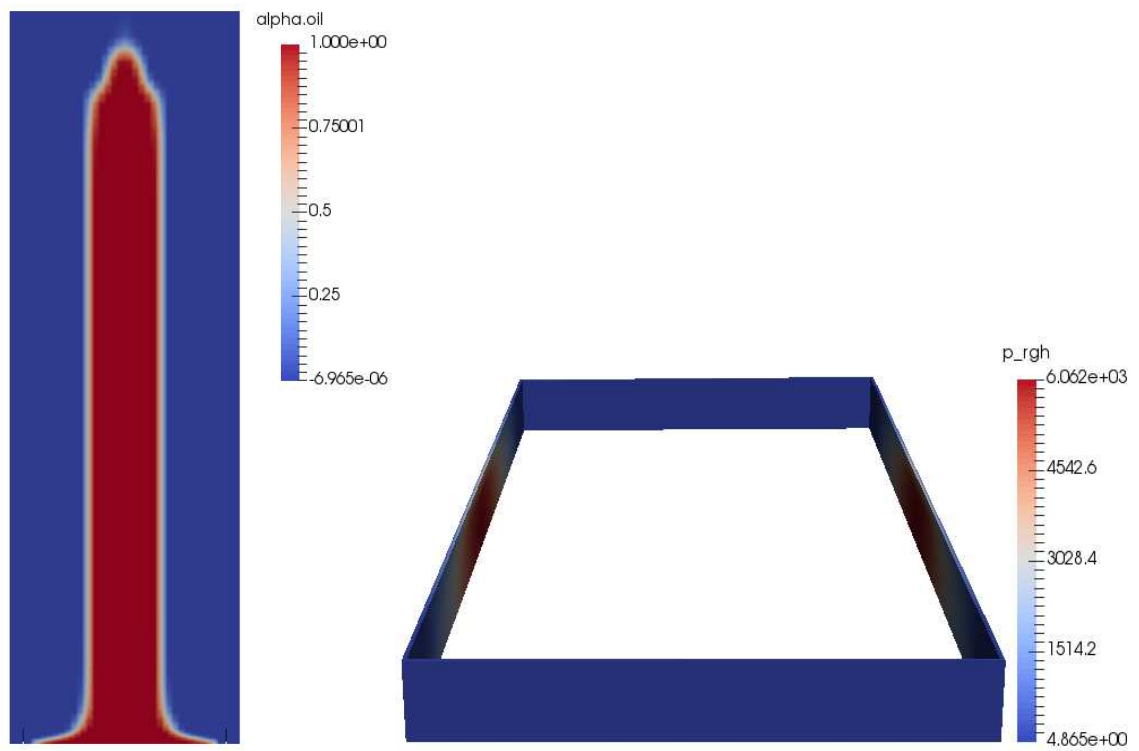


Figure 6.30: Flow behaviour and tensile damage of a plain concrete rectangular wall subjected to a centred load at  $t = 0.3s$

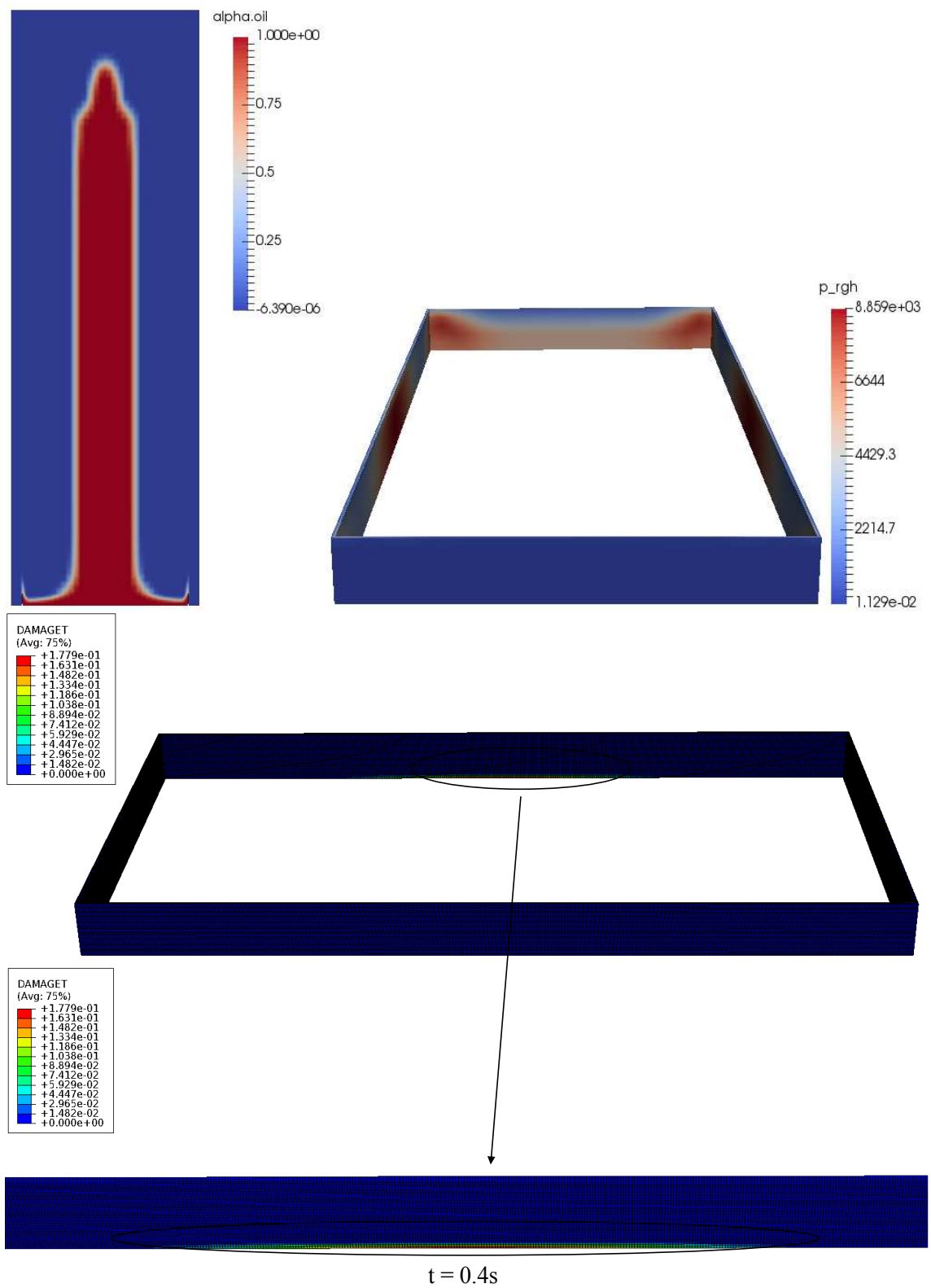


Figure 6.31: Flow behaviour and tensile damage of a plain concrete rectangular wall subjected to a centred load at  $t = 0.4s$

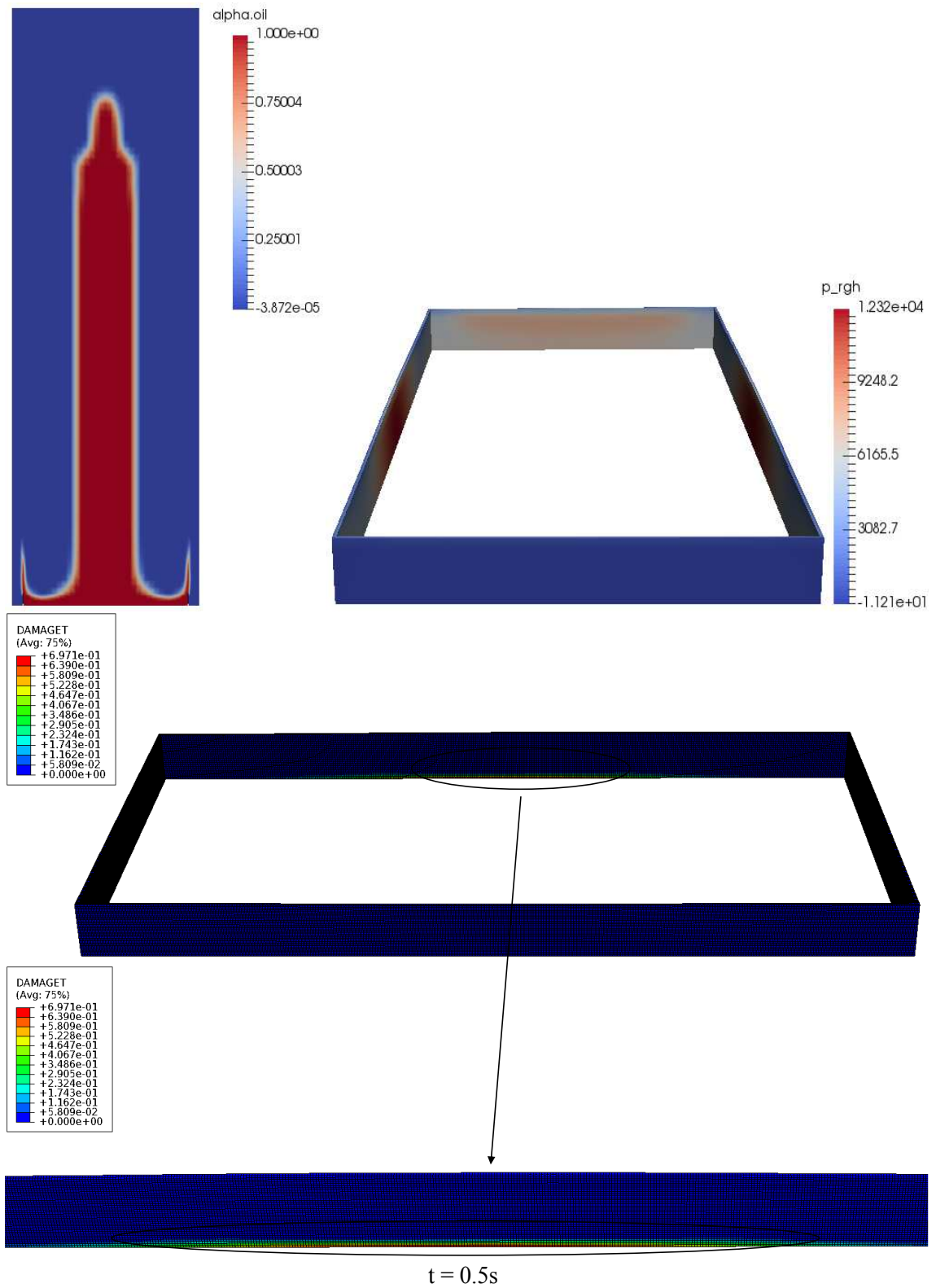


Figure 6.32: Flow behaviour and tensile damage of a plain concrete rectangular wall subjected to a centred load at  $t = 0.5s$

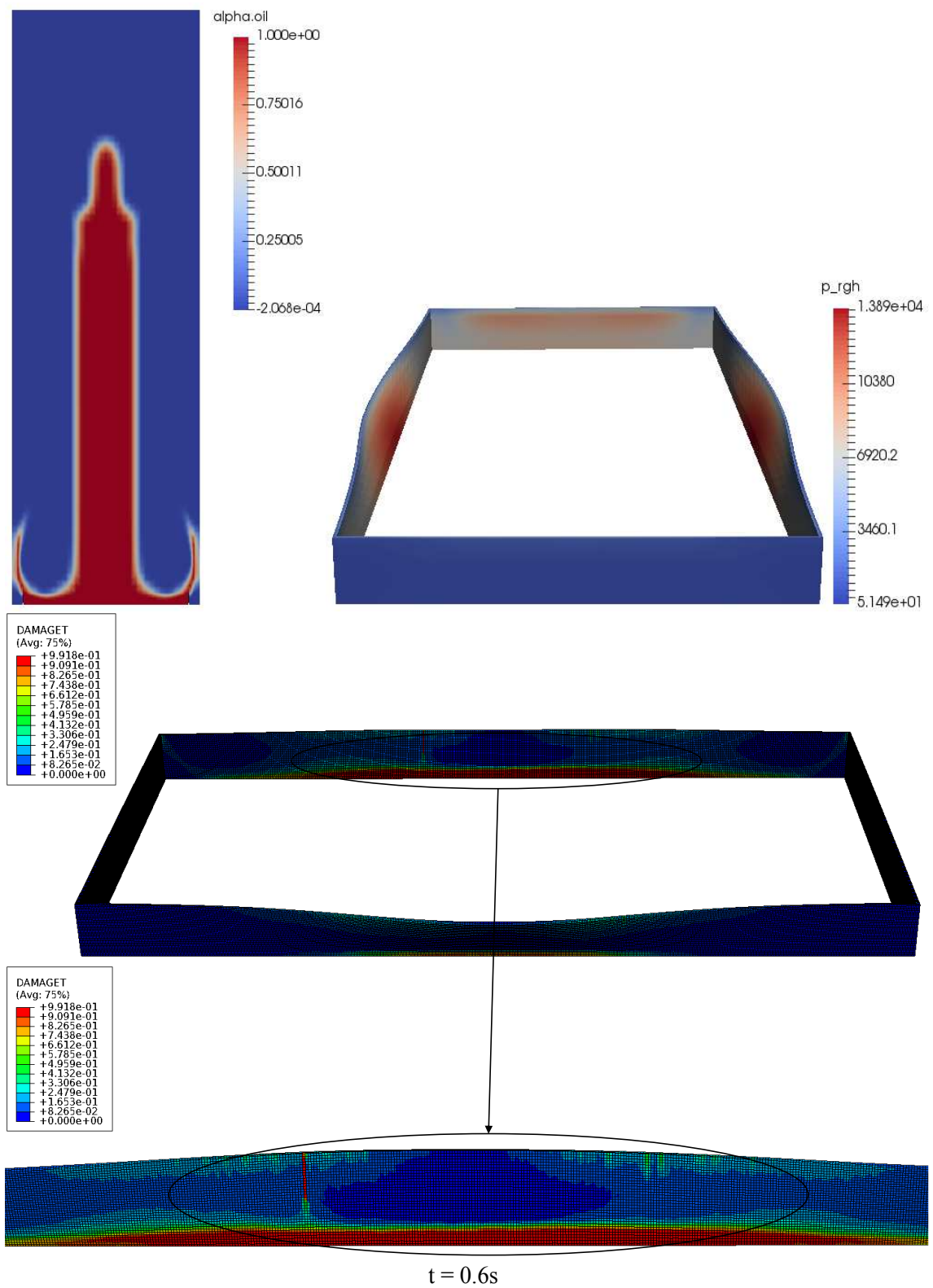


Figure 6.33: Flow behaviour and tensile damage of a plain concrete rectangular wall subjected to a centred load at  $t = 0.6s$

## Rectangular wall subjected to an off-centred load along the $x$ axis

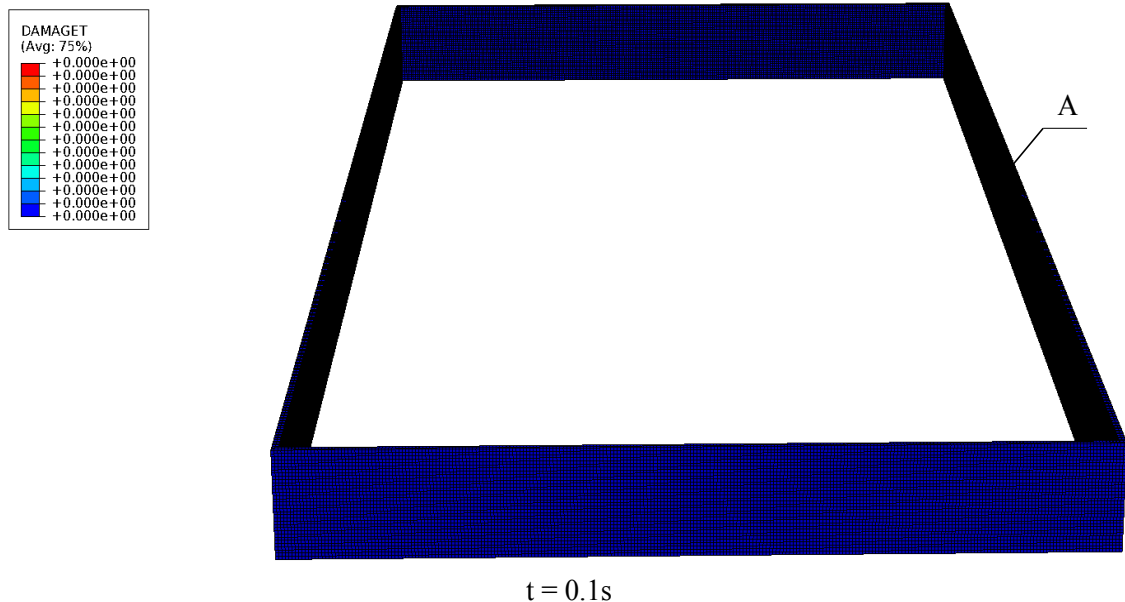
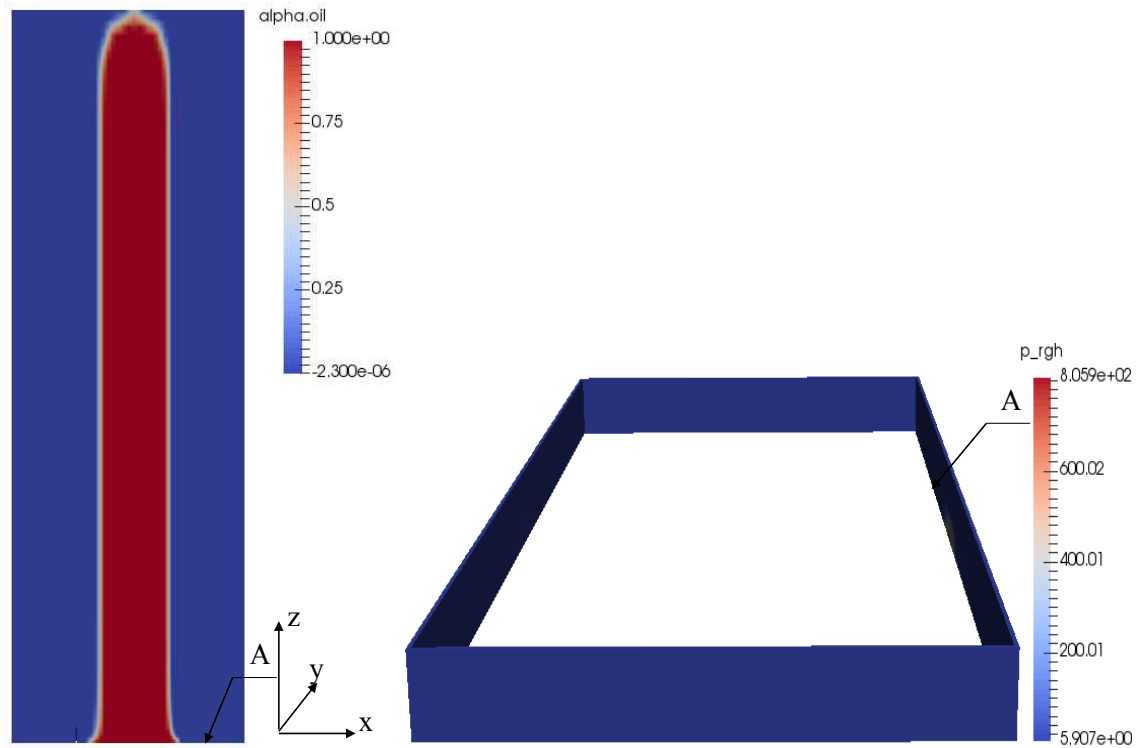


Figure 6.34: Flow behaviour and tensile damage of a plain concrete rectangular wall subjected to an off-centred load along the  $x$  axis at  $t = 0.1s$

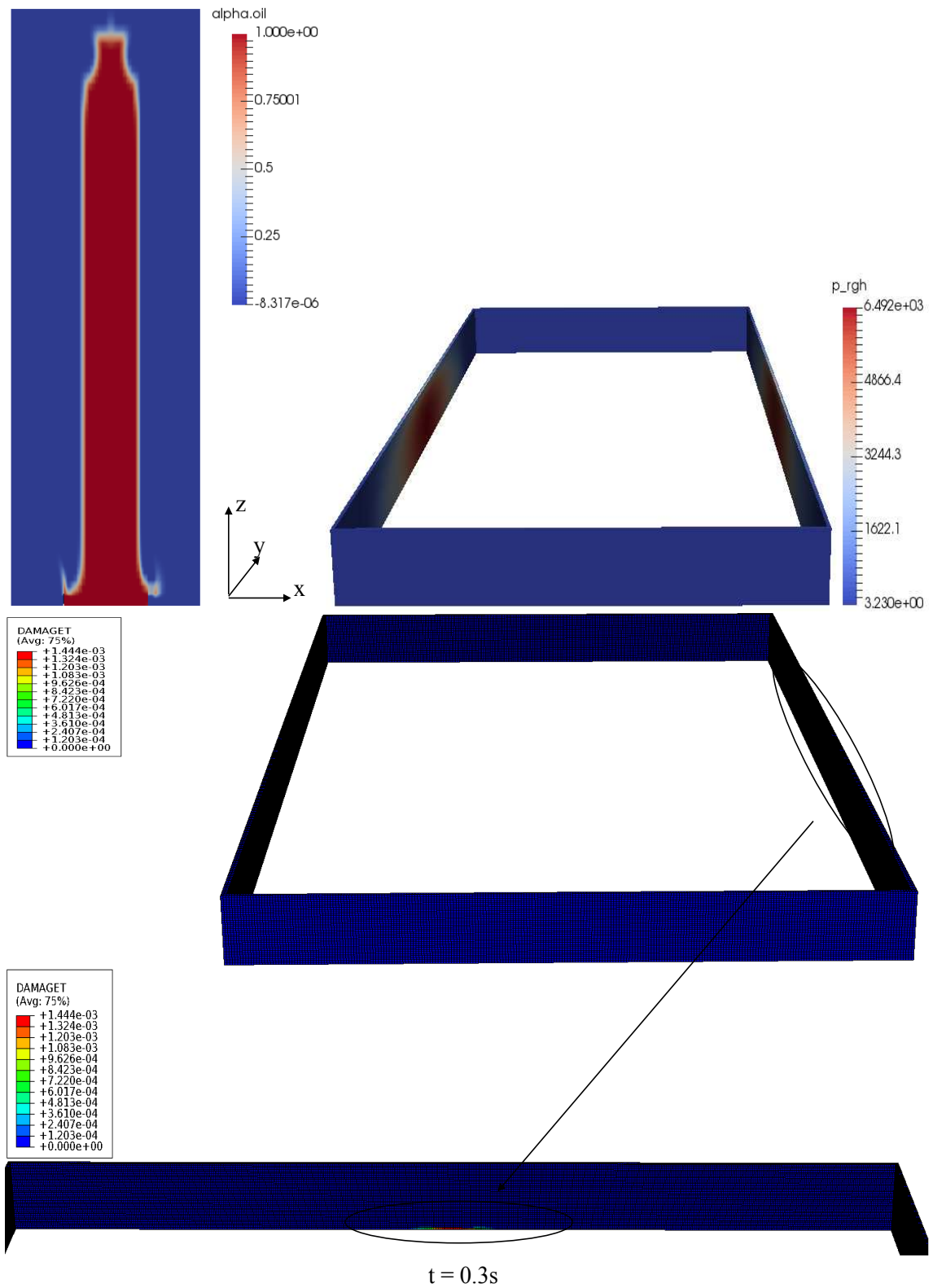


Figure 6.35: Flow behaviour and tensile damage of a plain concrete rectangular wall subjected to an off-centred load along the  $x$  axis at  $t = 0.3s$

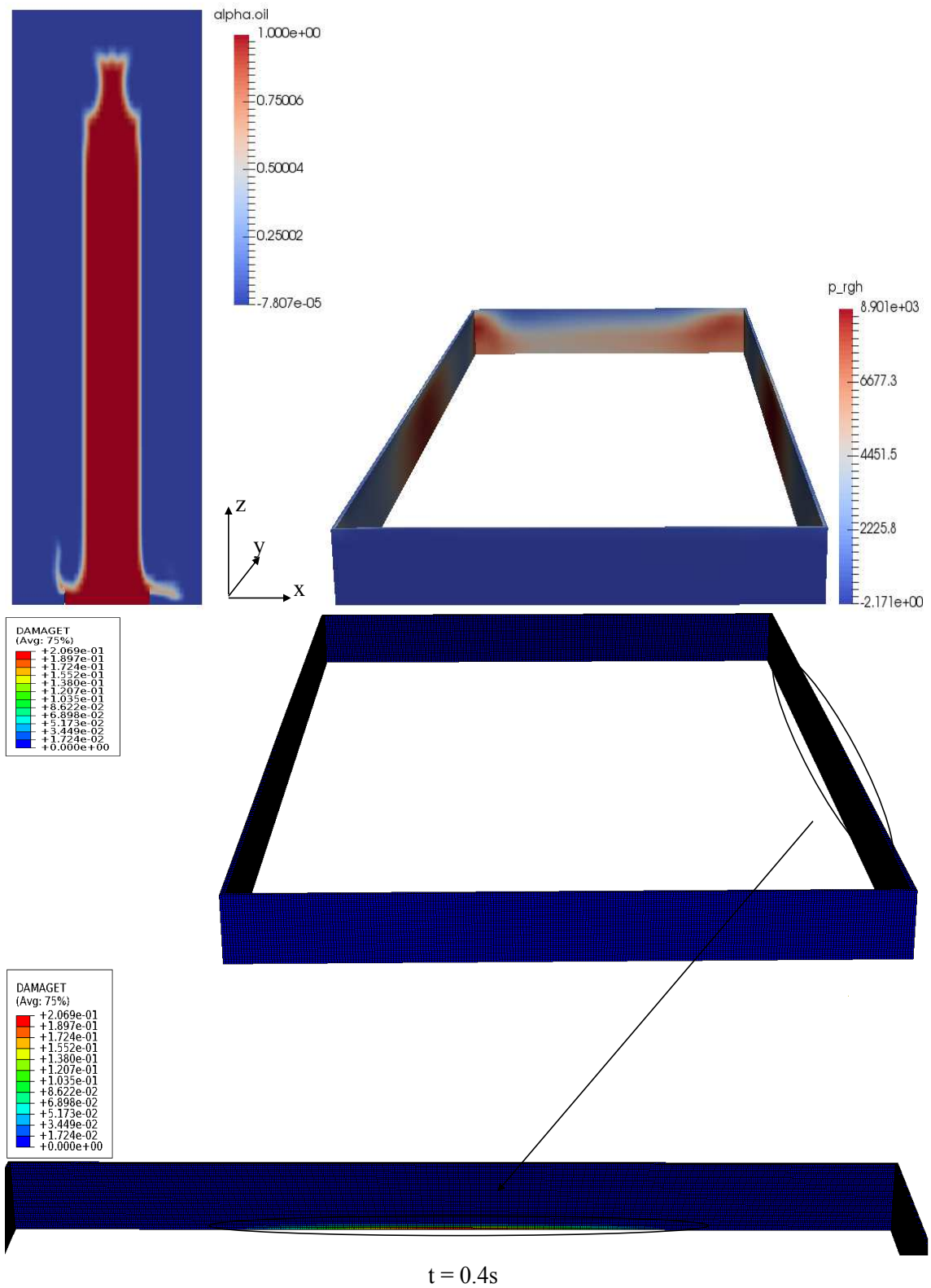


Figure 6.36: Flow behaviour and tensile damage of a plain concrete rectangular wall subjected to an off-centred load along the  $x$  axis at  $t = 0.4s$

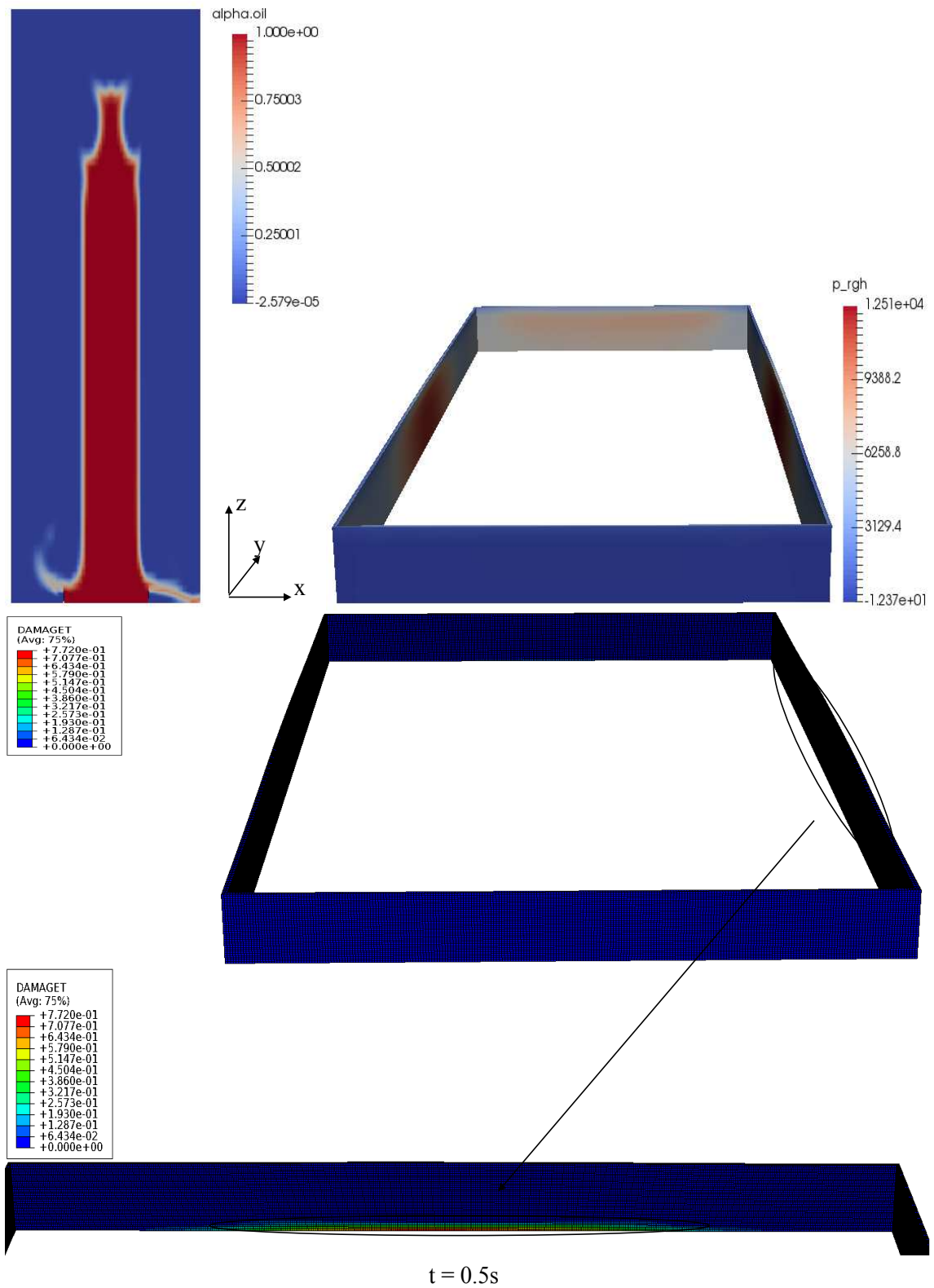


Figure 6.37: Flow behaviour and tensile damage of a plain concrete rectangular wall subjected to an off-centred load along the  $x$  axis at  $t = 0.5s$

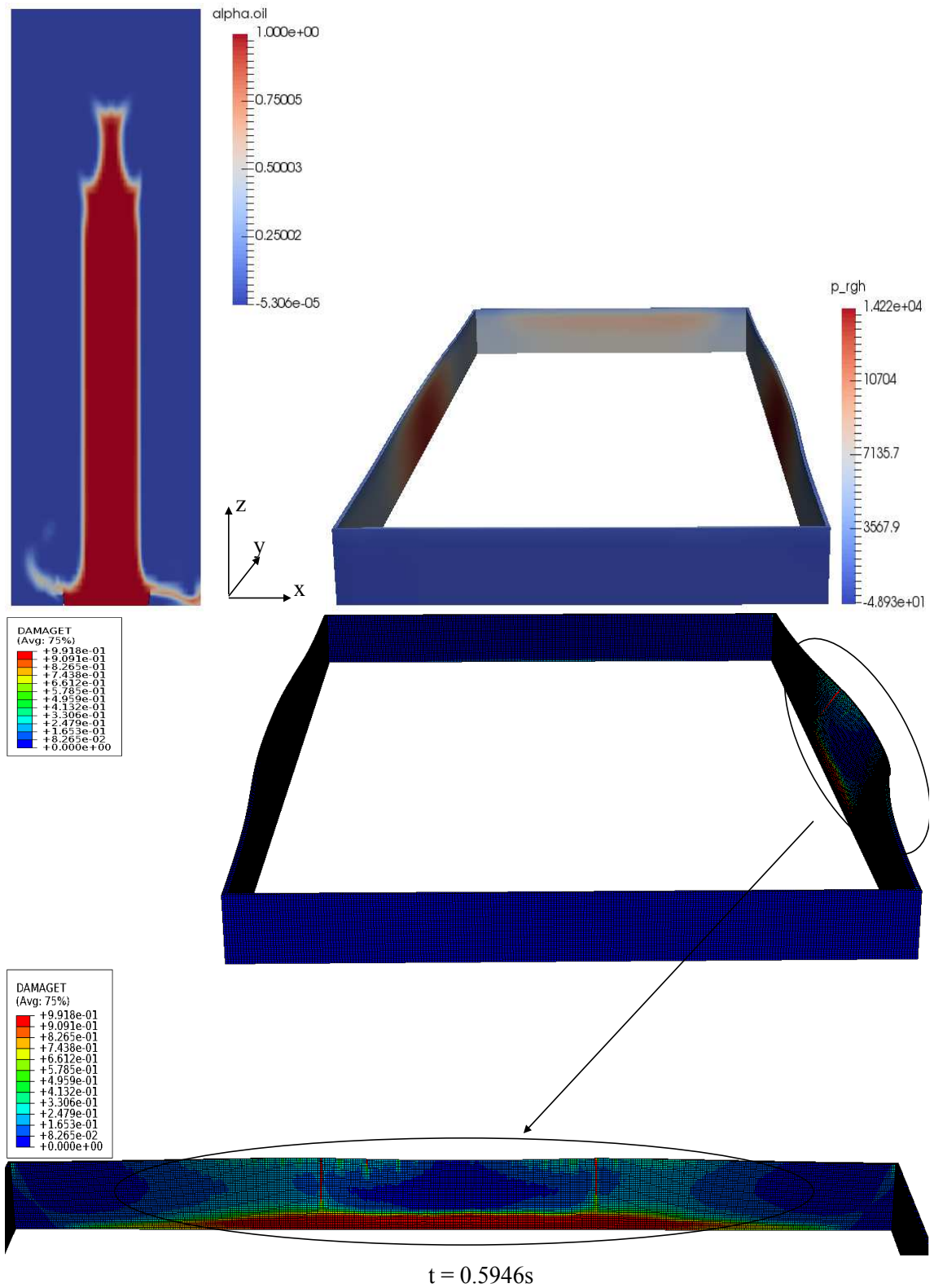
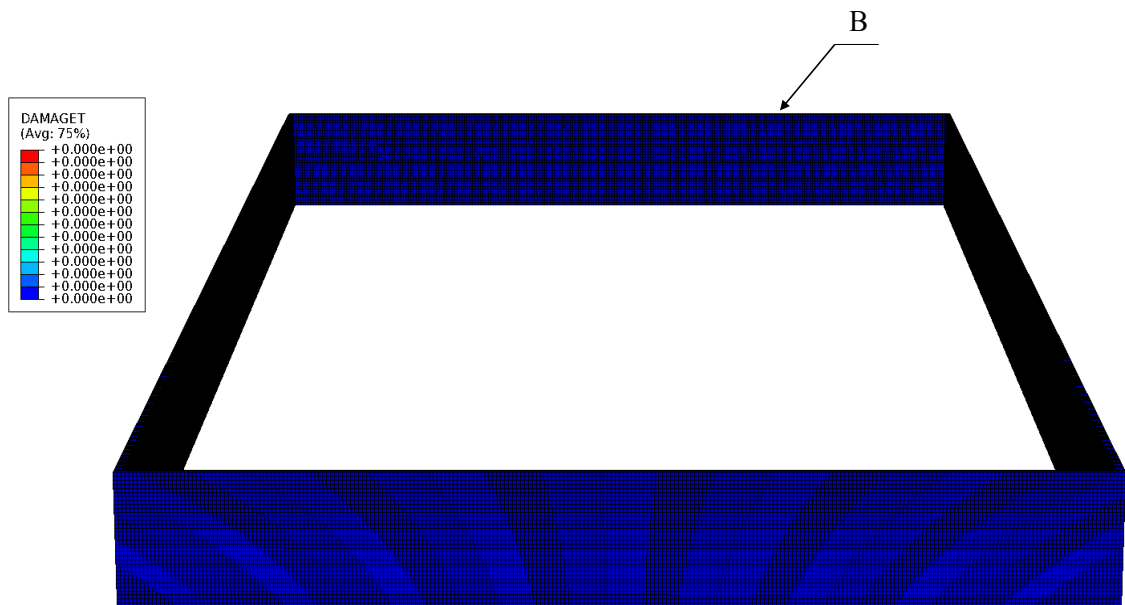
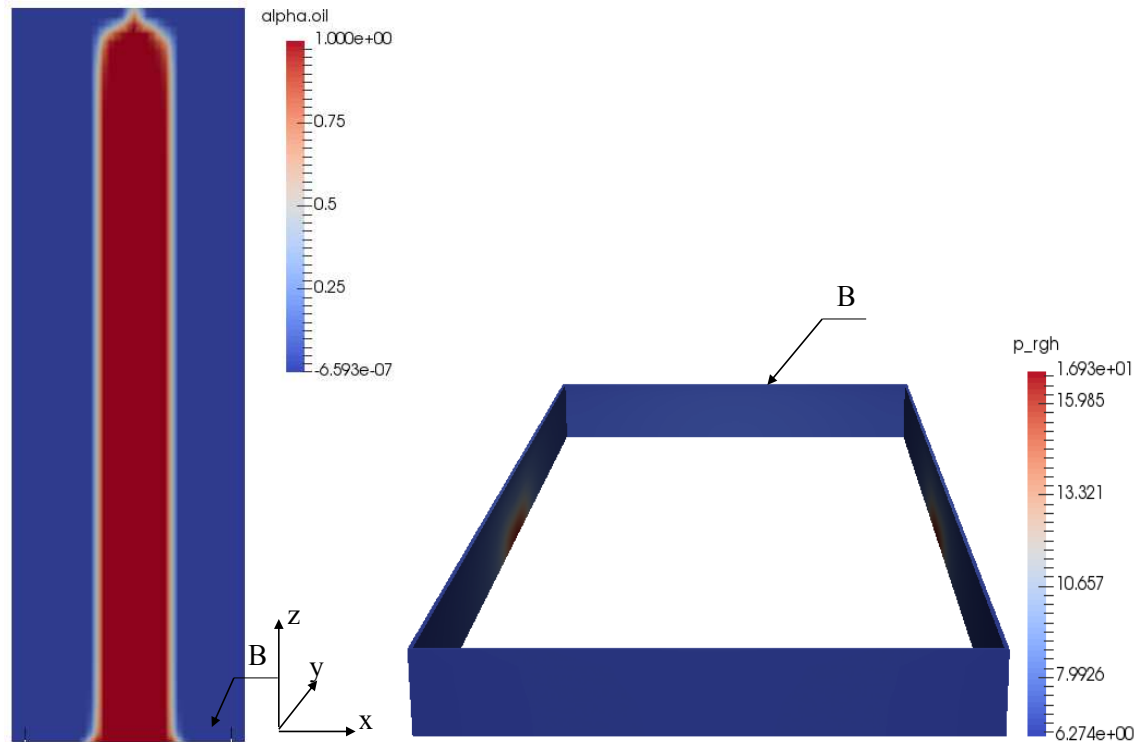


Figure 6.38: Flow behaviour and tensile damage of a plain concrete rectangular wall subjected to an off-centred load along the  $x$  axis at  $t = 0.6$ s

## Rectangular wall subjected to an off-centred load along the $y$ axis



$t = 0.1s$

Figure 6.39: Flow behaviour and tensile damage of a plain concrete rectangular wall subjected to an off-centred load along the  $y$  axis at  $t = 0.1s$

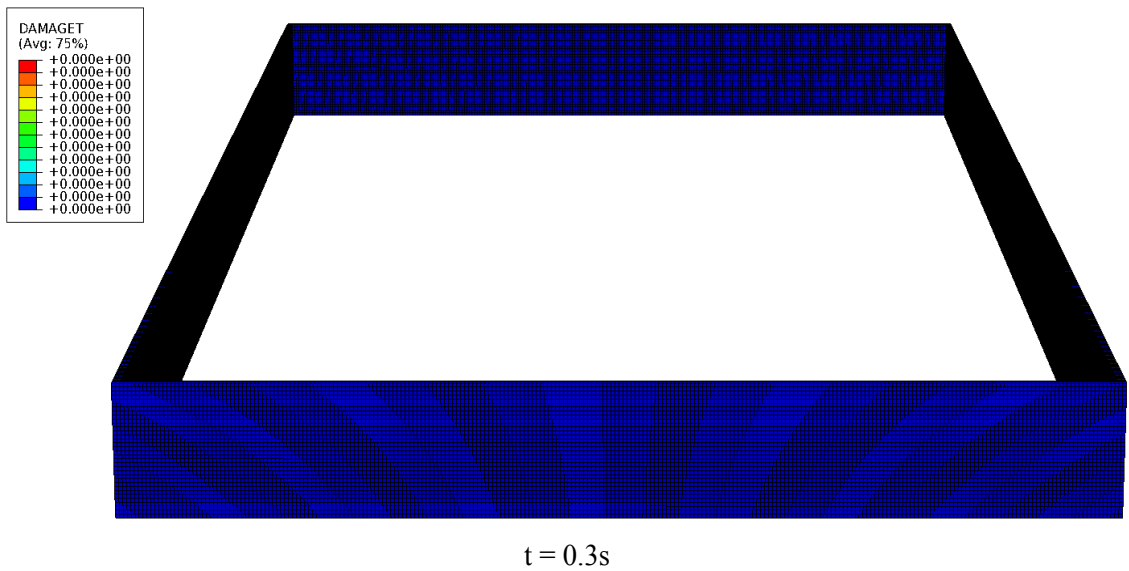
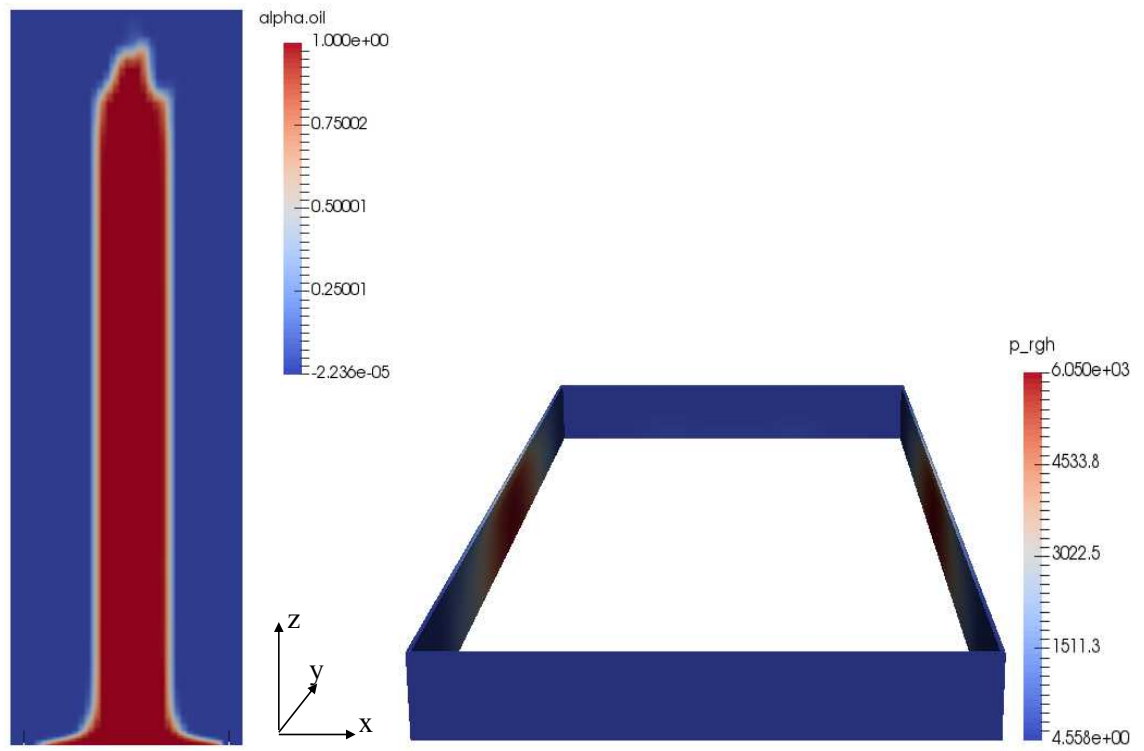


Figure 6.40: Flow behaviour and tensile damage of a plain concrete rectangular wall subjected to an off-centred load along the  $y$  axis at  $t = 0.3s$

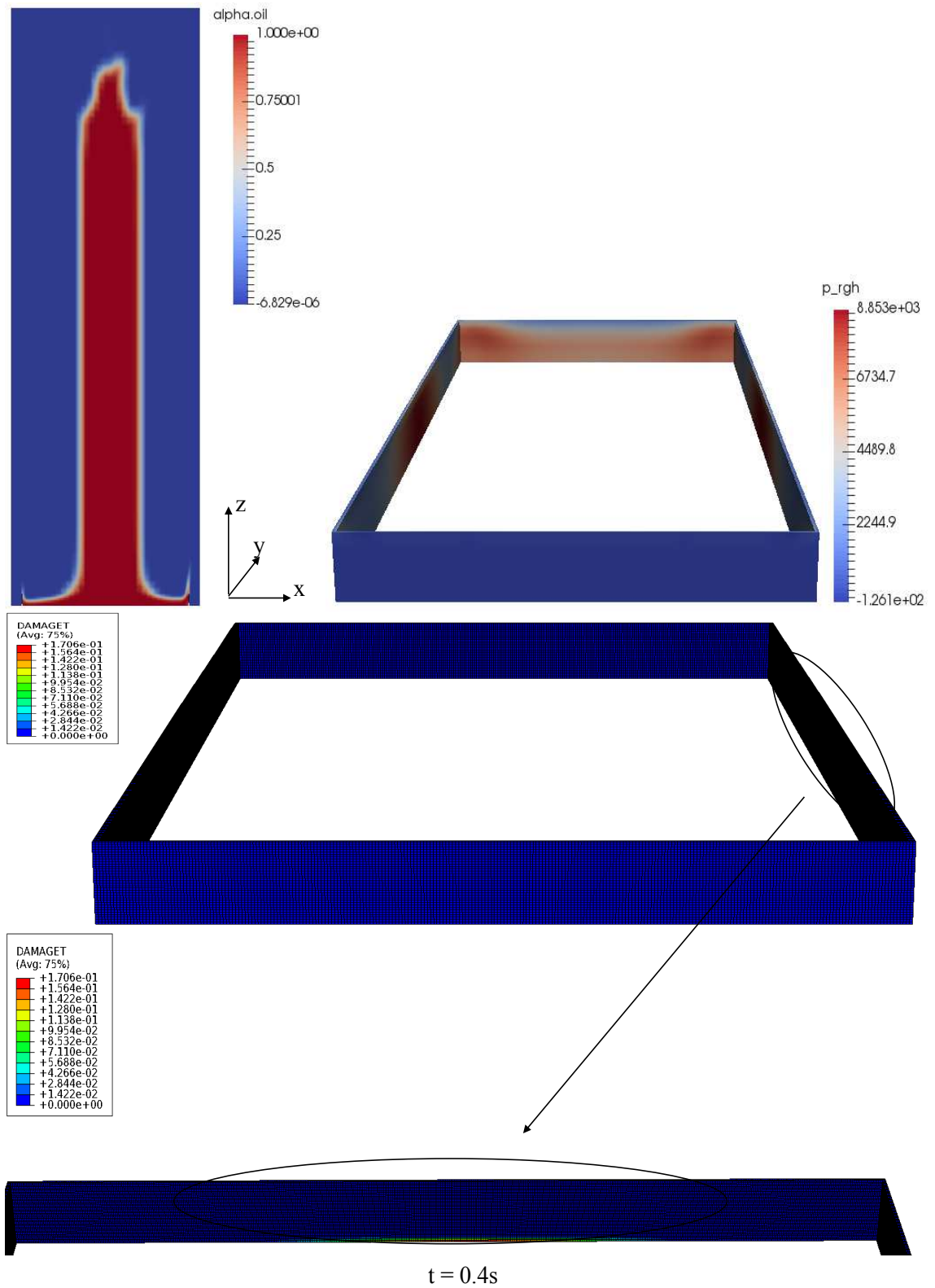


Figure 6.41: Flow behaviour and tensile damage of a plain concrete rectangular wall subjected to an off-centred load along the  $y$  axis at  $t = 0.4s$

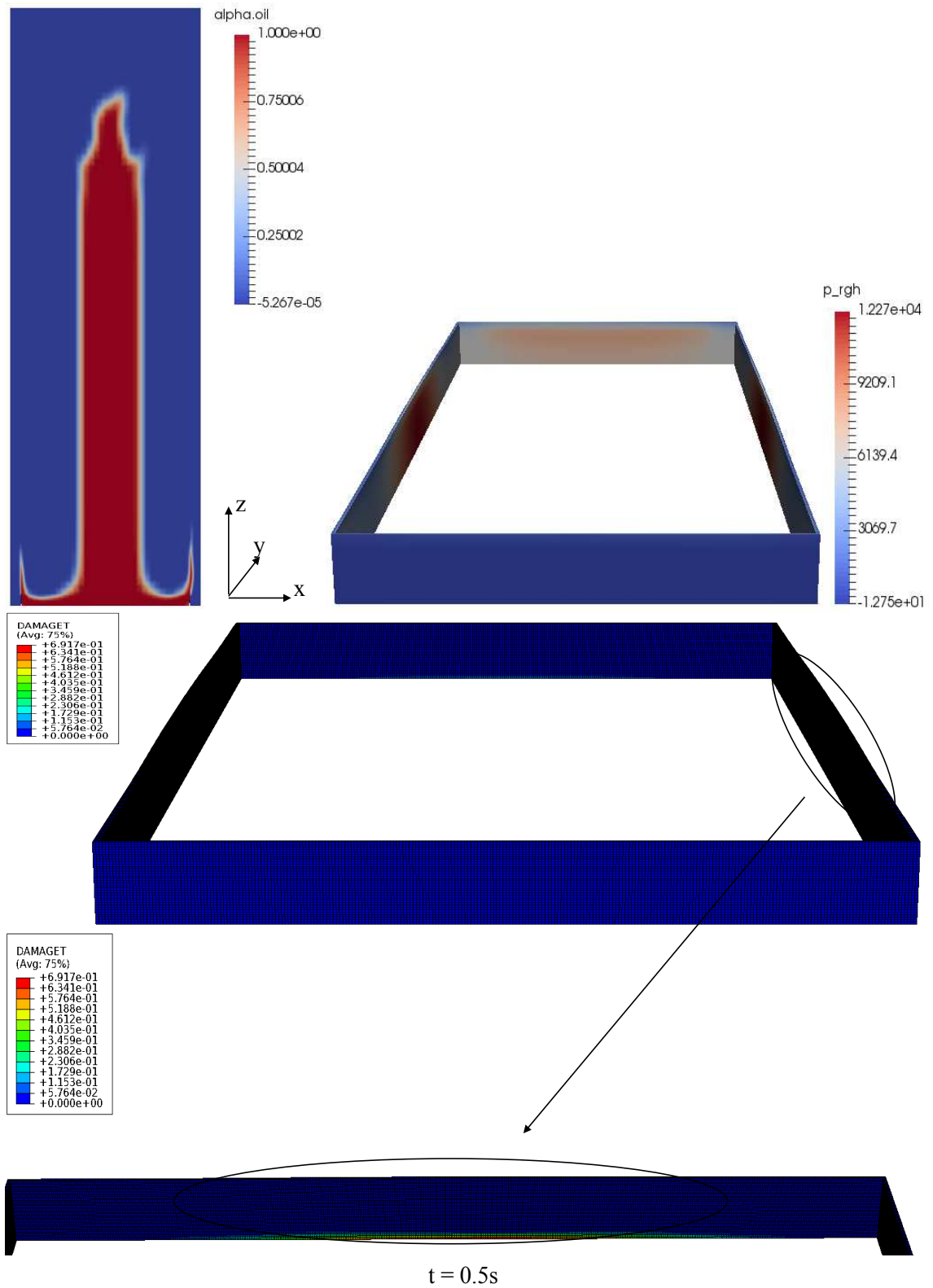


Figure 6.42: Flow behaviour and tensile damage of a plain concrete rectangular wall subjected to an off-centred load along the  $y$  axis at  $t = 0.5s$

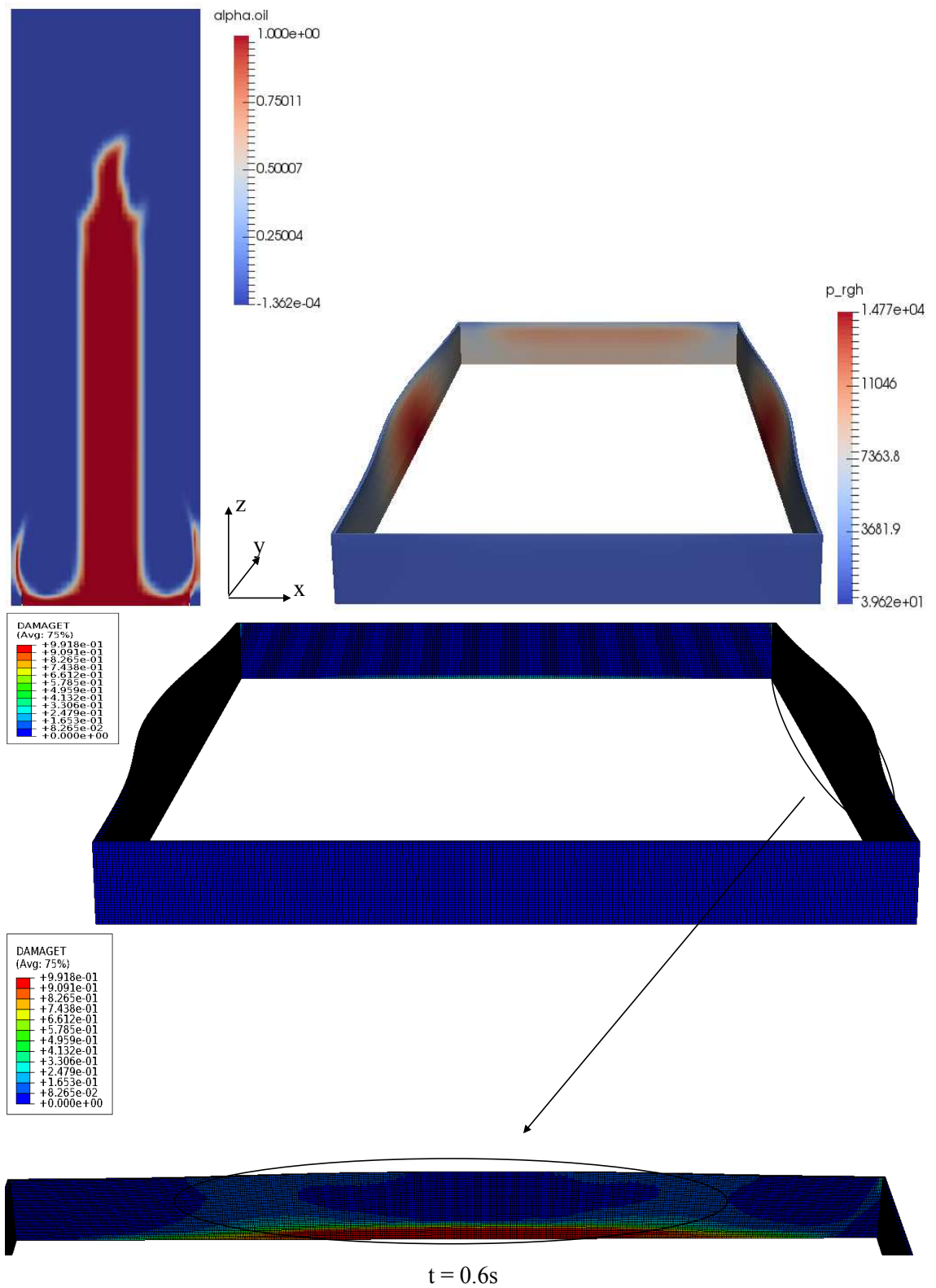


Figure 6.43: Flow behaviour and tensile damage of a plain concrete rectangular wall subjected to an off-centred load along the  $y$  axis at  $t = 0.6s$

### 6.3.1.6 Comparison of the behaviour of a rectangular wall subjected to a centred and an off-centred loads

Figure 6.44 presents a comparison in tensile damage between a centred, an off-centred load along the  $x$  axis and an off-centred load along the  $y$  axis for a rectangular bund wall. An off-centred load along the  $x$  axis causes more cracks in the structure than the two other cases when compared at the same time along with an earlier failure of the wall. Similar to the square wall, the first side impacted by the load is acting as a flat wall and the three other sides are not contributing to withstand the pressure. When the load is off-centred toward the longest side, the tensile damage is higher. The behaviour of the structure under a centred load and an off-centred loads along the  $y$  axis is very close in terms of the amount of the tensile damage, but with an earlier failure of the former case. Generally, the failure times are close to each other for the three different cases.

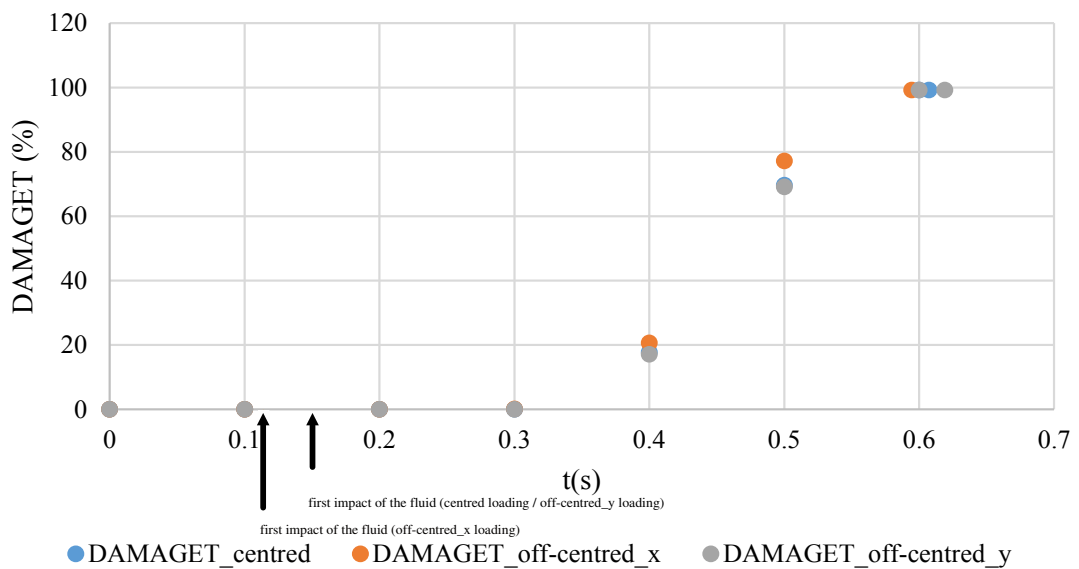


Figure 6.44: Comparison of the structural response of a plain concrete rectangular wall under a centred and an off-centred loads

### 6.3.1.7 Comparison of the behaviour of different shapes of the wall

Figure 6.45 depicts a comparison of the performance of the three different shapes of the bund wall in terms of tensile damage. Only the results corresponding to a centred

load are included for the comparison. The circular wall outperforms the other two shapes, where only minor damage was caused. However, the square and rectangular walls show lower performance. A square wall outperforms the rectangular wall in terms of the amount of tensile damage, when compared at similar times. For example, at  $t = 0.5\text{s}$ , the maximum tensile damage in the rectangular wall is 70%, while it is only 40% for a square wall. The circular and the square walls have a uniform geometry along two cross sectional axes giving them a uniform strength characteristic. The circular shape produces less damage because every part of the structure is subjected to the same load throughout the simulation time. However, a square wall exhibits loading initially only in the middle of each of the four sides of the bund wall while other regions of the wall are not contributing to withstanding the load. The worst case is for the rectangular bund wall, where initially only the two closest sides withstand the load. For the simulated case, the span of the closest sides is twice the shortest sides, which makes them more susceptible to flexure.

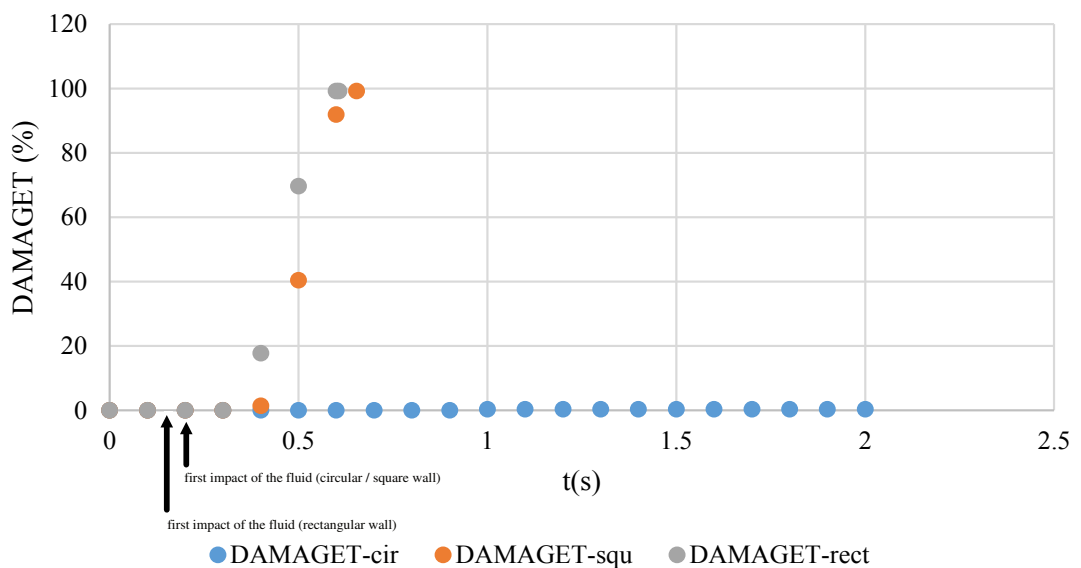


Figure 6.45: Comparison between different shapes of bund wall in terms of tensile damage

### **6.3.2 Simulation results of the reinforced concrete wall**

Figures 6.46, 6.47 and 6.48 present the simulation results of a reinforced concrete wall designed according to BS 8007:1987 as indicated in chapter 4. There is no damage occurring in the wall, which implies that if the structure is properly designed, it can withstand impact load. But, most of the current installations are old and standards might not have been strictly applied at that time. Furthermore, the standard tends to be very conservative, which imposes the use of many rebars, hence increasing the total cost of the structure. The problem of overtopping is still an issue, even if the structure does not fail. It is worth noting that even if a reinforced concrete wall does not fail under the impact load for this simulated case, its performance will still be questionable under other modes of dynamic loading, such as a failure of tanks in a domino effect, where the loading direction is very complex or in the case of an explosion. An example of a failure of a reinforced concrete wall is shown in Figure 2.2.

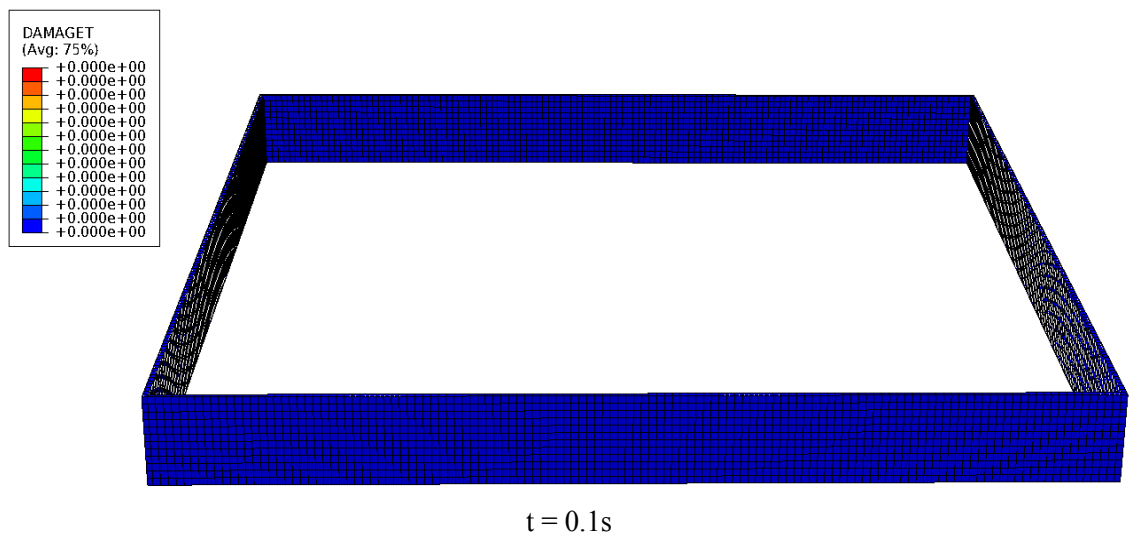
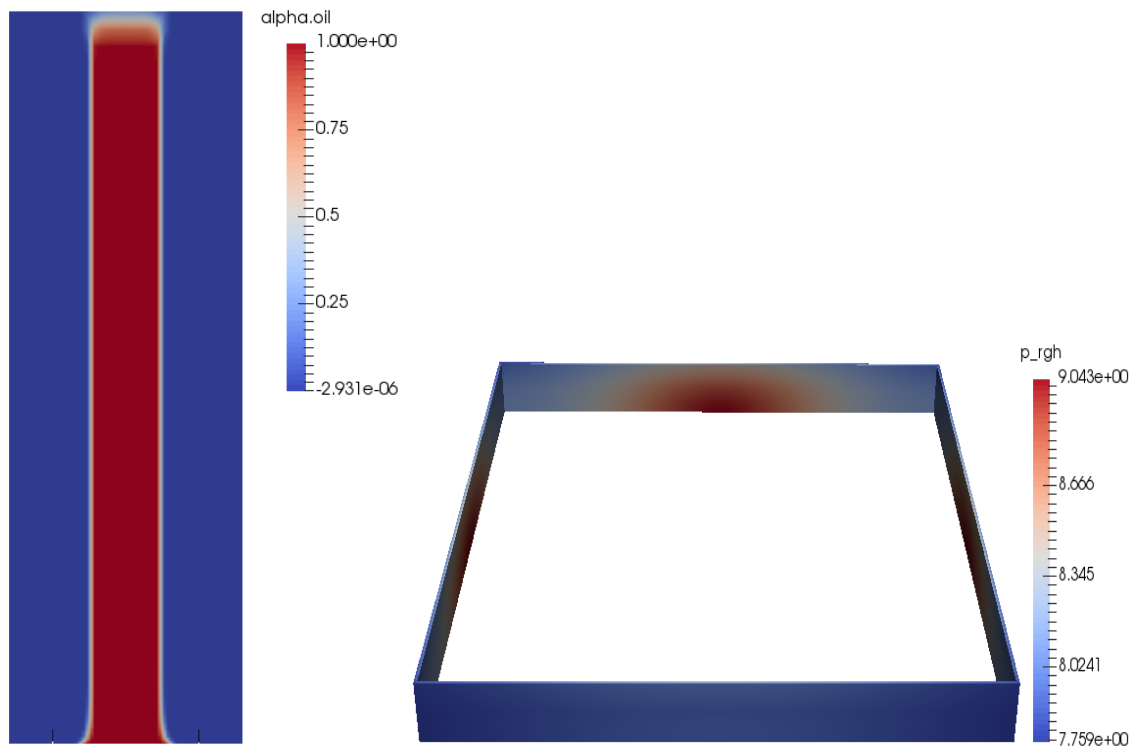


Figure 6.46: Flow behaviour and tensile damage of a reinforced concrete square wall subjected to a centred load at  $t = 0.1s$

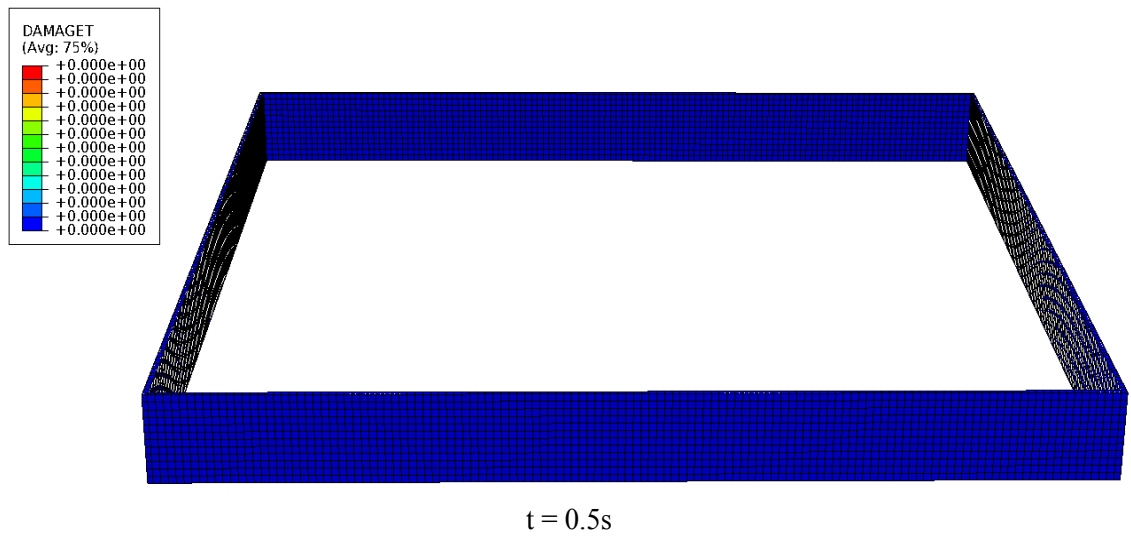
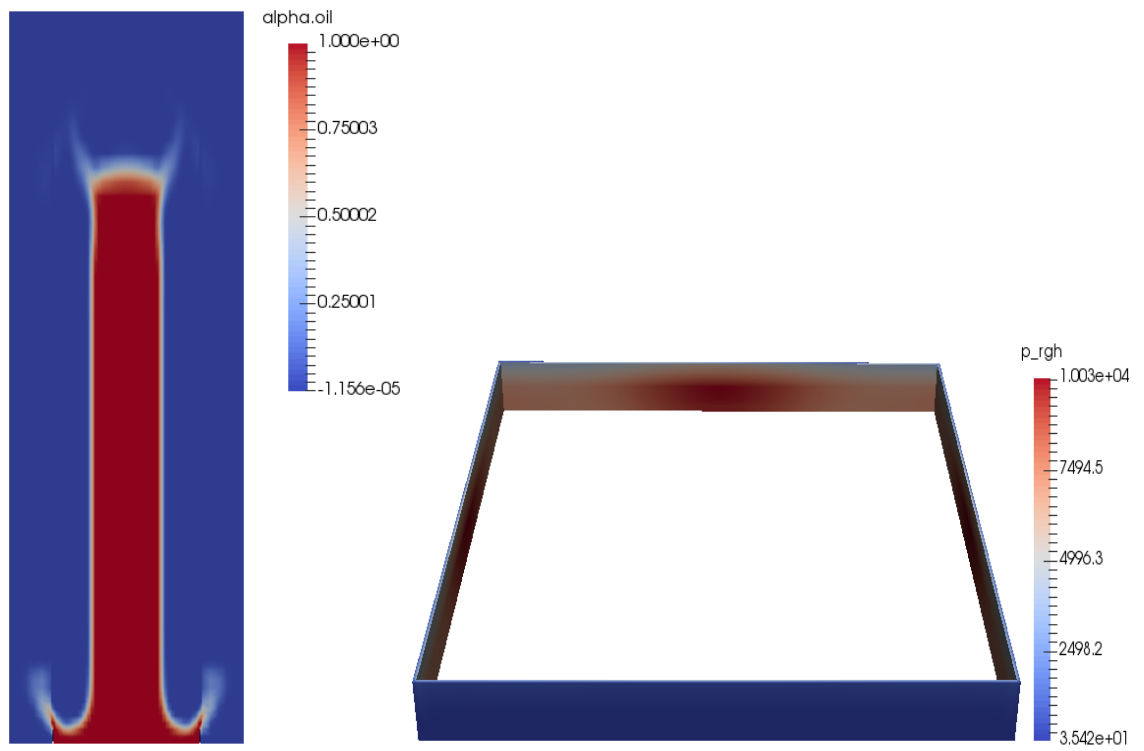


Figure 6.47: Flow behaviour and tensile damage of a reinforced concrete square wall subjected to a centred load at  $t = 0.5s$

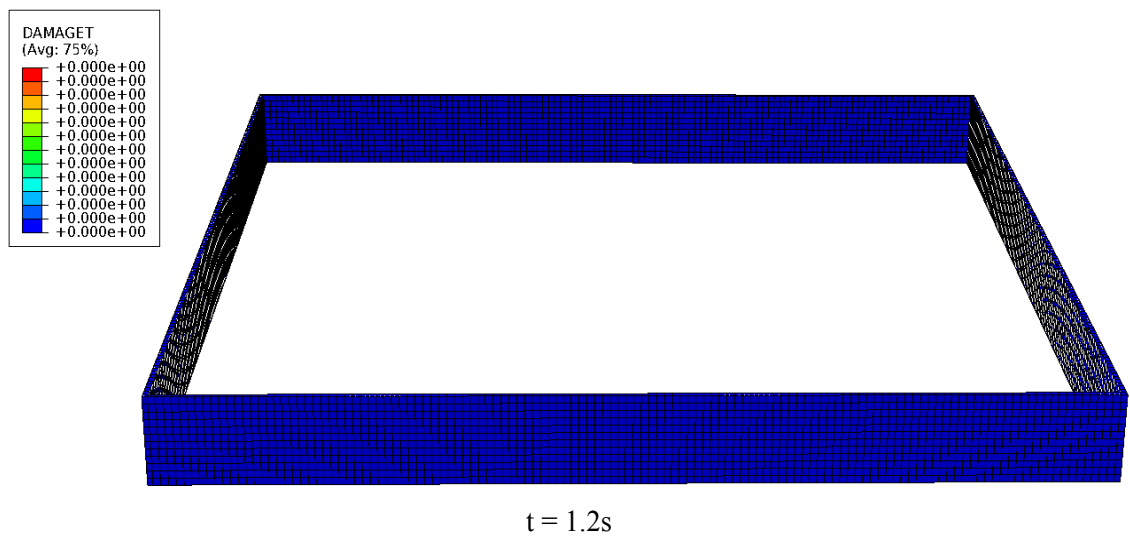
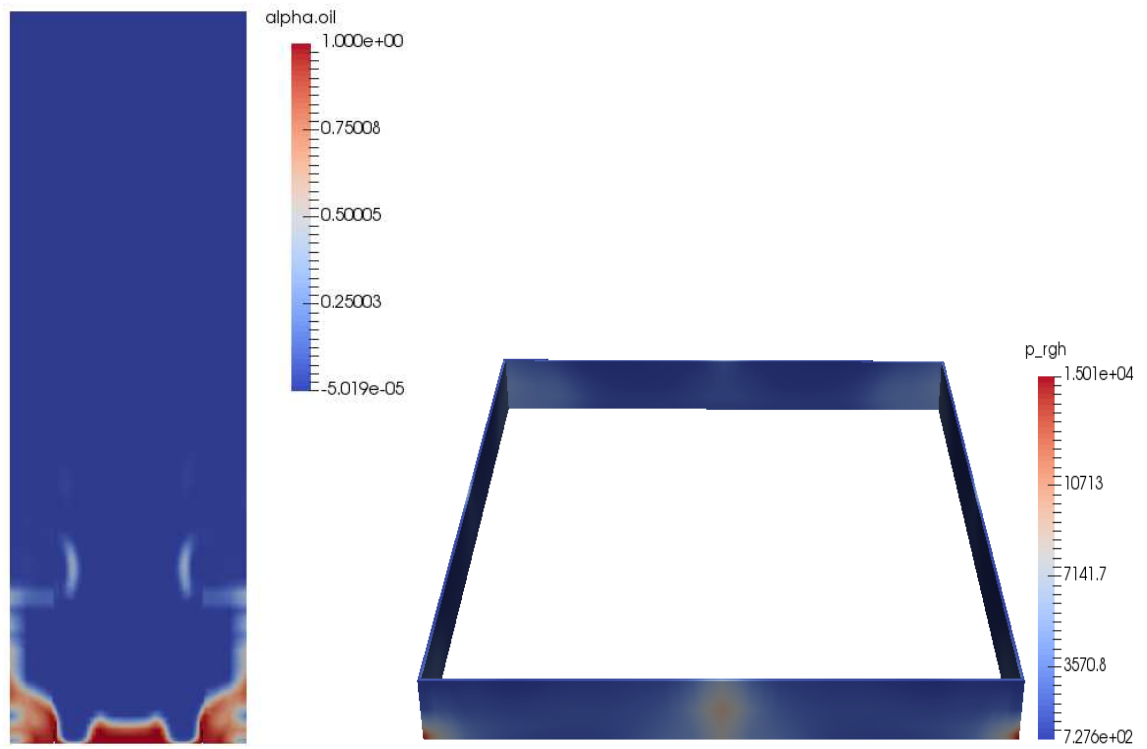


Figure 6.48: Flow behaviour and tensile damage of a reinforced concrete square wall subjected to a centred load at  $t = 1.2s$

### 6.3.3 Simulation results of UHP-FRC wall

Figures 6.49, 6.50, 6.51, 6.52, 6.53, 6.54, 6.55 and 6.56 present the simulation results of a square bund wall made of plain UHP-FRC and incorporating COAST at an angle of 80 degrees. Unlike the plain concrete wall, the tensile damage initiates first in the corners of the added baffle due to the concentration of the stress in these regions of the wall. The damage propagates then to the bottom of the wall and to a lesser extent, to the junction between the wall and the baffle. However, the damage remains localised next to the corners. From  $t = 2.4\text{s}$ , the tensile damage reaches a value of 2.96% and remains constant until the end of the simulation. The FSI simulation could capture the ductile behaviour of the UHP-FRC. Figures 6.49, 6.50, 6.51 and 6.52 indicate that the wall is deforming in the outer direction. As the entire column of the fluid collapses and the pressures decrease significantly from 40 KPa at  $t = 1\text{s}$  to 4 KPa at  $t = 1.2\text{s}$ , the bund wall deforms in the opposite direction. The structure keeps then deforming slightly until the end of the simulation, see Figures (6.54, 6.55 and 6.56). The maximum tensile damage at the end of the simulation is equal to 2.96%.

Figures 6.57, 6.58, 6.59, 6.60 and 6.61 present the simulation results of a square bund wall made of UHP-FRC that incorporates starter bars. This simulation was performed to investigate the effect of the starter bars on the structural integrity of the wall. The simulation was only run for 1s. By comparing the two simulations at the same times, it appears that the use of starter bars permits more localised damage in the vicinity of the corners and reduces it to a maximum value of less than 1%. A better representation of the maximum tensile damage is given in figures 6.62 and 6.63 for both of the simulated cases. A maximum strain rate of  $4 \times 10^{-2} \text{ s}^{-1}$  was obtained across the simulations incorporating UHP-FRC against a strain rate of  $10 \text{ s}^{-1}$  used to account for the dynamic properties of UHP-FRC. The strain rate in Othman (2016) was chosen on the basis of the maximum rate recorded by steel strain gauges with the same strain rate considered for both of UHP-FRC and steel which explains the difference obtained.



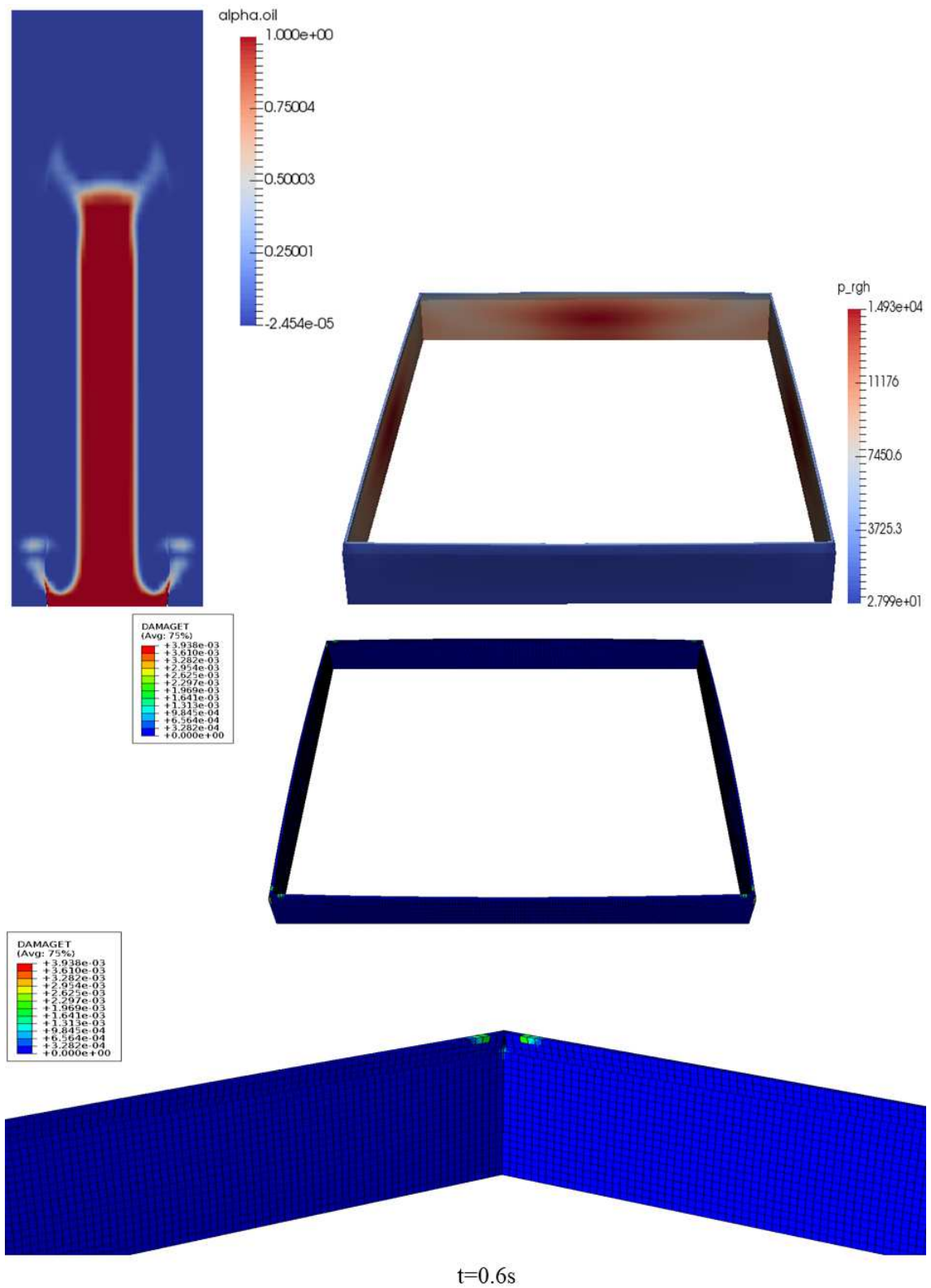


Figure 6.50: Flow behaviour and tensile damage of a UHP-FRC square wall subjected to a centred load and incorporating COAST at  $t = 0.6s$

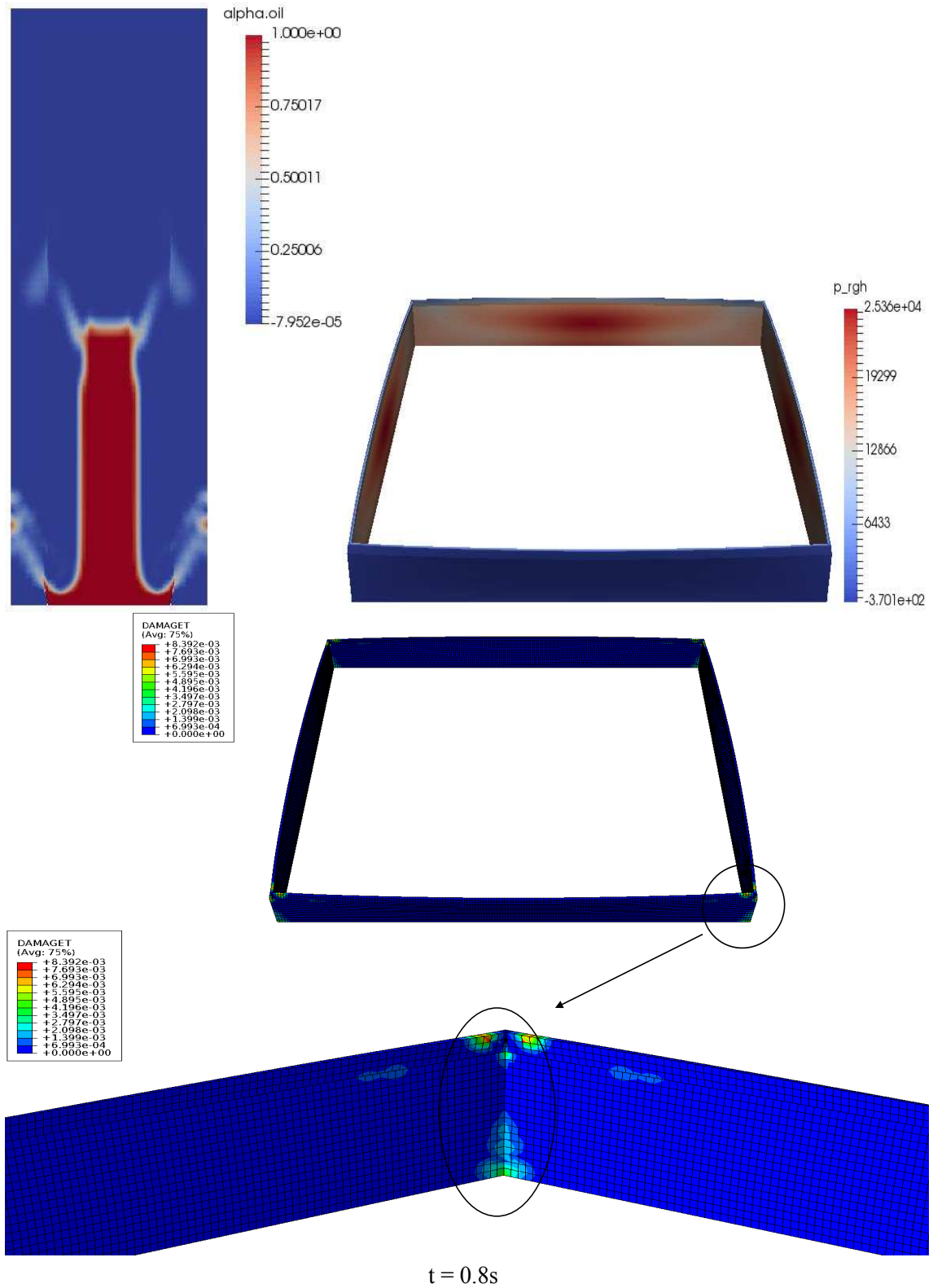


Figure 6.51: Flow behaviour and tensile damage of a UHP-FRC square wall subjected to a centred load and incorporating COAST at  $t = 0.8s$

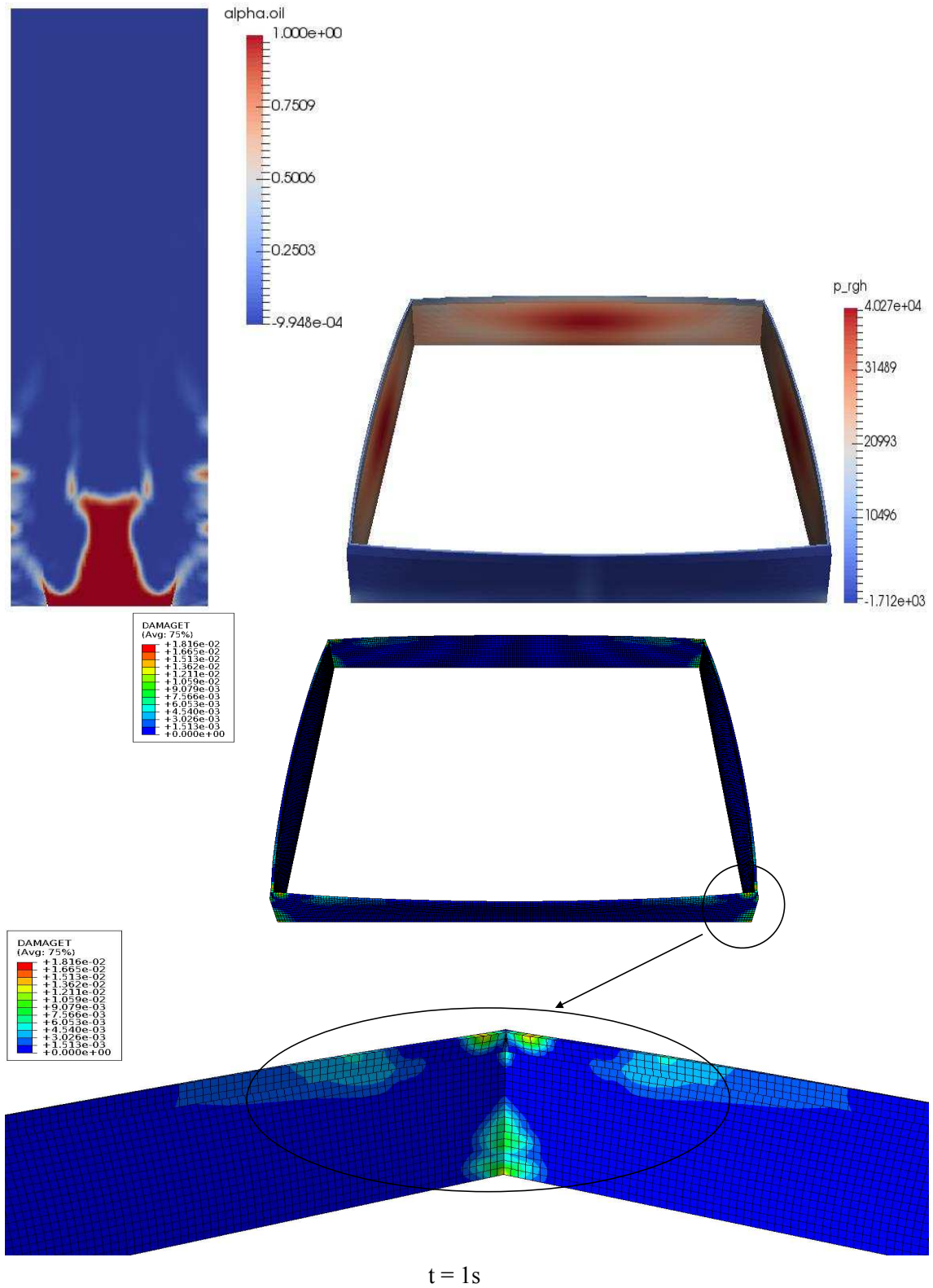


Figure 6.52: Flow behaviour and tensile damage of a UHP-FRC square wall subjected to a centred load and incorporating COAST at  $t = 1s$

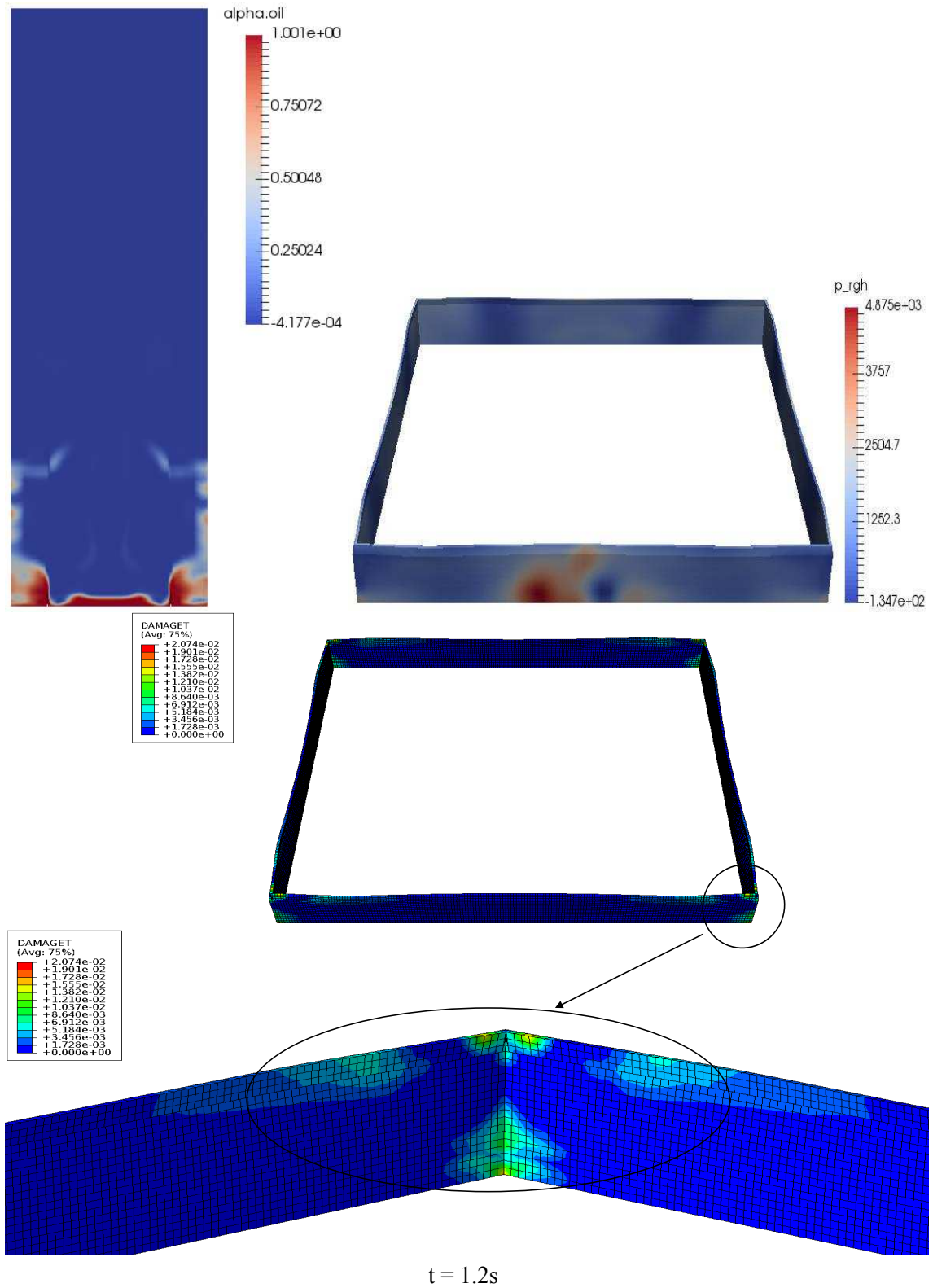


Figure 6.53: Flow behaviour and tensile damage of a UHP-FRC square wall subjected to a centred load and incorporating COAST at  $t = 1.2s$

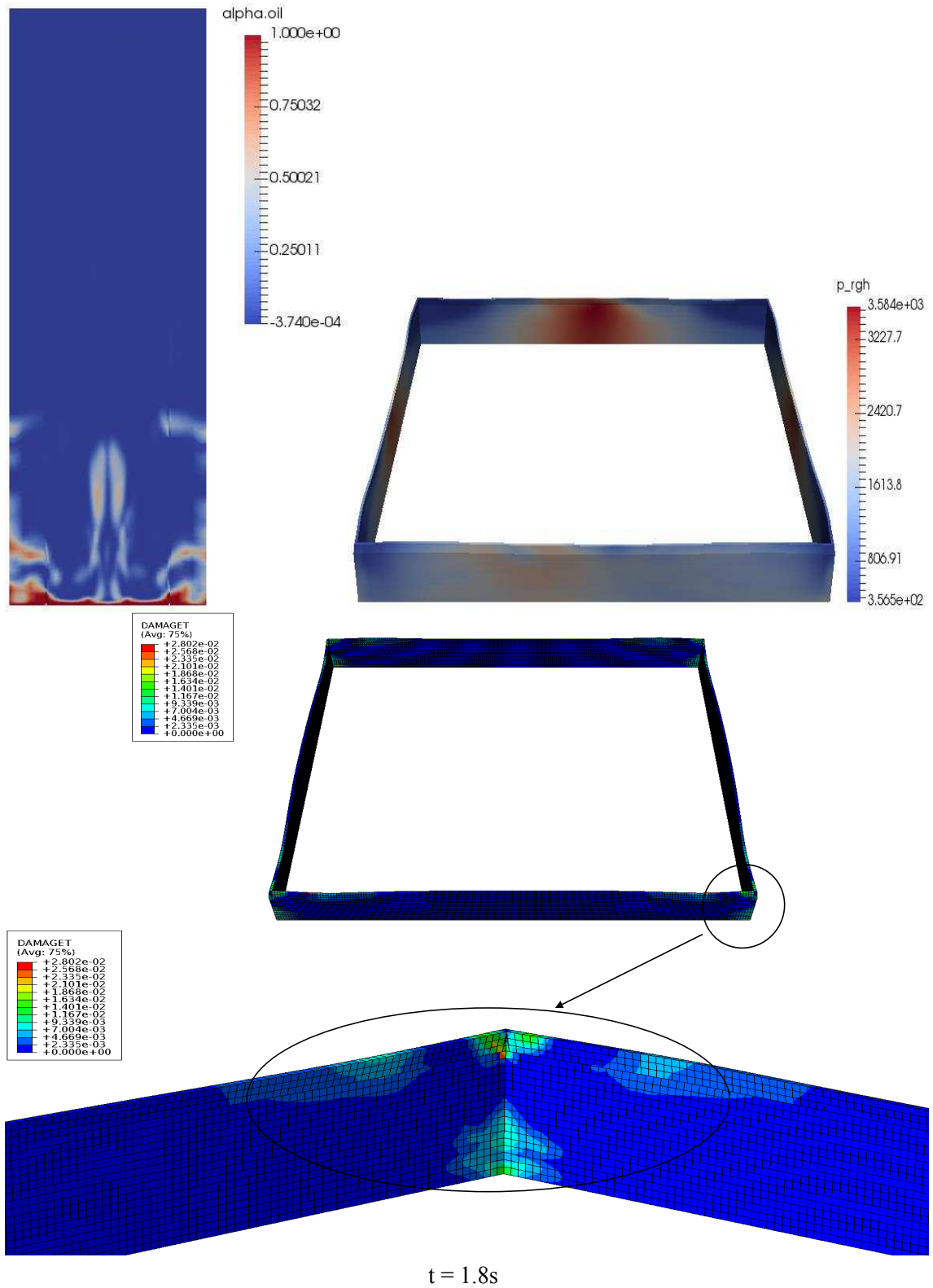


Figure 6.54: Flow behaviour and tensile damage of a UHP-FRC square wall subjected to a centred load and incorporating COAST at  $t = 1.8s$

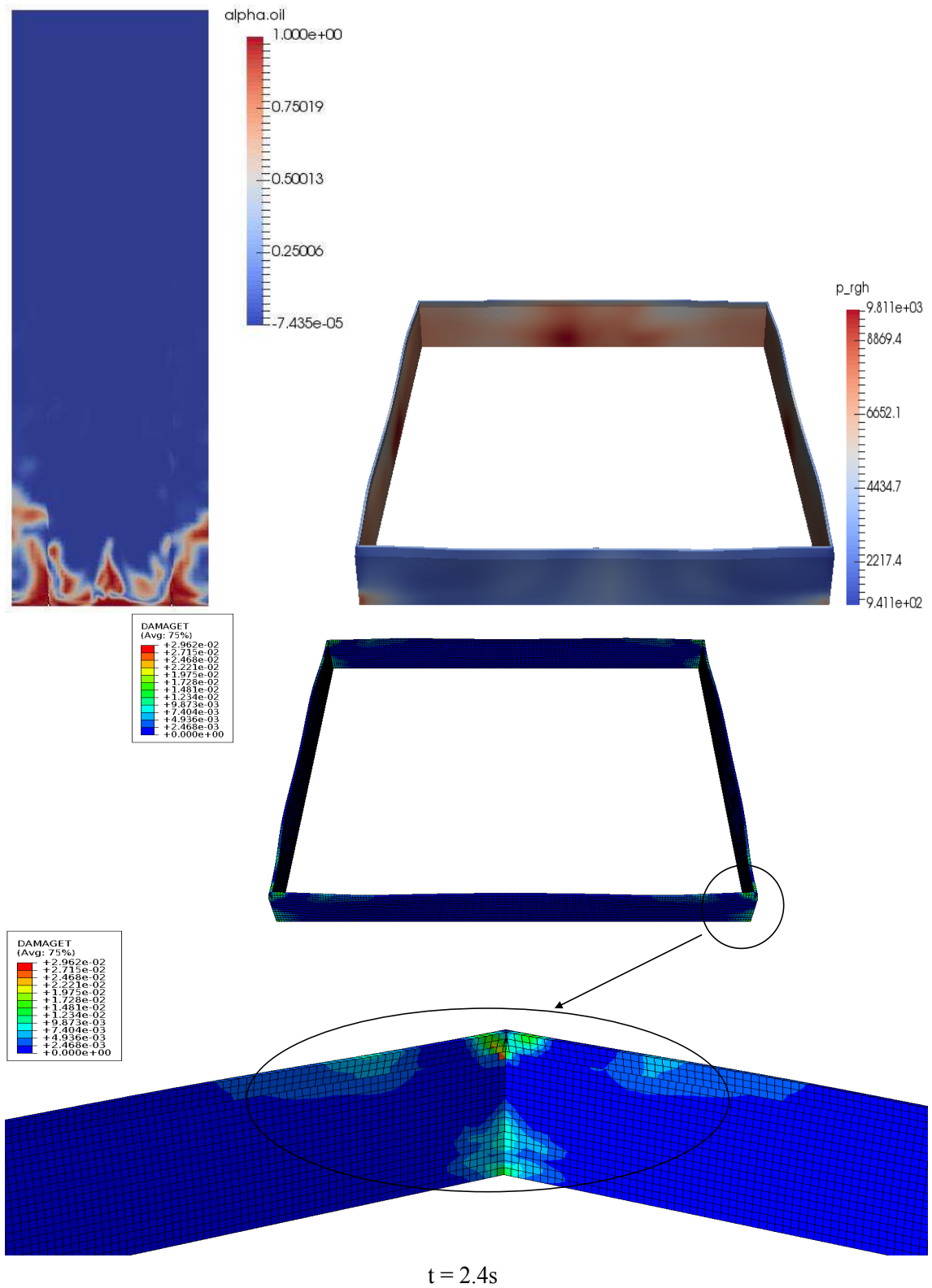


Figure 6.55: Flow behaviour and tensile damage of a UHP-FRC square wall subjected to a centred load and incorporating COAST at  $t = 2.4s$

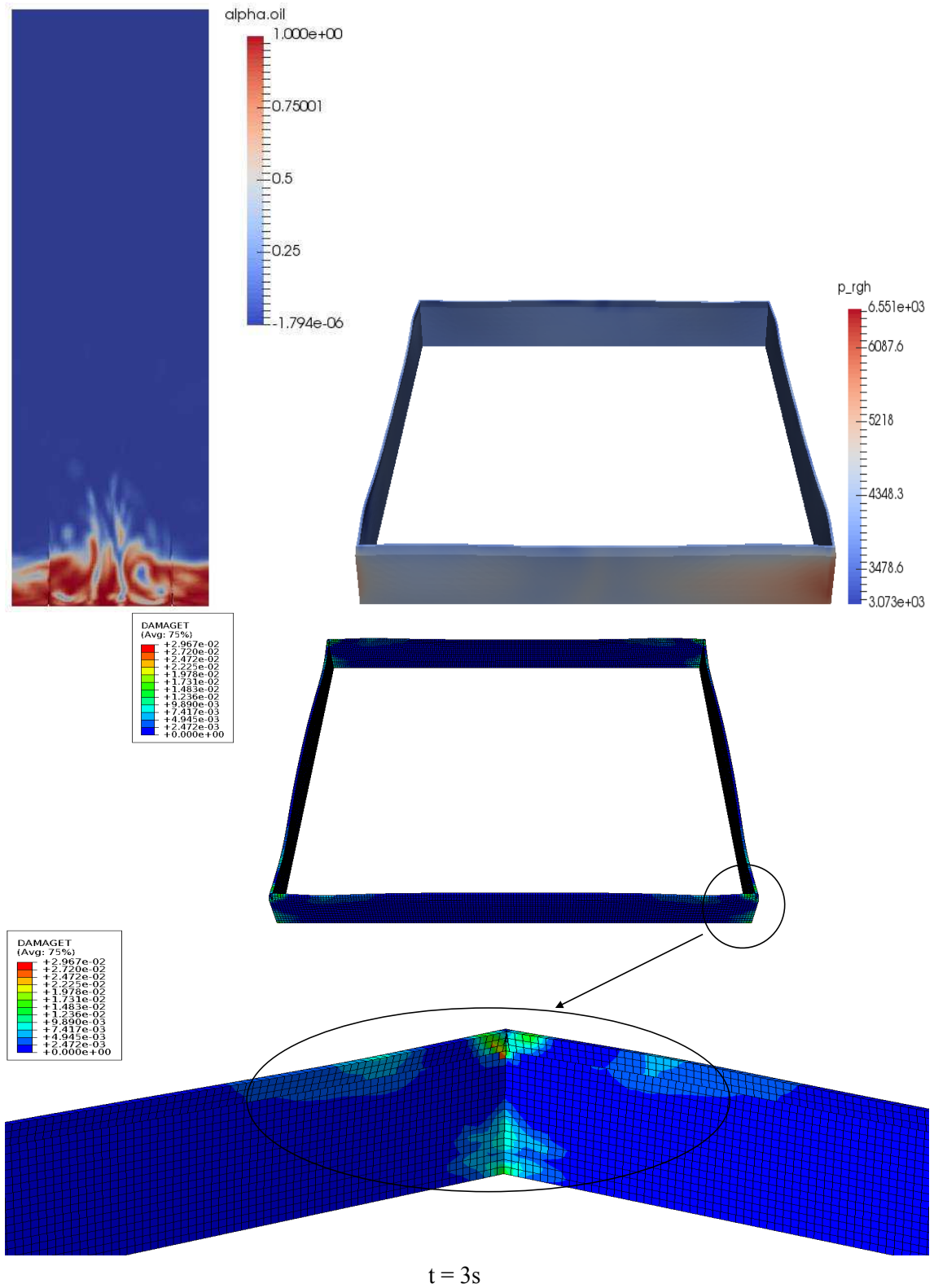


Figure 6.56: Flow behaviour and tensile damage of a UHP-FRC square wall subjected to a centred load and incorporating COAST at  $t = 3s$

## UHP-FRC wall incorporating COAST and starter rebars

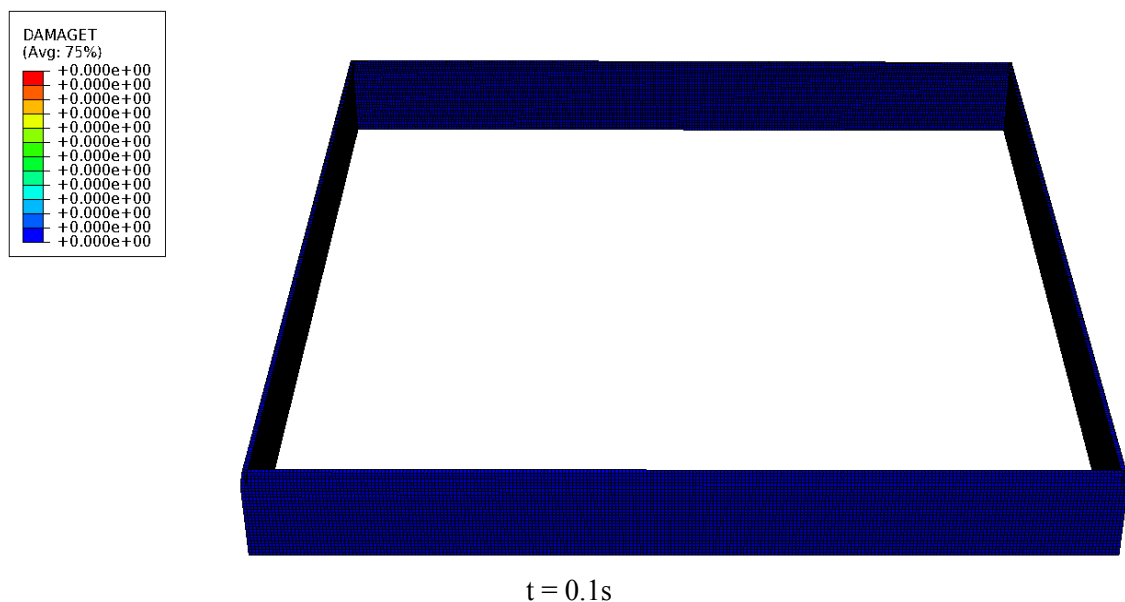
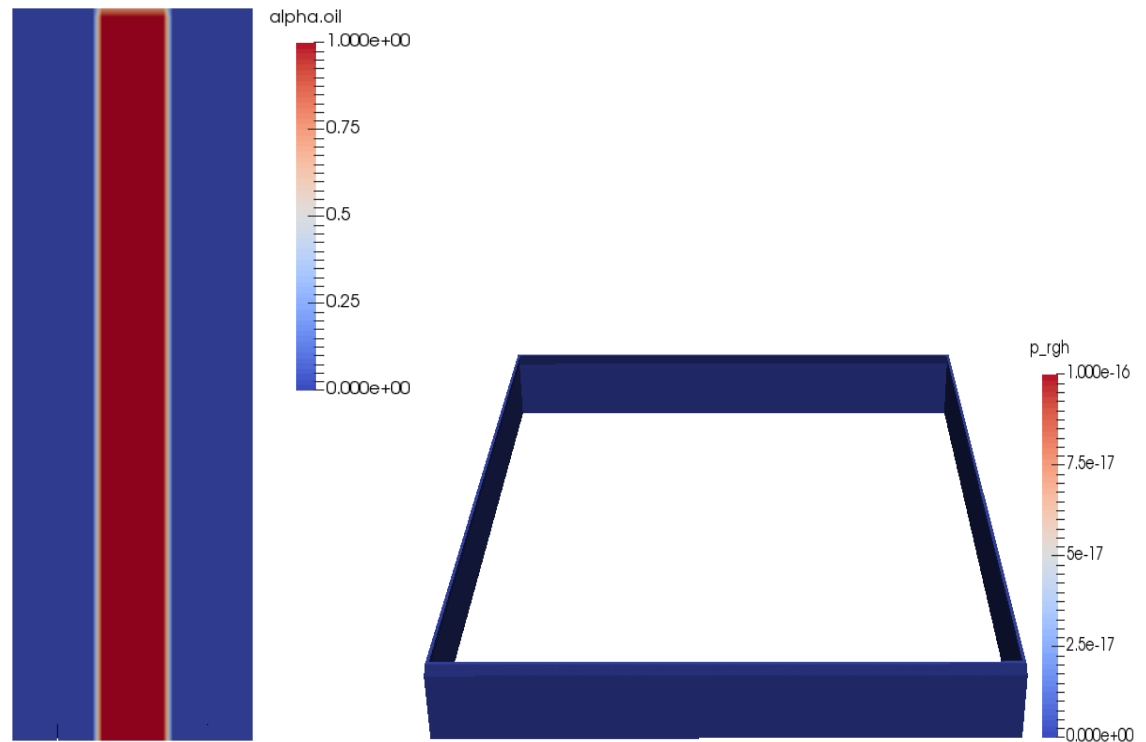


Figure 6.57: Flow behaviour and tensile damage of a UHP-FRC square wall subjected to a centred load and incorporating COAST and starter rebars at  $t = 0.1s$

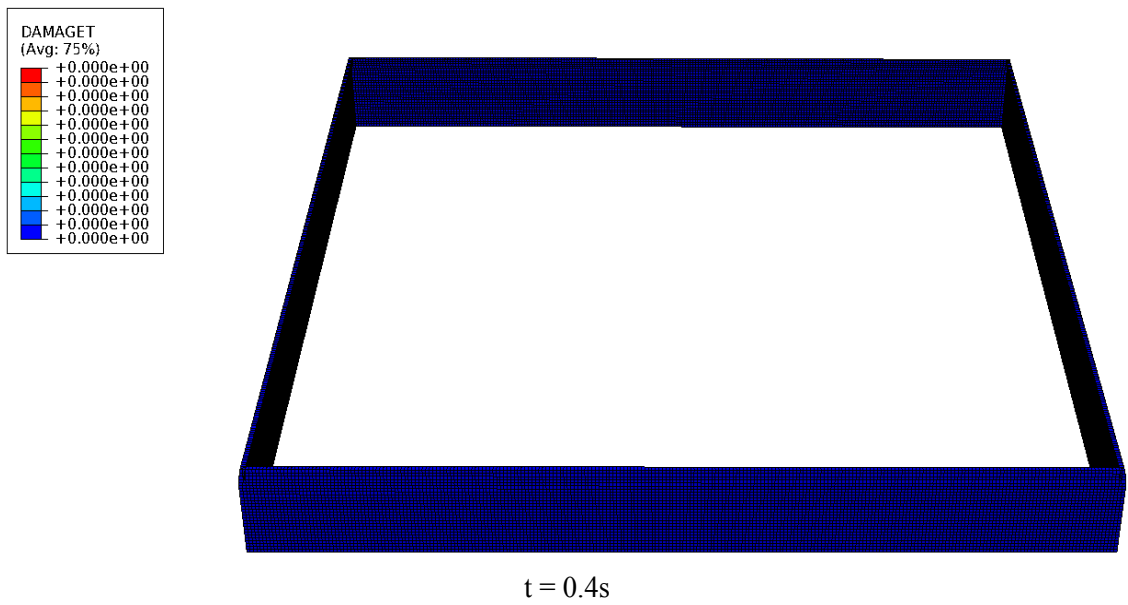
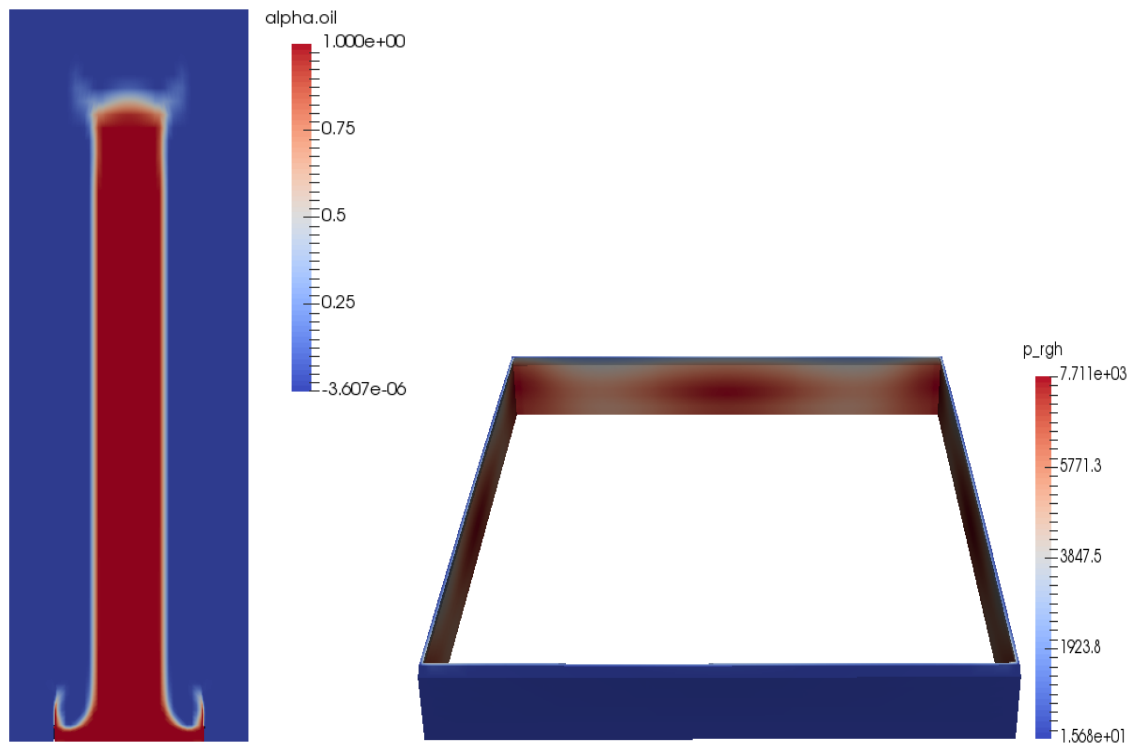


Figure 6.58: Flow behaviour and tensile damage of a UHP-FRC square wall subjected to a centred load and incorporating COAST and starter bars at  $t = 0.4s$

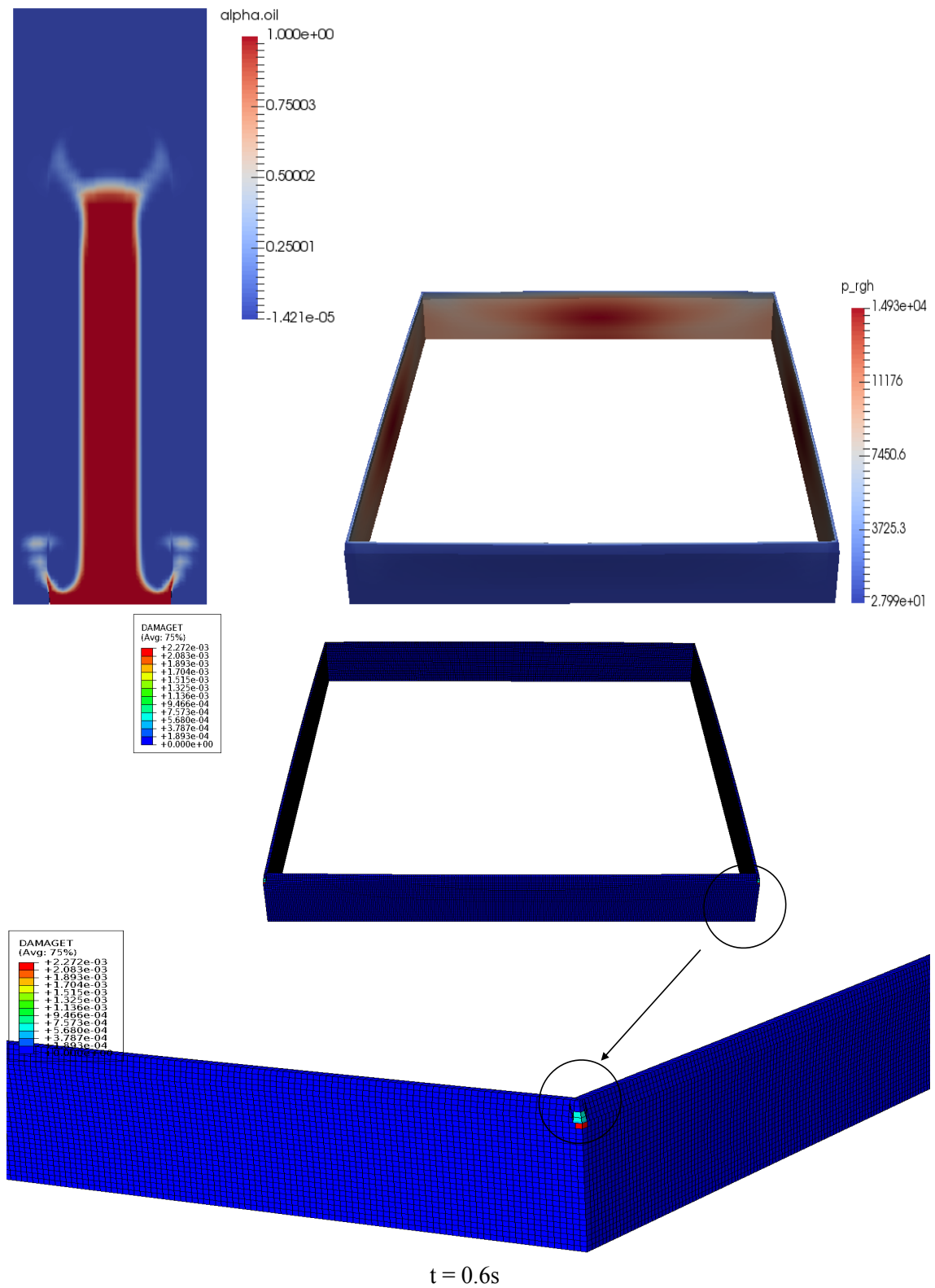


Figure 6.59: Flow behaviour and tensile damage of a UHP-FRC square wall subjected to a centred load and incorporating COAST and starter bars at  $t = 0.6s$

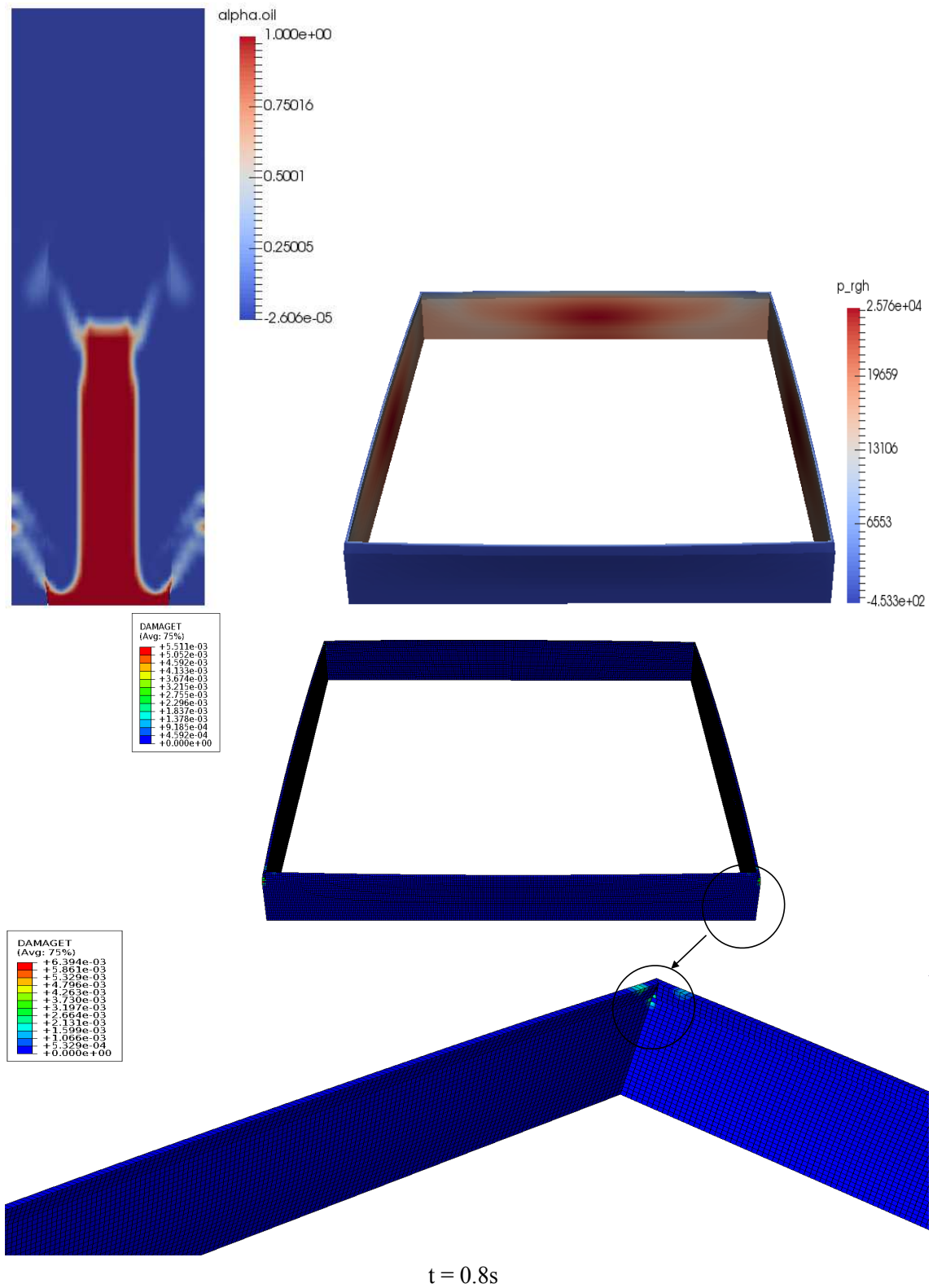


Figure 6.60: Flow behaviour and tensile damage of a UHP-FRC square wall subjected to a centred load and incorporating COAST and starter bars at  $t = 0.8s$

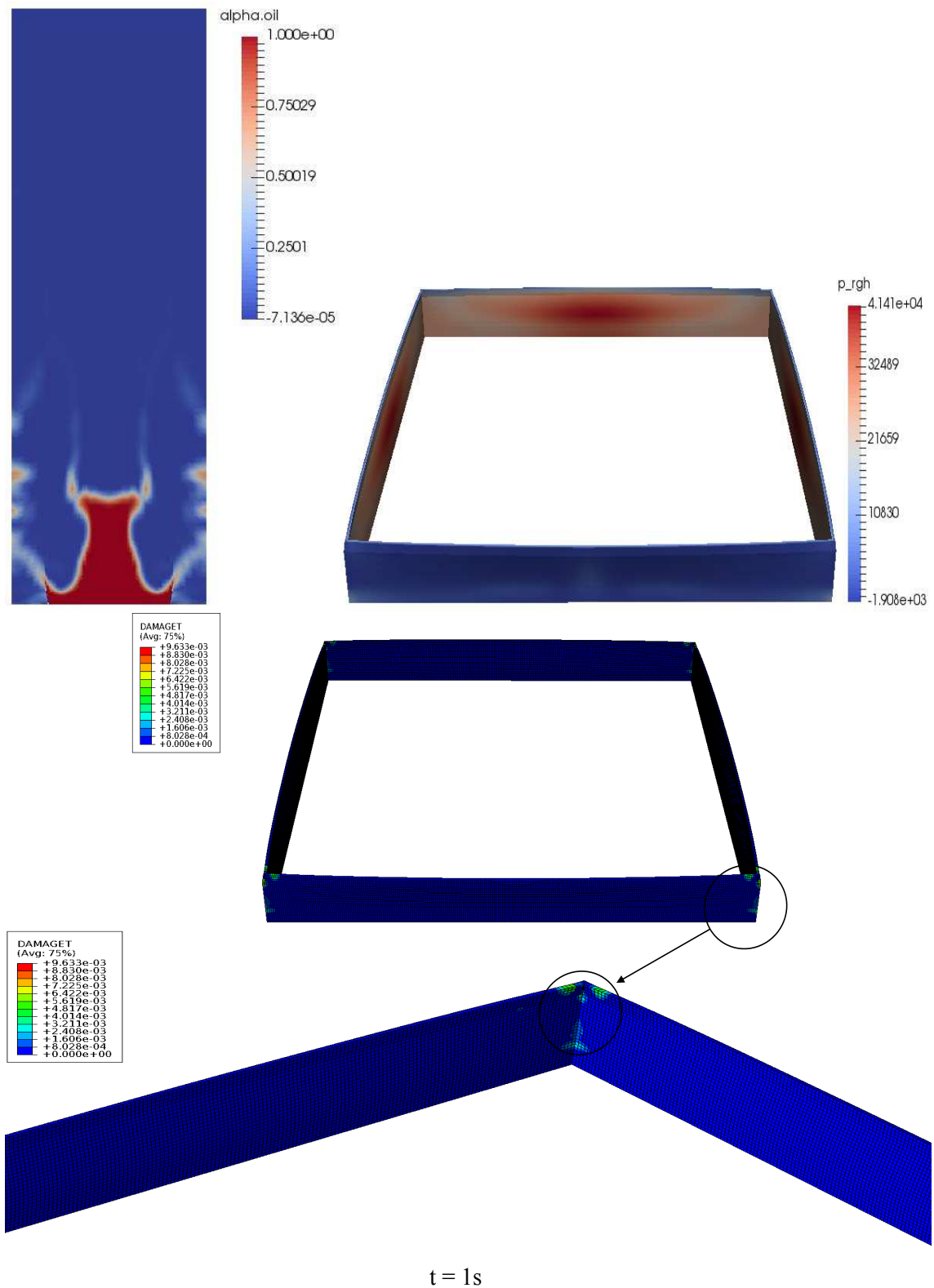


Figure 6.61: Flow behaviour and tensile damage of a UHP-FRC square wall subjected to a centred load and incorporating COAST and starter bars at  $t = 1s$

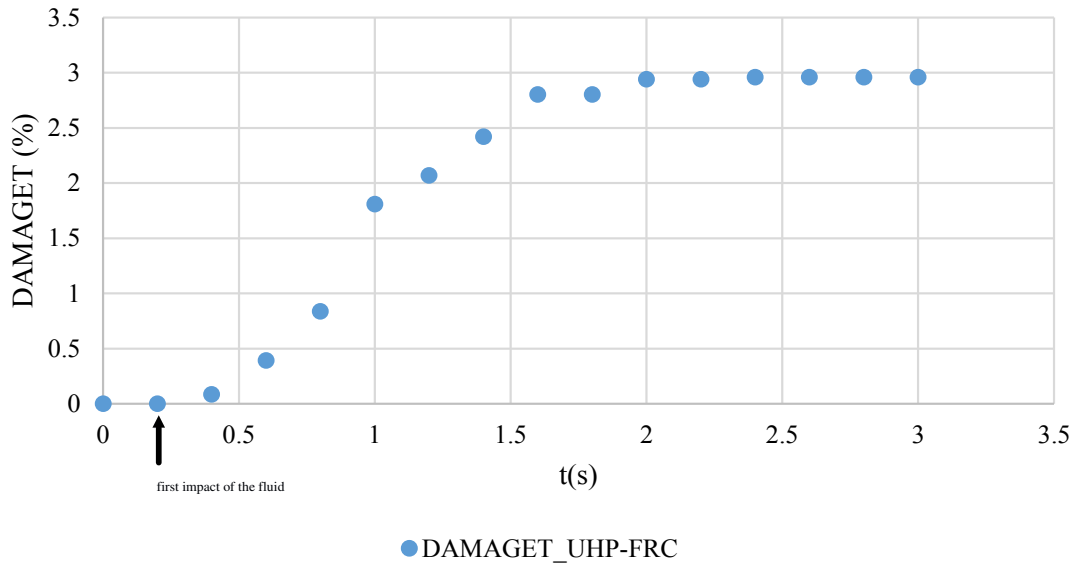


Figure 6.62: Tensile damage of UHP-FRC square wall incorporating COAST

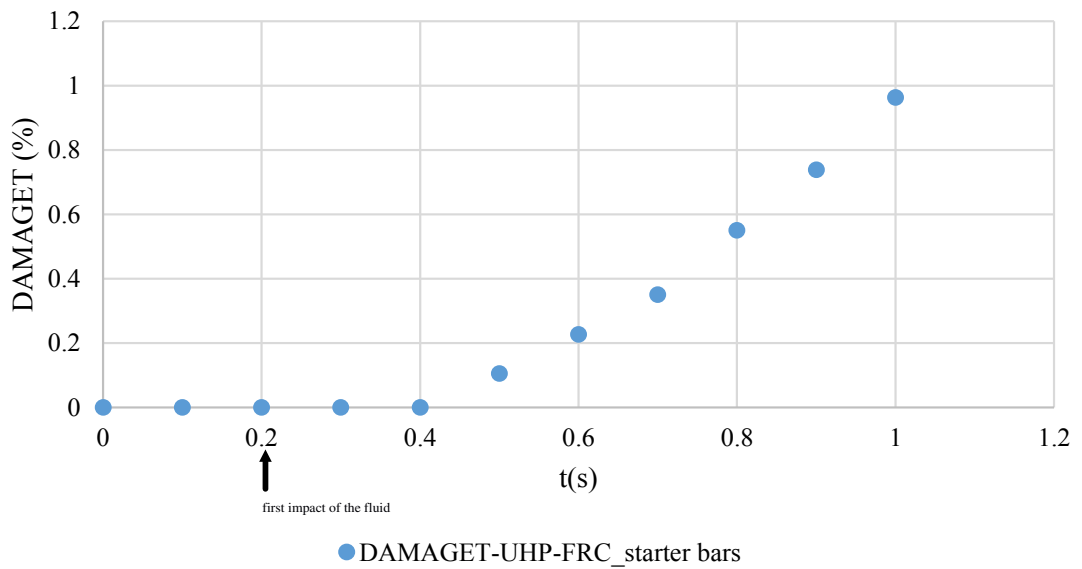


Figure 6.63: Tensile damage of UHP-FRC square wall incorporating COAST and starter bars

### 6.3.3.1 Comparison between plain UHP-FRC wall and UHP-FRC wall incorporating starter rebars

Figure 6.64 presents a comparison between a bund wall made of plain UHP-FRC and a bund wall incorporating starter bars in terms of tensile damage. The starter bars contribute to reduce the tensile damage by approximately 50% at  $t = 1$  s. This

design of the bund wall incorporating COAST and starter bars is the new design of the bund wall proposed by this research work.

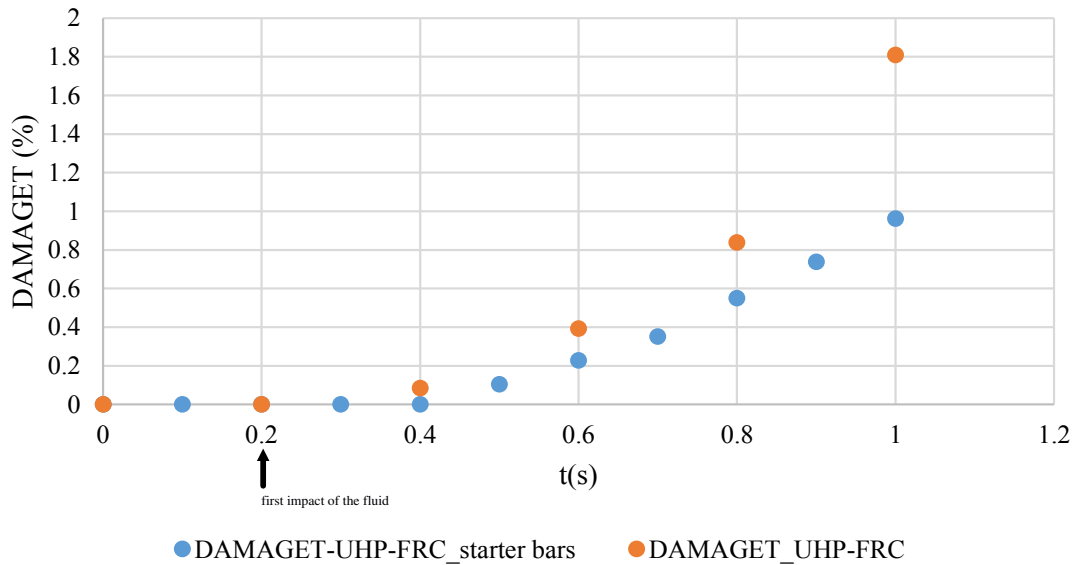


Figure 6.64: Comparison of the structural response between UHP-FRC wall and UHP-FRC wall incorporating starter bars

### 6.3.4 Comparison between plain and UHP-FRC walls

Figure 6.65 presents a comparison in tensile damage between a standard square bund wall made of plain concrete and a square bund wall made of plain UHP-FRC with the incorporation of COAST. The effect of using UHP-FRC is significant and aims to maintain the structural integrity of the bund wall. At  $t = 0.6\text{s}$ , the tensile damage for the plain concrete bund wall is equal to 98.9%, while it is only 0.39% for the UHP-FRC bund wall, which results in a reduction of more than 99%. The tensile damage that occurred at the UHP-FRC wall was very minor and would be repairable. This behaviour confirms what is stated in chapter 3 in terms of the ability of UHP-FRC for withstanding impact loading. The reduced number of voids and microcracks is another feature that makes this material a good choice for the bund walls as the escaped material cannot leak through it.

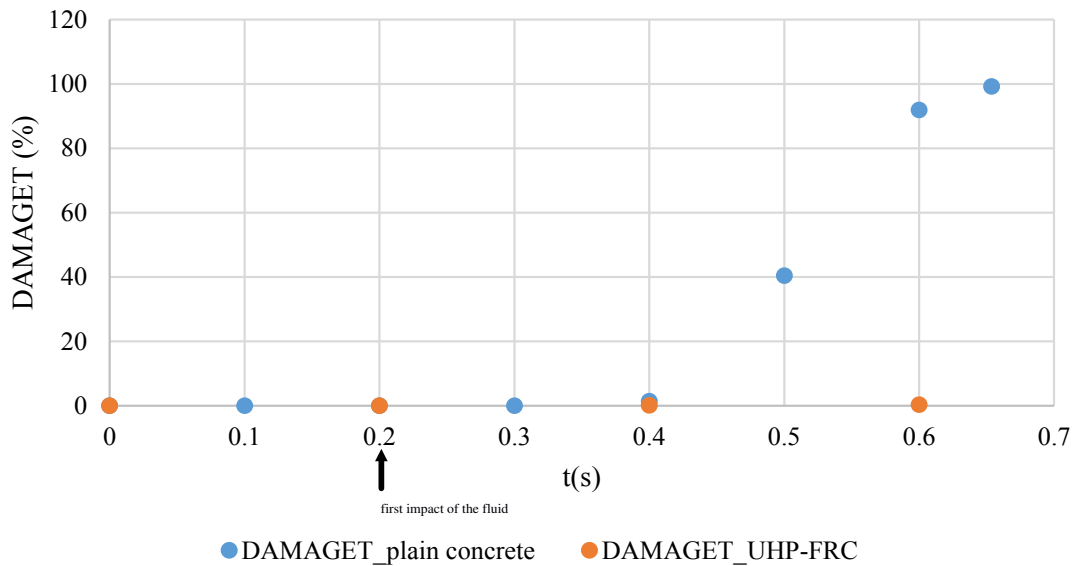


Figure 6.65: Comparison of the structural response between plain concrete wall and UHP-FRC wall

## 6.4 Critical appraisal of the FSI simulation

FSI modelling was successful in simulating the response of the bund wall under the impact loading. Although only the simulation of the flat wall was validated against the experiment, where only elastic deformations were caused, the other simulations still give an insight into the behaviour of the structures. Bringing a structure to a state of damage under a soft impact is not possible to investigate experimentally due to the space limitation of the laboratory and the safety rules that impose restrictions on the fluids that can be used. Hard impact problems might be feasible to investigate in the laboratory since the velocity can be increased relatively more easily than in the case of soft impact problems. Reaching the amount of pressure that causes the damage can be achieved either through using greater heights of fluid or using a denser fluid.

For UHP-FRC, the orientation of fibres is random, which makes the material behaviour anisotropic. However, the CDP model uses the concept of isotropic damaged elasticity along with isotropic tensile and compressive plasticity, as stated in chapter 3. Additionally, the modelling of UHP-FRC with the CDP model does not take into

account the interaction of the fibres with the concrete matrix. These simplifications might affect the results, but to date, this tends to be the modelling approach of UHP-FRC used within the research community.

The coupled time step used in the modelling is 0.001s. Although, this is a reasonable choice for the physical impact time, the numerical stability, which requires very small time increments was violated. As stated in chapter 3, there is a requirement on the stable time increment in the case of using the explicit solver in Abaqus. At the start of each simulation, Abaqus issues a warning about the required time step, which ensures stable results. The stable time increment required across all the simulations was in the order of  $10^{-6}$ s. This is impossible to satisfy taking into account the limitations in the hardware used and the time constraints of the project. Satisfying the very tight increment for Abaqus will require using the same time step for OpenFOAM apart from increasing the communication time between the two software packages. For example, for the simulation of the flat wall using 2mm element length, the FSI simulation took up to 3 hours to simulate 0.15s, while only 5min was needed to run the fluid simulation separately. Simulating the bund wall took a significant time, in some cases it required more than a month using a computer with a core i7 processor. If the stable time increment is used, this will not only increase the time required for the simulation, but also the size of data which needs more disk space.

The sub-cycling option was selected as indicated in Figure 4.26, which allows Abaqus to preform sub-cycles for each time step sent from OpenFOAM. Despite that, some instability in the results for certain cases was still occurring, as indicated in Figure 6.66. As mentioned in chapter 3, Abaqus specifies that the variation in the total energy must be within 1% to accept the stability of the results. It is clear from Figure 6.66 that the variation of the total energy is more than 1%. Whilst, for some other cases, the violation of the stability time increment did not affect the stability of the results as indicated in Figure 6.67, that corresponds to the simulation of a rectangular bund wall made of plain concrete under a centred load. The sudden variation of the total energy occurring at the end of the simulation might be related

to the significant damage of the structure. A relationship between the stability of the results and problems involving damage is worth investigating in the future. Undertaking a mesh dependency is an essential step in FEA to ensure that the results do not change with elements size. Taking into account the constraints specified above, if a mesh refinement is performed without refining the time step, this might result in erroneous results. Simulating the problem of the collapse of the storage tank under impact load using the utilised software for this project will need much more powerful hardware to satisfy the requirements of each software package. Even though the FSI simulations need more refinements to ensure the accuracy of the results, they still give an insight into the problem as this was never solved previously.

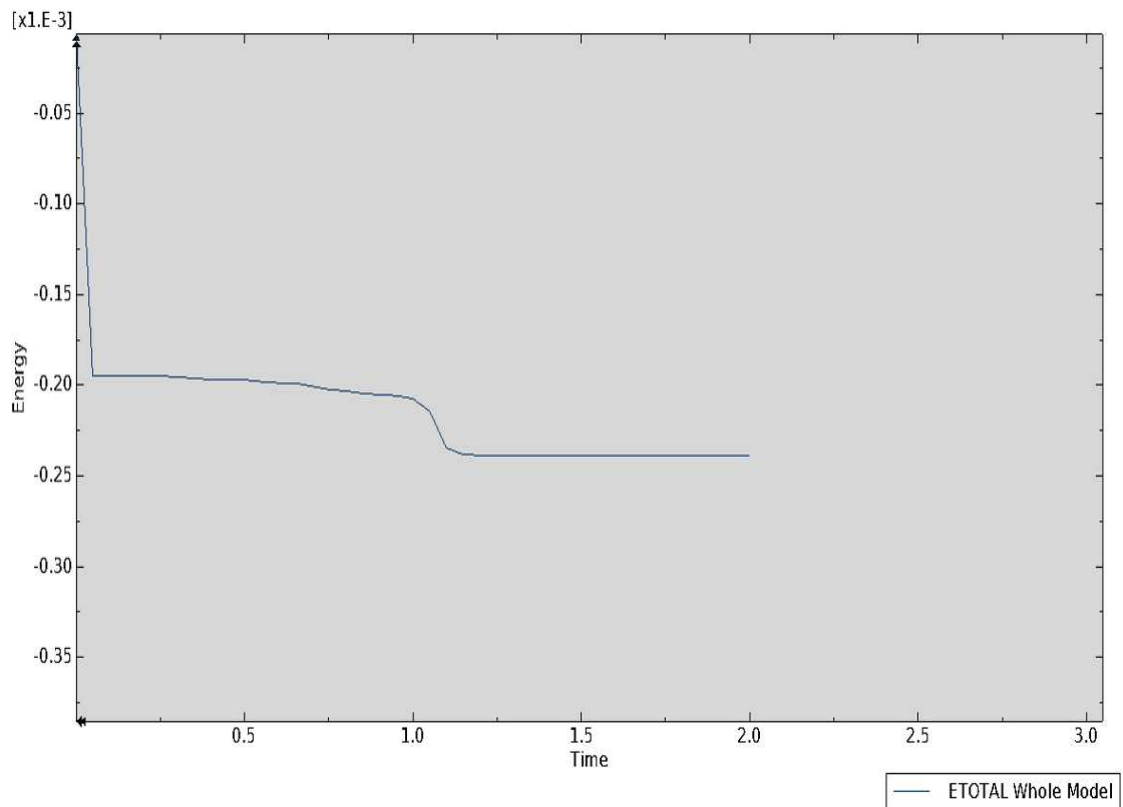


Figure 6.66: Total energy of the simulation of plain concrete circular wall

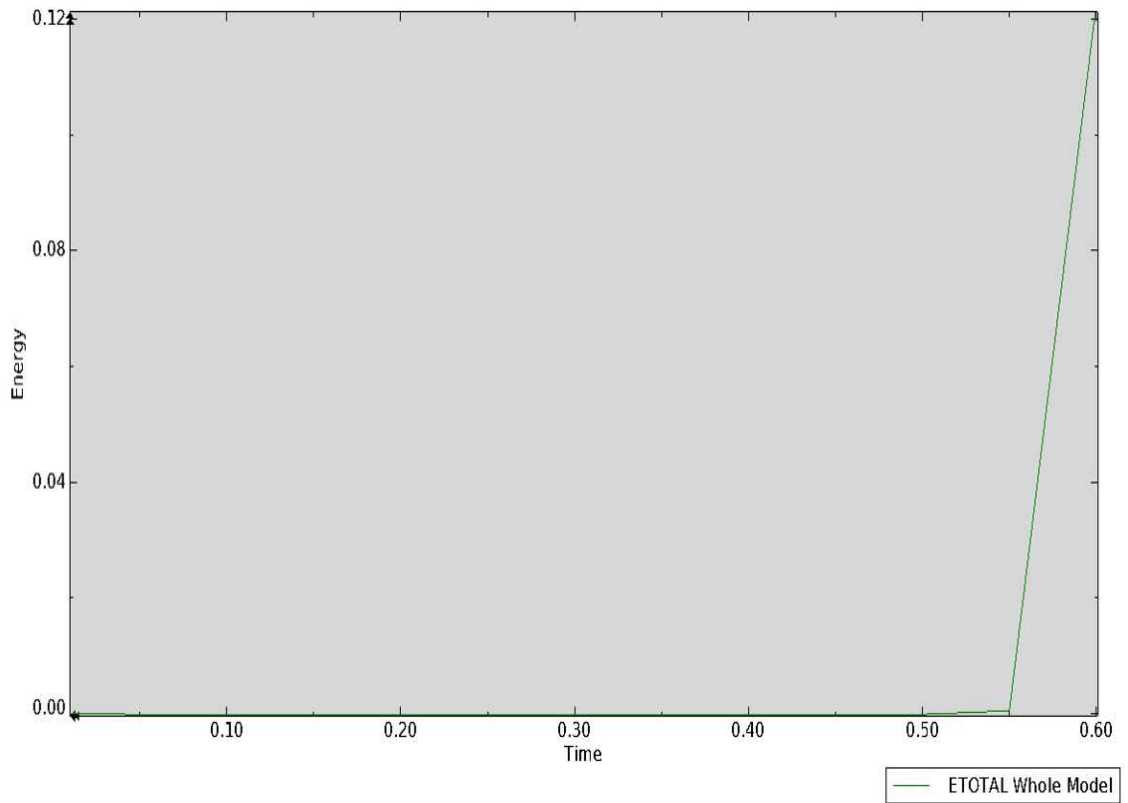


Figure 6.67: Total energy of the simulation of plain concrete rectangular wall

## 6.5 Similitude of structural model

The dimensional analysis is performed on the circular, square and rectangular bund walls depicted in Figures 6.68, 6.69 and 6.70, respectively.

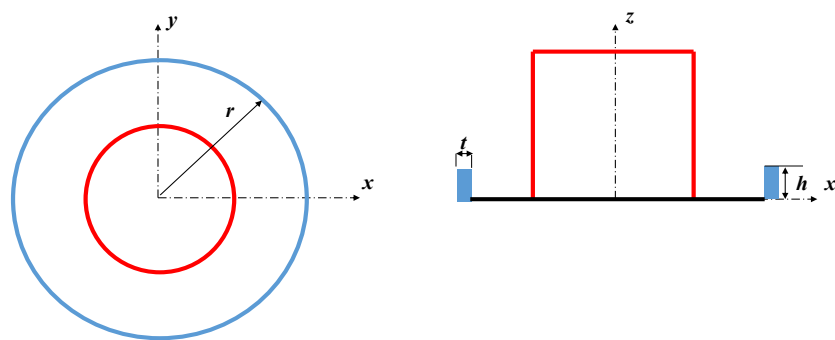


Figure 6.68: Circular bund

**Step 1:** listing of all pertinent variables

Variables related to the load:

- $U$ : velocity of the fluid flow

- $\rho_f$ : density of the fluid
- $t_i$ : any significant time

Variables related to the geometry:

- $t$ : thickness of the bund wall
- $h$ : height of the bund wall
- $r$ : radius of the bund wall

Variables related to the material:

- $E$ : modulus of elasticity
- $\sigma_y$ : yield stress of the material
- $\rho_m$ : density of the material

Predicted variable

- $u$ : displacement in the material

**Step 2:** Assigning the basic dimensions to the variables:

Here,  $M$ ,  $L$  and  $T$  are the adopted basic dimensions. The basic dimensions corresponding to each of the variable are listed in Table 6.3.

Table 6.3: Basic dimensions of the variables

Number of variable	Variable	Basic dimensions
1	$U$	$LT^{-1}$
2	$\rho_f$	$ML^{-3}$
3	$t_i$	$T$
4	$t$	$L$
5	$h$	$L$
6	$r$	$L$
7	$E$	$ML^{-1}T^{-2}$
8	$\sigma_y$	$ML^{-1}T^{-2}$
9	$\rho_m$	$ML^{-3}$
10	$u$	$L$

**Step 3:** Determining the required number of pi terms:

$r_d = n_d - k_d = 10 - 3 = 7$ , where  $r_d$ ,  $n_d$  and  $k_d$  are the number of pi terms, number of variables and number of basic dimensions, respectively.

**Step 4:** Selecting the repeating variables:

The repeating variables are  $t$ ,  $\rho_m$  and  $E$ .

**Step 5:** Deriving the pi terms:

1. Non-repeating variable  $U$

$$\Pi_1 = U(t^a \rho_m^b E^c) = LT^{-1} L^a (ML^{-3})^b (ML^{-1}T^{-2})^c \quad (6.1)$$

Select values for powers  $a$ ,  $b$  and  $c$  such that dimensions are all to the zero power.

$$L: 1 + a - 3b - c = 0 \longrightarrow a = 0$$

$$M: b + c = 0 \longrightarrow b = \frac{1}{2}$$

$$T: -1 - 2c = 0 \longrightarrow c = -\frac{1}{2}$$

This gives the first dimensionless group

$$\Pi_1 = U \sqrt{\frac{\rho_m}{E}} \quad (6.2)$$

This process is repeated for all variables which gives the following pi terms:

2. Non-repeating variable  $\rho_f$

$$\Pi_2 = \frac{\rho_f}{\rho_m} \quad (6.3)$$

3. Non-repeating variable  $t_i$

$$\Pi_3 = t_i \frac{E}{\rho_m t^2} \quad (6.4)$$

4. Non-repeating variable  $h$

$$\Pi_4 = \frac{h}{t} \quad (6.5)$$

5. Non-repeating variable  $r$

$$\Pi_5 = \frac{r}{t} \quad (6.6)$$

6. Non-repeating variable  $\sigma_y$

$$\Pi_6 = \frac{\sigma_y}{E} \quad (6.7)$$

7. Non-repeating variable  $u$

$$\Pi_7 = \frac{u}{t} \quad (6.8)$$

**Step 6:** Expressing the relationship between the pi terms

$$\Pi_7 = f(\Pi_1, \Pi_2, \Pi_3, \Pi_4, \Pi_5, \Pi_6) \quad (6.9)$$

which is in terms of the dimensionless numbers of this problem

$$\frac{u}{t} = f\left(U \sqrt{\frac{\rho_m}{E}}, \frac{\rho_f}{\rho_m}, t_i \sqrt{\frac{E}{\rho_m t^2}}, \frac{h}{t}, \frac{r}{t}, \frac{\sigma_y}{E}\right). \quad (6.10)$$

If the model is designed and operated so

$$\Pi_{1m_d} = \Pi_{1p_d}, \quad (6.11)$$

$$\Pi_{2m_d} = \Pi_{2p_d}, \quad (6.12)$$

$$\Pi_{3m_d} = \Pi_{3p_d}, \quad (6.13)$$

$$\Pi_{4m_d} = \Pi_{4p_d}, \quad (6.14)$$

$$\Pi_{5m_d} = \Pi_{5p_d} \quad (6.15)$$

and

$$\Pi_{6m_d} = \Pi_{6p_d}, \quad (6.16)$$

it follows that

$$f(\Pi_{1m_d}, \Pi_{2m_d}, \Pi_{3m_d}, \Pi_{4m_d}, \Pi_{5m_d}, \Pi_{6m_d}) = f(\Pi_{1p_d}, \Pi_{2p_d}, \Pi_{3p_d}, \Pi_{4p_d}, \Pi_{5p_d}, \Pi_{6p_d}). \quad (6.17)$$

From equations 6.9 and 6.17, it is apparent that

$$\Pi_{7m_d} = \Pi_{7p_d}. \quad (6.18)$$

By using a scale factor  $n_s$  between model and prototype, i.e. all the dimensions are divided by the same scale factor, it follows from equations 6.14 and 6.15 that

$$h_{p_d} = n_s h_{m_d} \quad (6.19)$$

and

$$r_{p_d} = n_s r_{m_d}. \quad (6.20)$$

By using the same materials of bund wall and fluid between model and prototype, equations 6.16 and 6.12 are satisfied automatically giving

$$\left(\frac{\sigma_y}{E}\right)_{p_d} = \left(\frac{\sigma_y}{E}\right)_{m_d} \quad (6.21)$$

and

$$\left(\frac{\rho_f}{\rho_m}\right)_{p_d} = \left(\frac{\rho_f}{\rho_m}\right)_{m_d}. \quad (6.22)$$

And, if using the same velocity between the model and prototype by satisfying equation 6.11, i.e

$$U_{p_d} = U_{m_d}, \quad (6.23)$$

and a time scale that satisfies equation 6.13

$$(t_i)_{p_d} = (n_s t_i)_{m_d}, \quad (6.24)$$

The displacement in the prototypes is

$$u_{p_d} = n_s u_{m_d} \quad (6.25)$$

Using the same method, the relationship between the pi terms for the square bund wall is

$$\frac{u}{t} = f\left(U\sqrt{\frac{\rho_m}{E}}, \frac{\rho_f}{\rho_m}, t_i\sqrt{\frac{E}{\rho_m t^2}}, \frac{h}{t}, \frac{l}{t}, \frac{\sigma_y}{E}\right), \quad (6.26)$$

where  $l$  is the length of the square bund wall.

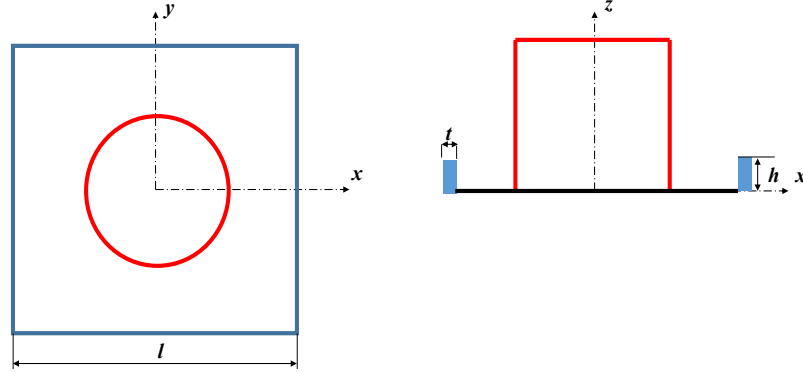


Figure 6.69: Square bund

The relationship between the pi terms for the rectangular bund wall is

$$\frac{u}{t} = f\left(U\sqrt{\frac{\rho_m}{E}}, \frac{\rho_f}{\rho_m}, t_i\sqrt{\frac{E}{\rho_m t^2}}, \frac{h}{t}, \frac{l}{t}, \frac{w}{t}, \frac{\sigma_y}{E}\right), \quad (6.27)$$

where  $l$  and  $w$  are the length and the width of the rectangular bund wall, respectively.

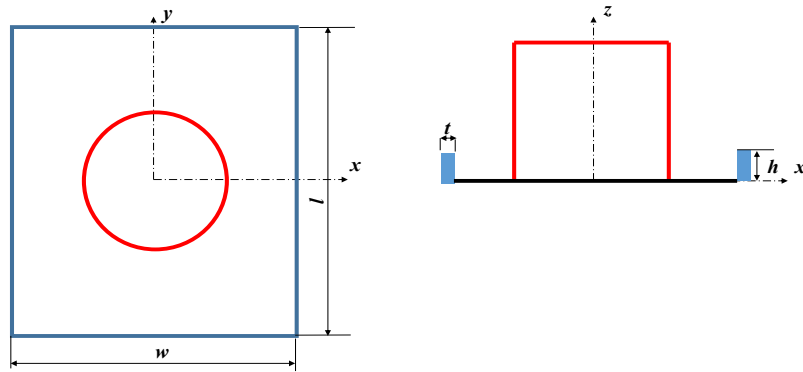


Figure 6.70: Rectangular bund

## 6.6 Summary

This chapter presented the FSI simulation results of the collapse of a storage tank with various configurations. The modelling was performed by coupling InterFOAM solver in OpenFoam 17.06 software to the explicit solver of Abaqus 2017 via MpCCI

4.5.2 software. The coupling approach was first validated against experimental results by simulating the response of a flat wall made of plain concrete under the impact of water flow. The various numerical simulations covered the investigation of the performance of bund walls made of plain concrete with circular, square and rectangular shapes. The modes of failure comprised a centred load, where the tank occupies a central location and an off-centred load with the tank biased towards one side of the bund wall. Another simulation studied the performance of a reinforced concrete wall designed according to the BS 8007:1987 standard. The last part of the simulations consisted of studying the performance of a new design of bund wall. UHP-FRC was adopted as an alternative material for the wall construction, as it is a good candidate to resist impact loading and can reduce the number of voids and micro-cracks. For the new design, the incorporation of COAST as a mitigation technique was proposed to reduce the overtopping quantities. This work provided an insight into the behaviour of the bund wall under dynamic load which was never studied previously where previous studies only focused on quantifying the overtopping quantities, dynamic pressures and investigating the effect of incorporating mitigation measures. This work allows to provide a guidance on the most efficient construction of bund walls to minimise the crack. The main outcomes of this chapter are summarised below:

- The use of plain concrete might compromise the structural integrity of the bund wall. Square and rectangular bund walls totally lose their integrity, while a circular shape has a better performance. The circular bund walls are rarely used in the industry and shapes similar to the square and rectangular walls are more often adopted in the UK.
- An off-centred loading, which represents a more realistic representation of the loading configuration causes more extensive failure to the structure. The magnitude of the bias of the load towards a certain side depends on the site specific conditions. A random value was chosen in these simulations merely to allow a comparison against a centred load configuration.
- A structure designed properly to the standard, which is very conservative is

less likely to fail under impact loading but huge quantities of material can escape the banded area resulting in serious spill effects. The standard might not be appropriate to cope with other dynamic loading such as explosion.

- The use of UHP-FRC allows a significant reduction in the amount of damage and confines damage near the corners of the wall. This might be reduced if round corners are constructed instead of the sharp ones. A reduction in the tensile damage of more than 99% compared to the plain concrete, was achieved with the use of UHP-FRC
- Some limitations related to the hardware used and the time constraints of the project did not permit further refinement of the simulations. This caused some stability issues in the FEA results, but gave a substantial insight into the extent of the problem.

# Chapter 7

## Conclusions and future works

### 7.1 Introduction

This research project investigated the structural integrity of bund wall systems under the catastrophic collapse of storage tanks. The investigation included conducting many simulations to confirm firstly the performance of InterFOAM under many configurations of tank and wall arrangements and secondly, to study the performance of the bund wall via FSI modelling. The main results of this project indicate that old bund wall structures, especially those which are not designed according to the standard are susceptible to fail under extreme loading conditions and that a considerable amount of stored material can overtop the bund wall and result in serious consequences. While many publications highlight that the available bund walls are not designed to withstand dynamic loading, no previous research attempted to investigate their behaviours in the wake of catastrophic failure of storage tanks. The available research in the literature only studied the dynamic pressures exerted on the bund wall and the related overtopping fractions along with the effect of incorporating mitigation measures on the losses in stored material. The main novelty of this work lies in studying the performance of bund wall under impact loading which can provide guidance to regulators, operators and managers on the best configuration of the bund wall to reduce the incurred damage to the structure. Furthermore, incorporating UHP-FRC as a construction material is a new idea, as well as the solving approach using FSI modelling, which allows the solution to the problem to be explored more precisely. The aim and the objectives have been achieved, as outlined in chapter 1, by studying the performance of InterFOAM and validating the results against the experimental data, conducting an optimisation study of the

mitigation techniques, studying the structural integrity of the bund walls themselves and performing a preliminary dimensional analysis study to predict the behaviour of the structure at the full scale.

## **7.2 Conclusions**

### **7.2.1 The performance of InterFOAM**

The performance of InterFOAM was studied through conducting extensive CFD simulations on various bund wall and tank arrangements with validation provided against experimental results. The investigation included studying the effect of separation distance between the tank and the bund wall, the capacity of the tank, high collar bund walls, height of the fluid, shapes of the bund walls and the temperature of the fluid released. The simulation results were validated against the experimental results of the dynamic pressures and overtopping fractions from secondary data sources. The solver was better at predicting the values of overtopping fractions than the dynamic pressures. InterFOAM allowed the generation of good results for dynamic pressures at 38.53% and 43.11% for overtopping fractions, where the relative error is less than 15%. The extensive number of simulations under many configurations allowed the identification of the range of radii where InterFOAM gives accurate results. The relative error becomes important when separation distances increase. A relative error in dynamic pressure is below 10% for separation distances less than 0.822m This problem was reported in Ash (2010) as well. However, the CFD results obtained from InterFOAM outperformed the results obtained from Ash (2010) with a significant reduction in the relative error for dynamic pressures. The maximum relative error for dynamic pressures obtained in Ash (2010) is 1089% while it is only 90% obtained in only one case in this work and below 15% for a significant number of simulations.

### **7.2.2 The optimisation of mitigation measure**

The mitigation measure COAST reported in Ash (2010) was optimised in this research project. COAST at an inclination angle of 80 degrees is the adopted mitigation technique. While Ash (2010) proposed that the use of MOTIF in combination with COAST allows to significantly minimise the overtopping fractions, CFD simulations conducted in this research showed that for small separation distances, the inclusion of MOTIF modifies the flow structure in such a way it hits the top of the wall at the first impact. This can increase the risk of failure by increasing the overturning moment. The inclusion of COAST permits significant reductions in overtopping quantities. The cost of incorporating COAST is not significant compared to the cost of the bund wall if taking into account the savings in the losses. These simulations were supplemented by modelling the partial failure of storage tanks, as it is a more frequent problem (Atherton, 2008). The incorporation of MOTIF allowed a significant reduction in overtopping fractions and dynamic pressures for the partial failures.

### **7.2.3 The structural integrity of the bund wall**

FSI simulations permitted the investigation of the performance of the bund walls under the catastrophic failure of storage tanks. Through this study, walls made of plain concrete, reinforced concrete and UHP-FRC were studied. The plain concrete walls failed in most of the cases with the exception of the circular bund wall, where only minor damage occurred. A more realistic simulation of the actual problem was conducted through investigating the case of a structure being subjected to an off-centred load. This represents the case of a fluid flow hitting an obstacle, which diverts its direction. This case causes an earlier failure of the structure. This indicates that many of the current installations are at risk. The simulation of a reinforced concrete wall designed according to the standard shows that the bund wall can withstand the dynamic loading, but a considerable amount of materials can be lost. The use of UHP-FRC with the incorporation of COAST can alleviate this problem of overtopping and diminish the damage. A reduction of 99% of damage

can be achieved using UHP-FRC when compared to plain concrete. Although the cost of UHP-FRC is much higher than the standard concrete, its use is still beneficial taking into consideration its features of packing density and ductility.

#### **7.2.4 The benefit to stakeholders and beneficiaries**

The outcomes of this project can be of a high importance for regulators, operators and managers, especially where bund walls are old and sites are classified as upper-tier. The benefits of this project will allow greater understanding of the behaviour of the current bund walls and to plan for the construction of new walls, with the purpose of reducing the impacts in the case of sudden releases. Although the catastrophic failure of storage tanks is not frequent and the current regulation does not place a requirement on providing a structure appropriate for dynamic loading, many publications highlight that the impacts of such failures are disastrous and the current bund walls are not able to cope with such circumstances.

### **7.3 Recommendations for future work**

This research project presented preliminary results of the behaviour of bund walls. Therefore, it is open to further future works related to CFD and FEA modelling alike.

#### **7.3.1 Recommendations related to CFD**

- The effect of the ground can be modelled in future simulations as this can change the flow behaviour. For the purpose of evaluating the performance of the solver, the ground was considered smooth, while in real sites, the ground is usually rough with the possibility of using porous rough materials.
- A mesh sensitivity study must be performed to ensure that the results do not vary significantly with the mesh size.
- Solving the collapse of the storage tank using the newly developed solver InterIsoFOAM which offers an alternative of the MULES interface capturing

method by employing an isoadvect algorithm (Roenby et al., 2016). This might enhance the results, where significant relative errors were obtained.

- Investigating the problem of collapse of a storage tank using different fluids such as diesel, at temperatures representative of each season in the UK.
- Studying the failure of storage tanks in a domino effect, as this will exert different pressures on the bund wall and the flow structure will be different from the case of a single tank failure.
- Only the angle of optimisation of COAST was optimised in this study and the dimensions of the baffle was taken from Ash (2010). Future works can optimise the width of the baffle along with studying the effect of other shapes of COAST such as curved baffles.

### **7.3.2 Recommendations related to FEA**

- Considering the effect of a hard impact combined with a soft impact. A hard impact can be caused by debris flying from a tank shell or its accessories hitting the wall.
- Performing a structural optimisation study to reduce the quantity of the material needed. There are numbers of software packages that perform the design optimisation such as ISIGHT.
- Performing a mesh dependency study for the wall by satisfying the stable time increment. This will require running the simulations on much more powerful hardware than the one used in this project.
- In this study, only the square bund wall was simulated when using UHP-FRC and incorporating COAST. Future works can focus on investigating the effect of varying the height of the wall as well as studying the performance of rectangular bund walls.
- Performing a cost analysis study of the use of UHP-FRC over the use of reinforced concrete.

- Simulating the behaviour of the wall under other modes of dynamic loading such as explosion conditions.

### **7.3.3 Recommendations related to dimensional analysis**

Preliminary study was conducted for the purpose of predicting the structural behaviour of the bund wall at the full scale by applying the Buckingham theorem. This study can be developed further by conducting more simulations to obtain the design curves that allow to predict the crack width at the full scale.

## **7.4 Summary**

The significance of this study is that it gives a solution to provide structures able to withstand the impact loading and minimise the losses in materials to a reasonable extent. This was achieved through the use of UHP-FRC and the incorporation of minor modifications to the secondary containment. The series of simulations conducted allows an insight into this very important industrial problem and permits a reduction in the consequences on the economy, environment and immediate community. There is no previous research available in the literature which attempted to study the structural performance of the bund wall under impact loading which makes this research novel.

# References

- Acker, P. and Behloul, M. (2004), Ductal® technology: A large spectrum of properties, a wide range of applications, *in* ‘Proc. of the Int. Symp. on UHPC Kassel, Germany’, pp. 11–23.
- Anderson, J. D. (1995), *Computational fluid dynamics: The basics with applications*, McGraw-Hill.
- ARIA (2006), ‘Failure of an artho-cresol storage tank’.
- ARIA (2009), ‘Sudden opening of a crude oil tank bottom’, online.
- Ash, J. W. (2010), Mitigation of the catastrophic failure of the primary containment in the bulk storage industry, PhD thesis, Liverpool John Moores University.
- Asprone, D., Cadoni, E. and Prota, A. (2009), ‘Tensile high strain-rate behavior of reinforcing steel from an existing bridge’, *ACI Structural Journal* **106**(4), 523–529.
- Atherton, W. (2008), An empirical investigation of catastrophic and partial failures of bulk storage vessels and subsequent bund wall overtopping and dynamic pressures, PhD thesis, Liverpool John Moores University.
- Banthia, N., Mindess, S., Bentur, A. and Pigeon, M. (1989), ‘Impact testing of concrete using a drop-weight impact machine’, *Experimental Mechanics* **29**(1), 63–69.
- Bathe, K.-J. (2014), *Finite element procedure*, Klaus-Jurgen Bathe.
- Belytschko, T., Liu, W. K., Moran, B. and Elkhodary, K. (2013), *Nonlinear finite elements for continua and structures*, John Wiley & Sons.
- BFUP and AFGC (2002), ‘Ultra high performance fibre-reinforced concretes: interim recommendations’, *AFGC/SETRA working group* .

- Blum, J. (2017), ‘Failures of floating-roof oil tanks during harvey raise concerns’, online.  
**URL:** <https://www.houstonchronicle.com/business/energy/article/Failures-of-floating-roof-tanks-during-Harvey-12269513.php>
- Boston University (2012a), ‘ME702-computational fluid dynamics - video lesson1’, online.
- Boston University (2012b), ‘ME702-computational fluid dynamics - video lesson25’, online.
- Brackbill, J. U., kothe, D. B. and Zemach, C. (1992), ‘A continuum method for modelling surface tension’, *Journal of computational physics* **100**(2), 335–354.
- Bredberg, J. (2000), On the wall boundary condition for turbulence models, Technical report, Department of Thermo and fluid dynamics- Chalmers University of Technology.
- BS 8007 (1987), ‘Code of practice for design of concrete structures for retaining aqueous liquids’.
- BS EN 1992-3 (2006), ‘Eurocode 2. design of concrete structures. liquid retaining and containing structures’.
- Campbell, R. L. (2010), Fluid-structure interaction and inverse design simulations for flexible turbomachinery, PhD thesis, The Pennsylvania State University.
- CEB-FIP (1988), *Concrete structures under impact and impulsive loading: synthesis report*, Comite euro-international du beton.
- Chang, J. I. and Lin, C.-C. (2006), ‘A study of storage tank accidents’, *Journal of Loss Prevention in the process industries* **19**(1), 51–59.
- Chanvillard, G. and Rigaud, S. (2003), Complete characterization of tensile properties of ductal uhpfr according to the french recommendations, in ‘Proceedings of the 4th International RILEM workshop High Performance Fiber Reinforced Cementitious Composites’, pp. 21–34.

- Clark, S. O., Deaves, D. M., Lines, I. G. and Henson, L. C. (2001), *Effects of secondary containment on source term modelling*, Her Majesty's Stationery Office.
- Copper, C. (2006), Epa provided quality and timely information on hurricane katrina hazardous material releases and debris management, Technical report, U.S. Environmental Protection Agency- Office of Inspector General.
- Dellinger, A. (2018), 'City evacuated, state of emergency declared in wisconsin county following oil refinery explosion', online.  
**URL:** <https://gizmodo.com/city-evacuated-state-of-emergency-declared-in-wisconsin-1825583765>
- Deshpande, S. S., Anumolu, L. and Trujillo, M. F. (2012), 'Evaluating the performance of the two-phase flow solver interfoam', *Computational Science and Discovery* **5**(1), 014016.
- Dugat, J., Roux, N. and Bernier, G. (1996), 'Mechanical properties of reactive powder concretes', *Materials and structures* **29**(4), 233–240.
- Eide, M. B. and Hisdal, J.-M. (2012), 'Ultra high performance fibre reinforced concrete (uhpfrc) - state of the art'.
- Environmental Containment Systems (2012), Secondary containment systems, Technical report, New Zealand Government.
- Fehling, E., Leutbecher, T. and Bunje, K. (2004), Design relevant properties of hardened ultra high performance concrete, in 'Int. Symp. on Ultra High Performance Concrete', Vol. 1, pp. 327–338.
- Figuroa, C., Vignon-Clemental, I., Jansen, K., Hughes, T. and Taylor, C. (2006), 'A coupled momentum method for modeling blood flow in the three-dimensional deformable arteries', *Computer Methods in Applied Mechanics and Engineering* (41-43), 5685–5706.
- Fraunhofer, S. (2018), *MpCCI documentation, version 4.5.2, part I, user manual*, Fraunhofer Institute for Algorithms and Scientific Computing SCAI, Germany.

- Godoy, L. A. (2007), ‘Performance of storage tanks in oil facilities following Hurricanes Katrina and Rita’, *Journal of performance of constructed facilities* **21**(6), 441–449.
- Graybeal, B. A. (2005), Characterization of the behavior of ultra-high performance concrete, PhD thesis, University of Maryland.
- Greenshields, C. J. (2015), Openfoam programmer guide- version 3.0.1, Technical report, OpenFOAM Foundation Ltd.
- Greenshields, C. J. (2018), Openfoam user guide- version 6, Technical report, OpenFOAM Foundation Ltd.
- Gyenes, Z. and Wood, M. H. (2014), Lessons learned from major accidents having significant impact on the environment, *in* ‘SYMPOSIUM SERIES’.
- Hassan, A. M. T. (2013), Ultra high performance fibre reinforced concrete for highway bridge applications, PhD thesis, University of Liverpool.
- Hedlund, F. H., Selig, R. S. and Kragh, E. K. (2015), ‘Large steel tank fails and rockets to height of 30 meters - rupture disk installed incorrectly’, *Safety and health at work* **7**(2), 130–137.
- Heyns, J. A. and Oxtoby, O. F. (2014), Modelling surface tension dominated multiphase flows using the vof approach, *in* ‘6th European Conference on Computational Fluid Dynamics’.
- Hirsch, C. (2007), *Numerical computational of internal and external flows: volume 1 fundamentals of computational fluid dynamics*, Elsevier.
- HSE (2001), ‘Comah major accidents notified to the european commission england, wales & scotland 1999-2000’.
- HSE (2011), ‘Buncefield: Why did it happen?’.
- HSE (2015a), ‘Control of major accident hazards (comah)’.
- URL:** <http://www.hse.gov.uk/comah/>

HSE (2015*b*), ‘Seveso iii directive’.

**URL:** <http://www.hse.gov.uk/seveso/index.htm>

Jasak, H. (1996), Error analysis and estimation for the finite volume method with applications to fluid flows, PhD thesis, Imperial College London, University of London.

JSCE (2008), Recommendations for design and construction of uhpfrc with multiple fine cracks, Technical report, Japan society of civil engineers.

Lee, J. and Fenves, G. L. (1998), ‘Plastic-damage model for cyclic loading of concrete structures’, *Journal of engineering mechanics* **124**(8), 892–900.

Leith, W. (2014), ‘Advances in earthquake science: the 50th anniversary of the great alaskan quake’.

Lopes, P. (2013), Free-surface flow interface and air-entrainment modelling using OpenFOAM, PhD thesis, University of Coimbra.

Lubliner, J., Oliver, J., Oller, S. and Onate, E. (1989), ‘A plastic-damage model for concrete’, *International Journal of Solids and Structures* **25**(3), 299–326.

McNaughton, J. (2013), Turbulence modelling in the near-field of an axial flow tidal turbine using code Saturne, PhD thesis, University of Manchester.

Megdiche, I. (2013), Localization of a swimming robot in a cylindrical above-ground tank, Master’s thesis, Rice University.

Menter, F. R., Kuntz, M. and Langtry, R. (2003), ‘Ten years of industrial experience with the SST turbulence model’, *Turbulence, heat and mass transfer* **4**(1), 625–632.

Morgan, G. C. J. (2012), Application of the interFoam VOF code to coastal wave/structure interaction, PhD thesis, University of Bath.

Mufson, S. (2017), ‘Chemical companies have already released 1 million pounds of extra air pollutants thanks to harvey’, online.

**URL:** <https://www.washingtonpost.com/news/energy-environment/wp/2017/09/04/chemical-companies-have-already-released-1-million-pounds-of-extra-air-pollutants-thanks-to-harvey/>

Munson, B. R., Young, D. F. and Huebsh, T. H. O. W. W. (2010), *Fundamentals of fluid mechanics, sixth edition*, Don Fowley.

National Research Council (1968), *The great Alaska earthquake of 1964*, National Academies.

Othman, H. A. B. (2016), Performance of ultra-high performance fibre reinforced concrete plates under impact loads, PhD thesis, Ryerson University.

Raja, R. S. (2012), Coupled fluid structure interaction analysis on a cylinder exposed to ocean wave loading, Master's thesis, Chalmers University of Technology.

Richard, P. and Cheyrezy, M. (1994), Reactive powder concrete with high ductility and 200-800 MPa compressive strength, in 'ACI Spring Convention, San Francisco, SP'.

Roenby, J., Bredmose, H. and Hrvoje, J. (2016), 'A computational method for sharp interface advection', *Royal Society open science* **3**(11), 160405.

Ross, M. R. (2006), Coupling and simulation of acoustic fluid-structure interaction systems using localized lagrange multipliers, PhD thesis, University of Colorado.

Rusche, H. (2002), Computational fluid dynamics of dispersed two-phase flows at high phase fractions, PhD thesis, Imperial College London, University of London.

Sahasrabudhe, S. N., Rodriguez-Martinez, V., O'Meara, M. and Farkas, B. E. (2017), 'Density, viscosity, and surface tension of five vegetable oils at elevated temperatures: Measurement and modeling', *International journal of food properties* **20**(sup2), 1965–1981.

Sasson, M., Chai, S., Beck, C., Jin, Y. and Rafieshahraki, J. (2016), 'A comparison between smoothed-particle hydrodynamics and RANS volume of fluid method in modelling slamming', *Journal of ocean engineering and science* .

- Schmidt, M. S. (2017), ‘Atmospheric tank failures: mechanisms and an unexpected case study’, *Process Safety Progress* **36**(4), 353–361.
- Shakir, A. S. (2017), Impact Response of recycled aggregate concrete filled steel tube columns strengthened with CFRP, PhD thesis, University of Liverpool.
- Sicklinger, S. (2014), Stabilized co-simulation of coupled problems including fields and signals, PhD thesis, Technical University of Munich.
- Simulia (2016), *Abaqus analysis user guide*.
- Skjold, T., Van Wingerden, K., Abiven, R. and Larsen, O. (2008), Accident investigation following the vest tank explosion at slovag, Technical report, Gexcon.
- Sonin, A. A. (2001), ‘The physical basis of dimensional analysis’.
- Swedish Accident Investigation Board (2008), ‘Olycka med utslapp av svavelsyra vid kemira kemi ab i helsingborg m ian, den 4 februari 2005’.
- Tezduyar, T. E., Sathe, S., Schwaab, M., Pausewang, J., Christopher, J. and Crabtree, J. (2008), ‘Fluid-structure interaction modeling of ringsail parachutes’, *Computational Mechanics* **43**(1), 133–142.
- U.S. Chemical Safety and Hazard Investigation Board (2002), ‘Csb investigation report: refinery incident (1 killed, 8 injured, offsite environmental impact), motiva enterprises llc, delaware city refinery, delaware city, delaware, on july 17, 2001.’.
- U.S. Chemical Safety and Hazard Investigation Board (2009), ‘Investigation report, allied terminal, inc.- catastrophic tank collapse’.  
**URL:** <https://www.csb.gov/allied-terminals-fertilizer-tank-collapse/>
- U.S. Chemical Safety and Hazard Investigation Board (2018), ‘Csb releases factual update on explosion and fire at husky refinery located in Superior, Wisconsin’.  
**URL:** <https://www.csb.gov/csb-releases-factual-update-on-explosion-and-fire-at-husky-refinery-located-in-superior-wisconsin/>

- Voo, J., Foster, S. J., Gilbert, R. I. and Gowripalan, N. (2003), Design of distributed regions in reactive powder concrete bridge girders, *in* ‘High Performance Materials in Bridges’, pp. 117–127.
- Wall, W. and Rabczuk, T. (2008), ‘Fluid-structure interaction in lower airways of ct-based lung geometries’, *International Journal for Numerical Methods in Fluids* **57**(5), 653–675.
- Walton, I. (2014), Containment systems for the prevention of pollution, Technical report, CIRIA.
- Wilcox, D. C. (2006), *Turbulence modeling for CFD, third edition*, DCW Industries.
- Yang, S. L., Millard, S. G., Soutsos, M. N., Barnett, S. J. and Thanh Trung, L. (2009), ‘Influence of aggregate and curing regime on the mechanical properties of ultra-high performance fibre reinforced concrete (uhpfr)’’, *Construction and Building Materials* **23**(6), 2291–2298.
- Yue, W., Lin, C.-L. and Patel, V. C. (2003), Numerical investigation of turbulent free surface flows using level set method and large eddy simulation, Technical report, IIHR-Hydroscience and Engineering, The University of Iowa.

# Appendices

# Appendix A

## CFD appendix

```
1 |*-----* C++ *-----*\
2 | \
3 |  \
4 |   \
5 |    \
6 |     \
7 |      \
8 | FoamFile
9 | {
10 |   version      2.0;
11 |   format       ascii;
12 |   class        volScalarField;
13 |   object       alpha.oil;
14 | }
15 | // *****
16 |
17 | dimensions      [0 0 0 0 0 0];
18 |
19 | internalField   uniform 0;
20 |
21 | boundaryField
22 | {
23 |
24 |   atmosphere
25 |   {
26 |     type          inletOutlet;
27 |     inletValue    uniform 0;
28 |     value         uniform 0;
29 |   }
30 |
31 |   front
32 |   {
33 |     type          zeroGradient;
34 |   }
35 |
36 |   back
37 |   {
38 |     type          zeroGradient;
39 |   }
40 |
41 |   left
42 |   {
43 |     type          zeroGradient;
44 |   }
45 |
46 |   right
47 |   {
48 |     type          zeroGradient;
49 |   }
50 |
51 |   bottom
52 |   {
53 |     type          zeroGradient;
54 |   }
55 |
56 |   bund
57 |   {
58 |     type          zeroGradient;
59 |   }
60 |
61 |   tank
62 |   {
63 |     type          zeroGradient;
64 |   }
65 |
66 |   tank
67 |   {
68 |     type          zeroGradient;
69 |   }
70 |
71 | }
72 |
73 | // *****
74 |
75 |
76 | //
77 |
```

Figure A.1: Boundary conditions for alpha-oil field

```

1  /*----- C++ -----*/
2  |-----|
3  | \ / | F i e l d | OpenFOAM: The Open Source CFD Toolbox
4  |  V  | O p e r a t i o n | Version: 3.0.1
5  | / \ | A n d | web: www.OpenFOAM.org
6  |-----|
7  /*-----*/
8  FoamFile
9  {
10     version      2.0;
11     format        ascii;
12     class         volVectorField;
13     location      "0";
14     object        U;
15 }
16 // *****
17
18 dimensions      [0 1 -1 0 0 0 0];
19
20 internalField   uniform (0 0 0);
21
22 boundaryField
23 {
24     atmosphere
25     {
26     }
27     {
28         type      pressureInletOutletVelocity;
29         value      uniform (0 0 0);
30     }
31
32     front
33     {
34     }
35     {
36         type      fixedValue;
37         value      uniform (0 0 0);
38     }
39
40     back
41     {
42     }
43     {
44         type      fixedValue;
45         value      uniform (0 0 0);
46     }
47
48     left
49     {
50     }
51     {
52         type      fixedValue;
53         value      uniform (0 0 0);
54     }
55
56     right
57     {
58     }
59     {
60         type      fixedValue;
61         value      uniform (0 0 0);
62     }
63
64     bund
65     {
66     }
67     {
68         type      fixedValue;
69         value      uniform (0 0 0);
70     }
71
72     tank
73     {
74     }
75     {
76         type      fixedValue;
77         value      uniform (0 0 0);
78     }
79 }
80
81
82 // *****
83

```

Figure A.2: Boundary conditions for velocity field

```

1  /*----- C++ -----*/
2  |=====|
3  | \ / \ / | F i e l d | OpenFOAM: The Open Source CFD Toolbox
4  |  \ / \ / | O p e r a t i o n | Version: 3.0.1
5  |   \ / \ / | A n d | web: www.OpenFOAM.org
6  |    \ / \ / | M a n i p u l a t i o n |
7  |-----*/
8  FoamFile
9  {
10     version      2.0;
11     format        ascii;
12     class         volScalarField;
13     object        p_rgh;
14 }
15 // ***** //
16
17 dimensions      [1 -1 -2 0 0 0 0];
18
19 internalField   uniform 0;
20
21 boundaryField
22 {
23
24     atmosphere
25     {
26         type      totalPressure;
27         p0        uniform 0;
28         u;
29         phi       phi;
30         rho       rho;
31         psi       none;
32         gamma     1;
33         value     uniform 0;
34     }
35
36     front
37     {
38         type      fixedFluxPressure;
39         value     uniform 0;
40     }
41
42     back
43     {
44         type      fixedFluxPressure;
45         value     uniform 0;
46     }
47
48
49     left
50     {
51         type      fixedFluxPressure;
52         value     uniform 0;
53     }
54
55     right
56     {
57         type      fixedFluxPressure;
58         value     uniform 0;
59     }
60
61     bottom
62     {
63         type      fixedFluxPressure;
64         value     uniform 0;
65     }
66
67     bund
68     {
69         type      fixedFluxPressure;
70         value     uniform 0;
71     }
72
73     tank
74     {
75         type      fixedFluxPressure;
76         value     uniform 0;
77     }
78
79 }
80 }
81
82 // ***** //
83

```

Figure A.3: Boundary conditions for pressure field

```

1  |----- C++ -----|
2  | \ / \ / \ / \ / \ / |
3  |  \ / \ / \ / \ / \ |
4  |   \ / \ / \ / \ / \ |
5  |    \ / \ / \ / \ / \ |
6  |     \ / \ / \ / \ / \ |
7  |      \ / \ / \ / \ / \ |
8  |-----|
9  | FoamFile
10 | {
11 |     version      2.0;
12 |     format        ascii;
13 |     class         volScalarField;
14 |     location      "0";
15 |     object        k;
16 | }
17 | // * * * * * //
18 | dimensions      [0 2 -2 0 0 0];
19 |
20 | internalField   uniform 0.000828;
21 |
22 | boundaryField
23 | {
24 |
25 |     atmosphere
26 |     {
27 |         type      inletOutlet;
28 |         inletValue  uniform 0.000828;
29 |         value      uniform 0.000828;
30 |     }
31 |
32 |     front
33 |     {
34 |         type      kLowReWallFunction;
35 |         value      uniform 0.000828;
36 |     }
37 |
38 |     back
39 |     {
40 |         type      kLowReWallFunction;
41 |         value      uniform 0.000828;
42 |     }
43 |
44 |     left
45 |     {
46 |         type      kLowReWallFunction;
47 |         value      uniform 0.000828;
48 |     }
49 |
50 |     right
51 |     {
52 |         type      kLowReWallFunction;
53 |         value      uniform 0.000828;
54 |     }
55 |
56 |     bottom
57 |     {
58 |         type      kLowReWallFunction;
59 |         value      uniform 0.000828;
60 |     }
61 |
62 |     bund
63 |     {
64 |         type      kLowReWallFunction;
65 |         value      uniform 0.000828;
66 |     }
67 |
68 |     tank
69 |     {
70 |         type      kLowReWallFunction;
71 |         value      uniform 0.000828;
72 |     }
73 |
74 | }
75 |
76 | // * * * * * //
77 |
78 |
79 |
80 |
81 |
82 |
83 |
84 |
85 |
86 |
87 |
88 |

```

Figure A.4: Boundary conditions for turbulent kinetic energy

```

1  /*----- C++ -----*/
2  |-----|
3  | \ / \ / \ / | Field | OpenFOAM: The Open Source CFD Toolbox
4  |  \  \  \  | O peration | Version: 3.0.1
5  |   \   \   | A nd | web: www.OpenFOAM.org
6  |    \    \  | M anipulation |
7  |-----|
8  FoamFile
9  {
10     version      2.0;
11     format       ascii;
12     class        volScalarField;
13     location     "0";
14     object       omega;
15 }
16 // ***** //
17
18 dimensions      [0 0 -1 0 0 0 0];
19
20 internalField   uniform 0.343;
21
22 boundaryField
23 {
24
25     atmosphere
26     {
27         type      inletOutlet;
28         inletvalue uniform 0.343;
29         value     uniform 0.343;
30     }
31
32     front
33     {
34
35         type      omegawallFunction;
36         value     uniform 0.343;
37     }
38
39     back
40     {
41         type      omegawallFunction;
42         value     uniform 0.343;
43     }
44
45     left
46     {
47         type      omegawallFunction;
48         value     uniform 0.343;
49     }
50
51     right
52     {
53         type      omegawallFunction;
54         value     uniform 0.343;
55     }
56
57     bottom
58     {
59         type      omegawallFunction;
60         value     uniform 0.343;
61     }
62
63     bund
64     {
65         type      omegawallFunction;
66         value     uniform 0.343;
67     }
68
69     tank
70     {
71         type      omegawallFunction;
72         value     uniform 0.343;
73     }
74
75     {
76         type      omegawallFunction;
77         value     uniform 0.343;
78     }
79 }
80
81
82 // ***** //
83

```

Figure A.5: Boundary conditions for specific dissipation rate







```

1  /*----- C++ -----*/
2  |=====|
3  | \      | F i e l d | OpenFOAM: The Open Source CFD Toolbox
4  |  \     | O p e r a t i o n | Version: plus
5  |   \    | A n d | web: www.openFOAM.com
6  |    \   | M a n i p u l a t i o n |
7  |-----|
8  FoamFile
9  {
10     version      2.0;
11     format        ascii;
12     class         dictionary;
13     location      "system";
14     object        fvSolution;
15 }
16 // *****
17
18 solvers
19 {
20     "alpha.oil.*"
21     {
22         nAlphaCorr      2;
23         nAlphaSubCycles 1;
24         cAlpha          1;
25
26         MULESCorr       yes;
27         nLimiterIter    3;
28
29         solver          smoothSolver;
30         smoother        symGaussSeidel;
31         tolerance       1e-8;
32         relTol          0;
33     }
34
35     "pcorr.*"
36     {
37         solver          PCG;
38         preconditioner  DIC;
39         tolerance       1e-5;
40         relTol          0;
41     }
42
43     p_rgh
44     {
45         solver          PCG;
46         preconditioner  DIC;
47         tolerance       1e-07;
48         relTol          0.05;
49     }
50
51     p_rghFinal
52     {
53         $p_rgh;
54         relTol          0;
55     }
56
57     "(U|k|omega).*"
58     {
59         solver          smoothSolver;
60         smoother        symGaussSeidel;
61         tolerance       1e-06;
62         relTol          0;
63         minIter         1;
64     }
65 }
66
67 PIMPLE
68 {
69     momentumPredictor  no;
70     nOuterCorrectors   1;
71     nCorrectors        3;
72     nNonOrthogonalCorrectors 0;
73 }
74
75 relaxationFactors
76 {
77     equations
78     {
79         ".*"          1;
80     }
81 }
82
83 // *****
84

```

Figure A.9: fvSolution dictionary



# Appendix B

## FEA appendix

---

**From:** KUERES Karl [<mailto:Karl.KUERES@3ds.com>]  
**Sent:** 24 July 2017 10:00  
**To:** Megdiche, Islem <[I.Megdiche@2015.ljmu.ac.uk](mailto:I.Megdiche@2015.ljmu.ac.uk)>  
**Cc:** DAVIES-TAYLOR Clint <[Clint.DAVIES-TAYLOR@3ds.com](mailto:Clint.DAVIES-TAYLOR@3ds.com)>  
**Subject:** RE: Questions about modelling the bund wall

Hi Islem,

Sorry for the delay in responding.

I have run through some testing on a simple model using the CDP model.

Firstly I wanted to rule out that the application of the loading as a factor in the unsymmetric nature of the results – so to eliminate any potential unsymmetric effects from the SPH/contact I tried with a simple pressure load.

- ➔ Even in this case, following the onset of plasticity, the result is not symmetric. In fact the result (as you have seen in your plots) appears to be quite noisy

I suspect that this is a factor of the brittle nature of the failure/post-yield response of the material. For un-reinforced material the loss of stiffness (one would expect) would be very sudden – this could lead to some numerical sensitivities – including mesh sensitivities as the response could depend on the instant that the material points are calculated to fail.

Have you already tried running the same cases with reinforced concrete? This is typically done using rebar:

Figure B.1: Confirmation of the non-symmetry of the CDP model - email (part 1)

---

## 2.2.4 Defining rebar as an element property

Or else you can use the Embedded Elements technique to embed the reinforcement elements in the concrete mesh:

### 35.4.1 Embedded elements

It would certainly be worth applying some meaningful reinforcements to see if this stabilizes the response.

With regards to the choice between solid or shell elements – this is typically a choice based on geometric conditions and the expected dominant response (in this case for failure).

For your case – if the loading is such that you expect the dominant cause of failure to be through bending then shell elements could be applicable. However on the other hand if you would expect a significant variation of the stress/strain through the thickness of the wall – this would not be captured by shell elements and so several solid elements through thickness would be needed. Also if the impact loading is expected to cause damage through crushing of the concrete – again I think solid elements would be best.

Finally you have asked about optimization – from your description I would suspect that Isight, rather than TOSCA, would be most suitable to allow you to vary different geometry/material/loading parameters. I have copied in my colleague, Clint Davies-Taylor, who can explain which tools you should have access to already and to work through adding any licenses if necessary.

I hope this helps,

Karl

*Best Regards,*

Karl KUERES  
3DEXPERIENCE Engagement Manager, SIMULIA Growth

---

Office: +44 19 2583 0900 (Ext. 1009)



Figure B.2: Confirmation of the non-symmetry of the CDP model - email (part 2)